UNIVERSITAT DE BARCELONA

Compositional and structural characterisation of Ni-phyllosilicates in hydrous silicate type Ni-laterite deposits

Cristina Villanova de Benavent

UNIVERSITAT DE BARCELONA

DEPARTAMENT DE CRISTAL·LOGRAFIA, MINERALOGIA I DIPÒSITS MINERALS
FACULTAT DE GEOLOGIA

Compositional and structural characterisation of Ni-phyllosilicates in hydrous silicate type Ni-laterite deposits

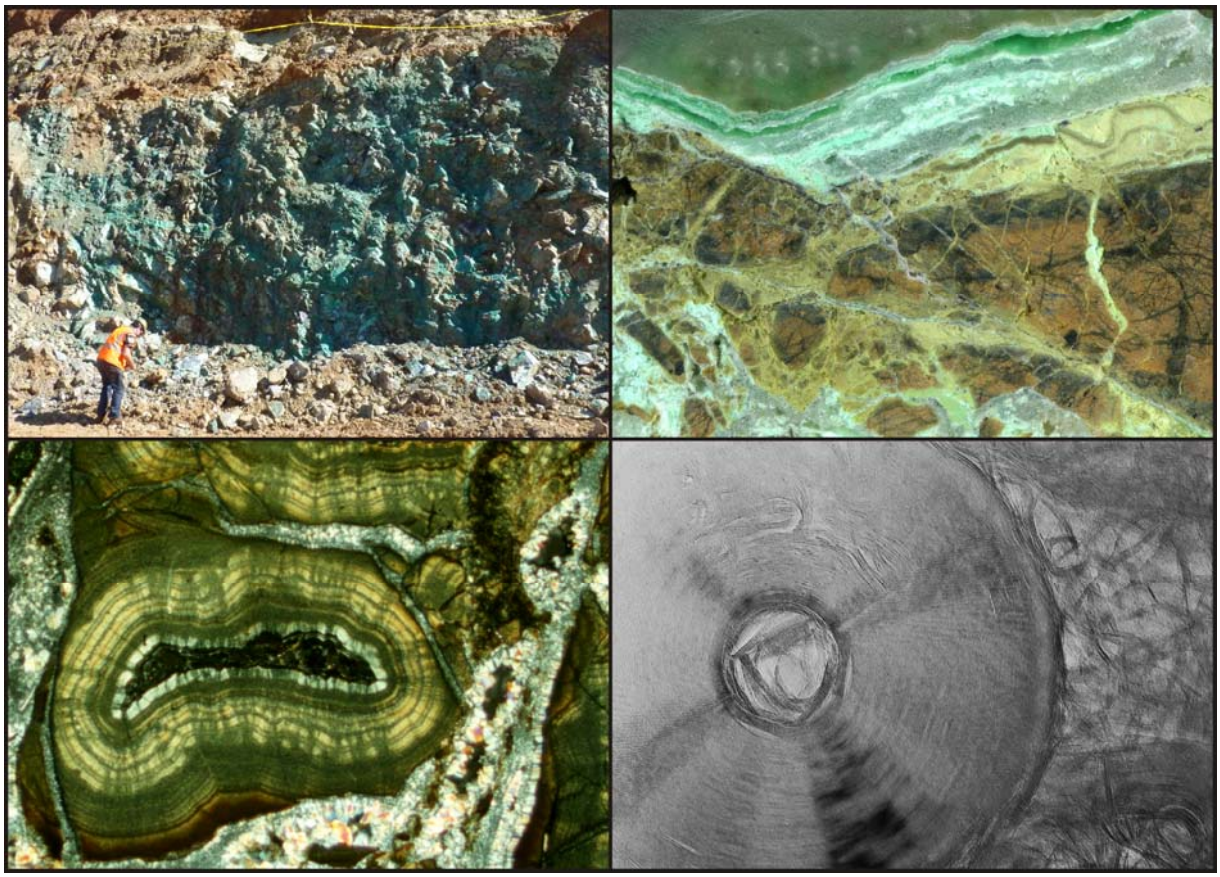

PhD Thesis

Cristina Villanova de Benavent

October 2015

UNIVERSITAT DE BARCELONA
DEPARTAMENT DE CRISTAL·LOGRAFIA, MINERALOGIA I DIPÒSITS MINERALS
FACULTAT DE GEOLOGIA

Compositional and structural characterisation of Ni-phyllosilicates in hydrous silicate type Ni-laterite deposits

Tesi doctoral presentada per
Cristina Villanova de Benavent

Memòria presentada per optar al títol de doctora per la Universitat de Barcelona amb Menció Internacional

Tesi realitzada dins del Programa de Doctorat de Ciències de la Terra per la Universitat de Barcelona, sota la direcció del Dr. Joaquín A. Proenza i el Dr. Salvador Galí

La Doctoranda | Els Directors

Cristina Villanova de Benavent | **Joaquín Antonio Proenza Fernández** | **Salvador Galí i Medina**

Barcelona, octubre de 2015

ACKNOWLEDGEMENTS

First of all, I would like to extend my most sincere thanks to my PhD advisors, Joaquín A. Proenza and Salvador Galí. Their limitless patience, dedication and interest have been a very positive influence during the development of this thesis.

Special thanks are given to Joan Carles Melgarejo, who introduced me to the fascinating world of Mineralogy and who trusted me ten years ago to start a first research work.

This thesis was possible thanks to the hospitality and generosity of the staff in Falcondo Glencore Xstrata Nickel (formerly Falconbridge Dominicana C por A), in particular of Francisco Longo, for the field trip logistics, the inestimable help during sample collection, and field work in general.

I am also grateful to the Emeritus Professor John F. Lewis for his vast knowledge on the geology of Hispaniola, without whom this thesis would not have been possible.

The investigation of Ni-phyllosilicates was conducted thanks to (by order of appearance in Chapter 3: Materials & Methods): Xavier Alcobé and Maria Barba (XRD, CCiT-UB), Maite Garcia-Vallès and Mercedes Aguilar (DTA-TG, UB), Dolors Barso, Montserrat Sibila, Fadoua Zoura Oumada, Vicenç Planella (thin section facility, UB), Jesús Montes Rueda (thin section facility, UGr), Eva Prats, Javier García-Veigas and Anna Domínguez (SEM and FESEM, CCiT-UB), Xavier Llovet (EMP, CCiT-UB), Josep Roqué-Rosell and Fèlix Mata (TEM sample preparation, CCiT-UB), Isabel Nieto, José Damián Montes (TEM sample preparation, UGr), Claudia Magrini (TEM sample preparation, UniSi), Joaquim Portillo, Aránzazu Villuendas, Joan Mendoza (TEM, CCiT-UB), Fernando Nieto and María del Mar Abad (TEM, UGr), Cecilia Viti and Enrico Mugnaioli (TEM, UniSi), Tariq Jawhari (micro-Raman spectroscopy, CCiT-UB), Elena Bailo (micro-Raman spectroscopy, WITec), Josep Roqué-Rosell (X-ray absorption spectroscopy by synchrotron radiation, Diamond Light Source and Lawrence Berkeley Laboratory), Jordi Bellés (flow-through experimental setup, IDAEA-CSIC), Rafael Bartrolí (ICP-AES, IDAEA-CSIC).

I would also like to acknowledge all the coauthors who made accurate scientific revisions of my texts and from whom I learnt some of the secrets of scientific writing: Esperança Tauler, Josep Roqué-Rosell and Cristina Domènech (UB), Fernando Nieto and Antonio García-Casco (UGr), Cecilia Viti (UniSi), Josep Mª Soler and Jordi Cama (IDAEA-CSIC).

The successive anonymous reviewers (and M. Alain Baronnet), who made constructive comments and observations that helped to improve my papers, are also sincerely acknowledged.

It is worth noting that the fruitful conversations with Frederick J. Wicks at the IMA2014 Meeting and with Michel Cathelineau at the SGA2015 Meeting contributed to this thesis as well and deserve to be mentioned here.

In addition, I would like to thank the help extended by some colleagues who provided me rare and/or old papers that completed the list of references for this thesis: Montgarri Castillo i

Oliver (Liversidge, 1874; Maksimović,1973), Sergey Silantsyev (Rukavishnikova, 1956; Vitovskaya & Berkhin, 1968, 1970), Alexander Schopf (Spangenberg, 1938; 1949), Mathieu Chassé (Caillère, 1965). I thank also Alicja Lacinska, for providing me samples LIZ-1 and LIZ-2, Àngels Canals for sample TLC and Esperança Tauler for sample SEP (see Chapter 6).

The administrative help of the secretaries of the Departament de Cristal·lografia, Mineralogia i Dipòsits Minerals (UB) is also gratefully acknowledged, for their patience and ability to solve any kind of issue.

And last but not least, I thank the unconditional support from my parents, Antonio and Guillermina, who always encouraged me to do whatever I wanted in life and to pursue my dreams; from Hèctor, with remarkable patience and kindness; and from my entire family as well. I sincerely thank the scientific and personal support from friends and colleagues, in particular Montgarri Castillo i Oliver, Thomas Aiglsperger, who were excellent office mates; but also Esperança Tauler, Cristina Domènech, Marc Campeny, Sandra Amores, Lídia Butjosa, Amaia Castellano, Lisard Torró, Mariona Tarragó, Raül Benages, Juan Hernández (UB), Pura Alfonso, Abigaíl Jiménez (UPC), Fernando Nieto, Fernando Gervilla, Antonio García-Casco, Idael Blanco, Juan Cárdenas (UGr), Darío Chinchilla, Lorena Ortega, Ricardo Castroviejo (UCM); and specially Cecilia Viti and Enrico Mugnaioli who warmly welcomed me in the Università degli Studi di Siena, and Enrico Capezzuoli, Rocco Novellino, Cristina Fornacelli, Andrea Brogi, Massimiliano Ciacci, Alessio Casagli, Marco Meccheri, Luca Foresi, Ivan Martini, Elisa Ambrosetti, Giovanna Giorgetti, Barbara Terrosi (UniSi), with whom I spent some unforgettable moments during these five years.

This PhD thesis was economically possible thanks to the funding provided by the FPU pre-doctoral and the "Estancias Breves" scholarships given by the Spanish Ministry of Education, the Spanish projects CGL2009-10924, CGL2012-36263 (co-financed by Fondo Europeo de Desarrollo Regional: FEDER), CGL2011-30153 and CGL2012-32169, the Catalan projects SGR 2009-444 and SGR 2014-1661. In addition, the grants given by the Society of Geology Applied to Mineral Deposits (SGA) to attend the 2011, 2013 and 2015 Biennial Meetings; by the International Union of Crystallography to attend the 2013 Meeting of the Spanish Mineralogical Society (SEM), the grants given by the SEM and the International Mineralogical Association (IMA) to attend the 2014 IMA Meeting, and the "Borsa de viatges" travel grants given by the Facultat de Geologia (Universitat de Barcelona) are sincerely acknowledged.

ABSTRACT

Ni-bearing Mg-phyllosilicates (commonly known as garnierites) are significant ore minerals in many Ni-laterite deposits worldwide. However, the characterisation of these mineral phases is complex, as well as their classification and nomenclature, due to their fine-grained nature, low crystallinity and frequent occurrence as mixtures. The aim of this study is to shed some light to the nature of the Ni-bearing Mg-phyllosilicates occurring at the Falcondo Ni-laterite.

In this deposit, these minerals are found within the saprolite horizon mainly as fracture-fillings, coatings on joints and as breccias. The Falcondo garnierites display easily distinguishable different shades of green and characteristic textures, which correspond to different mineral phases. Five garnierite types were defined by X-ray diffraction (XRD), optical and electron microscopy, and electron microprobe (EMP) analyses: I) Ni-Fe-bearing serpentine-like, II) Ni-(Al)-bearing serpentine-like with minor talc-like, III) Ni-rich mixture of serpentine- and talc-like, IV) talc-like and V) sepiolite-falcondoite. The characterisation was completed with differential thermal analysis and thermogravimetry (DTA-TG), transmission electron microscopy (TEM), Raman spectroscopy, microfocus X-ray absorption spectroscopy (μXAS) and dissolution experiments, in order to gain further insight on these mineral phases from different points of view.

EMP oxide totals and DTA-TG indicate that talc-like contain higher H_2O than talc *sensu stricto* (about 4.5% mass loss at 200ºC, and up to 5% at 650ºC), and therefore the names kerolite-pimelite [$(Mg,Ni)_3Si_4O_{10}(OH)_2 \cdot nH_2O$] should be used instead of talc-willemseite [$(Mg,Ni)_3Si_4O_{10}(OH)_2$]. Compositional data showed continuous Mg-Ni solid solution along the joins lizardite-népouite/chrysotile-pecoraite (serpentine-like), kerolite-pimelite (talc-like) and sepiolite-falcondoite. The phases with larger amounts of talc-like displayed the highest Ni contents (up to 2.2 apfu out of 3 octahedral atoms). In addition, EMP analyses of the mixed phases showed deviations from the stoichiometric Mg-Ni solid solutions of serpentine and talc. This is best explained by mixing at the nanoscale, which was confirmed by XRD and high resolution TEM imaging. Furthermore, a detailed textural study by means of EMP quantified X-ray element imaging was used to explain the relationships between textural position, sequence of crystallization and mineral composition of the studied Ni-phyllosilicates. These results indicate several stages of growth with variable Ni content, pointing to recurrent changes in the physical-chemical conditions during the precipitation of the different Ni-phyllosilicates.

HRTEM and low magnification imaging enabled to measure the characteristic basal spacings of these phyllosilicates and to observe a wide variety of nanotextures, respectively: 15-sectored polygonal serpentine, chrysotile tubes, lizardite lamellae, kerolite-pimelite lamellae and sepiolite ribbons. In accordance with EMP results, chemical analyses by TEM showed that Ni is more concentrated in the kerolite-pimelite lamellae than in the serpentine particles. In addition, the HRTEM revealed that kerolite-pimelite lamellae replace the Ni-poor

serpentine particles. These observations evidence the processes of progressive Ni-enrichment within some Ni-bearing Mg-phyllosilicates.

Characteristic Raman bands were observed for serpentine-, talc- and sepiolite-like phases, and therefore this technique allowed discriminating the different garnierite types.

The synchtrotron radiation-based μXAS analyses were conducted to investigate the speciation of Fe (by Fe K-edge X-ray absorption near edge structure, XANES) and the local environment of Ni (by Ni K-edge extended X-ray absorption fine structure, EXAFS). The XANES results indicate that Fe in the weathered saprolite and in the garnierites is mostly oxidised, whereas in the primary serpentine from the ultramafic protolith it is in the ferrous form. The EXAFS spectra indicate that Ni is homogeneously distributed in the unweathered rock, and is accumulated in discrete domains (clusters) in the weathered saprolite and in all the garnierite types.

Finally, the dissolution experiments of a set of garnierites which cover a wide range of mineral compositions at acidic pH suggest that the dissolution rates are faster in serpentine-dominated garnierites than in talc (kerolite)-dominated garnierites or sepiolite-falcondoite, and that the dissolution is not congruent, being the serpentine component the first to dissolve in the garnierite mixtures of serpentine and talc (kerolite).

In summary, the various analytical techniques applied to the garnierites of this study provide an accurate outlook of their complex mineralogy, structures, textures and chemistry at different scales that provides further details on the formation of these Ni-bearing Mg-phyllosilicates in a lateritic environment.

TABLE OF CONTENTS

APPENDIXS

1. INTRODUCTION

1.1. Ni-Co LATERITE DEPOSITS

Ni (±Co) laterite deposits are regoliths formed by the chemical weathering of ultramafic rocks, mainly in tropical and subtropical latitudes (e.g. Elias, 2002; Freyssinet *et al*., 2005; Golightly, 1981). Under the high temperature and intense rainfall, typical of these environments, the most soluble elements (especially Mg and Si) are leached from primary rock-forming ferromagnesian minerals, and the least mobile elements (especially Fe, Al) accumulate in successive horizons of the lateritic profile (e.g. Freyssinet *et al*., 2005; Golightly, 2010 and references therein).

Although Ni (±Co) laterite deposits account only for about 40% of the current world's annual Ni production, they host over 60% of the world land-based Ni resources (Gleeson *et al*., 2003; Kuck, 2013), and the amount of Ni being extracted from laterite ores is increasing steadily (Mudd, 2010). About 10% of the world's Ni resources are found in the Caribbean region, mostly in the northern part, which include the Moa Bay and Punta Gorda deposits in eastern Cuba and the Falcondo deposit in central Dominican Republic (Dalvi *et al*., 2004; Lewis *et al*., 2006; Nelson *et al*., 2011). Other Ni-laterite deposits in the region include the Gloria deposit in Guatemala (Golightly, 2010) and the Meseta de San Felipe deposit in Camagüey in Central Cuba (Gallardo *et al*., 2010a). On the other hand, the major Ni laterite resources in the southern Caribbean include the Cerro Matoso in Colombia (Gleeson *et al*., 2004) and Loma de Hierro in Venezuela (Soler *et al*., 2008), both presently exploited. In terms of production and reserves, the Falcondo deposit is the largest hydrous Mg silicate-type Ni-laterite deposit of the Greater Antilles, with estimated Ni reserves of about 79.2 million dry tonnes at a grade of 1.3 wt.% Ni (Falcondo Annual Report, 2010; http://www.falcondo.com.do/ES/Publicaciones/brochures/Memoria_FALCONDO_2010.pdf).

Although there is no widely accepted terminology and classification, Ni (±Co) laterites are commonly grouped into three categories, according to the main Ni ore assemblage (Brand *et al*., 1998). These include: i) oxide laterite deposits in which the ore assemblage is principally Fe oxyhydroxides; ii) clay silicate deposits dominated by Ni-rich smectites; and iii) hydrous Mg silicate deposits in which the ore is mainly Mg–Ni phyllosilicates (**Fig. 1.1**).

The hydrous Mg silicate deposits generally have the highest Ni grade (1.8–2.5 wt.% Ni) and are characterised by a thick serpentine-dominated saprolite horizon covered by a relatively thin Fe-oxyhydroxide-dominated limonite horizon (laterite *sensu stricto* horizon). The main Ni ores are Ni-bearing serpentines that form the bulk of the saprolite, and "garnierites" (Mg-bearing Ni-phyllosilicates) that occur mostly as veins and fracture coatings concentrated in the lowermost part of the saprolite horizon, toward the base of the profile (e.g. Golightly, 1981; Elias, 2002; Freyssinet *et al*., 2005; Butt & Cluzel, 2013). These deposits are formed under conditions of a low water table and continuous tectonic uplift (Butt & Cluzel, 2013; Freyssinet *et al*., 2005).

1.2. MINERALOGY OF NI-PHYLLOSILICATES

1.2.1. Definition of "garnierite"

The term “garnierite” is widely used in the literature to refer to the group of green, fine-grained, poorly crystallized Ni-bearing magnesium phyllosilicates, which include serpentine, talc, sepiolite, smectite and chlorite; often occurring as mixtures (e.g. Faust, 1966; Brindley & Hang, 1973; Springer, 1974; Brindley, 1978).

1.2.2. Nomenclature

"Garnierite" was initially the name of a single mineral species found in New Caledonia (Garnier, 1867), despite it was later proved to be a mixture of different Ni-hydrous silicates (e.g. Garnier, 1867; Pecora et al., 1949). Before and after its discovery in 1863, several names were proposed to designate other newly found Ni-Mg-phyllosilicates, such as nouméite, pimelite, alipite, desaulesite, revdanskite, röttisite, schuchardite, deweylite, gymnite, genthite and maufite (e.g. Liversidge, 1874b; Pecora et al., 1949; Faust, 1966) (**Table 1.1**). However, garnierite

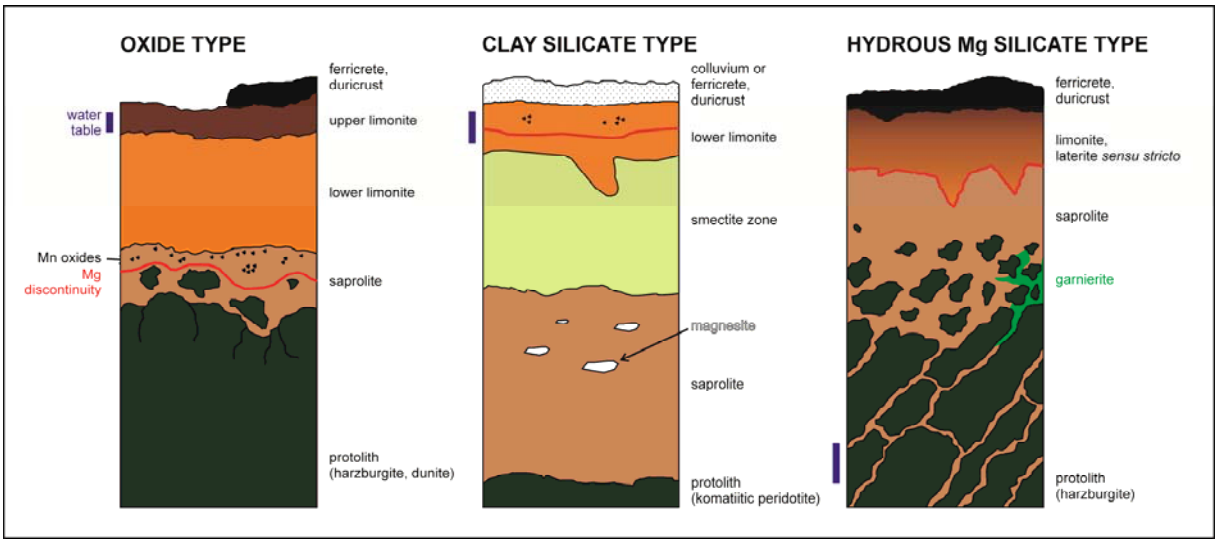

FIGURE 1.1. Schematic profiles of the three types of Ni-Co-laterites (based on Trescases, 1986; Elias *et al*., 2002; Gleeson *et al*., 2003; Freyssinet *et al*. 2005; Golightly, 2010; Butt *et al*., 2013).

and these other names were not recognized as new mineral species by the Commission on New Minerals, Nomenclature and Classification of the International Mineralogical Association (CNMNC-IMA). Later on garnierite became a convenient field term used by mine geologists to designate all green Ni-phyllosilicates (including even those reported before the discovery of garnierite *sensu stricto*) when more specific characterization was not possible (Brindley, 1978), and many authors used this term with this general meaning (Moraes, 1935; Pecora & Hobbs, 1942; Pecora *et al*., 1949; Lacroix, 1942; Varela, 1984). In order to avoid misunderstandings in this work, hereafter the name "garnierite" will be used as the general term, whereas "garnierite *sensu stricto*" will be applied to the individual mineral species described in New Caledonia.

Of all the aforementioned Ni-phyllosilicate names, only népouite (Ni-lizardite), pecoraite (Ni-chysotile), willemseite (Ni-talc), falcondoite (Ni-sepiolite) and nimite (Ni-chlorite) are valid species for the CNMNC. The other names used in the early studies to refer to newly-discovered species of related phyllosilicates became obsolete, or were found to be repetitive or to designate mixtures, not individual species. Many authors tried to compare their physical properties, textural features and mineral chemistry (e.g. Clarke, 1888, 1890, 1920; Liversidge, 1874b). Finally, Caillère (1936), Selfridge (1936), Alexeeva & Godlevsky (1937) and Spangenberg (1938) concluded that garnierite, nouméite, népouite and revdanskite, genthite, connarite, deweylite and maufite are not specific minerals, some are closely related if not identical, and are mixtures of different hydrated silicates (Genth, 1875; Caillère, 1936; Selfridge, 1936; Alexeeva & Godlevsky, 1937; Spangenberg, 1938; Pecora *et al*., 1949; Faust & Fahey, 1962; Faust, 1966; Burke, 2006).

In particular, garnierite and nouméite designated initially the same species. However, the mineral was finally called garnierite, and nouméite was given to another Ni-bearing silicate found in the same area in New Caledonia (Liversidge, 1874a; 1874b). Also, deweylite was described by Garnier (1878) as a nickel-free garnierite *sensu stricto*. Faust (1966) mentioned that deweylite is an equivalent name for gymnite. Ni-bearing gymnite was reported by Genth (1851) in Pennsylvania and was later called genthite by Dana (1867). This term was used to designate a nickel-bearing mineral found in the deposits of Riddle, Oregon (Clarke, 1888; Kay, 1906; Diller & Kay, 1924; Pecora & Hobbs, 1942; Pecora *et al*., 1949) and Webster, North Carolina (Ross *et al*., 1928). According to Faust (1966), röttisite, desaulesite and revdanskite are synonyms for pimelite. In addition, in some studies the name kerolite was used to classify some of the Ni-phyllosilicates into two groups: α-kerolite referred to the serpentine-like phases, whereas β-kerolite was used for the talc-like minerals (e.g. Rukavishnikova, 1956; Caillère & Hénin, 1957; Varela, 1984). Regardless of the lack of consensus

TABLE 1.1. Summary of the names used in the literature to refer to Ni-bearing Mg-phyllosilicates along history.

NAME	TYPE LOCALITY	DEFINITION	OTHER NAMES	CHEMICAL FORMULAE	IMA STATUS	REFERENCES
Garnierite *sensu stricto*	New Caledonia (Garnier, 1867, 1876)	Mixture of pimelite and serpentine-group minerals (Faust, 1966), variety of nouméite (Des Cloizeaux, 1878)	-	$(Mg,Ni)^{10}Si^{8}$ + 3H [Liversidge, 1874b; Brush, 1872; Dana 1875]; (Mg,Ni)Si + nH [Garnier, 1878]	Not approved	Garnier (1867), Brush (1872), Liversidge (1874a, 1874b), Dana (1875), Typke (1876), Garnier (1876, 1878), Des Cloizeaux (1878), Hood (1883), Pecora *et al*. (1949), Huggins (1961), Kato (1961), Faust (1966), Springer (1974), Wells *et al*. (2009)
noumeïte	Nouméa, New Caledonia (Liversidge, 1874b, 1888)	Mixture of pimelite and serpentine-group minerals (Faust, 1966)	nouméite (Glasser, 1907), nouméaite (Clarke, 1890)	-	Not approved	Liversidge (1874a, 1874b, 1880), Des Cloizeaux (1878), Hood (1883), Faust (1966)
népouite	Népoui, New Caledonia (Glasser, 1907)	Ni equivalent of lizardite (Brindley & Wan, 1975)	antigorite nickelifère (Glasser, 1907; Caillère, 1936), α-kerolite (Rukavishnikova, 1956; Caillère & Hénin, 1957)	$2SiO^{2}$, 3(Ni,Mg)O, $2H^{2}O$ [Glasser, 1907], $(Ni_{1.59}Mg_{0.67}Fe^{3+}_{0.05})_2Si_{2.17}Al_{0.22}O_5(OH)_4$ [Wells *et al*., 2009]	Valid (pre-IMA - "grandfathered")	Glasser (1907), Caillère (1936), Gritsaenko *et al*. (1943), Rukavishnikova (1956), Maksimović (1973, 1975), Springer (1974), Brindley & Wan (1975)
pecoraite	Wolfe Creek meteorite crater, Halls Creek Shire, Western Australia, Australia (White *et al*., 1967; Faust et al., 1969)	Ni equivalent of chrysotile (Faust *et al*., 1969)	Ni-clinochrysotile (Faust *et al*., 1969)	$Ni_{5.41}Mg_{0.10}Fe^{2+}_{0.08}Al_{0.22}Si_{4.05}O_{10}(OH)_8$ [Faust *et al*., 1969]	Approved (Fleischer, 1969)	White *et al*. (1967), Faust *et al*. (1969), Fleischer (1969), Faust *et al*. (1973), Nickel (1973), Nickel *et al*. (1979), Bailey (1980), Milton *et al*. (1981), Milton *et al*. (1983), Frost *et al*. (2008)
karpinskite	Mednorudyanskoye Cu Deposit, Nizhny Tagil, Sverdlovskaya Oblast', Middle Urals, Urals Region, Russia (Rukavishnikova, 1956)	-	-	(Ni,Mg)O $2SiO_2$ H_2O [Rukavishnikova, 1956], $(Mg_{1.30}Ni_{0.70})Si_2O_5(OH)_2$ [Anthony *et al*., 2001]	Questionable/ doubtful (Fleischer, 1957; Nickel & Nichols, 2009)	Rukavishnikova (1956), Fleischer (1957a, 1957b), Spencer (1958), Anthony *et al*. (2001), Nickel & Nichols (2009)
willemseite	Scotia Talc Mine, Barberton Mountain, Transvaal, South Africa (Hiemstra & De Waal, 1968b)	Ni equivalent of talc	-	$H_{3.67}(Ni_{4.23}Mg_{1.61}Fe^{3+}_{0.20}Fe^{2+}_{0.04}Co_{0.06}Ca_{0.05})(Si_{7.89}Al_{0.07})O_{24}$ [De Waal, 1970b], $(Ni_{3.4}Mg_{2.2}Fe^{3+}_{0.4})(Si_{7.8}Al_{0.08})O_{20}(OH)_4$ [Villanova-de-Benavent *et al*., 2014d]	Approved (Fleischer, 1969)	Hiemstra & De Waal (1968b), Fleischer (1969), De Waal (1970b), Bailey (1980), Villanova-de-Benavent *et al*. (2014d)

TABLE 1.1. (CONTINUED).

NAME	TYPE LOCALITY	DEFINITION	OTHER NAMES	CHEMICAL FORMULAE	IMA STATUS	REFERENCES
kerolite	Ząbkowice-Frankenstein, Lower Silesia, Dolnośląskie, Poland (Breithaupt, 1923)	Structure with talc affinity with extra water (Brindley, 1978)	cerolite (Brindley *et al*., 1977)	$R_3Si_4O_{10}(OH)_2.nH_2O$ with R mainly Mg and n about 0.8-l.2 [Brindley *et al*., 1977], $(Mg,Ni)_{3.04}(Al,Fe)_{0.01}(Si_{3.93}Al_{0.02}Fe_{0.02})O_{10}(OH)_2 \cdot 0.89H_2O$ [Brindley *et al*., 1979]	Discredited (Nickel & Nichols, 2009)	Genth (1891), Breithaupt (1923), Maksimović (1966), Stoch (1974), Brindley *et al*. (1977), Brindley *et al*. (1979), Bailey (1980)
pimelite	Kosemütz, near Frankenstein, Upper Silesia, Poland (Klaproth, 1788; Karsten, 1800)	Ni equivalent of kerolite (Maksimović, 1966)	grüner chrysopraserde (Klaproth, 1788), β-kerolite (Rukavishnikova , 1956)	$(Mg,Ni)_{3.04}(Al,Fe)_{0.01}(Si_{3.93}Al_{0.02}Fe_{0.02})O_{10}(OH)_2 \cdot 0.89H_2O$ [Brindley *et al*., 1979]	Discredited 2006 (Burke, 2006)	Klaproth (1788), Karsten (1800), Liversidge (1874b), Hood (1883), Spangenberg (1938), Faust (1966), Manceau & Calas (1985), Decarreau *et al*. (1987), Burke (2006)
falcondoite	mined by Falconbridge Dominicana C. por A., Dominican Republic (Springer,	Ni equivalent of sepiolite (Springer, 1976)	-	$\{(Ni_{0.58}Mg_{0.42})_8 \cdot (H_2O)_4 \cdot (OH)_4(Si_{12}O_{30})\} \cdot (H_2O)_8$ [Springer, 1976], $(Mg_{7.32\text{-}5.18}Ni_{0.67\text{-}2.81})Si_{12}O_{30}(OH)_4(OH_2)_4 \cdot 8(H_2O)$ [Tauler *et al*., 2009]	Approved 1976 (Springer, 1976)	Walker (1888), Caillère (1936), Hotz (1964), Faust (1966), Maksimović (1969), Springer (1976), Bailey (1980), Tauler et al. (2009)
brindleyite	Marmara bauxite deposit, Megara, Western Attikí, Greece (Maksimović, 1972)	Ni equivalent of amesite (Mg-Al-serpentine) and berthierine (Fe-Al-serpentine) (Fleischer, 1973)	nimesite (Maksimović, 1972)	$(Ni_{2.56}Mg_{0.51}Fe_{0.34}Al_{1.74}Ti_{0.08})_8(Si_{2.54}Al_{1.46}) \cdot (OH)_{9.02}$, $(Ni_{1.81}Mg_{0.54}Fe_{0.27}Al_{2.50}Ti_{0.08})_8(Si_{2.62}Al_{1.38}) \cdot (OH)_{8.0}$ [Maksimović, 1972]	Approved 1973 (Fleischer, 1973)	Maksimović (1972), Fleischer (1973), Maksimović & Bish (1978)
nimite	Scotia Talc Mine, Barberton Mountain, Transvaal, South Africa (Hiemstra & De Waal, 1968a)	Ni equivalent of clinochlore ($Mg\text{-}Fe^{2+}$-chlorite)	schuchardite (Fleischer, 1969)	$H_{15.42}(Ni_{5.23}Mg_{3.33}Fe^{3+}_{0.72}Fe^{2+}_{0.51}Co_{0.07}Ca_{0.09}Mn_{0.01}Al_{1.97})(Si_{6.02}Al_{1.98})O_{36}$ [De Waal, 1970a], $(Ni_{4.5}Mg_{4.0}Al_{2.0}Fe^{2+}_{1.3}Fe^{3+}_{0.1})(Si_{6.2}Al_{1.8})O_{20}(OH)_{16}$ [Villanova-de-Benavent *et al*., 2014d]	Approved (Fleischer, 1969)	Hiemstra & De Waal (1968a), Fleischer (1969), De Waal (1970a), Bailey (1980), Villanova-de-Benavent *et al*. (2014d)
deweylite	-	Mixture of lizardite and stevensite (Faust & Fahey, 1962), Ni-free garnierite (Garnier, 1878), gymnite (Genth, 1875; Faust, 1966), variety of gymnite (Genth, 1851)	-	$4MgO\ 3SiO_2\ 6H_2O$ [Genth, 1874, Palache, 1935], $(Mg_{4.83}Fe^{2+}_{0.45}Ca_{0.02})Si_{4.60}O_{10}(OH)_8$ [Faust & Fahey, 1962]	Not approved	Genth (1875, 1891), Garnier (1878), Kato & Minato (1960), Kato (1961), Lapham (1961), Faust & Fahey (1962), Morandi & Poppi (1971), Speakman & Majumdar (1971), Fleischer (1975), Bish & Brindley (1978), Bailey (1980)

TABLE 1.1. (CONTINUED).

NAME	TYPE LOCALITY	DEFINITION	OTHER NAMES	CHEMICAL FORMULAE	IMA STATUS	REFERENCES
gymnite	-	deweylite (Genth, 1875; Faust, 1966)	-	-	Not approved	Genth (1875), Faust (1966)
genthite	Pennsylvania, USA (Genth, 1874)	Mixture of pimelite and Ni-serpentine (Faust, 1966), nickel-gymnite (Genth, 1875)	-	2NiO 2MgO $3SiO_2$ $6H_2O$ [Palache, 1935]	Not approved	Genth (1851, 1891), Dana (1867), Liversidge (1874b), Clarke (1888, 1890), Kay (1906), Diller & Kay (1924), Ross (1925), Ross *et al.* (1928), Palache (1937), Pecora & Hobbs (1942), Pecora *et al*. (1949)
connarite	Hans Georg mine, Röttis, Sachsen, Germany (Breithaupt, 1859)	Mixture (Faust, 1966), member of the schuchardite group (Spangenberg, 1938)	comarite (Glasser, 1907), komarite, conarite, konnarite	$(Ni,Mg)_8(Si_4O_{10})_3(OH)_4 \cdot 6H_2O$ [Berman, 1937]	Not approved	Breithaupt (1859), Glasser (1907), Berman (1937)
röttisite	Hans Georg mine, Röttis, Sachsen, Germany (Breithaupt, 1859)	pimelite (Faust, 1966)	-	-	Not approved	Breithaupt (1859), Faust (1966)
de saulesite	Franklin, New Jersey, USA (Koenig, 1889)	pimelite (Faust, 1966), a variety of genthite, same as genthite with magnesia lacking (Wilkerson, 1962)	-	4NiO $3SiO_2$ $6H_2O$ [Palache, 1937]	Not approved	Koenig (1889), Wilkerson (1962), Faust (1966)
revdanskite	Revdinsk, Ural Mountains, Russia (Hermann, 1867)	quartz with pimelite (Faust, 1966)	refdanskite, revdinite, revdinskite, rewdanskite, rewdjanskit, rewdinskit	-	Not approved	Herman (1867), Liversidge (1874b), Faust (1966)
alipite	Frankenstein, Poland (Schmidt, 1844)	Chemically similar to willemseite ≠ spec. grav. (Liversidge, 1874b), pimelite (Faust, 1966)	alizit, aalizite, alipidite	-	Not approved	Schmidt (1844), Glocker (1846), Liversidge (1874b), Faust (1966)
maufite	Umvukwe, Great Dyke, Zimbabwe (Keep, 1930)	Interstratified clinochlore-lizardite (Burke, 2006)	-	(Mg,Ni,Fe,O) $2Al_2O_3$ $3SiO_2$ $4H_2O$ [Keep, 1930]; $MgAl_4Si_3O_{13} \cdot 4H_2O$ [Nickel & Nichols, 2009]	Not approved	Keep (1930a, b), Foshag (1930), Burke (2006), Wicks *et al.* (in press)

on the Ni-Mg-phyllosilicates nomenclature, the invalid name garnierite as a general term has been used during the following decades (e.g. Gleeson *et al*., 2003; Freyssinet *et al*., 2005; Proenza *et al*., 2008; Tauler *et al*., 2009; Wells *et al*., 2009; Galí *et al*., 2012; Villanova-de-Benavent *et al*., 2014b).

However, some Ni-bearing Mg-phyllosilicates are accepted mineral species by the CNMNC, such as willemseite (Ni analogue of talc) and nimite (Ni-dominant mineral of the chlorite group). Both were firstly reported in Bon Accord, Barberton District, South Africa (Hiemstra & De Waal, 1968a, b), and a detailed characterisation of both was later published (De Waal, 1970a, b).

For a summarised nomenclature of Ni-bearing Mg-phyllosilicates see **Table 1.1**, and a more detailed list is included in the **Appendix A1.1**.

1.2.3. Classification

Along history and worldwide, several works published data on garnierites, and many papers tried to summarise nomenclatures following different criteria. However, the classification and nomenclature of Ni-bearing Mg-phyllosilicates represents a complex, long-lasting controversy, because of their fine-grained nature, poor crystallinity and frequent occurrence as intimate mixtures of different mineral species (Brindley & Hang, 1973). Brindley and co-authors, after various studies, distinguished two groups of garnierites (Brindley & Hang, 1973; Brindley & Maksimović, 1974; Brindley, 1978, 1980). The first group includes the 1:1 layer minerals: lizardite-népouite, chrysotile-pecoraite and berthierine-brindleyite; and the second group comprises the 2:1 layer minerals: talc-willemseite, kerolite-pimelite, clinochlore-nimite, and sepiolite-falcondoite. The most common garnierites found in nature are lizardite-népouite and kerolite-pimelite (Brindley, 1978). For these minerals, the terminology "serpentine-like" (or "7 Å-type") and "talc-like" (or "10 Å-type") garnierites, respectively, has been widely used (Brindley & Hang, 1973, Brindley & Maksimović , 1974; Wells *et al*., 2009; Galí *et al*., 2012). In addition, an intermediate phase between talc-like and serpentine-like end members, karpinskite and its Ni equivalent, Ni-karpinskite $(Mg,Ni)_2Si_2O_5(OH)_2$, was reported by Rukavishnikova (1956), but it is not accepted by the CNMNC (Nickel & Nichols, 2009).

All these phyllosilicate series have in common the substitution of Mg by Ni in the octahedral layer, and this cation exchange is possible thanks to the similar size (ionic radii) and charge of Mg and Ni (Brindley, 1978). Actually, Klaproth and Garnier already noticed the inverse relationship between NiO and the sum ∑(MgO+FeO) (Faust, 1966; Garnier, 1878).

As a summary, the current classification of Ni-bearing Mg-phyllosilicates is shown in **Table 1.2**.

Serpentine-like

Although Faust (1966) reported that three Ni-bearing species of the serpentine group had been detected (Ni-chrysotile, Ni-lizardite and Ni-antigorite), very few studies on Ni-antigorite are found. Brindley (1978) stated that Ni-dominant antigorite has not so far been identified. On one hand, népouite, the nickel analogue of lizardite was named after the type locality, Népoui (New Caledonia), and the first description and chemical data in literature appear in Glasser (1907). In some later studies "antigorites nickélifères" was used as a synonym of népouite (e.g. Caillère, 1936). Further data on népouite was published by Gritsaenko *et al.* (1943), Maksimović (1973, 1975), Brindley & Wan (1975) and Manceau & Calas (1985a). Appart from New Caledonia, other localities mentioning the presence of népouite are South Africa (De Waal, 1978; 1979), Serbia (Maksimović, 1973), Russia (Talovina *et al*., 2008) and Morocco (Brindley & Maksimović, 1975). On the other hand, pecoraite was first mentioned in the Wolfe Creek meteorite crater (Western Australia) as the nickel analogue of clino-chrysotile (White *et al.*, 1967). Afterwards it was studied in detail by Faust and coauthors, who named it after W. T. Pecora (Faust *et al*., 1969). Pecoraite was also reported and analysed in the Nullagine region (Western Australia) in an oxidised Ni-sulphide ore (Nickel *et al*., 1977; 1979), in Pennsylvania (USA) in chromite ore (Hess, 1980), and in Missouri (USA) in quartz and calcite geodes as a replacement of millerite (Milton *et al*., 1983).

Talc-like

First, it is worth noting that the term "talc-like" does not refer to the normal composition and/or structure of talc (Brindley & Hang, 1973). Actually, the characterisation of talc-like garnierites is controversial. Maksimović (1966) was the first to differences (Brindley, 1978). Both kerolite and

TABLE 1.2. Summary of the classification of Mg-Ni phyllosilicates, including the ideal structural formulae and the classification codes by Dana (Gaines *et al*., 1997) and Nickel-Strunz (Strunz & Nickel, 2001). Not recognised mineral names are written in *italics*.

	Ideal formula	Dana classification	Nickel-Strunz classification
1:1 layer silicates			
Kaolinite-serpentine group		71.1 (Phyllosilicates, sheets of 6-membered rings with 1:1 layers)	9.ED (Silicates-germanates, phyllosilicates with kaolinite layers composed of tetrahedral and octahedral nets)
Lizardite	$Mg_3Si_2O_5(OH)_4$	71.1.2b.2	9.ED.15
Népouite	$Ni_3Si_2O_5(OH)_4$	71.1.2b.3	9.ED.15
Chrysotile	$Mg_3Si_2O_5(OH)_4$	71.1.5.1	9.ED.15
Pecoraite	$Ni_3Si_2O_5(OH)_4$	71.1.2d.4	9.ED.15
Berthierine	$(Fe,Mg,Al)_3Si_2O_5(OH)_4$	71.1.2c.2	9.ED.15
Brindleyite	$(Ni,Al)_3(Si,Al)_2O_5(OH)_4$	71.1.2c.3	9.ED.15
2:1 layer silicates			
Pyrophyllite-talc group		71.2 (Phyllosilicates, sheets of 6-membered rings with 2:1 layers)	9.EC (Silicates-germanates, phyllosilicates with mica sheets, composed of tetrahedral and octahedral nets)
Talc	$Mg_3Si_4O_{10}(OH)_2$	71.2.1.3	9.EC.05
Willemseite	$Ni_3Si_4O_{10}(OH)_2$	71.2.1.4	9.EC.05
Kerolite	$Mg_3Si_4O_{10}(OH)_2{\cdot}nH_2O$	-	-
Pimelite	$Ni_3Si_4O_{10}(OH)_2{\cdot}nH_2O$	-	-
Chlorite group		71.4 (Phyllosilicates, sheets of 6-membered rings interlayered 1:1, 2:1 and octahedra)	9.EC (Silicates-germanates, phyllosilicates with mica sheets, composed of tetrahedral and octahedral nets)
Clinochlore	$(Mg,Fe^{2+})_6(Si,Al)_4O_{10}(OH)_8$	71.4.1.4	9.EC.55
Nimite	$(Ni,Mg,Al)_6(Si,Al)_4O_{10}(OH)_8$	71.4.1.5	9.EC.55
Sepiolite group		74.3 (Phyllosilicates, modulated layers with joined strips)	9.EE (Silicates-germanates, phyllosilicates, single tetrahedral nets of 6-membered rings connected by octahedral nets/bands)
Sepiolite	$Mg_4Si_6O_{15}(OH)_2{\cdot}6H_2O$	74.3.1b.1	9.EE.25
Falcondoite	$Ni_4Si_6O_{15}(OH)_2{\cdot}6H_2O$	74.3.1b.2	9.EE.25

pimelite have been historically classified as either members of the talc group or of the smectite group by different authors. Faust (1966) reported that pimelite behaved as a montmorillonite group-mineral under the optical microscope as seen in Beyschlag & Krusch (1913), and this was confirmed by X-ray powder diffraction (Spangenberg, 1938). However, many studies misidentified the starting material as pimelite and reached erroneous conclusions. A significant literature exists verifying that pimelite has a structure with talc affinity. Many authors proved that kerolite and pimelite do not exhibit intracrystalline swelling (e.g. Slansky, 1955; Maksimović, 1973; Brindley & Hang, 1973). In addition, according to Guggenheim *et al*. (2006), these mineral phases are 2:1 layer trioctahedral phyllosilicates without interlayer positions, so they belong to the talc-pyrophillite group. However, according to Brindley (1978), 2:1 phyllosilicates with small particle size cannot be classified sharply as swelling or non-swelling minerals, because this feature depends on the amount of swelling and non-swelling layers interstratified.

The main difference with talc and its Ni analogue willemseite, is that kerolite and pimelite contain extra water in their strucures, being their ideal structural formulae $(Mg,Ni)_2Si_2O_5(OH)_2{,\cdot}nH_2O$ with n between 0.75 and 1.25 (Brindley, 1978). At first, the additional water was thought to occupy interlayer positions based on $d_{(001)}$ ~ 10 Å (like cations in micas) (Brindley & Hang, 1973). However, afterwards some data stated that $d_{(001)}$ ~ 9.5-9.6 Å, so the last explanation is either invalid or incomplete. Much of the excess water is removable at temperatures up to 300ºC and probably occupies external positions (Brindley *et al*., 1979). The presence of molecular water in kerolite and pimelite was proven by IR spectrometry with the absorption in the 1900 nm band (Brindley *et al*., 1979). The large surface area of these minerals and the small crystal size are coherent with a large amount of adsorbed water (Brindley, 1978). The slightly

increased spacing with respect to that of talc (9.35 Å) may account for random layer stacking in kerolite-pimelite, compared to close packed talc layers (Brindley, 1978).

Despite both the Mg and Ni talc-like end members kerolite and pimelite, respectively, are discredited mineral species by the CNMNC (Nickel & Nichols, 2009), they are included in the recommendations for the nomenclature of phyllosilicates by the Association Internationale Pour l'Étude des Argiles (AIPEA; Guggenheim *et al*., 2006) and these names are still used nowadays (Wells *et al*., 2009; Proenza *et al*., 2008; Galí *et al*., 2012; Villanova-de-Benavent *et al*., 2014b; 2014c; Cathelineau *et al*., 2014; 2015).

1.2.4. Worldwide distribution

Ni-bearing Mg-phyllosilicates have a widespread distribution around the world. They have been extensively described in New Caledonia (e.g. Kato, 1961; Caillère, 1965; Troly *et al.*, 1979; Pelletier, 1983; Wells *et al*., 2009), but some other important occurrences have been reported in Australia (Nickel, 1973; Nickel *et al*., 1979; Elias *et al.*, 1981; Gaudin *et al*., 2004a; 2004b; 2005), Brazil (Pecora, 1944; Brindley & de Souza Jefferson, 1975; Esson & Carlos, 1978; Barros de Oliveira, 1995; Colin *et al*., 1985; 1990), Colombia (Lopez-Rendon, 1986; Gleeson *et al*., 2004), Cuba (Proenza *et al*., 2007a), Czech Republic (Brindley *et al*., 1979), the Dominican Republic (Brindley & Wan, 1975; Springer, 1976), Germany (Springer, 1974), Greece (Brindley & Wan, 1975), Indonesia (Golightly, 1979; Fu *et al*., 2010; 2014; Sufriadin *et al*., 2011; 2012), India (Naganna & Phene, 1968; Som & Joshi, 2002), the Ivory Coast (Nahon *et al*., 1982), Japan (Sudo & Anzai, 1942), Kosovo (Brindley & Hang, 1973; Brindley *et al*., 1979), Madagascar (Brindley, 1978), Morocco (Ducloux *et al*., 1993; Favreau & Dietrich, 2006), the Philippines (Ogura, 1986; Wang, 2010), Poland (Spangenberg, 1938; Spangenberg & Müller, 1949; Haranczyk & Prchazka, 1974; Wiewióra, 1978; Wiewióra *et al*., 1982; Dubińska *et al*., 2000), Russia (Rukavishnikova, 1956; Vitovskaya & Berkhin, 1968; 1970; Talovina *et al*., 2008; 2009), Serbia (Maksimović, 1973; Brindley *et al*., 1979), South Korea (Song *et al*., 1995), Spain (Suárez *et al*., 2011), Taiwan (Brindley & Wan, 1975), the United States of America (e.g. Genth, 1891; Ross & Shannon, 1926; Pecora & Hobbs, 1942; Montoya & Baur, 1963) and Venezuela (Soler *et al*., 2008).

Most of these Ni-bearing Mg-phyllosilicates are formed after weathering of ultramafic rocks in laterites, however, some may have a hydrothermal origin, like Bou Azzer in Morocco (Ducloux *et al*., 1993) and those found in the Urals Region (e,g, Talovina *et al*., 2008; 2009). Furthermore, others may form in other settings, such as from alteration of the Wolfe Creek meteorite, in which pecoraite was described for the first time (White *et al*., 1967; Faust *et al*., 1969; Faust *et al*., 1973), the particular Bon Accord orebody, in South Africa (also supposedly a meteorite occurrence; De Waal & Hiemstra, 1968a; 1968b; De Waal, 1970a; 1970b; De Waal, 1978; 1979; Tredoux *et al*., 1989), in which willemseite was firstly reported; and from weathering of a Ni sulfide deposit in Western Australia (Nickel & Bridge, 1975; Nickel *et al*., 1977).

In the case of the Falcondo Ni-laterite deposit, in the Dominican Republic, as a result of the Al-poor nature of the ultramafic protolith, previous results have shown that garnierites consist mainly of the combination of three solid solutions: serpentine-like $[(Mg,Ni)_3Si_2O_5(OH)_4]$, talc-like $[(Mg,Ni)_3Si_4O_{10}(OH)_2\cdot(H_2O)]$ and sepiolite–falcondoite $[(Mg,Ni)_4Si_6O_{15}(OH)_2\cdot 6(H_2O)]$ (Proenza *et al*., 2008; Tauler *et al*., 2009; Galí *et al*., 2012). However, except for the sepiolite–falcondoite series (Springer, 1976; Tauler *et al*., 2009), little work has been done on the mode of occurrence, textures and composition of these Ni-phyllosilicates.

A detailed list of Ni-phyllosilicate occurrences is included in **Appendix A1.2**.

1.2.5. State of the art

Early studies

The vast majority of the studies on garnierites are based on classical or conventional mineral identification techniques. Bulk compositions obtained by traditional chemical techniques and other methods that required sample grinding (infrared spectroscopy, X-ray diffraction, thermal analysis and thermogravimetry) are available from early publications (e.g. Liversidge, 1874b; Genth, 1891; Glasser, 1907; Ross *et al*., 1928; Pecora *et al*., 1949; Rukavishnikova, 1956; Montoya & Baur, 1963). Most detailed studies date from the late 1960s to early 1980s (Brindley & Hang, 1973; Springer, 1974; Brindley & Wan, 1975, Brindley *et al*., 1979; Brindley *et al*., 1980) and recent works

are scarce (e.g. Song *et al*., 1995; Pelletier, 1996; Talovina *et al*., 2008; Sufriadin *et al*., 2012; Villanova-de-Benavent *et al*., 2014b).

It is only in the past few years that detailed additional information, including mode of occurrence in the field, petrography and relations between garnierites and their host rocks, is provided (Cluzel & Vigier, 2008; Wells *et al*., 2009) and new cutting edge techniques have been used, like transmission electron microscopy (TEM), Raman spectroscopy and synchrotron radiation X-ray absorption spectroscopy.

Transmission electron microscopy studies

The fine grained nature and low crystallinity of garnierites requires the use of high magnification techniques such as transmission electron microscopy (TEM). Recent works have reported the vast variety of serpentine forms at the nanometre scale: lizardite lamellae, chrysotile tubes, chrysotile cones, polygonal serpentine, polyhedral serpentine and antigorite (Cressey *et al*., 1994; Baronnet & Devouard, 1996; 2001; 2005; 2007; Dódony, 1997; Devouard *et al*., 1997; Viti & Mellini, 1998; Dódony *et al*., 2002; Grobéty, 2003; Andréani *et al*., 2004; 2008, Mugnaioli *et al*., 2007; Cressey *et al*., 2008; 2010; Padrón-Navarta *et al*., 2008) from various geological settings: from oceanic serpentinites (e.g. Auzende *et al*., 2002), meteorites (Akai, 1988; Zega *et al*., 2006) and kimberlites (Mitchell & Putnis, 1988). Those works emerged as steps forward on the crystallography of serpentine minerals complementing previous works based on X-ray diffraction (Selfridge, 1936; Whittaker, 1953; 1954; 1955a; 1955b; 1955c; 1955d; Zussman, 1955; Wicks & Zussman, 1975; Wicks & Plant, 1979; Mellini, 1982; Mellini & Zanazzi, 1987; Mellini & Viti, 1994) and TEM (Zussman & Brindley, 1957; Yada, 1967; 1971; 1979; 1984; Cressey, 1979; Mellini, 1986). Serpentine group minerals are 1:1 trioctahedral phyllosilicates that develop different structural forms because of a geometrical misfit between tetrahedral and octahedral sheets (Mellini, 2014). The three most common varieties are lizardite (planar lamellae), antigorite (modulated structure) and chrysotile (tubes). In addition, other microstructures may be found, such as polygonal serpentine (e.g. Chisholm, 1992; Dódony, 1997; Baronnet & Devouard, 2005), polyhedral serpentine (e.g. Zega *et al*., 2004; Andréani *et al*., 2008; Cressey *et al*., 2008) and chrysotile cones (e.g. Andréani *et al*., 2008). In particular, polygonal serpentines develop rolled fibres, larger than chrysotile tubes, with 15 or 30 sectors separated by 24º and 12º, respectively (e.g. Baronnet & Devouard, 2005; Andréani *et al*., 2008; Mellini, 2014). Up-to-date studies report that these sectors are actually composed of lizardite lamellae growing parallel to the c axis (Mugnaioli, 2007; Mellini, 2014; and references therein).

Although, a limited number of exhaustive TEM works on Ni-bearing phyllosilicates exists up to the present (Uyeda *et al*., 1973; Esson & Carlos, 1978; Poncelet *et al*., 1979; Pelletier, 1983; Soler *et al*., 2008; Tauler *et al*., 2009; Suárez *et al*., 2011), and high resolution imaging and electron diffraction studies are scarce. In general, the results obtained allowed identifying particles with different basal spacings: 7 Å (serpentine-like), 10 Å (talc-like) and 12 Å (sepiolite like) (e.g. Uyeda *et al*., 1973; Esson & Carlos, 1978). In addition, it is worth noting that the recognition of the different serpentine group minerals and other phyllosilicates is easily performed using TEM (Brindley, 1978). Unfortunately, most of these publications are based on crushed and dispersed material onto TEM grids, omitting the textural information of the assemblages and the relationships between different phases. The intrinsic difficulty of the specimen preparation may explain the few TEM performed on garnierite minerals. TEM represents a powerful instrument to unravel the mineralogy, chemistry, and textural features of phases which commonly occur as low crystallinity, fine grained mixtures at the nanometre scale.

Raman spectroscopy studies

Again, the Mg end members of serpentine group minerals have been extensively studied by Raman spectroscopy, mainly to distinguish among the "polymorphs" lizardite, chrysotile and antigorite (Rinaudo *et al*., 2003; Groppo *et al*., 2006; Petriglieri *et al*., 2014).

However, available mineral databases of micro-Raman spectra lack trustworthy references of most garnierite-forming minerals. A very detailed, recent study on the kerolite-pimelite series provides valuable hints on the variation of the Raman effects with Ni content (Cathelineau *et al*., 2014; 2015). Although, the other references for Raman spectroscopy on Ni-phyllosilicates are for a népouite from New Caledonia and for a willemseite from South Africa, in the RRUFF database, and the site states that the identification of these minerals

are not yet confirmed (http://rruff.info/Willemseite; 2014, march 4; http://rruff.info/nepouite; 2014, march 6).

Nevertheless, serpentine group minerals (antigorite, lizardite and chrysotile) are easily identified by this technique, as each of them displays characteristic Raman bands (Rinaudo *et al*., 2003), so Raman spectroscopy becomes a useful method to identify mineral phases even when they are fine grained, complementary to other mineral identification and characterisation techniques.

Synchrotron radiation studies

Pioneering synchrotron radiation studies by Manceau and coauthors dealed with the distribution of Ni in Ni-bearing Mg-phyllosilicates from New Caledonia (Manceau & Calas, 1985a; 1985b; Manceau *et al*., 1985; Manceau & Calas, 1986; Manceau, 1990). The EXAFS measurements on minerals of the lizardite-népouite and kerolite-pimelite series indicate that the intracrystalline distribution of Ni within the phyllosilicates is not forming a homogeneous Ni-Mg solid solution but is segregated into discrete domains or clusters (Manceau & Calas, 1985a). This work also pointed out that the Ni distribution within lizardite-népouite was probably derived from the transformation of earlier serpentines by a Ni-enrichment and a subsequent loss of Mg. However, in the case of kerolite-pimelite the work suggests that Ni heterogeneity takes place when these phases precipitate from an aqueous solution.

Nevertheless, there are still missing gaps in the study of Ni in Ni-bearing phyllosilicates. Up to now most of the XAS work has been done by means of bulk analysis on serpentine- and talc-like garnierite samples (Manceau & Calas, 1985a; 1985b; Manceau *et al*., 1985; Manceau & Calas, 1986; Manceau, 1990; Decarreau, 1992), with no data on sepiolite-like garnierites; or across several meters of a laterite profile (e.g. Fan & Gerson, 2011; Dublet *et al*., 2012), without taking into account the garnierite mineralogy and textures, and their relationship with the host saprolite. In addition, the aforementioned literature focuses on Ni, and the distribution and speciation of Fe in this environment has not been studied.

1.3. AIM OF THIS STUDY

Taking into account that Ni-bearing Mg-phyllosilicates are significant, but understudied ore minerals, with no consensus on their nomenclature and classification, the aim of this study is to provide new data of the Falcondo Ni-laterite deposit on the mode of occurrence, mineralogy, textural relationships and mineral chemistry with the intention of gaining further insight into the structure and mineral chemistry of Ni-bearing Mg-phyllosilicates.

1.4. OUTLINE OF THIS THESIS

In order to achieve the aforementioned aims, a selection of samples of garnierites and related rocks from the saprolite horizon of the Falcondo Ni-laterite deposit (Dominican Republic) was studied. The geological setting of this deposit is explained in **Chapter 2**. These samples were analysed by means of various techniques (detailed in **Chapter 3**) to obtain a multiscale approach to their structure, chemistry and textures at the micrometre and nanometre scale. A first characterisation was performed by X-ray powder diffraction (XRD), Differential Thermal Analysis and Thermogravimetry (DTA-TG), optical microscopy (OM), Scanning Electron Microscopy (SEM), Electron Microprobe (EMP), and the results are included in **Chapter 4**. Further textural and chemical information was obtained by the Transmission Electron Microscopy (TEM) nanoscale study, displayed in **Chapter 5**. Later, the well-characterised mineral samples were analysed by micro-Raman spectroscopy to establish characteristic Raman effects in the different Ni-bearing Mg-phyllosilicates, discussed in **Chapter 6**. In addition, the local environment of Ni and the speciation of Fe were investigated through synchrotron-based X-ray absorption spectroscopy, as explained in **Chapter 7**. Furthermore, to assess the dissolution kinetics of Ni-bearing Mg-phyllosilicates, a series of dissolution-precipitation experiments were developed under atmospheric conditions, and the results are presented in **Chapter 8**. Finally, the general conclusions that can be extracted from this multiscale approach are presented in **Chapter 9**.

The XRD, DTA-TG, optical and scanning electron microscopy and EMP results were included in Villanova-de-Benavent *et al*. (2011a, 2011b, 2013, 2014b, 2014c). The TEM imaging and electron diffraction patterns were shown in Villanova-de-Benavent et al. (2011a, 2011b, 2014c; *in press*). The Raman spectroscopy characterisation is included in Villanova-de-Benavent *et al*. (2012), and the X-ray absorption spectroscopy synchrotron

radiation study in Roqué-Rosell *et al*. (2012, Geochimica et Cosmochimica Acta, *submitted*). Preliminary results of the dissolution-precipitation experiments were presented and discussed in Villanova-de-Benavent *et al*. (2014a).

2. THE FALCONDO NI-LATERITE DEPOSIT

2.1. GEOLOGICAL SETTING

The main nickel laterite deposits in the central Dominican Republic occur over the serpentinised Loma Caribe peridotite belt (**Fig. 2.1**), which is about 4–5 km wide and extends NW for 95 km from La Vega to Loma Sierra Prieta, north of Santo Domingo; its south-eastern part is exposed as thin fault slices (Lewis & Jiménez, 1991; Lewis *et al*., 2006). The peridotite is interpreted, from airborne magnetics and drilling, to extend south-eastward below the surface to the coast (Lewis *et al*., 2006). The Loma Caribe belt is bounded by reverse faults dipping eastward at 75–80° (Mann *et al*., 1984). The major faults within the body are shear zones that strike parallel to the northwest trend of the belt and the foliation of the serpentinised peridotite. These faults and other basic structures in the central area of the Loma Caribe peridotite massif have been mapped (Haldemann *et al*., 1979; **Fig. 2.1**), although they have not been systematically studied. The structural information derived from the shear foliation attitudes within the serpentinites near the western and eastern contacts may indicate that the body is wedge-shaped with depth (Haldemann *et al*., 1979).

The Loma Caribe peridotite forms the core of a Mesozoic age Median Belt (Bowin, 1966; Lewis & Draper, 1990), which includes two major metavolcanic units: 1) the Maimón Formation (Fm.) to the northeast of the peridotite belt represents a primitive island arc tholeiitic unit of Lower Cretaceous age, and 2) the Duarte Complex to the southwest of the peridotite belt formed by mantle plume—related oceanic plateau basalts of Upper Jurassic–Lower Cretaceous age (Lewis *et al*., 2002). The Maimón Fm. is unconformably overlain by the Peralvillo Fm. (volcanic arc andesites, diorites, basalts, tuffs, breccias and conglomerates of Late Cretaceous age), and the Duarte Fm. is unconformably overlain by the Siete Cabezas Fm. (volcanic arc basalts with minor tuffs and wackes of Cenomanian age; Haldemann *et al*., 1979; Lewis *et al*., 2002; Proenza *et al*., 2007). The peridotite belt also hosts some dolerite dykes. In addition, diorite bodies outcrop along the faulted margins of the peridotite belt, and some gabbroic intrusives occur in the Peralvillo Fm. (**Fig. 2.1**; Lithgow, 1993; Escuder-Viruete *et al*., 2006).

Based on the mineralogy and textural features of the ultramafic rocks, the Loma Caribe peridotite was interpreted by Lewis & Jiménez (1991) as a (serpentinised) harzburgitic oceanic mantle forming part of a dismembered ophiolite complex. The ultramafic body includes podiform chromitites within dunites and suggests that most of the peridotite is part of the transition zone of the mantle section of harzburgite-type alpine peridotite complexes.

The Loma Caribe ultramafic rocks originally formed in the upper mantle below an evolving suprasubduction oceanic lithosphere (Lewis *et al*., 2006). The peridotites would have likely been partially serpentinised by the hydrothermal reaction of oceanic water with the mantle rock as they moved upwards through the forearc/arc lithosphere prior to their final emplacement in their current crustal tectonic position. The tectonic emplacement occurred as early as the late Albian, as a result of the collision of an oceanic plateau (the Duarte plateau terrane) with the primitive Caribbean island-arc (Maimón- Amina terrane) at Aptian time (Lewis *et al*., 2002). This event resulted in the northward emplacement (obduction) of the peridotite over the Maimón Formation. In the middle to late Eocene, Hispaniola underwent southwest contraction (Mann *et al*., 1991). Many of the mid-Cretaceous thrust structures were reactivated at this time, resulting in thrusting of the peridotite in a northeast direction over the Peralvillo Fm. (Draper *et al*., 1996). Uplifting of the northwestern margin of the Cordillera Central occurs along three reverse or thrust mapped faults (Bonao, Hatillo and Hispaniola Fault Zones). The northwesterly striking segment of the Oligocene age strike-slip Hispaniola Fault Zone comprises the Loma Caribe ultramafic body (Mann *et al*., 1984). Further exhumation of the peridotite in the Oligocene is well-documented in the La Vega area (Lewis & Jiménez, 1991).

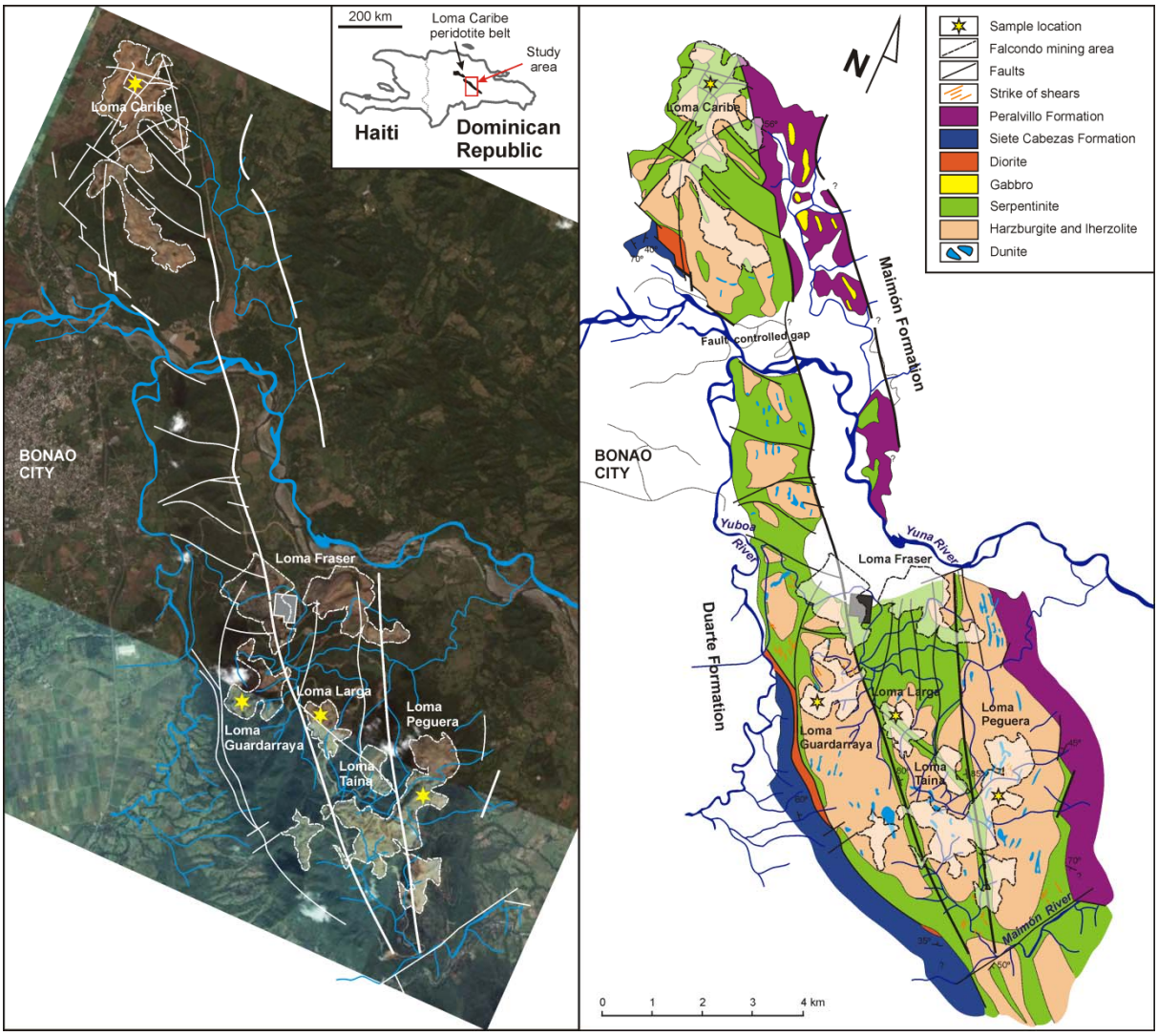

FIGURE 2.1. Orthophotograph showing the mining zones of the Falcondo deposit, including the location of the Loma Caribe peridotite belt in the Dominican Republic (left) and geological map of the same area (right) (modified from Haldemann *et al*., 1979).

Both "fresh" and serpentinised peridotites have been exposed to weathering and erosion since the early Miocene. These processes were followed by uplift, block faulting and subsequent cycles of laterisation (Haldemann *et al*., 1979). The Miocene land surface was broken into blocks by vertical movements related to transpressional deformation along major faults. At least four physiographic cycles have been recognised corresponding to different surface levels (Lewis *et al*., 2006). Geomorphological observations indicate that block-faulting postdates the first of the laterisation cycles (Haldemann *et al*., 1979).

Under supergene conditions, the serpentinised peridotites of Loma Caribe evolved in a similar way to that of the ophiolite-related, hydrous Mg silicate deposits found (and exploited) in the arcs of the West Pacific, e.g. in the Philippines, Indonesia and New Caledonia (Golightly, 2010).

The Falcondo Glencore exploitation area is located near the city of Bonao and crossed by the river Yuna. It is divided in eight areas or *lomas* (hills), from north to south: Loma Ortega, Caribe, Fraser, Taína, Larga, Guardarraya and Peguera (**Fig. 2.1**).

2.2. THE FALCONDO Ni-LATERITE PROFILE

As other hydrous silicate-type Ni-laterite deposits, the weathering profile in Falcondo is divided into three main horizons: the unweathered protolith at the bottom, a thick saprolite horizon and a limonite horizon at the top (**Fig. 2.2**). However, the mine geologists have subdivided profile into six zones (A

to F) on the basis of nickel and iron contents, texture, and proportion of rocky fragments. These zones are, from the base to the top: unweathered ultramafic (F), serpentinised peridotite (E), hard serpentine (D), soft serpentine (C), lower limonite (B) and upper limonite (A), which may be covered by a hematitic cap (**Fig. 2.2**; Haldemann *et al.*, 1979; Lithgow, 1993; Lewis *et al.*, 2006). The zones E, D and C represent the saprolite horizon, whereas the zones B and A correspond to the limonite horizon. The thickness of the laterite profile varies from 1 to 60 m (Haldemann *et al.*, 1979). Likewise, the thickness of the different zones in the profile varies vertically and laterally in all exposures in the Falcondo deposit (Fig.6 in Lewis *et al.*, 2006).

The unweathered ultramafic protoliths are clinopyroxene-rich harzburgite, lherzolite, fine-grained black dunite and sheared dark green serpentinite. In general, the major constituent of the host ultramafic rocks is olivine (Fo89–92, 0.35–0.55 wt.% NiO) followed by orthopyroxene (En89–92, NiO < 0.1 wt.%) and minor clinopyroxene (#Mg = 86–95) (Haldemann *et al.*, 1979; Lithgow, 1993; Lewis *et al.*, 2006; Marchesi *et al.*, 2012).

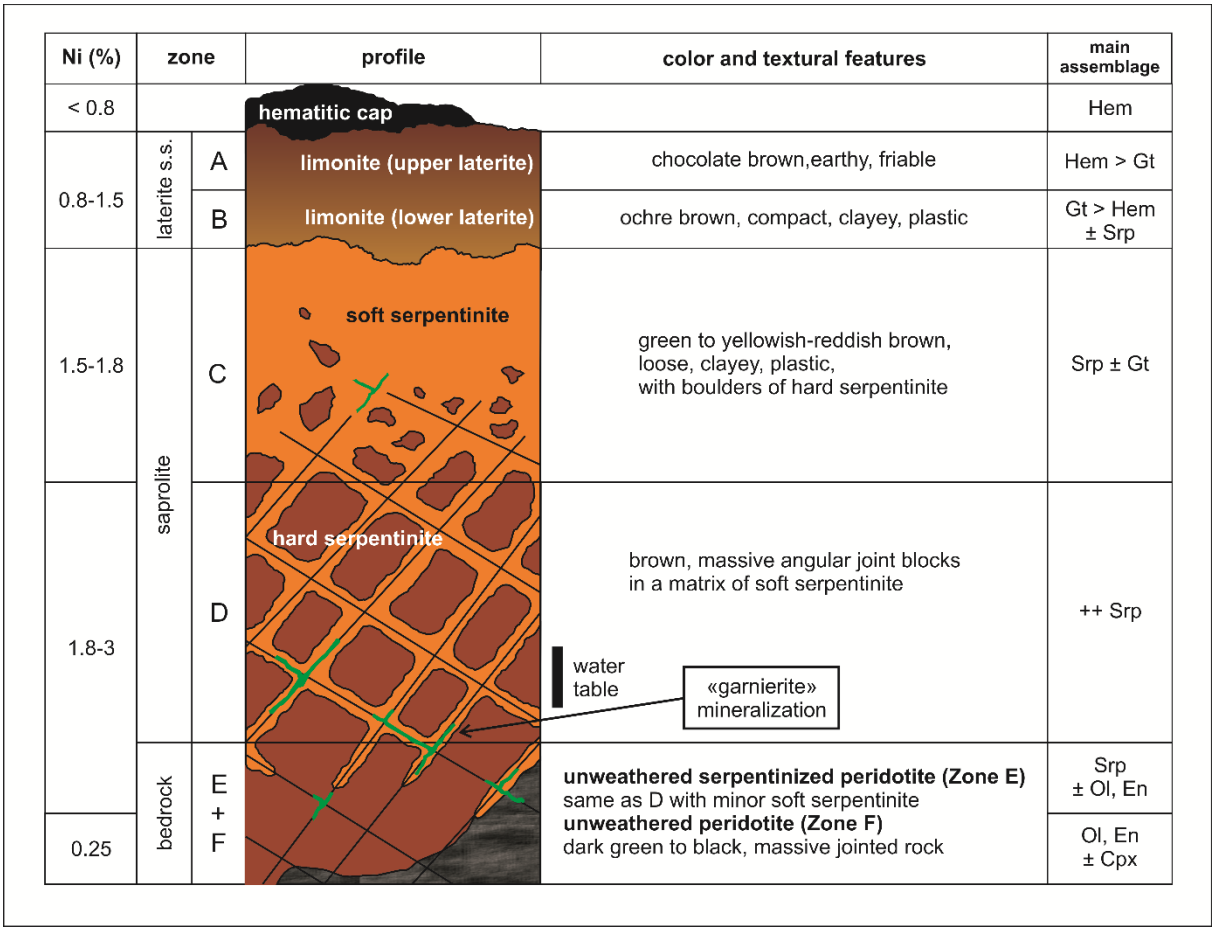

FIGURE 2.2. Schematic lateritic profile of the Falcondo deposit, showing the position of garnierites, and including major textural features, main mineral assemblage and Ni content of each zone of the profile (modified from Lithgow, 1993; Lewis *et al.*, 2006; Tauler *et al.*, 2009). Total height of the profile is up to 60 m (Haldemann *et al.*, 1979). Mineral abbreviations based on Whitney & Evans (2010). Legend: Hem = hematite, Gt = goethite, Srp = serpentine, Ol = olivine, En = enstatite, Cpx = clinopyroxene.

3. MATERIALS AND METHODS

3.1. SAMPLING

Sixty-three samples were collected in the saprolite horizon of different *lomas* (hills) in the Falcondo Ni-laterite deposit during different field works (performed in 2007, 2008 and 2011). From these, twenty-one were selected as the most representative for this thesis.

These samples were studied by means of various techniques in order to obtain a multiscale approach to their structure, chemistry and textures at the micrometre and nanometre scale. X-ray powder diffraction (XRD), Differential Thermal Analysis and Thermogravimetry (DTA-TG), optical microscopy (OM), Scanning Electron Microscopy (SEM), Electron Microprobe (EMP) results are included in **Chapter 4**. The Transmission Electron Microscopy (TEM) results are in **Chapter 5**. The micro-Raman spectroscopy characterisation is presented in **Chapter 6**. The synchrotron radiation study is in **Chapter 7**. The dissolution-precipitation experiments by flow-through are explained in **Chapter 8**.

3.2. POWDER X-RAY DIFFRACTION (XRD)

3.2.1. Sample preparation

Different greenish-coloured garnierite types were separated hand-picking, in order to obtain the most pure phase specimens, and carefully ground in an agate mortar and pestle. Thirty-five samples were prepared by manual pressing of the powders, by means of a glass plate to get a flat surface, in cylindrical standard sample holders of 16 millimetres of diameter and 2.5 millimetres of height.

3.2.2. Analytical conditions

The diffractograms were obtained in a PANalytical X'Pert PRO MPD Alpha1 powder diffractometer in Bragg-Brentano $\theta/2\theta$ geometry of 240 millimetres of radius, nickel filtered Cu Kα radiation (λ = 1.5418 Å), and 45 kV – 40 mA.

During analysis, sample was spun at 2 revolutions per second. A variable divergence slit kept an area illuminated constant (10 mm) and a mask was used to limit the length of the beam (12 mm). Axial divergence Soller slits of 0.04 radians were used. Samples were scanned from 3 to 80º 2θ with step size of 0.017º and measuring time of 50 s per step, using a X'Celerator detector (active length = 2.122º). The sample preparation and analysis was performed in the Centres Científics i Tecnològics of the Universitat de Barcelona (CCiT-UB). The software X'Pert Highscore® was used to substract the background of the patterns, to detect the peaks and to assign mineral phases and their corresponding d_{hkl} to each peak.

3.3. DIFFERENTIAL THERMAL ANALYSIS AND THERMOGRAVIMETRY (DTA-TG)

The same powders studied by XRD were later analysed by Differential Thermal Analysis coupled with Thermogravimetry (DTA-TG) in the Departament de Cristal·lografia, Mineralogia i Dipòsits Minerals, Facultat de Geologia, of the Universitat de Barcelona. The samples (approximately 50 mg each) were analysed in a Netzsch STA 409 C/CD instrument using an alumina crucible, from 25 to 1000ºC at 10ºC/min, under a dry air atmosphere with a flow rate of 80 ml/min. The resulting diagrams were processed with the software Netzsch Proteus Analysis®.

3.4. OPTICAL MICROSCOPY (OM)

Sixty-seven polished thin sections and eight polished sections were prepared for a detailed petrographic study under polarised light optical microscopy.

3.5. SCANNING ELECTRON MICROSCOPY (SEM-EDS)

Some polished thin sections and polished sections were carbon-coated to improve sample conductivity, prevent charging and damage under the electron beam. The samples were examined under the Environmental Scanning Electron Microscope (ESEM) Quanta 200 FEI, XTE 325/D8395, coupled to an INCA Energy Dispersive Spectrometer (EDS) 250 EDS microanalysis system with the operating conditions of 20 kV and 5 nA.

3.6. ELECTRON MICROPROBE ANALYSIS (EMP)

Nineteen polished thin sections and four polished sections were selected to be analysed by Electron Microprobe.

3.6.1. Analytical conditions

Point analysis were performed in a Cameca Electron Microprobe Analyser SX-50 in the CCiT-UB, equipped with four wavelength dispersive spectrometers (WDS) and an energy dispersive spectrometer (EDS). Analysis conditions were 20 kV, 15 nA, 2 µm beam diameter, counting time of 20 seconds per element and a takeoff angle of 40º. The software used in the acquisition of the analyses is XMAS (SAMx, France), using the matrix effect correction model PAP (Pouchou & Pichoir, 1991).

The calibration standards used are the following: hematite (Fe, LIF, Kα), rutile (Ti, PET, Kα), periclase (Mg, TAP, Kα), rhodonite (Mn, LIF, Kα), Al_2O_3 (Al, TAP, Kα), Cr_2O_3 (Cr, PET, Kα), metallic vanadium (V, LIF, Kα), diopside (Si, TAP, Kα), NiO (Ni, LIF, Kα) and wollastonite (Ca, PET, Kα).

Additional analyses were obtained in a JEOL JXA-8230 EMP, with five WDS spectrometers and one EDS spectrometer in the same facility, equipped with five WDS and one EDS. The operation conditions were 20 kV, 10nA, 2 µm beam diameter and counting time of 20 s per element, and using the same calibration standards. The matrix effect correction model implemented in the JEOL software in this case is the XPP (Pouchou & Pichoir, 1991).

3.6.2. Calculation of the structural formulae

The structural formulae of serpentine and talc-like garnierite mixtures were calculated using 7 or 11 oxygens for normalisation, depending on the dominant phase. The final formula was recalculated by considering the proportion of the talc-like (or serpentine-like) phase in the mixture. This proportion can be calculated on the basis of the formulae proposed by Brindley & Hang (1973) [**Eq. 1** and **2**] and by Soler *et al*. (2008) [**Eq. 3** and **4**]:

$$X_1 = 2 - 1.5 \times \frac{SiO_2}{MgO} \text{ [Eq. 1]}$$

$$X_2 = 1.5 \times \frac{SiO_2}{MgO} - 1 \text{ [Eq. 2]}$$

where X_1 is the proportion of serpentine layers in 10 Å-type (talc-like) garnierites and X_2 is the proportion of talc layers in 7 Å-type (serpentine-like) garnierites; and SiO_2/MgO is the mole ratio of the oxides, calculated using the atoms per formula unit of these elements (here Mg includes Ni and other octahedral cations).

$$Xserp = \frac{1}{2} \times \left(4 - \frac{3}{\frac{Mg+Ni}{Si}}\right) \text{ [Eq. 3]}$$

$$Xtalc = 1 - Xserp \text{ [Eq. 4]}$$

Xserp and *Xtalc* are the serpentine and talc mole fractions in the garnierite mixture, respectively; and (Mg+Ni)/Si is the atomic ratio of these elements.

Both methods are based on the relationship between the cations in the octahedral and tetrahedral sites in serpentine and talc (equal to 3/2 and 3/4 respectively), and are equivalent (as X_1 in **Eq. 1** and *Xserp* in **Eq. 3** are the same). The formula used in this study for the calculation of the talc component in garnierites is presented in **Eq. 5**:

$$Xtlc = 1.5 \times \frac{\sum tetra}{\sum octa} - 1 \text{ [Eq. 5]}$$

where *Xtlc* is the talc component in garnierite mixtures (in mole fraction); and $\sum tetra$ and $\sum octa$ are the sum of the atoms per formula unit of cations occupying the tetrahedral (Si and Al) and octahedral (Mg, Ni and Fe) sites, respectively.

Minerals of the sepiolite-falcondoite series were normalised to 32 oxygens, and the serpentine from the saprolite was normalised to 7 oxygens. All Fe was considered to be Fe^{3+} in both the saprolite serpentine and the Fe-bearing garnierites, in accordance with Brindley & Hang, 1973; Golightly & Arancibia, 1979; Wells *et al*., 2009. The Fe^{3+} and Al could not be allocated to the tetrahedral layer because this site was fully occupied by Si in most cases (as reported by Golightly & Arancibia, 1979).

3.6.3. X-ray quantitative element imaging

Back-scattered electron (BSE) and elemental XR images (maps) for Si, Fe, Mg, Ni and Al were obtained by means of WDS scanning of four of the samples with the Cameca SX50 operating at 20 keV and 200 nA or 100 nA (noted in the figures), a focused beam of 5 µm, step (pixel) size of 3 µm, and counting time of 20-30 ms/pixel. García-Casco (2007) has documented that high beam current combined with short counting time (milliseconds) avoids problems of beam damage to silicate

minerals. These maps were processed with software *DWImager* (Torres-Roldán & García-Casco, unpublished) in order to show particular textures and mineral composition features. The images presented represent maps quantified using the same software following the procedure of Bence & Albee (1968) for matrix correction, using an internal mineral standard of the mineral on interest analysed with the microprobe in the scanned areas (as indicated in the figures), and the α-factor table of Kato (2005); see also http://www.nendai.nagoya-u.ac.jp/gsd/a-factor/). These quantified images show pixel-sized mineral analyses of minerals of interest expressed in atoms per formula unit and atomic ratios (color code), as indicated in then figure captions. In all quantitative map images mineral phases not considered for illustration are masked out, and the resulting images are overlain onto a reference grey-scale BSE image having the same spatial resolution (pixels) that contains the basic textural information of the scanned areas.

All ternary mineral composition diagrams were prepared using software *CSpace* (Torres-Roldán *et al*., 2000). The quantified pixels of the X-ray distribution images, appropriately filtered for minerals and/or voids and polish defects not to be represented in the triangular plots, and the spot analyses used to calibrate the images are plotted in these ternary diagrams. Note that there is a close fit between spot analyses and quantified pixel compositions. The subtle divergences are the result of matrix effects (for these plots a single internal standard was used for all minerals of the scanned areas). The latter images were calculated using software *DWImager* and are expressed as absolute frequency (colour code), as indicated in the figures.

The atomic concentration of elements per formula units is abbreviated apfu. Mineral group and end-member abbreviations are after Whitney & Evans (2010); except falcondoite (Fal), willemseite (Wil), kerolite (Ker), pimelite (Pim), népouite (Nep), pecoraite (Pec), karpinskite (Krp).

3.7. TRANSMISSION ELECTRON MICROSCOPY (TEM)

3.7.1. Specimen preparation

Nine samples were selected to be studied by TEM, based on the information obtained previously by XRD, OM and EMP. Three different methods of specimen preparation were combined, due to the difficulties posed by the friability of the material, and thirty-seven grids were prepared with similar outcomes (**Fig. 3.1**).

First, twelve additional 30 micrometre-thick polished thin sections were prepared with Canada balsam or an equivalent thermo-fusible resin. Representative areas containing garnierites to be studied by TEM were selected under the optical microscope. A 3.05 mm Ø single-hole copper grid with a single 1 mm Ø hole was attached onto each area of interest using a regular two-component glue (Araldit ®) or cyanochrylate-based glue (SuperGlue ®). In the case of Araldit®, five hours after its application, the adhesive is slightly hardened, so the excess of glue inside the grid and in its surroundings can be removed easily. Two days after the attachment of the grids, a sharp cutter is used to cut the rock out of the grid. On the other hand, with SuperGlue® a sharp cutter or nail is used to cut the rock around the grid (**Fig. 3.1a**). Finally the grid is detached from the glass slide of the thin section with heat. In order to remove glue remainings, the grid may be immersed in acetone. In order to get a thinner specimen, the rock side of the grid may be polished gently using a specific paper.

These grids were finally ion-thinned by a Gatan 600 ion mill and a Gatan PIPS 691 at the Centro de Instrumentación Científica in the Universidad de Granada (CIC-UGR) (Suárez *et al.,* 2011), and by a Gatan 600 Duo Mill at the Dipartimento di Scienze Fisiche, della Terra e dell'Ambiente of the Università degli Studi di Siena (UniSi).

Second, fragments of other selected samples about 2 mm thick and up to 1 cm long were hand-picked or cut off from the sample by means of a low speed precision saw.

The fragment was cut and hand polished in order to obtain a 30 micrometre-thick sheet with a diameter of 3 mm and two parallel mirror-like surfaces, using alumina polishing papers of different sizes (finishing with 9 μm, 3 μm and 1 μm). The polished sample was finally glued to a copper grid.

The grids were ion-thinned by a Fischione 1010 Low Angle Ion Milling & Polishing System and a Gatan PIPS 691 at the CCiT-UB (**Fig. 3.1c**). It is worth noting that the aforementioned specimen preparation methods preserve the original texture of the mineral phases.

Third, other samples were carefully separated by hand-picking, ground in an agate mortar, suspended

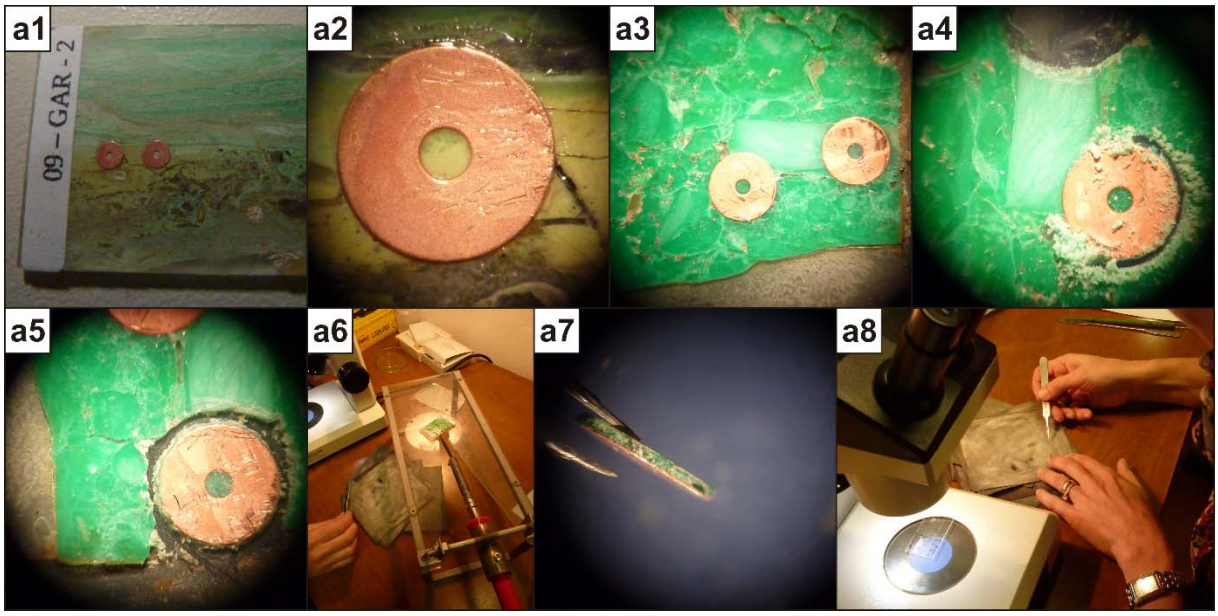

FIGURE 3.1. The three specimen preparation methods used for the TEM observations in this study: **a1-8**) thin section, **b1-13**) manual polishing, **c1-10**) ion milling of the samples prepared as thin sections and manually polished, **d1-6**) crushed sample suspended in ethanol. **a1**) The sample is prepared as a thin section using a thermofusible resin and the single hole copper grids are attached onto the selected areas; **a2**) detail of one of the copper grids attached onto sample 09-GAR-2(Si); **a3**) detail of two copper grids attached onto sample GAR-1(Si); **a4-6**) one of the grids being cut off from sample GAR-1(Si) and detached by heating; **a7**) detail of the thickness of one grid from sample GAR-1(Si) before the final gentle hand polishing depicted in **a8** (scale: the outer diameter of the single hole copper grid is 3 mm).

with ethanol and put on a copper grid in order to obtain additional, higher quality EDX analyses (e.g. López Munguira & Nieto, 2000; Abad *et al*., 2001) (**Fig. 3.1d**). Both ion-milled samples and powders were carbon-coated prior to the TEM study.

3.7.2. Analytical conditions

The TEM study was performed by Philips CM20 (CIC-UGR) and a Jeol JEM2010 (UniSi), equipped with Energy Dispersive X-ray spectrometer detectors (Oxford-Isis) and operating at 200 kV. Additional images and electron diffraction patterns were obtained in a Jeol JEM2100 at 200 kV (CCiT-UB) as well.

In the CM20 quantitative chemical analyses were obtained, with an EDAX solid-state EDX detector, using STEM mode (resolution of 0.8 Å in the TEM mode and 2 Å in the STEM mode). In this case, a scan window was defined to include the entire particle of interest. Albite, biotite, muscovite, spessartine, olivine and titanite standards were used to obtain K-factors for the transformation of intensity ratios to concentration ratios according to Cliff & Lorimer (1975).

3.7.3. Processing of HRTEM images and selected area electron diffraction (SAED) patterns

The phyllosilicate lattice fringes in High Resolution TEM were measured using the "Measure Features" script in the software Digital Micrograph™ (Gatan) available online (http://www.dmscripting.com/alphabeticscriptlisting.html).

The spacings in the electron diffraction patterns were calculated with the expression in [**Eq. 6**]:

$$d_{hkl}(\text{Å}) = \frac{C}{D} = \frac{\lambda \times L}{D} \quad \text{[Eq. 6]}$$

being d_{hkl} the spacing in ångstroms; C the camera constant (equals 34.4 in the Philips CM20, CIC-UGR); λ the electron wavelength at 200 kV (0.025 nm); L the camera length of the microscope (120 cm in the Jeol JEM2010, UniSi); and D the distance measured in the SAED pattern (in millimetres on the digital photo printed to 153 mm in length in the case of CIC-UGR, and in centimetres on the Kodak® SO163 film sized 3.25x4 inch in UniSi).

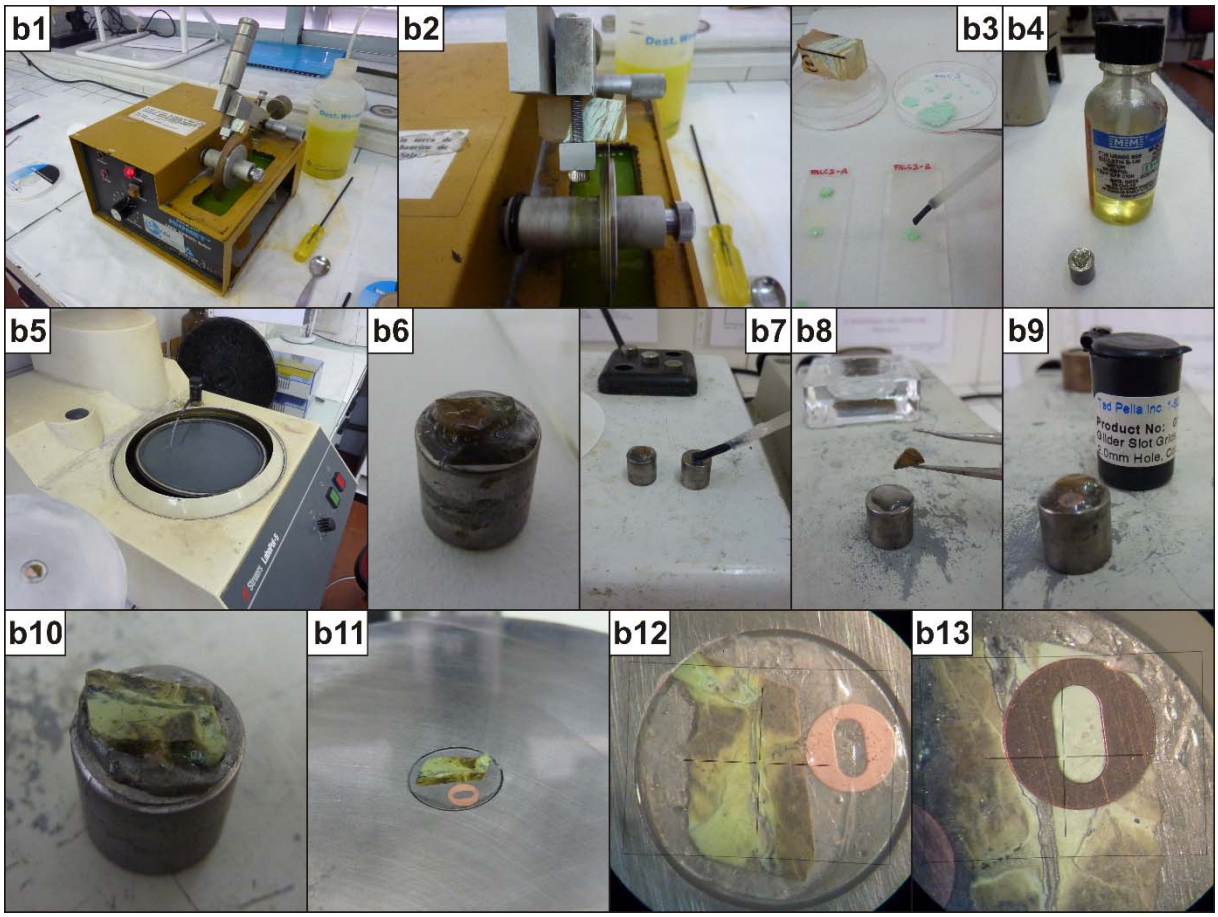

FIGURE 3.1. (CONTINUED). **b1**) the low speed precision saw used to prepare small portions of sample; **b2**) detail of sample FALC-3 being cut by the low speed precision saw; **b3**) the same sample being embedded in **b4**) M-Bond 610® special resin; **b5**) water-refrigerated polisher used in this procedure; **b6**) sample LC-101saprnear-1 before the first polish; **b7-9**) sample LC-101sapr(near-1) before the second polish, a single hole copper grid is attached near the sample as a reference for 30 micrometre thickness (**b9**); **b10**) sample LC-101serp-1 before the first polish; **b11-12**) sample LC-101serp-1 during the second polish; **b13**) grid attached to the area in sample LC-101serp-1 selected for the TEM study (scale: the outer diameter of the single hole copper grid is 3 mm).

3.7.4. Calculation of the structural formulae

The atoms per formula unit (apfu) were calculated based on the theoretical number of negative charges of each mineral (14, 22 and 32 for serpentine, talc and sepiolite, respectively). Fe was calculated as Fe^{3+}, coherent with the references presented in **Section 3.6.2**.

3.8. MICRO-RAMAN SPECTROSCOPY

Eight representative samples of garnierites from the Falcondo Ni-laterite as well as five Ni-free phyllosilicates from other localities were selected and analysed by micro-Raman spectroscopy directly from polished sections or polished thin sections.

3.8.1. Analytical conditions

Results were obtained with a HORIBA JobinYvon LabRam HR 800 dispersive spectrometer equipped with an Olympus BXFM optical microscope in the CCiT-UB. Non polarized Raman spectra were obtained in confocal geometry by applying a 1064 nm laser, using a 100x objective (beam size around 2 μm), with 10 measurement repetitions for 60 seconds each. Different laser wavelengths were tested in order to obtain the best possible spectra avoiding fluorescence due to crystalline defects and fluorescence emitting centres: 325 nm (near ultraviolet), 532 nm (green), 785 nm (red) and 1064 nm (near infrared). An InGaAs detector cooled at -110ºC was used for the 1064 nm laser line excitation. The instrument was calibrated by

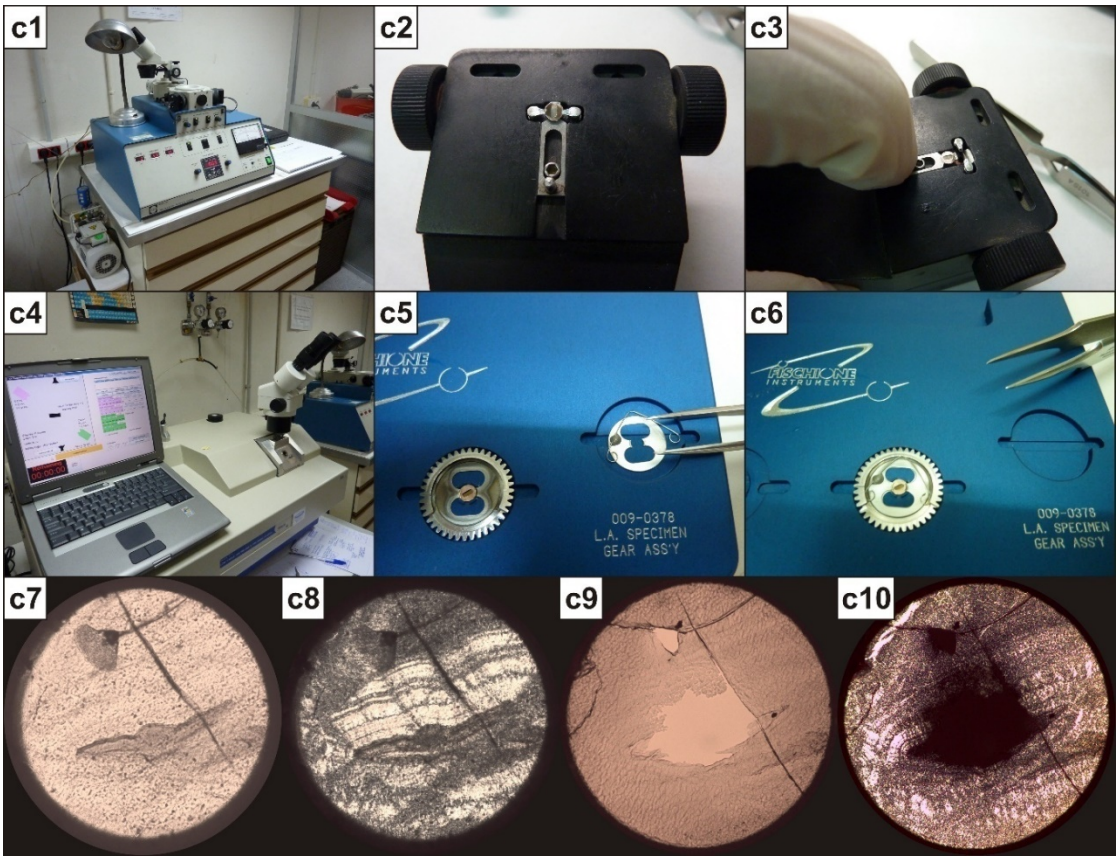

FIGURE 3.1. (CONTINUED). **c1**) The Gatan 691 ion miller (CCiT-UB), and **c2-3**) two photographs showing the procedure of loading the grids in the sample holder for the Gatan ion miller; **c4**) the Fischione 1010 ion miller (CCiT-UB), **c5-6**) and the sample holder system in the Fischione ion miller; **c7-10**) example of specimen LC100-AB4 before (**c7-8**) and after ion milling (**c9-10**), under plane polarised light (**c7, 9**) and crossed polars (**c8, 10**). Note the hole in the center in **c9-10**.

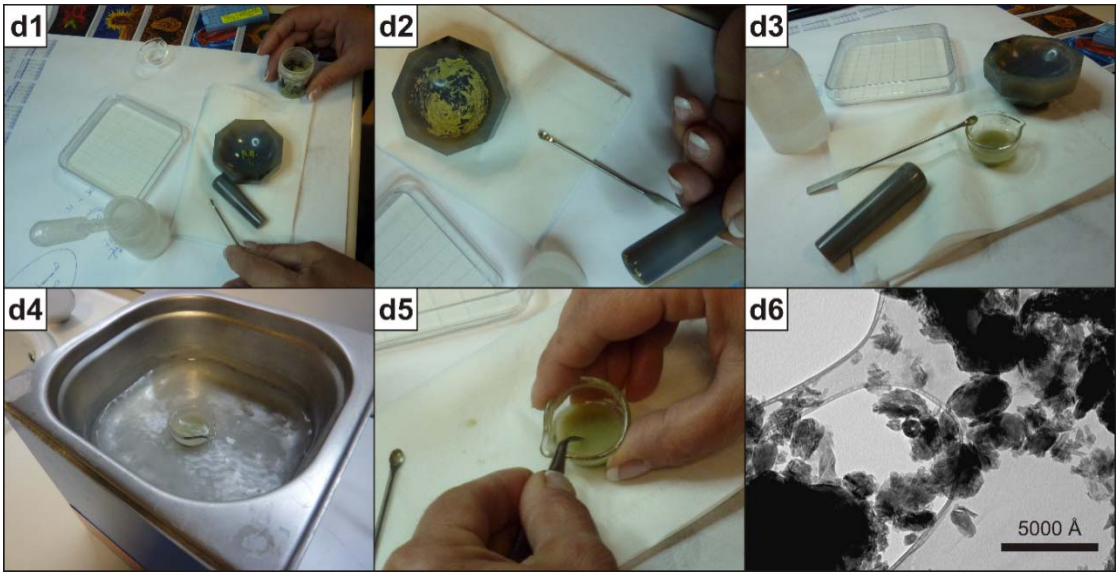

FIGURE 3.1. (CONTINUED). **d1**) The sample is hand-picked with the help of a spatula or a pair of tweezers; **d2**) the sample is ground using agate mortar and pestle; **d3**) the powder is diluted with ethanol; **d4**) the resulting suspension is put in an ultrasonic bath for a few seconds to avoid possible particle clustering; **d5**) a copper grid is introduced in the suspension in order to capture an adequate amount of particles; **d6**) low magnification TEM image depicting some particles on a copper grid prepared by this method as an example (sample LC-11-008; obtained in a CM20, CIC-UGr).

checking the position of the metallic Si band at ~520 cm^{-1}.

The micro-Raman spectra were processed using the LabSpec® software (JobinYvon). The final spectra were produced by extracting the background fluorescence, and in some cases the white lamp was also removed in order to minimise the instrument noise.

3.8.2. Micro-Raman map

An area from a sample containing saprolite and two different types of garnierite was mapped. Micro-Raman map allowed distinguishing different zones in the selected area by their respective characteristic Raman spectrum.

This map was performed using a WITec alpha300RA+ Confocal Raman Imaging Microcoscope, with a 532 nm laser. The size of the area is 6750×1000 μm, with 100 scanned lines and 675 analysed points per image (one analysis every 10 μm), and 0.3 seconds of integration time (202.5 seconds per line). The map was obtained after scanning the area, grouping the areas with similar Raman spectra (clustering) in the range 150-750 cm^{-1} (where serpentine and talc phases display more differences in band position and intensity) and merging the areas into one single image in which the colour scale represents characteristic Raman signal. The map and the spectra associated to it were processed using the software WITec Project version 2.08.

3.9. SYNCHROTRON RADIATION STUDY

A first set of analyses were obtained in the Diamond Light Source synchrotron facility, in Oxford, United Kingdom (Roqué-Rosell *et al*., 2011). Later five samples, previously examined under optical microscopy and EMP (see **Sections 3.4** and **3.6**), were selected for a more exhaustive synchrotron radiation study.

For the present work the synchrotron experiments were performed on the beamline 10.3.2 of the Advanced Light Source in the Lawrence Berkeley National Laboratory (California, USA). (Marcus *et al*., 2004). This is a hard X-ray microprobe on a bending magnet, delivering a monochromatic beam with a spot size ranging from about 1 to 15 μm. It is a beamline dedicated to environmental sciences with a 2-bounce Si(111) water-cooled monochromator that covers the energy range from 2.45 keV to about 17 keV, and a 7 element Canberra Ge detector. The experiments consisted of three steps as in Mosselmans *et al*. (2008; 2009) and Roqué-Rosell *et al*. (2010). The first step allows identifying a good area of the sample by screening it and looking at the X-ray fluorescence counts from the multi-channel analyzer (MCA). The second step consists of performing X-ray fluorescence (μXRF) mapping to obtain the distribution of several elements simultaneously in the chosen region of interest (ROI). And the third and last step is to collect X-ray absorption spectroscopy (μXAS) spectra on one or more spots of interest identified by the μXRF mapping.

3.9.1. Micro-X-ray fluorescence spectroscopy (μXRF)

The μXRF elemental maps have been obtained by taking into account the intensity of the fluorescence lines corresponding to Cr Kα at 5.415 keV, Fe Kα at 6.405 keV and Ni Kα at 7.48 keV, when rastering 4×4 mm areas of conventional polished thin sections at 2° to the beam. This fluorescence geometry was used to minimize overabsorption in the subsequent experiments below. The incident X-ray beam size was 5×5 μm and the step size of 5 μm (which fits within the mineral aggregate size range from 10 to 500 μm) using an incident excitation energy of 10 keV.

In addition, a chemical map for Fe was performed to plot the distribution of the different Fe-bearing phases present in the ROIs. The Fe map relies on the fact that the Fe-K edge XANES varies with its chemical state, and thus different energies allow plotting the different excited species that have different sensitivities. In order to obtain distribution of Fe^{2+} and Fe^{3+}, a set μXRF mappings were obtained at the energies of 7.1, 7.11, 7.113, 7.125, 7.133, 7.35 and 10 keV. This allowed mapping in a range of energies immediately below, immediately above and far above the Fe K-edge. Then, these maps were combined into a multi energy map that provides a rough Fe K-edge XANES spectra on each measured pixel.

The multi energy maps from each ROI have been subsequently analysed with weighted sums of the representative species found on the same samples. These representative Fe K-edge spectra have been used as single compounds and have been fitted on every μXRF pixel across the different energies as in Sutton *et al*. (1995). This allowed plotting the distribution of the most relevant Fe bearing mineral phases with a 5 μm spatial resolution. The XY

Display and Chemical Mapping scripts for μXRF acquisition and analysis were used to obtain the elemental and chemical maps respectively. These scripts are freely distributed and available at https://sites.google.com/a/lbl.gov/microxas-lbl-gov/software.

3.9.2. Microfocus X-ray absorption spectroscopy (μXAS)

In order to identify and quantify the Fe-bearing minerals in the samples, a series of Fe K-edge μXANES were performed on representative selected spots in fluorescence geometry. A metal Fe foil was measured in transmission mode for calibration prior to the experiments. Every measurement was taken by scanning the monochromator about 300 eV above the Fe K-edge (7.112 keV). To optimize the signal to noise ratio, about 40 spectra were acquired at each point. The resulting spectra have been fitted by means of principal components analysis (PCA) using the PCA package that can be found at https://sites.google.com/a/lbl.gov/microxas-lbl-gov/software. This software implements the PCA as described by Ressler *et al*. (2000). It analyses a set of spectra to see if each measurement acquired can be represented as linear combinations of a smaller number of component spectra. In the present study, a range of Fe-bearing mineral standards acquired at the ALS beamline 10.3.2 have been used to fit the measured Fe K-edge μXANES. The standards used in the PCA fittings are freely available and can be downloaded from the website https://sites.google.com/a/lbl.gov/microxas-lbl-gov/databases.

The local environment of Ni within the samples has been determined by means of Ni K-edge μEXAFS following the same fluorescence geometry. A Ni metal foil was measured for calibration prior to the experiments. Every single measurement was taken by scanning the monochromator at about 700 eV above the Ni K-edge (8.333 keV). To optimize the signal to noise ratio as many as 500 spectra were acquired at each point in order to achieve sufficient data quality. The EXAFS fittings were performed using the Athena® package (Ravel & Newville, 2005) and the refinement included only single scattering events, to account for the averaged distances and the coordination numbers of Ni within the phyllosilicates. The parameters chosen to be refined corresponded to the atomic potentials, the interatomic distance, the Debye–Waller factor, and the shell occupancy numbers. The length of the EXAFS signal is important to determine the number of parameters available to fit according to the relationship described by Galoisy (1995). In the present EXAFS experiments, for a data length Δk of 9.5 Å−1 and a filtering window in real space about 2.1 Å the number of independent parameters (Nind) that can be refined is 12. This is enough to distinguish between Ni and Mg second shells. However there were not enough Nind parameters to model multiple environments simultaneously on the same spectrum.

In order to model the partial substitution of Ni by Mg within the crystalline structure the Nind impose some limitation in terms of the EXAFS fitting. This was overcome by performing simultaneously a lineal combination with k3-weighted χ(k) for second shells one corresponding to Ni and another to Mg. This implied refining the Ni and Mg shells with the constraint that the sum of the two components equals one, to account for Ni local environment. When doing that the same degree of disorder has been also defined in both shells by forcing them to share the same Debye-Waller factor. This additional last assumption kept the Nind acceptable, and allowed the accounting for the amount of Ni and Mg second shells within the phyllosilicates.

3.10. FLOW-THROUGH DISSOLUTION EXPERIMENTS

Seven representative samples were selected for this study as the most representative in terms of mineralogy and chemical composition. In the experiments, a known mass of these samples was placed in a reaction cell (ca. 35 mL in volume) with a continuous flow of a solution with well constrained pH (**Fig. 3.2a-c**) until steady state was achieved (from 1000 up to 3000 hours).

3.10.1. Sample characterisation and preparation

A few grams of the selected samples were carefully hand-picked, and any possible impurities were removed using a binocular, a sharp cutter and a pair of tweezers. The samples were ground using an agate mortar and pestle, and were sieved in order to obtain a particle size between 53 and 106 μm (**Fig. 3.2d-g**). The specific surface area ($m^2 \cdot s^{-1}$) of the resulting specimens was determined by the Brunauer-Emmett-Teller (BET) method (Brunauer *et al*., 1938) with a Micromeritics ASAP 2000 surface area analyser using 5-point N_2 absorption

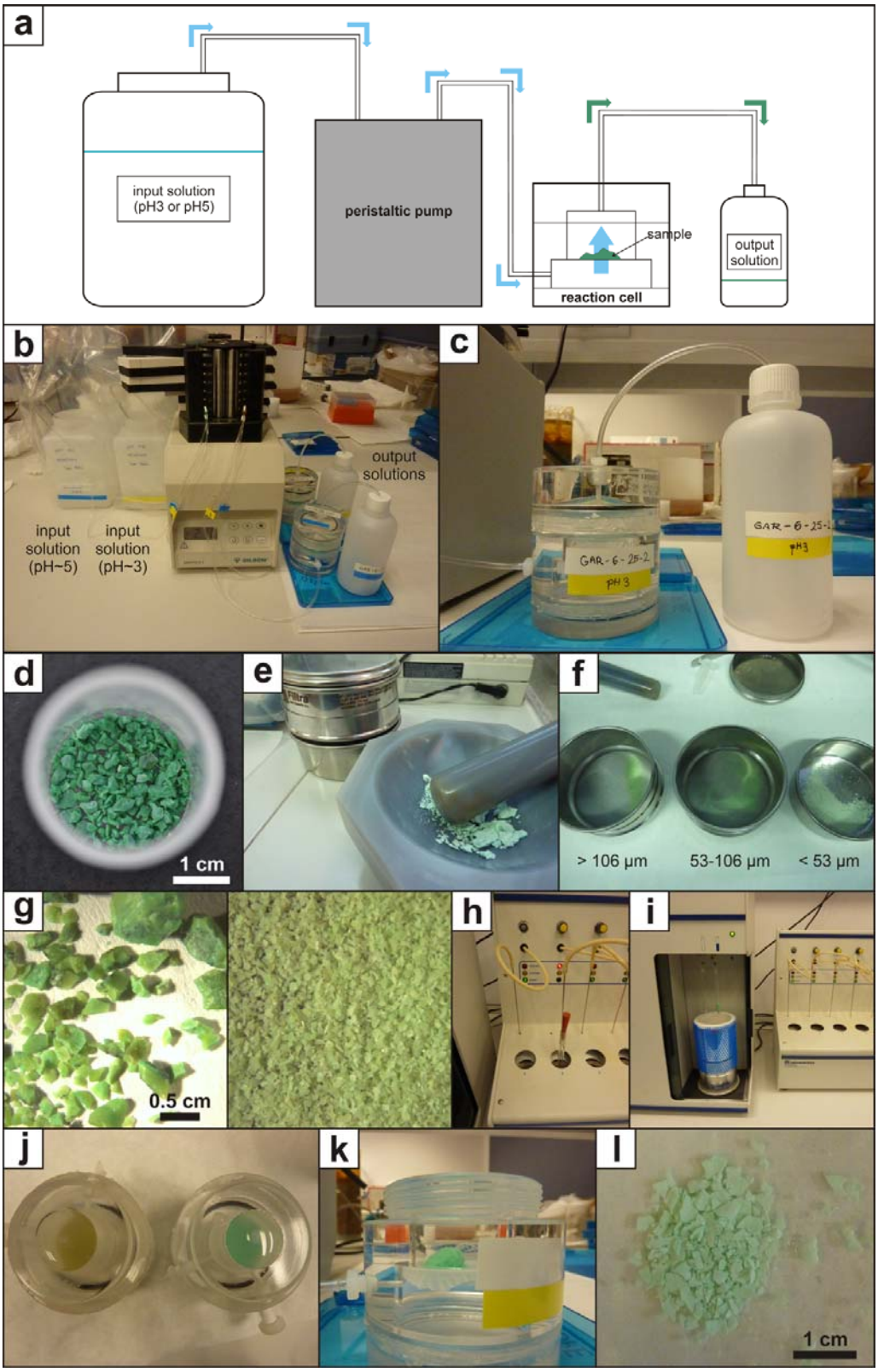

FIGURE 3.2. The flow-through experimental setup and the corresponding sample preparation procedure: **a**) scheme of the experimental setup; **b**) photograph of the experimental setup in the laboratory for sample GAR-6; **c**) close-up of the experimental setup for sample GAR-6; **d**) approximately 3 grams of hand-picked sample GAR-2; **e**) FALC-3 in the agate mortar during grinding; **f**) sample GAR-2 being sieved; **g**) sample 09GAR-2 before (left) and after (right) grinding and sieving; **h**) sample in a glass tube during heating before BET; **i**) sample in glass tube during BET; **j**) samples 09GAR-2 (left) and LC100IV (right) inside their respective reaction cells, from above; **k**) sample FALC-3 inside the reaction cell; **l**) sample FALC-3 dried after the experiment.

isotherms (**Fig. 3.2h-i**). The samples were then placed into the reaction cells, filled with the input solution and closed (**Figs. 3.2j-k**).

Simultaneously with the experiment, a portion of the samples was powdered to be analysed by XRD, following the procedure described in **Section 3.2**, and some hand picking particles of each sample were included in resin, polished and carbon-coated to be analysed by EMP with the same conditions described in **Section 3.6**. The structural formulae of serpentine and talc-like garnierite mixtures were calculated according to **Section 3.6.2**.

After the experiment, each cell was dismantled and the sample was vacuum-dried, weighted, BET measured and stored (**Fig. 3.2l**). Some particles were examined under a Field Emission Scanning Electron Microscope (FESEM) Jeol JSM-7100 at 20 kV in the CCiT-UB. The particles were first mounted on a metal sample holder and carbon-coated in order to study their morphology, and were later included in resin, polished and carbon-coated to analyse variations in the chemical composition and internal texture after the experiment.

3.10.2. Experimental setup

The non-stirred flow-through experiments were carried out by using reaction cells composed of two chambers; a lower chamber with an inner diameter of 33 mm and an upper chamber with an inner diameter of 26 mm. The two chambers are separated by a 5 μm-thick nylon mesh, on which the mineral powder was placed (**Figs. 3.2h, j**). Once the steady state was attained, the dissolution rate R (mol m^{-2} s^{-1}) was calculated from the release of Si, Mg and Ni according to the expression (Nagy *et al*., 1991) [**Eq. 7**]:

$$v_j R = \frac{q}{A}\left(C_{j,out} - C_{j,inp}\right) \text{[Eq. 7]}$$

in which v_j is the stoichiometric coefficient of j in the dissolution reaction; q is the fluid volume flux through the system ($m^3 \cdot s^{-1}$); A is the reactive surface area (m^2); and $Cj_{,inp}$ and $C_{j,out}$ are the concentrations of component j (Si, Mg, Ni) in the input and the output solutions, respectively (mol·s^{-3}). The error in the calculated dissolution rates is approximately 15%.

The cells were connected with the input solutions by a tube (inner diameter 38 μm) through a Gilson peristaltic pump that controlled an average input flow rate of 0.04 mL·min^{-1} (details in Cama & Acero, 2005), and the output solution was collected in a closed plastic bottle (**Figs. 3.2a-c**).

Input solutions were prepared with Millipore MQ water (18.2 MΩ cm at 25 ºC) and reagent grade HCl (Merck). The pH of the output solution was measured with a ThermoScientific Orion© combined glass electrode at room temperature (~25ºC). The uncertainty was ±0.02 pH units. Concentrations of Si, Ni, Mg, Fe and Al were measured by Inductively Coupled Plasma-Optical Emission Spectrometry (ICP-AES), using a Thermo Jarrel-Ash spectrometer equipped with a CID detector, at the IDAEA-CSIC facility. The accuracy of ICP-AES measurement was estimated to be around 3%. The detection limits for Si, Ni, Mg, Fe and Al were 7×10^{-7}, 9×10^{-8}, 2×10^{-6}, 2×10^{-7} and 8×10^{-7} mol·L^{-1}, respectively.

The binary diagrams were elaborated with the KaleidaGraph® 4.0 program (Synergy Software).

4. MINERALOGY, TEXTURES AND MINERAL CHEMISTRY OF GARNIERITES AND RELATED ROCKS

4.1. MODE OF OCCURRENCE OF GARNIERITES IN THE FALCONDO NI-LATERITE DEPOSIT

Garnierite mineralisation exposed in the mining pit is concentrated in discrete zones from tens to one hundred metres long and up to five metres thick (**Fig. 4.1a, b**). They are found mainly within the lowermost part of the saprolite horizon (**Fig. 4.1c**) as well as in unweathered serpentinised peridotite at the base of the profile (**Fig. 4.1d**) and in the soft serpentine zone in the upper saprolite horizon (**Fig. 4.1e**).

The garnierites occur mainly as mm–cm veins in fractures (**Fig. 4.1c–h**), as well as thin coatings on joints and fault planes which are oriented in random directions (**Fig. 4.1i–k**). The coatings on fault plane surfaces commonly contain slickensides (**Fig. 4.1l**). Garnierites are also found in two different kinds of breccias: i) weathered serpentinised ultramafic rock (saprolite) fragments cemented by garnierite, and ii) silicified Ni-sepiolite fragments cemented by a later generation of garnierite. In addition, another type of breccia is found in the laterite profile, not containing garnierite, and consisting of saprolite clasts cemented by Ni-free sepiolite and silica/quartz (**Fig. 4.1m, n**).

The garnierites occur in various shades of green. Apart from the sepiolite-falcondoite species, with typical white to pale green colour and remarkable schistosity, four types of garnierite have been distinguished according to their colour and will be hereafter named type I to IV: Type I is yellowish pale green, type II is apple green, type III is dark green, and type IV is bluish green. Type IV is the dominant phase and the other phases are less common but quite distinctive. Type I occurs as millimetre-thick infillings in fractures (**Fig. 4.1c**). Types II and III form millimetre to centimetre-scale fracture infillings and coatings (**Fig. 4.1c, g, i**). Finally type IV occurs as thin coatings and fillings in fractures (**Fig. 4.1g**), and coexists with other garnierite types, typically superimposed to the yellowish green and apple green types. In addition, all the above four types of garnierites also occur as cementing material in breccia with saprolite clasts. Finally, the sepiolite–falcondoite (classified here as type V) commonly forms centimetre-thick vein fillings (**Fig. 4.1h**).

4.2. MINERALOGY AND TEXTURES

Fifteen samples were selected for this chapter, which are listed in **Table 4.1**. Representative photos of these samples are displayed in **Figure 4.2**. The phases composing these samples were analysed by XRD, and a selection of the obtained patterns is presented in **Figure 4.3**. Ten samples of garnierite from the saprolite horizon contain characteristic XRD patterns of talc- and serpentine-like garnierites and display the four greenish colour types reported previously (**Fig. 4.3**). The other four samples were identified as Ni-sepiolite and falcondoite, respectively. Different types of garnierite may coexist in the same sample, as seen in **Figure 4.2**, however, it is important to point out that sepiolite-falcondoite are never directly related to serpentine- and talc-like garnierites. The same powders used in XRD were analysed by DTA-TG, and the results are shown in **Figure 4.4** and **Table 4.2**. The samples were prepared as thin sections and studied under optical and electron microscopy, and representative optical micrographs of characteristic textures are displayed in **Figure 4.5**.

4.2.1. Saprolite serpentine

Saprolite, which represents the weakly weathered protolith, is the most common host for garnierites. In the studied samples, saprolite is reddish to dark brown and is crosscut by a close fine mesh of black veinlets (**Fig. 4.1a, b**) and consists mainly of serpentine (**Fig. 4.2a**) and Fe oxides and oxyhydroxides. Close to the fractures and to the edges of saprolite fragments, where the serpentinite is further altered (**Fig. 4.1a, b**), the serpentine is greenish grey to black in colour. Under the optical microscope, serpentine forms yellow veins wrapping reddish brown cores of serpentine and Fe oxides and oxyhydroxides, preserving the previous mesh textures of the serpentinised olivine.

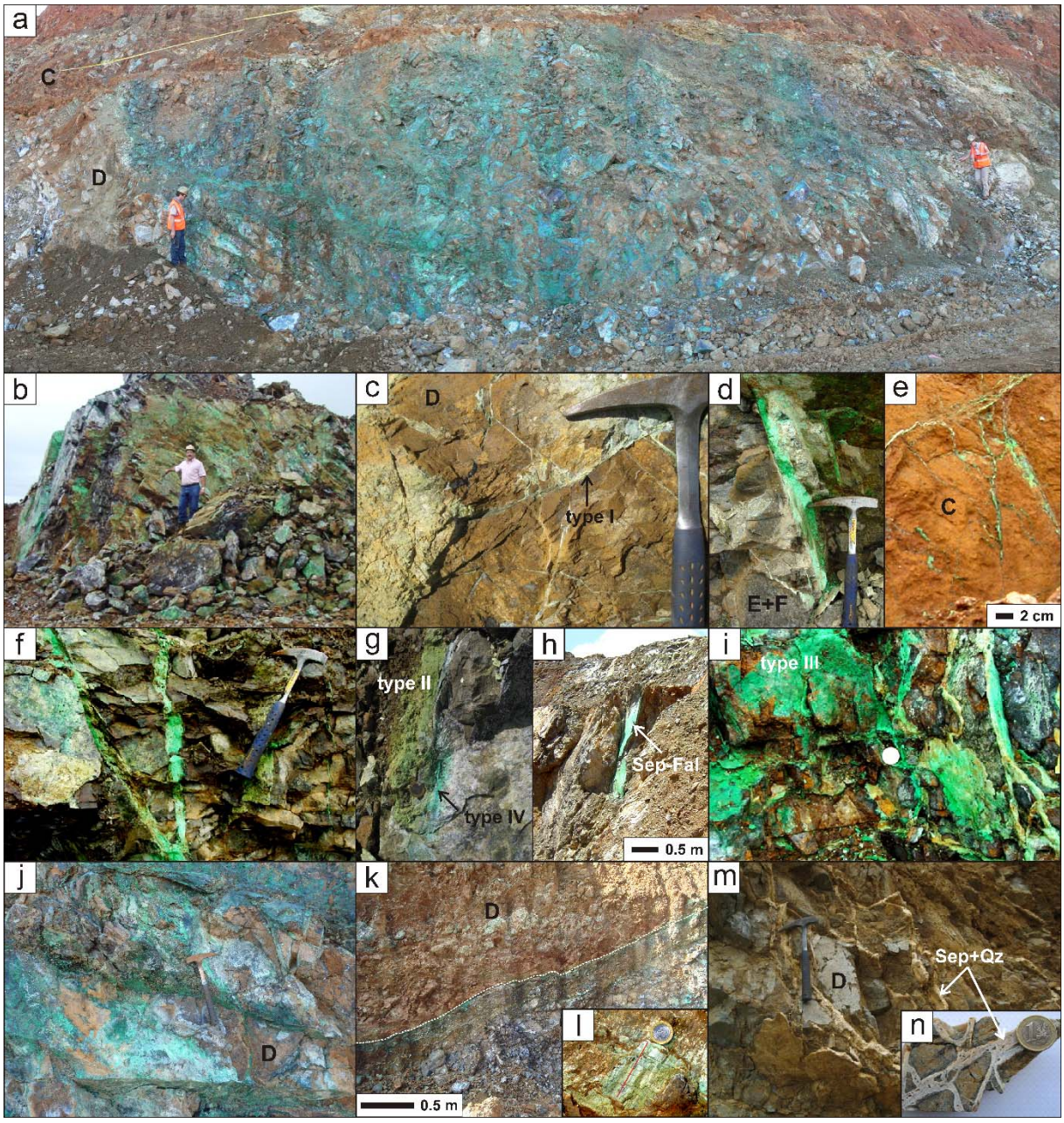

FIGURE 4.1. Occurrence of garnierite mineralisations in the Falcondo deposit: **a–b**) garnierite outcrops in zone D; **c**) veinlets of type I crossing saprolite (zone D); **d**) garnierite veins cutting unweathered serpentinised peridotites (zone E + F); **e**) veinlets within upper saprolite horizon (zone C); **f**) type III in veins; **g**) types II and IV in veins; **h**) vein of sepiolite–falcondoite; **i**) type III forming coatings in fractures; **j**) veins and coatings on joints with random orientations, k) garnierite mineralisation along a fault plane; **l**) slickenside with visible direction of movement; **m**) breccia of saprolite clasts cemented by sepiolite and quartz/silica; **n**) detail of sample collected from m). Legend: I–IV = types I–IV, Sep = sepiolite, Fal = falcondoite, Qz = quartz.

Serpentine near fractures and edges of fragments is pale yellow and shows diffuse cores under the optical microscope. The groundmass of serpentine contains scattered tiny anhedral relict chromite grains, altered to ferrian chromite (**Fig. 4.5a, b**). Relict crystals of primary silicates are extremely rare. Intergrowths of a Ni-bearing talc-like phase are common near cracks, and are interpreted as replacements of serpentine (**Fig. 4.5b**, lower left).

4.2.2. Type I garnierite

Type I (yellowish pale green) garnierite occurs as millimetre to centimetre-thick veins in the saprolite (**Fig. 4.2a**). These veins are often crosscut or

TABLE 4.1. Summary of the samples selected for this study, including a brief hand specimen description, the mineralogy obtained by XRD, the average structural formulae and Ni content (in atoms per formula unit and oxide weight percent) of each phase from EMP.

Samples	Description	Type(s)	Mineralogy (XRD)	Structural formula (EMP) [number of analyses averaged]	Ni content (apfu)	NiO content (%.wt)
LC-101, 09GAR-2, RD-1	Saprolite breccia cemented by type I (yellowish pale green), in turn wrapped by type IV (bluish green) (Fig. 4.2a).	saprolite	serpentine (7.25 Å)(Fig. 4.3a)	$(Mg_{2.48}Ni_{0.14}Fe_{0.20})(Si_{2.01}Al_{0.03})O_5(OH)_4$ [35]	0.05-0.43	1.19-10.53
		type I (yellowish pale green)	serpentine (7.26-7.32 Å) (Fig. 4.3b)	$(Mg_{2.31}Ni_{0.34}Fe_{0.17})Si_{2.30}O_{5.84}(OH)_{3.36}\cdot 0.22H_2O$ [39]	0.06-0.73	1.51-14.58
		type IV (bluish green)	talc	$(Ni_{1.92}Mg_{1.08})Si_{3.76}O_{9.43}(OH)_{2.23}\cdot 0.89H_2O$ [137]	1.06-2.58	15.18-33.50
LC100	Saprolite breccia cemented by type II (apple green), in turn wrapped by type IV (bluish green) (Fig. 4.2b).	saprolite	serpentine	$(Mg_{2.49}Ni_{0.17}Fe_{0.13})(Si_{2.03}Al_{0.05})O_5(OH)_4$ [20]	0.08-0.24	2.09-6.42
		type II (apple green)	serpentine (7.30 Å) + talc (10.20-10.54 Å) (Fig. 4.3c)	$(Mg_{2.09}Ni_{0.87}Fe_{0.05})(Si_{2.32}Al_{0.09})O_{6.53}(OH)_{3.39}\cdot 0.31H_2O$ [66]	0.15-1.42	3.77-26.62
		type IV (bluish green)	talc (9.94 Å) (Fig. 4.3f)	$(Ni_{1.95}Mg_{1.04})Si_{3.69}O_{9.24}(OH)_{2.30}\cdot 0.85H_2O$ [109]	1.08-2.58	18.37-44.39
GAR-1	Massive dark green aggregate (Fig. 4.2c), breccia with massive dark green aggregate cementing light green clasts of sepiolite and other phyllosilicates embedded in an amorphous silica/quartz matrix (Fig. 4.2d).	type III (dark green)	serpentine (7.33 Å) + talc (10.52 Å) and minor sepiolite (12.20 Å) (Fig. 4.3d)	$(Ni_{2.56}Mg_{0.43})Si_{2.97}O_{7.44}(OH)_{3.02}\cdot 0.49H_2O$ [27]	2.10-2.81	32.43-49.71
		breccia clasts (Fig. 4.3c)	quartz	$Ni_{0.002}Mg_{0.001}Si_{0.998}O_2$ [15]	0.001-0.005	0.08-0.63
			sepiolite (12.23 Å)	$Ni_{5.12}Mg_{2.36}Si_{12.24}O_{15}(OH)_2\cdot 6H_2O$ [1]	5.12	26.98
			serpentine + talc (not detected in XRD)	$(Mg_{1.63}Ni_{1.33}Fe_{0.03})(Si_{2.29}Al_{0.01})O_{7.20}(OH)_{3.12}\cdot 0.44H_2O$ [8]	0.54-2.32	11.61-41.50
			talc (not detected in XRD)	$(Ni_{2.11}Mg_{0.88})Si_{4.08}O_{10.20}(OH)_{1.92}\cdot 1.04H_2O$ [2]	1.97-2.26	30.44-32.01
GAR-2, GAR-3	Saprolite breccia cemented by type III (dark green) (Fig. 4.2e).	saprolite	serpentine	$(Mg_{2.45}Ni_{0.10}Fe_{0.28})(Si_{2.01}Al_{0.01})O_5(OH)_4$ [13]	0.05-0.15	1.15-3.63
		type III (dark green)	serpentine (7.40 Å) + talc (10.56 Å) (Fig. 4.3e)	$(Ni_{1.95}Mg_{1.03}Fe_{0.02})Si_{3.09}O7.75(OH)_{2.90}\cdot 0.55H_2O$ [40]	1.43-2.53	23.51-45.24
GAR-6	Saprolite breccia cemented by type IV (bluish green) (Fig. 4.2f).	saprolite	serpentine	$(Mg_{2.39}Ni_{0.18}Fe_{0.25})(Si_{2.00}Al_{0.02})O_5(OH)_4$ [2]	0.17-0.19	4.48-4.80
		type IV (bluish green)	talc (10.14 Å) and traces of serpentine (7.34 Å)	$(Ni_{1.90}Mg_{1.10})(Si_{3.61}Al_{0.01})O_{9.06}(OH)_{2.40}\cdot 0.81H_2O$ [17]	1.42-2.25	24.26-38.91
GAR-4, GAR-5	Aggregates of type IV (bluish green) in a matrix of a second generation of garnierite and microcrystalline quartz, with some scarce saprolite fragments (Fig. 4.2g).	saprolite	serpentine	$(Mg_{2.32}Ni_{0.15}Fe_{0.27})(Si_{1.97}Al_{0.11})O_5(OH)_4$ [6]	0.11-0.21	2.84-5.19
		type IV (bluish green)	talc (10.02 Å) (Fig. 4.3g)	$(Ni_{1.38}Mg_{1.62})(Si_{3.81}Al_{0.02})O_{9.56}(OH)_{2.18}\cdot 0.91H_2O$ [209]	0.47-2.58	7.77-41.03
FALC-1	White to pale green sets of wavy sheets of Ni-sepiolite-falcondoite (Fig. 4.2h-i).	type V (sepiolite-falcondoite)	sepiolite	$Mg_{6.35}Ni_{1.07}Fe_{0.01}Si_{12.23}Al_{0.01}O_{15}(OH)_2\cdot 6H_2O$ [10]	0.63-1.55	0.95-13.16
FALC-2			sepiolite	$Mg_{4.96}Ni_{2.30}Si_{12.35}O_{15}(OH)_2\cdot 6H_2O$ [29]	0.85-3.94	3.70-8.56
FALC-3			sepiolite (12.15 Å) (Fig. 4.3i)	$Mg_{4.07}Ni_{3.90}Fe_{0.01}Si_{11.91}Al_{0.12}O_{15}(OH)_2\cdot 6H_2O$ [4]	2.29-5.24	5.43-22.44
FALC-4			sepiolite (12.07 Å) (Fig. 4.3h)	$Mg_{7.02}Ni_{0.51}Fe_{0.12}Si_{12.11}Al_{0.02}O_{15}(OH)_2\cdot 6H_2O$ [16]	0.34-0.60	12.25-26.82
GAR-7	Pale green Ni-sepiolite-falcondoite embedded in a matrix of amorphous silica, with flaky white sepiolite.	type V (sepiolite-falcondoite)	sepiolite (12.27 Å) (Fig. 4.3j)	$Mg_{6.02}Ni_{1.60}Fe_{0.02}Si_{12.16}O_{15}(OH)_2\cdot 6H_2O$ [30]	1.01-2.39	2.06-3.53

superimposed by millimetric veinlets of type IV (bluish green) garnierite and white quartz. Type I garnierite is characterised by a maximum diffraction peak between 7.26 and 7.32 Å, which coincides with the characteristic basal spacing range of the serpentine group minerals (**Fig. 4.3b**).

Two weak endothermic peaks are observed at 80 and 624 ºC and a strong exothermic peak at 816 ºC (**Fig. 4.4a1**; **Table 4.2**). Mass loss is produced in three steps: 3.4, 9.0 and 1.1 % (**Fig. 4.4a2**). In general, the DTA and TG curves obtained are comparable to the curves for serpentine group minerals published by Viti (2010). However, the endothermic and exothermic peaks for antigorite, lizardite, polygonal serpentine and chrysotile are at slightly higher temperatures than those obtained in type I garnierite. The peaks in the range of 550 to 800ºC occur at relatively low temperatures (620ºC), more similar to the thermal effects of chrysotile than to those of antigorite, lizardite or polygonal serpentine (Viti, 2010). Endothermic peaks at about 600 ºC are attributed to the loss of structural water in serpentine minerals (Caillère & Hénin, 1957).

Under the optical microscope this garnierite type consists of a yellowish brown heterogeneous material, intergrown with Fe oxyhydroxides (**Fig. 4.5a-d**). In addition, a nickeliferous talc-like phase may be present as seen in the backscattered electron image in **Fig. 4.5e**.

4.2.3. Type II garnierite

Type II (yellowish or apple green) occurs as coatings on angular saprolite fragments (**Fig. 4.2b**). This garnierite is in turn superposed by type IV garnierite and millimetre-thick veinlets of whitish quartz. The Type II garnierite is characterised by a very intense and sharp diffraction peak at 7.30 Å, and a lower broad peak at 10.20-10.54 Å, corresponding to the basal spacings of serpentine and talc, respectively (**Fig. 4.3c**). This suggests that the sample is a serpentine-like phase with talc-like impurities. It must be noted that type II "garnierites" show a diffraction peak at 1.51 Å, thus indicating the presence of lizardite (and/or its Ni analogue népouite) (Milton *et al*., 1983). The lack of this peak in the remaining serpentine-bearing "garnierites" suggests that the serpentine mineral is chrysotile and/or its Ni equivalent pecoraite (**Fig. 4.3c**).

Weak endothermic peaks at 109, 635 and 805 ºC, and a strong exothermic peak at 817 ºC are observed (**Fig. 4.4b1**; **Table 4.2**). Mass loss is performed in three steps: 3.74, 9.52 and 1.88 % (**Fig. 4.4b2**; **Table 4.2**). Results are comparable to those obtained in type I garnierite, except for endothermic peaks at ~100 and ~800ºC. All the thermal effects observed are typical of serpentine minerals (Caillère & Hénin, 1957). The TG curve is similar to that presented in Sufriadin *et al*. (2012) for sample KR-1.

Under the optical microscope, this garnierite consists of colourless to yellowish, slightly anisotropic serpentine aggregates up to 0.5 mm in length (**Figs. 4.5g-h**), frequently enveloped by a very fine grained brownish grey fibrous matrix of a Ni-talc-like phase (**Figs. 4.5i-j**) or being replaced by fine grained Ni-talc-like (**Figs.4.5k-m**). This matrix and replacements may show spindle-shaped features (**Fig. 4.5n-q**). Associated to this garnierite voids filled with euhedral elongated quartz crystals are frequent (**Fig. 4.5i-j**).

4.2.4. Type III garnierite

Type III (dark green) garnierite shows a characteristic dull to greasy luster, and consists of friable aggregates up to 15 cm in length (**Fig. 4.2c**). They also occur as matrix in breccias with: a) millimetre to centimetre-sized fragments, composed of fine-grained, whitish green mixture of Ni-sepiolite and quartz (**Fig. 4.2d**), and b) brownish orange, centimetre scale, angular saprolite clasts (**Fig. 4.2e**). This dark green garnierite is characterised by a diffraction peak at 7.30–7.38 Å and a slightly broader peak at 9.86–10.46 Å, both having similar intensities (**Fig. 4.3c**) suggesting a mixture of serpentine-like and talc-like phases.

Endothermic peaks at 102 and 575ºC are observed (**Fig. 4.4c1**; **Table 4.2**). Mass loss is performed in three steps: 7.21, 5.53 and 2.32 % (**Fig. 4.4c2**; **Table 4.2**). The DTA curve is similar to that of talc (Caillère & Hénin, 1957). The TG curve is comparable to those of serpentine group minerals, but with a larger initial weight loss (**Fig. 4.4g**).

Under the optical microscope, type III garnierite occurs as greenish to intense green homogeneous coatings, frequently presenting botryoidal features, intergrown with quartz crystals (**Figs. 4.5r-t**). The euhedral terminations of the quartz crystals, in addition to the presence of several pores in the matrix, suggest that quartz and garnierites have grown in voids. In addition, this garnierite occurs as

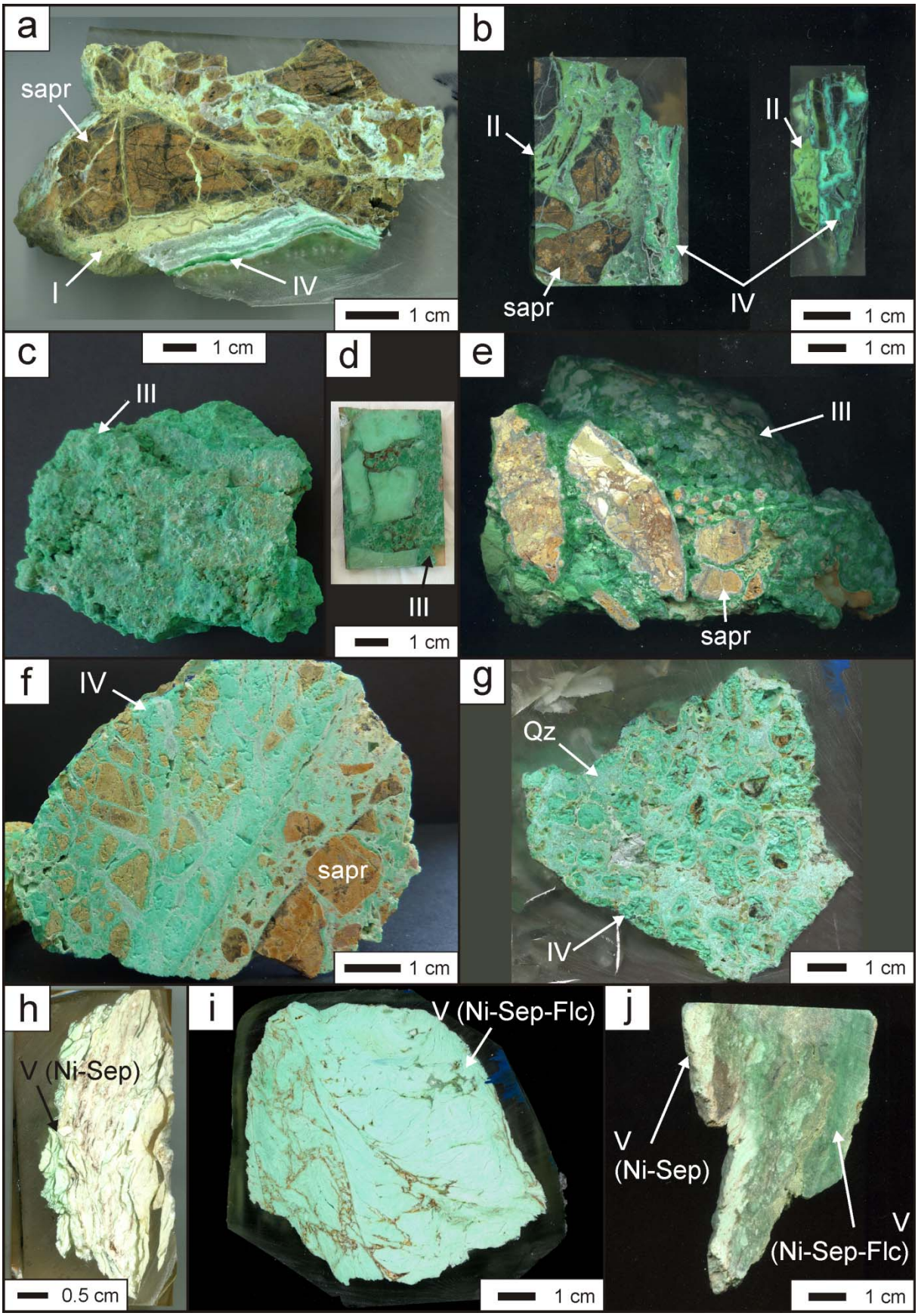

FIGURE 4.2. Hand specimens of the samples selected for this study: a) LC-100Aa. b) LC-100B, c-d) GAR-1, e) GAR-2, f) GAR-6, g) GAR-4, h) FALC-4 (F-0), i) FALC-3 (F-3), j) GAR-7. Legend: I–V = types I–V, sapr = saprolite fragment, Qz = quartz, Ni-Sep = Ni-sepiolite, Fal = falcondoite. See text for explanation.

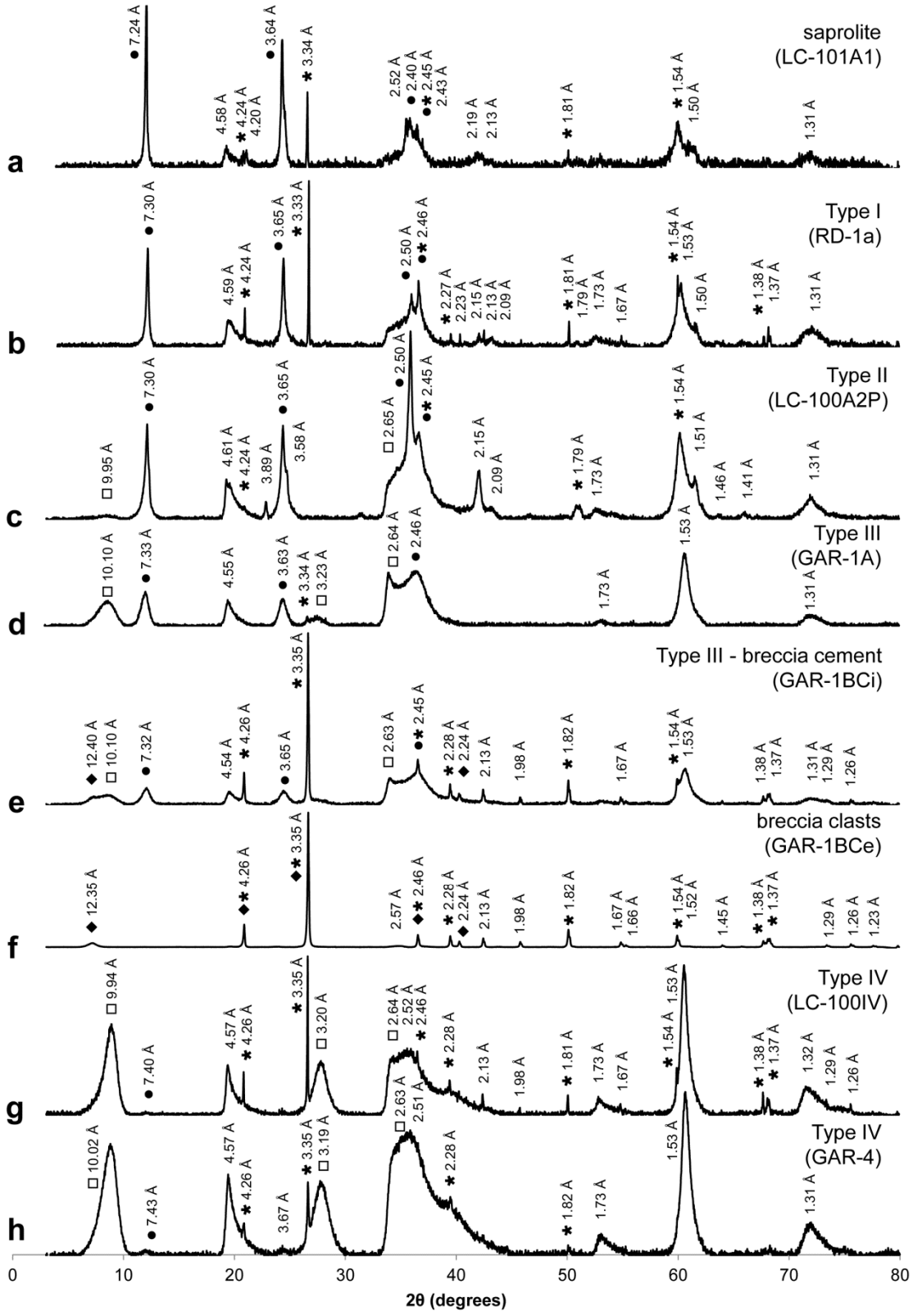

FIGURE 4.3. Selected X-ray powder difractograms of the studied garnierites from the Falcondo Ni-laterite deposit and related assemblages: **a**) saprolite (sample LC-101A1); **b**) type I garnierite (RD-1a); **c**) type II (LC-100A2P); **d**) type III (GAR-1A); **e**) type III-cement of garnierite breccias (GAR-1BCi); **f**) clasts of garnierite breccias (GAR-1BCe); **g**) type IV (LC-100IV); **h**) type IV (GAR-4). Legend: black circles (●) = d-spacings of serpentine-like structures, empty squares (□) = of talc-like structures, black diamonds (◆) = of sepiolite-like structures, and asterisks (✱) = of quartz.

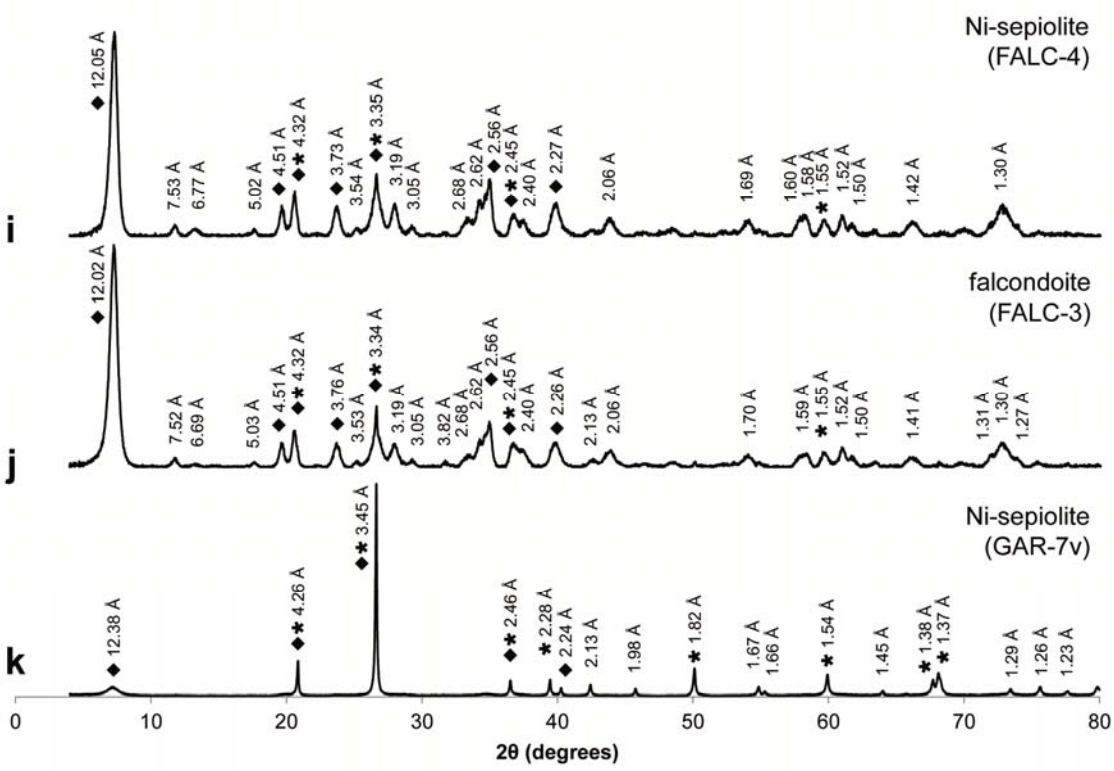

FIGURE 4.3. (CONTINUED). i) Ni-sepiolite (FALC-4), j) falcondoite (FALC-3), k) Ni-sepiolite embedded in a silica matrix (GAR-7v). Legend: black circles (●) = d-spacings of serpentine-like structures, empty squares (□) = of talc-like structures, black diamonds (◆) = of sepiolite-like structures, and asterisks (✱) = of quartz.

coatings on types II and IV garnierites (**Figs. 4.5u-v**).

4.2.5. Type IV garnierite

Type IV (bluish green) garnierite occurs as millimetre to centimetre sized coatings superimposed over other garnierite types and saprolite fragments (**Fig. 4.2a, b**). It also occurs as cement in breccias with centimetre to millimetre-size, rounded, brownish orange saprolite clasts. The saprolite clasts may contain narrow greenish white quartz veinlets (**Fig. 4.2f**), and up to 2 cm long rounded, non-spherical granules embedded in a greenish white, microcrystalline quartz matrix coexisting with millimetric angular, dark brown and/or orange saprolite fragments (**Fig. 4.2g**). Type IV garnierite shows a broad diffraction peak at 9.58–10.02 Å suggesting that it consists uniquely of a talc-like phase with minor quartz impurities (**Fig. 4.3d**).

Smooth endothermic peaks at 96 and 889 ºC and exothermic peaks at 398 and 777 ºC are observed (**Fig. 4.4d1**, **Table 4.2**). Mass loss is performed in four steps: 3.42, 1.19, 2.83 and 3.06 % (**Fig. 4.4d2, Table 4.2**). The remarkable mass loss at low temperatures of this sample confirms that the name kerolite-pimelite is the most suitable in this case, replacing their non-hydrated but accepted equivalent "talc-willemseite", as talc has a single mass loss of about 6% above 800 ºC (**Fig. 4.4g2**). Also, the differential thermal analysis is different from that of talc, in which only a strong endothermic peak at about 1000 ºC appears (Caillère & Hénin, 1957; **Fig. 4.4g1**).

Under the optical microscope, type IV garnierite consists of yellow to brown, banded, botryoidal aggregates, and is grey to yellow in crossed polars. It is commonly intergrown with, superimposed and/or crosscut by quartz veinlets (**Figs. 4.5z-ae**). In the samples where type IV forms rounded granules, the saprolite fragments are coated by botryoidal garnierite, and this in turn is enveloped by the microcrystalline quartz matrix (**Fig. 4.5z**). This matrix is formed by equigranular rounded quartz grains of about 0.1 mm accompanied by disaggregated, angular, talc-like fragments up to 0.5 mm long, which are dark brown under plane polarised light and grey to orange under crossed

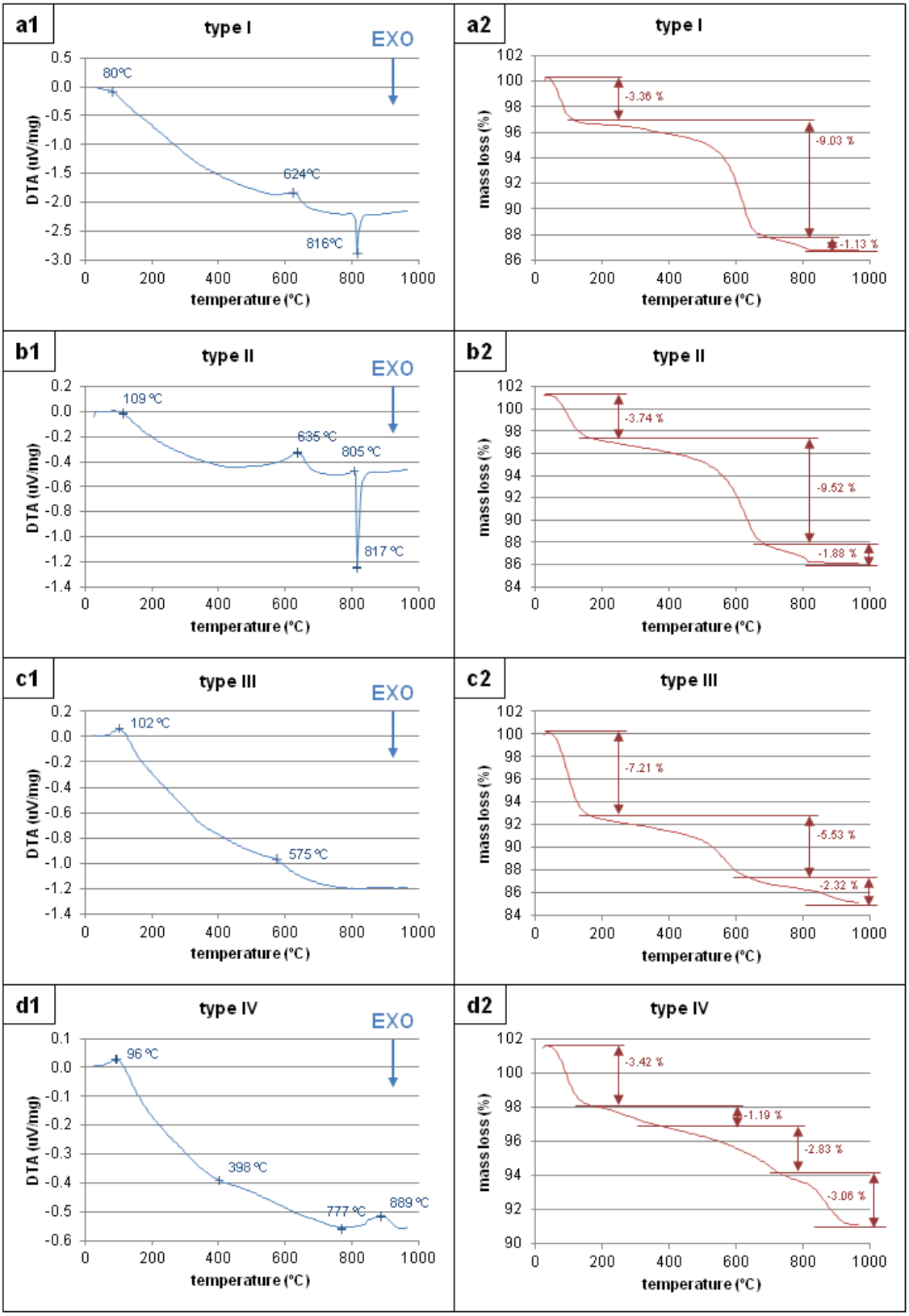

FIGURE 4.4. Differential Thermal Analysis (**a1-g1**) and Thermogravimetry (**a2-g2**) curves of some of the samples selected for this study: **a1-a2**) type I (sample RD-1a), **b1-b2**) type II (LC-100A2), **c1-c2**) type III (GAR-2), **d1-d2**) type IV (LC-100A2).

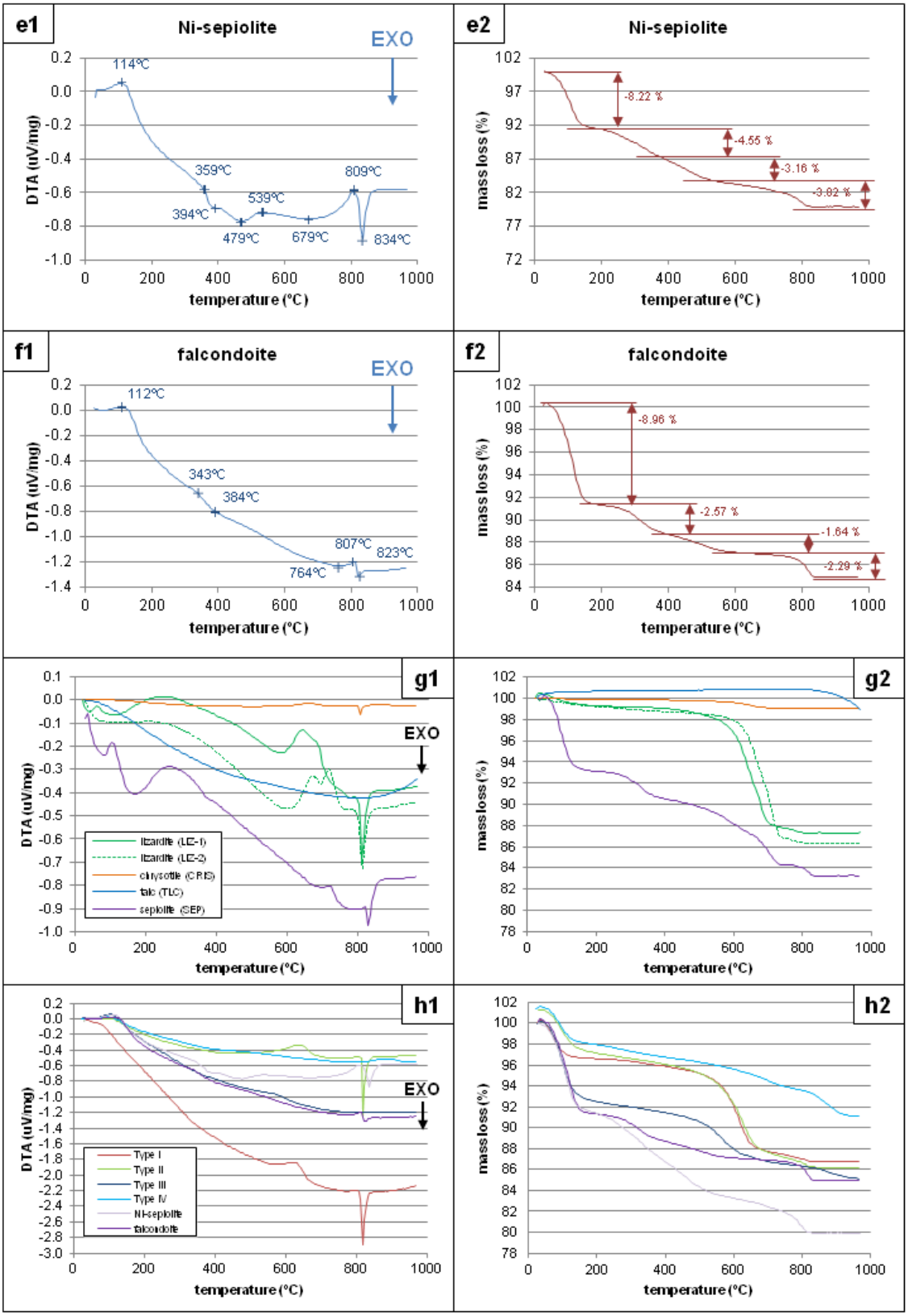

FIGURE 4.4. (CONTINUED). **e1-e2**) Ni-sepiolite (FALC-4), **f1-f2**) falcondoite (FALC-3), **g1-g2**) all the samples together to be compared to Ni-free phyllosilicates as a reference (**h1-h2**): LIZ-1 (lizardite from Lizard, Cornwall, UK), LIZ-2 (lizardite from Isolad'Elba, Italy), CRIS (chrysotile from Huelva, Spain), TLC (talc from León, Spain), SEP (sepiolite from Setcases, Catalunya). See **Appendix A2** for the characterisation of these Ni-free phyllosilicates.

TABLE 4.2. Differential Thermal Analysis peaks (legend: T = temperature; exo = exothermic; endo = endothermic) and Thermogravimetry losses in weight percent (legend: T range = temperature range) of the main types of garnierites from Falcondo analysed.

Type I	RD-1a	**Type II**	LC-100A2	**Type III**	GAR-2	**Type IV**	LC-100A2	**Ni-Sepiolite**	FALC-4 (F-0)	**Falcondoite**	FALC-3 (F-3)
T (ºC)	DTA peak	T (ºC)	DTA peak	T (ºC)	DTA peak	T (ºC)	DTA peak	T (ºC)	DTA peak	T (ºC)	DTA peak
80.0	endo	108.9	endo	102.2	endo	96.3	endo	114.4	endo	112.1	endo
624.4	endo	635.0	endo	575.1	endo	397.9	exo	359.4	endo	343.0	endo
816.3	exo	804.7	endo			776.6	exo	394.4	exo	383.9	exo
		816.9	exo			888.9	endo	479.4	exo	541.9	endo
								539.4	endo	763.7	exo
								679.4	exo	807.4	endo
								809.4	endo	823.0	exo
								834.4	exo		
Type I	RD-1a	**Type II**	LC-100A2	**Type III**	GAR-2	**Type IV**	LC-100A2	**Ni-Sepiolite**	FALC-4 (F-0)	**Falcondoite**	FALC-3 (F-3)
T range (ºC)	TG loss (%)	T range (ºC)	TG loss (%)	T range (ºC)	TG loss (%)	T range (ºC)	TG loss (%)	T range (ºC)	TG loss (%)	T range (ºC)	TG loss (%)
25-130	3.36	25-180	3.74	25-170	7.21	25-180	3.42	25-200	8.22	25-170	8.96
130-690	9.03	180-700	9.51	170-625	5.53	180-380	1.19	200-390	4.55	170-400	2.57
690-1000	1.13	700-1000	1.88	625-1000	2.32	380-745	2.83	390-525	3.16	400-645	1.64
						745-1000	3.06	525-1000	3.82	645-1000	2.29

TABLE 4.2. (CONTINUED). Differential Thermal Analysis peaks (legend: T = temperature; exo = exothermic; endo = endothermic) and Thermogravimetry losses in weight percent (legend: T range = temperature range) of the main types of garnierites from Falcondo analysed. See **Appendix A2** for the characterisation of these Ni-free phyllosilicates.

Lizardite	LIZ-1	**Lizardite**	LIZ-2	**Chrysotile**	CRIS	**Talc**	TLC	**Sepiolite**	SEP
T (ºC)	DTA peak	T (ºC)	DTA peak	T (ºC)	DTA peak	T (ºC)	DTA peak	T (ºC)	DTA peak
42.7	exo	140.1	exo	506.4	exo	812.6	exo	85.5	exo
67.7	endo	210.1	endo	666.4	endo			110.5	endo
127.7	exo	605.1	exo	806.4	exo			175.5	exo
257.7	endo	680.1	endo					275.5	endo
587.7	exo	700.1	exo					700.5	exo
647.7	endo	720.1	endo					725.5	endo
687.7	endo	795.1	endo					795.5	exo
782.7	exo	815.1	exo					820.5	endo
797.7	endo							830.5	exo
812.7	exo								

Lizardite	LIZ-1	**Lizardite**	LIZ-2	**Chrysotile**	CRIS	**Talc**	TLC	**Sepiolite**	SEP
T range (ºC)	TG loss (%)	T range (ºC)	TG loss (%)	T range (ºC)	TG loss (%)	T range (ºC)	TG loss (%)	T range (ºC)	TG loss (%)
25-300	1.31	25-300	1.22	25-200	0.94	800-1000	1.69	25-200	6.99
300-800	11.85	300-800	12.57					200-400	2.65
								400-750	6.31
								750-1000	1.07

polars (**Fig. 4.5z-ab**). The banded aggregates are often fractured and crosscut by quartz veinlets of up to 0.1 mm thick, and may show microscopic shearing (**Fig. 4.5aa-ab**). These features suggest that type IV and microcrystalline quartz precipitated from a colloidal silica gel, while the saprolite clasts are interpreted as relicts. The X-ray diffraction patterns and textures of the type IV garnierite are similar to those reported for garnierites from New Caledonia (e.g. sample G6, Figs. 7 and 9 in Wells *et al*., 2009).

4.2.6. Type V garnierite

Ni-sepiolite and falcondoite form white to pale green compact sets of schistose, friable, soft material (**Figs. 4.2h, i, 4.3i, j**). These textures are easily distinguishable from those observed in the other garnierites described above (see Tauler *et al*., 2009 for a detailed study). Ni-sepiolite also occurs as fibrous aggregates embedded in a microcrystalline quartz matrix (**Figs. 4.2j, 4.3k**), which appear as silicified clasts in garnierite-cemented breccias in **Fig. 4.2d**.

In the DTA curve of Ni-sepiolite and falcondoite smooth endothermic peaks at 112-114, 343-359, 539 and 807-809ºC, two weak exothermic peak at 384-394 and 479ºC, and a strong exothermic peak at 823-834ºC are observed (**Fig. 4.4e1**, **Table 4.2**). The TG curve is characterised by a weight loss in four steps (8.22, 4.55, 3.16, 3.82 % for Ni-sepiolite and 8.96, 2.57, 1.64, 2.29 % for falcondoite) (**Fig, 4.4e2**; **Table 4.2**), which do not show the typical ratios 6:4:3:1 (Caillère & Hénin, 1957; Tauler *et al*., 2009). These curves are comparable to published TG curves of Ni-sepiolites and falcondoites (Caillère & Hénin, 1957; Springer, 1976; Tauler *et al*., 2009) and that of **Fig. 4.4g**. According to Caillère & Hénin (1957) and references therein, weight loss at low temperatures represents the loss of zeolitic water and/or hygroscopic moisture. Frost & Ding (2003), suggest that the peak at 200ºC corresponds to the loss of adsorbed water and possibly to the beginning of the loss of structural water. The peaks at the region 300-600ºC indicate the loss of coordinated water (Nagata *et al*., 1974). The endothermic peak at 807-809ºC corresponds to the dehydroxylation of the structure, and the exothermic peak at 823-834ºC to the formation of pyroxene (Jones & Galán, 1988).

Under the optical microscope Ni-sepiolite-falcondoite appears as greenish, oriented, fibrous aggregates crosscut by quartz veinlets (**Fig. 4.5af**), and the typical sepiolite fibres are clearly visible under scanning electron microscope (**Figs. 4.5ag-ah**).

4.3. MINERAL CHEMISTRY

A selection of representative chemical analyses and their corresponding calculated structural formulae of the described garnierite types is listed in **Table 4.3**. Quantitative EMP maps were performed in selected areas of four samples (**Figs. 4.6-9**). All analyses considered valid (oxide totals above 80 wt.%, avoiding analyses contaminated by quartz and/or surrounding Fe oxyhydroxides) are plotted in the Mg+Fe-Si-Ni ternary diagram in **Fig. 4.10a, b**, and compared with the composition of garnierites and related phases found in the literature (**Fig. 4.10c**), and in the Ni-Fe, Ni-Mg, Fe-Mg and Ni-Xtlc binary diagrams in **Fig. 4.11**.

In general, oxide totals of the analyses of serpentine- and talc-like garnierites are below the ideal values for these structure types. Most of the studied garnierites are Al-free with only very few having significant Al content. Only saprolite Ni-serpentine and type I garnierite contain significant Fe.

4.3.1. Structural formulae

Saprolite serpentine

Serpentine from the saprolite has the structural formula of an ideal serpentine, with 2 tetrahedral cations and about 3 octahedral cations. The serpentine is characterised by a remarkable high Fe content (0.05-0.50 apfu, 1.48-13.54 wt.% Fe_2O_3), 0.05–0.43 apfu Ni (1.15-10.53 wt.% NiO) and variable Al (systematically below 0.17 apfu, 2.94 wt.% Al_2O_3). Its average structural formula is $(Mg_{2.46}Ni_{0.14}Fe_{0.20})(Si_{2.01}Al_{0.04})O_5(OH)_4$ (average of 76 analyses) (**Table 4.3**). Similar compositional attributes have been reported of the saprolite serpentine from the Loma Ortega 3 deposit in the northwestern block of the Loma Caribe massif (Gallardo *et al*., 2010b).

Talc-like replacements show Ni and Fe contents of 0.77–1.92 and 0.01–0.06 apfu, respectively, with the average structural formula $(Mg_{1.67}Ni_{1.26}Fe_{0.03})Si_{3.58}O_{9.00}(OH)_{2.31}\cdot 0.82(H_2O)$.
Rare relicts of primary hydrothermal serpentine were found as well, with the structural formula $(Mg_{2.56}Fe_{0.25}Ni_{0.08})Si_{1.98}O_5(OH)_4$, with Ni ranging from 0.02 to 0.14 apfu (0.62-3.41 wt.% NiO) and Fe from 0.11 to 0.54 apfu (2.88-7.16 wt.% FeO,

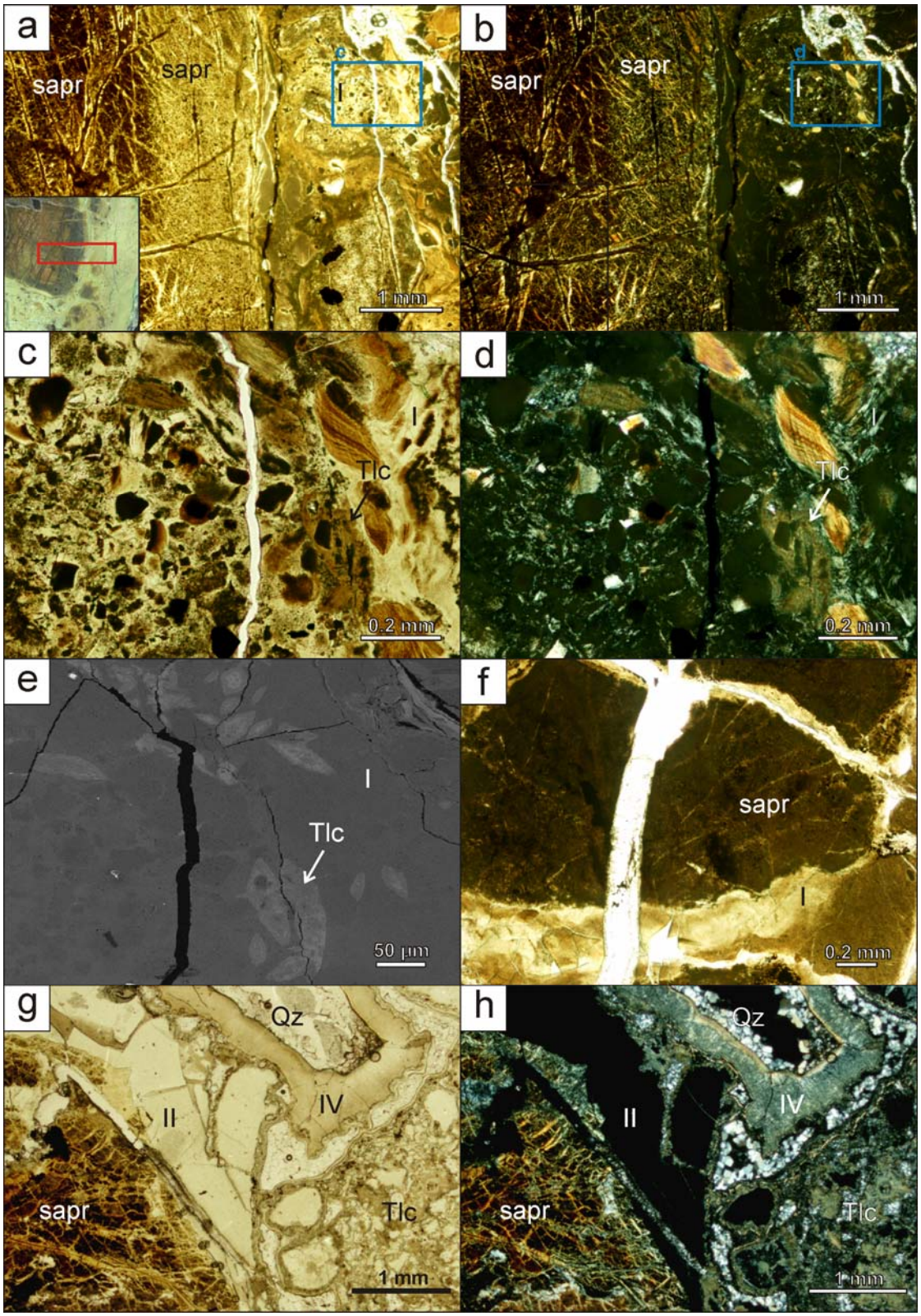

FIGURE 4.5. Optical and electron photomicrographs showing characteristic textures of the described garnierite typologies. **a–b**) Plane polarised light (**a**) and crossed polars images (**b**) of saprolite (sapr) and type I (I) garnierite; **c**) detail of the area in the blue box in **a**); **d**) detail of the area in the blue box in **b**); **e**) backscattered electron image of the area in **c** and **d** displaying brighter talc replacements in type I (Tlc) (sample LC-101a); **f**) plane polarised light of a type I vein crosscutting a saprolite fragment (sample 09-GAR-2); **g-h**) plane polarised light (**g**) and crossed polars images (**h**) of type II garnierite (II) with brownish grey talc-like matrix (Tlc), saprolite (sapr), quartz (Qz) and type IV (IV) garnierite (sample LC-100Bb).

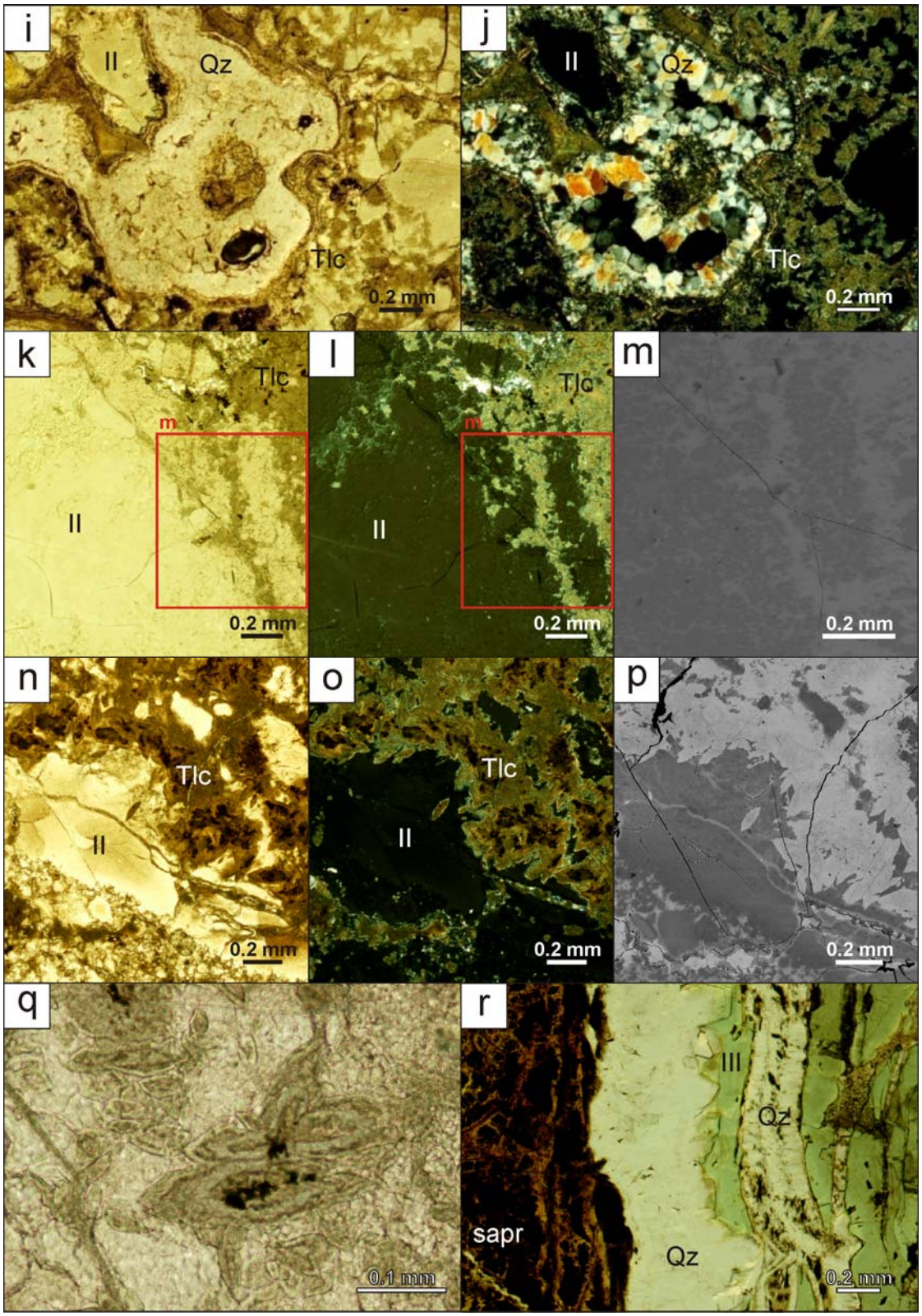

FIGURE 4.5. (CONTINUED). **i-j**) plane polarised light (**i**) and crossed polars image (**j**) of type II fragments (II) surrounded by brownish grey talc-like matrix (Tlc) (sample LC-100Bb); **k-m**) plane polarised light (k), crossed polars (**l**) and backscattered electron (**m**) images of talc-like replacements (Tlc) in type II (II) garnierite (sample LC-100Ab); **n-p**) plane polarised light (**n**), crossed polars (**o**) and backscattered electron (**p**) images of spindle-shaped talc-like particles (Tlc) in type II (II) garnierite (sample LC-100BD); **q**) close up plane polarised light image of spindle-shaped talc-like particles (sample LC-100Bb); **r**) plane polarised light image of type III garnierite (III) enveloping euhedral quartz crystals (Qz), over a saprolite fragment (sapr) (sample GAR-3b).

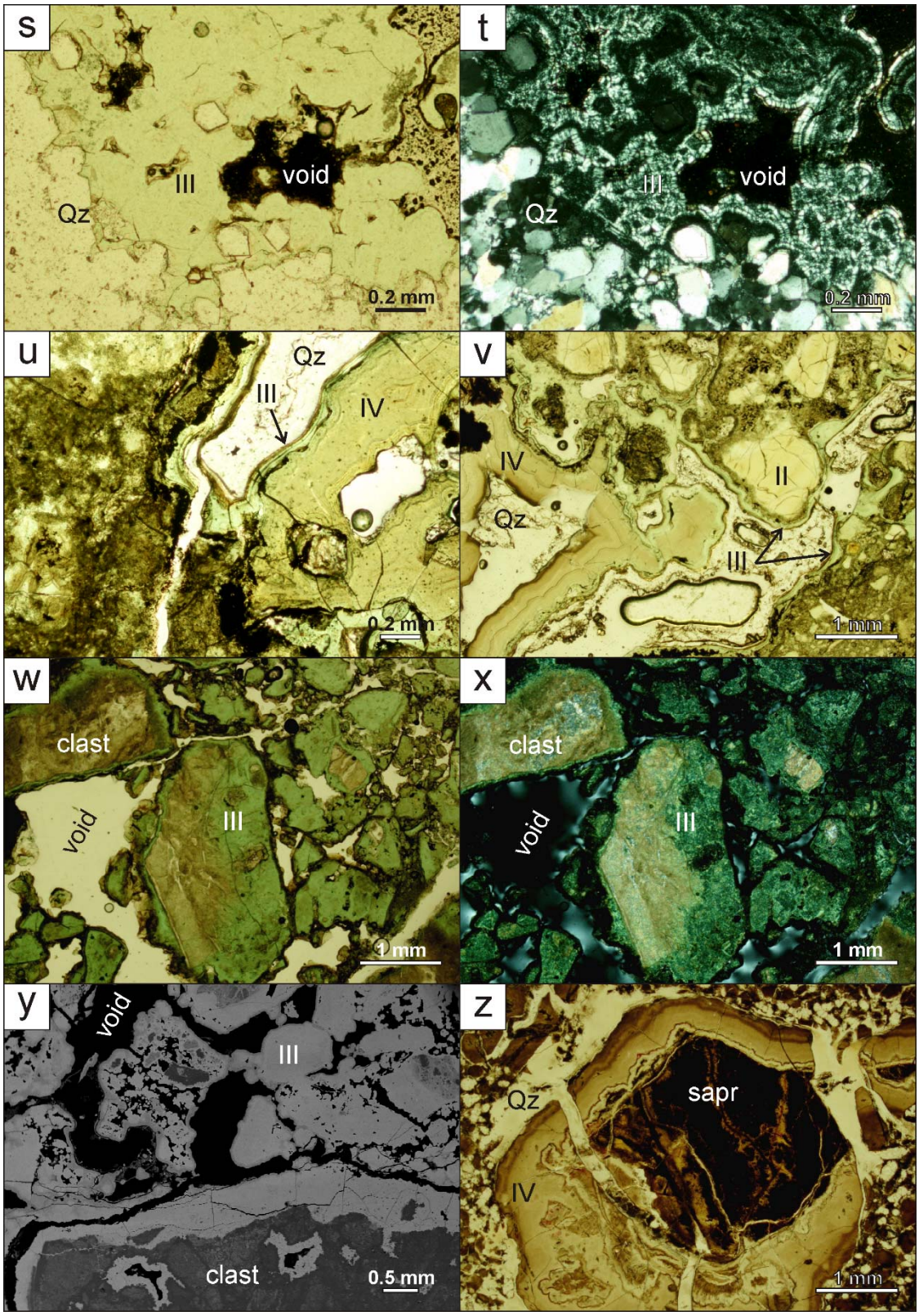

FIGURE 4.5. (CONTINUED). **s-t**) plane polarised light (**s**) and crossed polars (**t**) images of type III filling voids with euhedral quartz (sample GAR-2c), **u-v**) plane polarised light images depicting the paragenetic sequences of the various garnierite types: **u**) IV is cemented by III and quartz (Qz) (LC-100Bb), and **v**) II and IV are coated by III and quartz (Qz) (LC-100Aa-1), **w-y**) plane polarised light (**w**), crossed polars (**x**) and backscattered electron (**y**) images of type III cementing silicified clasts of mixed phyllosilicates (sample GAR-1); **z**) plane polarised light image of a saprolite fragment (sapr) wrapped by type IV (IV) in a matrix of rounded quartz and type IV garnierite (sample GAR-4a).

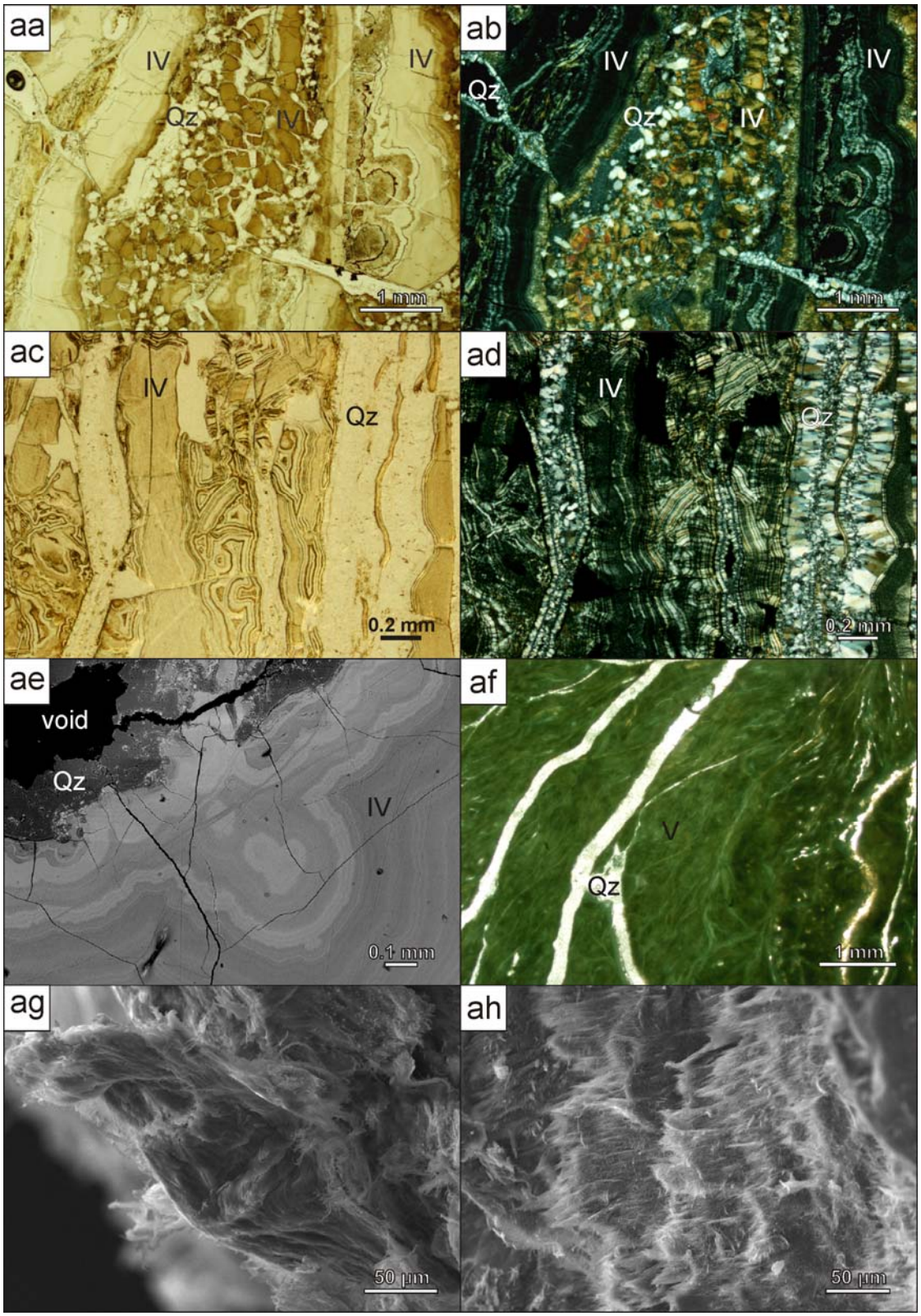

FIGURE 4.5. (CONTINUED). **aa-ab**) plane polarised light (**aa**) and crossed polars (**ab**) images of type IV botryoidal aggregates in a matrix of rounded quartz and garnierite, crosscut by microcrystalline quartz veinlets (sample GAR-4a); **ac-ad**) plane polarised light (**ac**) and crossed polars (**ad**) images of of type IV botryoidal aggregates interstratified with quartz layers (sample 09GAR-2); **ae**) electron backscattered image of botryoidal aggregates, the brighter layers correspond to areas with higher Ni (sample LC-100B); **af**) intense green colour in falcondoite aggregates, because the section is thick (FALC-3); **ag-ah**) secondary electron images of Ni-sepiolite (**ag**) (sample FALC-3) and falcondoite (**ah**) (sample FALC-3).

with one analysis at 0.54 apfu and 12.79 wt.%) (average of 7 analyses).

Type I garnierite

The structural formulae of type I garnierite deviate slightly from that of ideal serpentine with an average cation content of 2.08 apfu in the tetrahedral site and 2.76 apfu in the octahedral site when calculated using 7 oxygens. The average structural formula of the type I garnierite is $(Mg_{2.22}Ni_{0.26}Fe_{0.17})Si_{2.10}O_{5.84}(OH)_{3.36}$. Comparable results were obtained for the 7 Å-type garnierites by Brindley & Hang (1973). Fe and Ni contents are relatively high (0.07–0.32 and 0.03–0.59 apfu, respectively). Serpentine-like garnierites with a similar Fe content were reported by Wells *et al*. (2009). When recalculated using the average Xtlc of 0.22, the structural formula is $(Mg_{2.31}Ni_{0.34}Fe_{0.17})Si_{2.30}O_5(OH)_4 \cdot nH_2O$, with Ni ranging from 0.06 to 0.73 apfu (0.84-14.58 wt.% NiO) and Fe from 0.09 to 0.28 apfu (1.66-8.91 wt.% Fe_2O_3) (**Tables 4.1**, **4.3**).

The Ni content of the spindle-shaped particles and other talc-like phases coexisting with type I garnierites is 0.97-2.56 apfu and its structural formula is $Mg_{1.25}Ni_{1.71}Fe_{0.02}Si_{3.59}O_{9.00}(OH)_{2.35} \cdot nH2O$, with Xtlc of 0.81 (average of 26 analyses).

Type II garnierite

The structural formulae of type II garnierite differ significantly from ideal serpentine. It has excess of tetrahedral occupancy (2.20 apfu) and an apparent deficit in the octahedral site (2.57 apfu). Similar values have been published for 7 Å-type garnierites by Brindley & Hang (1973) and Wells *et al*. (2009). The garnierite has higher Ni (0.15-1.42 apfu, 1.63-26.62 wt.% NiO) and lower Fe (up to 0.22 apfu, 7.70 wt.% Fe_2O_3) than type I, and is the only garnierite with remarkable Al content (up to 0.43 apfu, 6.23 wt.% Al_2O_3). Its average structural formula is $(Mg_{2.09}Ni_{0.87}Fe_{0.05})(Si_{2.53}Al_{0.09})O_{6.53}(OH)_{3.39}$, with an average Xtlc of 0.31 (66 analyses) (**Tables 4.1**, **4.3**). The talc-like fine-grained envelope has a composition of 1.22–3.04 Ni apfu and 0–0.02 Fe apfu, with an average structural formula of $(Ni_{2.31}M_{g0.68}Fe_{0.01})Si_{3.36}O_{8.41}(OH)_{2.64} \cdot nH_2O$, Xtlc of 0.68 (37 analyses).

Type III garnierite

When calculated on the basis of 7 oxygens, the structural formulae of type III garnierite also deviate from the ideal serpentine (with an average structural formula of $(Ni_{1.76}Mg_{0.55}Fe_{0.01})Si_{3.38}O_5(OH)_4$). On the basis of 11 oxygens, it has a tetrahedral cation deficit and a remarkable octahedral cation excess (with an average structural formula of $(Ni_{2.76}Mg_{0.87}Fe_{0.01})Si_{5.31}O_{10}(OH)_2$). When recalculated to an average Xtlc of 0.52, the final structural formula is $(Ni_{2.26}Mg_{0.72})Si_{3.04}O_{7.62}(OH)_{2.95} \cdot n(H2O)$ (96 analyses averaged). It has higher Ni (1.43–2.81 apfu; 23.51-49.71 wt.% NiO) and lower Fe (up to 0.05 apfu; 0.24 wt.% Fe_2O_3) contents than type II (**Tables 4.1**, **4.3**).

Type IV garnierite

The structural formula of the bluish green (type IV) garnierite is similar to that of ideal talc–willemseite, but the EMP analyses show low oxide totals. The brown botryoidal aggregates show a wide range of Ni concentrations (0.47–2.58 apfu, 7.77-40.52 wt.% NiO) as well as the lowest Fe contents (up to 0.03 apfu, 0.48 wt.% Fe_2O_3). Its average structural formula is $(Ni_{1.67}Mg_{1.33})Si_{3.80}O_{9.53}(OH)_{2.19} \cdot nH_2O$ and Xtlc of 0.91 (average of 153 analyses). The brown fragments in the microcrystalline quartz matrix have the structural formula $(Ni_{2.10}Mg_{0.90})(Si_{3.77}Al_{0.01})O_{9.46}(OH)_{2.22} \cdot nH_2O$, Xtlc 0.89, slightly higher Ni contents (2.02–2.14 apfu, 32.09-32.69 wt.% NiO) and practically no Fe (3 analyses) compared to the coexisting brown botryoidal aggregates. Finally, the veins cutting brown botryoidal aggregates have the structural formula $(Ni_{1.74}Mg_{1.15})(Si_{3.50}Al_{0.02})O_{8.80}(OH)_{2.50} \cdot nH_2O$, Xtlc 0.76, Ni from 0.80 to 2.32 (15.57-35.96 wt.% NiO) and Fe up to 0.04 (0.82 wt.% Fe_2O_3) (7 analyses) (**Tables 4.1**, **4.3**).

Type V garnierite

The composition of Ni-sepiolite and falcondoite is characterised by 0.34–5.24 apfu Ni (2.06-26.82 wt.% NiO) and very low Al and Fe contents (<0.15 and <0.27 apfu respectively, with one analysis having 0.49 apfu Fe). Their average structural formula is $Mg_{5.81}Ni_{1.68}Si_{12.21}O_{15}(OH)_2 \cdot 6(H_2O)$ (average of 89 analyses) (**Tables 4.1**, **4.3**).

TABLE 4.3. Representative EMP analyses of the saprolite serpentine and the garnierite types I to V. Calculations are based on 7 oxygens (saprolite serpentine, garnierite types I to III), 11 oxygens (garnierite types III and IV) and 32 oxygens (type V garnierite), and the structural formulae of garnierite types I to IV was recalculated taking into account the Xtlc (see **Section 3.6.2**). The recalculated analyses include the final number of oxygens of the structural formulae calculation.

ID #	A-i-14	LC100A1g221	LC100A1-G3-2	lc1011-18		A-d-88		(09GAR2)-59		lc1001-62		lc1001-28		lc1001-61	
Mineral	Srp	Srp	Srp	Srp		Srp		Srp		Srp		Srp		Srp	
Sample	LC-101	LC-100A	LC-100A	LC-101		LC-101		09-GAR-2		LC-100B		LC-100B		LC-100B	
Type	saprolite	saprolite	saprolite	type I		type I		Type I		type II		type II		type II	
SiO_2	40.15	43.58	42.67	44.58		44.88		42.56		40.86		42.57		41.79	
TiO_2	0.03	0	0.02	0.01		0.03		0.04		0.02		0.03		0	
Al_2O_3	0.17	0.65	0.97	0.04		0.01		0.02		2.46		1.26		0.22	
Cr_2O_3	0.49	0.01	0	0.02		0		0.02		0.03		0		0.03	
Fe_2O_3	5.76	1.70	3.27	5.32		4.07		2.81		0.77		0.5		0.36	
MnO	0.02	0.01	0	0.01		0.05		0.03		0.04		0		0.03	
MgO	36.46	35.88	34.74	31.2		28.63		26.3		28.97		21.62		12.62	
NiO	2.91	6.42	3.47	5.26		9.36		10.19		11.85		21.54		29.14	
CaO	0.02	0	0	0.11		0.07		0.1		0.05		0.03		0.02	
Sum Ox%	86.05	88.26	85.14	86.55		87.10		81.87		85.05		87.55		84.25	
Si	1.945	2.049	2.055	2.134	2.201	2.170	2.327	2.190	2.556	2.046	2.317	2.166	2.567	2.308	2.944
Al	0.01	0	0	0	0	0	0	0	0	0	0	0	0	0	0
Fe^{3+}	0.045	0	0	0	0	0	0	0	0	0	0	0	0	0	0
sum [IV] (T)	**2.000**	**2.049**	**2.055**	**2.134**	**2.201**	**2.170**	**2.327**	**2.190**	**2.556**	**2.046**	**2.317**	**2.166**	**2.567**	**2.308**	**2.944**
Ti	0.001	0	0.001	0	0	0	0	0.002	0.002	0.001	0.001	0.001	0.001	0	0
Al	0	0.036	0.055	0.002	0.002	0.001	0.001	0.001	0.001	0.145	0.164	0.076	0.090	0.014	0.018
Cr	0.019	0	0	0.001	0.001	0.000	0.000	0.001	0.001	0.001	0.001	0	0	0.001	0.002
Fe^{3+}	0.165	0.06	0.118	0.192	0.198	0.148	0.159	0.109	0.127	0.029	0.033	0.019	0.023	0.015	0.019
Mn	0.001	0	0	0	0	0	0	0.001	0.002	0.002	0.002	0	0	0.001	0.002
Mg	2.633	2.514	2.494	2.227	2.297	2.063	2.213	2.017	2.355	2.162	2.449	1.640	1.944	1.039	1.325
Ni	0.113	0.243	0.134	0.203	0.209	0.364	0.390	0.422	0.492	0.477	0.541	0.882	1.045	1.295	1.651
Ca	0.001	0	0	0.006	0.006	0.004	0.004	0.006	0.006	0.003	0.003	0.002	0.002	0.001	0.002
sum [VI] (O)	**2.933**	**2.853**	**2.803**	**2.631**	**2.713**	**2.583**	**2.770**	**2.558**	**2.986**	**2.82**	**3.194**	**2.620**	**3.104**	**2.366**	**3.019**
T / O	0.67	0.74	0.73	0.81	0.81	0.84	0.84	0.86	0.86	0.73	0.73	0.83	0.83	0.98	0.98
Xtlc				0.22		0.263		0.29		0.23		0.32		0.48	
Ni/Mg	0.043	0.097	0.054	0.091	0.091	0.176	0.176	0.209	0.209	0.221	0.221	0.538	0.538	1.246	1.246
oxygens	7	7	7	7	7.22	7	7.51	7	8.17	7	7.93	7	8.30	7	8.93

TABLE 4.3. (CONTINUED).

ID #	GAR 3-pto1-7			gar3b-81			GAR1-a2			LC101bc13		LC101b-c7		LC100Abc13		FAL3pto1_11	FAL4-19	GAR7-a7
Mineral	Srp			Srp			Srp			Tlc		Tlc		Tlc		Sep	Sep	Sep
Sample	GAR-3b			GAR-3b			GAR-1b			LC-101		LC-101		LC-100A		FALC-3	FALC-4	GAR-7
Type	type III			type III			type III			type IV		type IV		type IV		sep-falc	sep-falc	sep-falc
SiO_2	44.27			41.42			37.89			52.69		52.94		48.86		49.56	59.15	60.64
TiO_2	0			0.02			0			0		0		0		0	0.04	0.01
Al_2O_3	0.01			0.05			0			0		0.01		0.09		0.31	0.06	0
Cr_2O_3	0.01			0.01			0.01			0		0		0.01		0	0.02	0
Fe_2O_3	0.04			0.03			0.02			0.02		0.02		0.01		0.09	0.81	0.1
MnO	0.03			0.01			0			0		0		0.02		0.02	0.02	0
MgO	10.87			7.86			5.25			18.63		13.08		4.55		10.79	22.45	22.62
NiO	32.42			40.67			46.06			16.09		25.22		40.7		23.36	3.51	7.73
CaO	0			0.02			0			0.04		0.09		0.02		0	0.02	0.05
Sum Ox%	87.69			90.11			89.24			87.53		91.61		94.3		84.27	86.17	91.17
Si	2.366	3.719	3.136	2.274	3.574	2.7941	2.197	3.453	2.532	3.964	3.876	3.988	3.981	3.909	3.705	11.768	12.148	12.022
Al	0	0	0	0.003	0.005	0	0	0	0	0	0	0.001	0.001	0.008	0.008	0.087	0	0
Fe^{3+}	0	0	0	0	0.002	0	0	0.002	0	0.001	0.001	0.001	0.001	0.001	0.001	0.016	0	0
sum [IV] (T)	**2.366**	**3.719**	**3.1357**	**2.277**	**3.581**	**2.794**	**2.197**	**3.455**	**2.532**	**3.965**	**3.877**	**3.99**	**3.983**	**3.918**	**3.714**	**11.871**	**12.148**	**12.022**
Ti	0	0	0.000	0.001	0.001	0.001	0	0	0	0	0	0	0	0	0	0	0.006	0.001
Al	0.001	0.001	0.001	0.003	0	0.004	0	0	0	0	0	0.001	0	0.008	0	0.087	0.015	0
Cr	0	0.001	0.001	0	0.001	0.001	0	0.001	0.001	0	0	0	0	0.001	0.001	0	0.003	0
Fe^{3+}	0.002	0.003	0.002	0.001	0	0.002	0.001	0	0.001	0	0	0	0	0	0	0	0.125	0.015
Mn	0.001	0.002	0.002	0	0.001	0.001	0	0	0	0	0	0	0	0.001	0.001	0.004	0.003	0
Mg	0.866	1.361	1.148	0.643	1.011	0.790	0.454	0.713	0.523	2.089	2.043	1.469	1.466	0.543	0.514	3.819	6.874	6.685
Ni	1.394	2.191	1.847	1.796	2.823	2.207	2.149	3.377	2.476	0.974	0.952	1.528	1.525	2.619	2.483	4.462	0.580	1.233
Ca	0	0	0.000	0.001	0.002	0.001	0	0	0	0.003	0.003	0.007	0.007	0.002	0.002	0	0.004	0.011
sum [VI] (O)	**2.264**	**3.559**	**3.0006**	**2.445**	**3.839**	**3.007**	**2.604**	**4.091**	**3.000**	**3.066**	**2.998**	**3.005**	**2.999**	**3.174**	**3.001**	**8.301**	**7.611**	**7.933**
T / O	1.045	1.045	1.045	0.931	0.933	0.929	0.844	0.845	0.844	1.293	1.293	1.328	1.328	1.234	1.238	1.428	1.649	1.516
Xtlc		0.57			0.40			0.27		0.94		1.00		0.86		-	-	-
Ni/Mg	1.610	1.610	1.609	2.793	2.792	2.792	4.733	4.736	4.734	0.466	0.466	1.040	1.040	4.823	4.827	1.168	0.084	0.184
oxygens	7	11	9.28	7	11	8.6	7	11	8.06	11	10.76	11	10.98	11	10.43	32	32	32

4.3.2. X-ray element maps

A detailed study of quantified X-ray element maps shows the relationships between textural position, sequence of crystallization and mineral composition of the various garnierite samples. In order to examine the distribution of major element in the different garnierites, the elements Si, Mg, Ni, Fe and Al were scanned in four selected areas containing saprolite serpentine (**Fig. 4.6**), serpentine-like, talc-like garnierites and their mixture (**Fig. 4.7**), talc-like garnierite (**Fig. 4.8**), and sepiolite-falcondoite (**Fig. 4.9**). The element maps show a complex and variable texture and mineral composition. Note that there is a close fit between spot analyses (**Section 4.2.3**) and quantified pixel compositions (this section). The subtle divergences are the result of matrix effects (for these plots a single internal standard was used for all minerals of the scanned areas).

The textural and compositional features of saprolite serpentine are presented in **Figure 4.6**. The map shows a mesh texture in which Fe oxyhydroxide aggregates (brown areas in **Figure 4.6b**) are wrapped by Fe-bearing, Ni-poor serpentine, and this in turn is surrounded by serpentine with higher Ni. This indicates replacement of the primary olivine by the secondary saprolite serpentine (Ni-enriched), as the Ni-rich solution percolated through small fractures and discontinuities. In addition, a Ni-poor serpentine is also found in a vein, showing lower Fe and higher Al than the saprolite serpentine, similar to those of the oceanic hydrothermal serpentine.

The distribution of elements in talc-like, serpentine-like, intermediate phase and quartz is presented in **Figure 4.7**, and a detail of talc-like is shown in **Figure 4.8**. The texture of the talc-like phase is complex, characterised by an oscillatory banded, botryoidal fabric, suggesting several stages of talc-like growth. These bands present strong variationsin the Ni content, pointing to recurrent changes in the physical-chemical conditions in the aqueous medium during garnierite formation. However, the quantified XR maps suggest two compositional maxima for this talc-like phase, as shown in **Figures 4.7a** and **4.8a**. Voids and fractures are later filled by microcrystalline quartz. This quartz contains small amounts of Ni. This phase represents a poorly defined variety of Ni-bearing, microcrystalline quartz, probably chrysoprase (**Fig. 4.7b**). In **Figure 4.7c** it is also evident the post-depositional diffusion transport of Fe from relictic (saprolite) serpentine within adjacent talc. To be noted also is the presence of a phase with a homogeneous intermediate composition between talc- and serpentine-like, comparable to that of karpinskite, which stands out clearly in the images associated with serpentine. This is confirmed by the quantified Si/(Mg+Fe+Ni) image (**Fig. 4.7c**) that shows the correspondence between the theoretical values of this ratio in stoichiometric serpentine (0.67) and karpinskite (1.00) and the quantified pixels of both minerals. According to the triangular plot in **Fig. 7e**, some spot and pixel analyses located in between major clusters represent mixtures of minerals. However, a small cluster located midway in between talc and serpentine corresponds to the area identified as karpinskite in the quantified XR maps. Note that this cluster plots in the line representing the solid solution of karpinskite.

As seen in **Figure 4.9**, the textural and chemical variations suggest three stages of sepiolite crystallization, starting with homogeneous Ni-poor sepiolite aggregates, followed by Ni-rich sepiolite. In the last stage still Ni-richer sepiolite crystallized along fractures and/or channels. This progressive Ni enrichment in sepiolite was also observed by Tauler *et al*. (2009). Quartz crystallized in the wall of voids, within the matrix of sepiolite, and locally along fractures/channels. Ni-rich regions in quartz are noted at the rims of the quartz grains related to the third stage of Ni-rich sepiolite growth.

4.3.3. The Si–Mg–Ni system

All analyses performed on garnierite types I–IV, Ni-sepiolite–falcondoite (including results from Tauler *et al*., 2009) and saprolite serpentine are represented in the Mg+Fe-Si-Ni ternary plot in **Fig. 4.10a-b**, and compared with analyses of garnierites from other localities provided by other authors, shown in **Figure 4.10c**. In general, the analysed garnierites plot within the field limited by sepiolite–falcondoite and lizardite–népouite series. Serpentine and serpentine-like minerals with lower Ni and higher Fe concentrations (serpentine from saprolite and type I garnierite) plot near the lizardite end member. Type II displays intermediate Ni compositions between type I and III. Analyses of type I, II and III plot closer to the kerolite–pimelite series as they are richer in Ni. Some type I and II, and all type III garnierites plot close to the 50% Si line (Si/(Mg+Fe+Ni) = 1). The analyses of brown

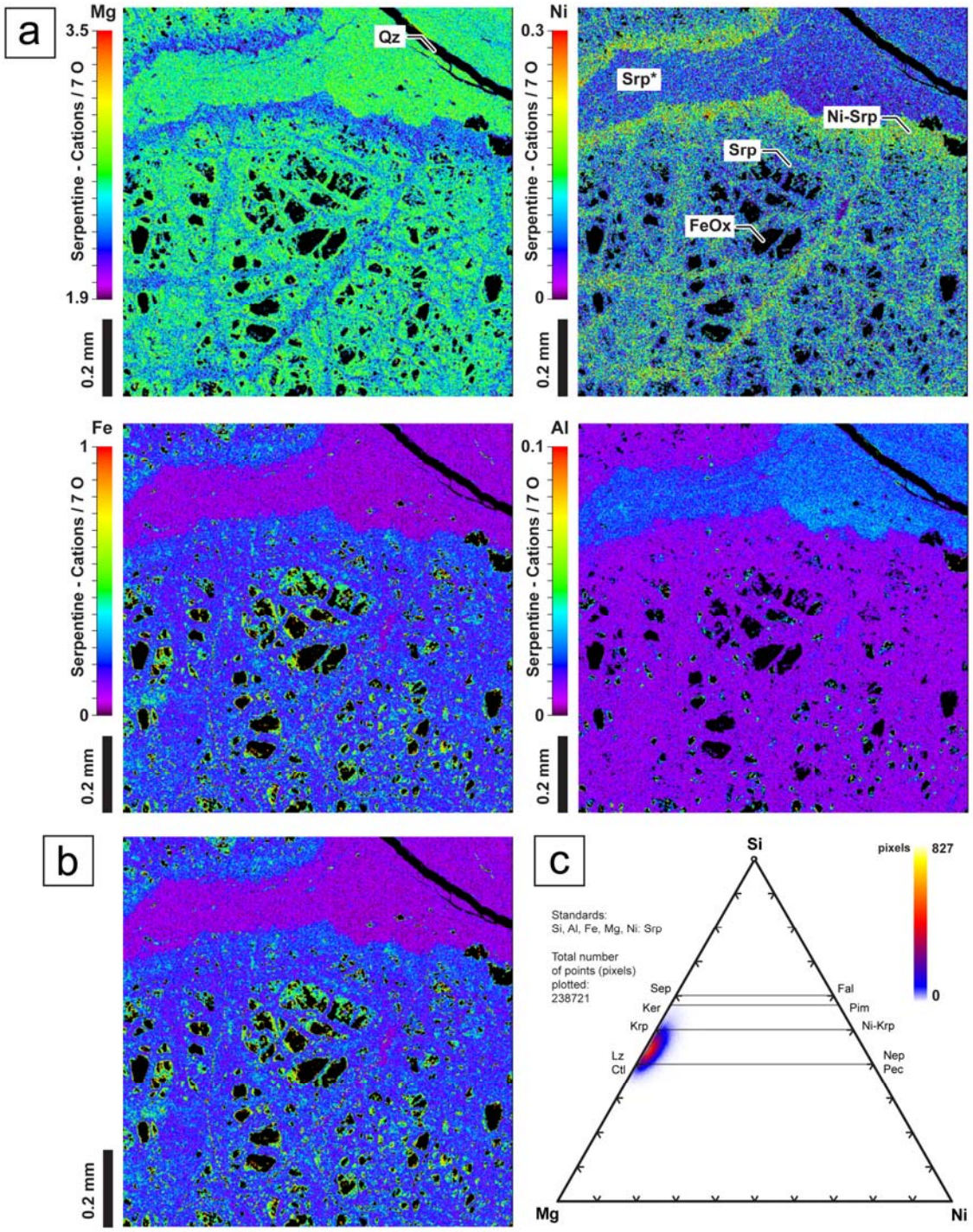

FIGURE 4.6. Quantitative element X-ray map of sample GAR-3b (200 nA). **a**) Textural and compositional features of saprolite Ni-serpentine and quartz, b) photomicrograph of the selected area, and **c**) triangular diagram showing the spot analyses and the quantified pixels of the scanned area expressed as absolute frequency (colour scale). In the X-ray maps the scaled (colour code) distribution of elements and elemental ratio is expressed in cations per fixed number of oxygens (i.e., charges) in the respective formula units. The mineral formulae were calculated using an internal standard of Ni-serpentine analysed in the scanned area. All pixels were quantified using a spot analysis of serpentine as internal standard. Stoichiometric Mg and Ni end members of the solid solutions of interest are indicated for reference. Legend: Qz = quartz, Srp = serpentine, Srp* = oceanic hydrothermal serpentine, Ni-Srp = Ni-bearing serpentine, FeOx = Fe oxyhydroxides, Sep = sepiolite, Fal = falcondoite, Ker = kerolite, Pim = pimelite, Krp = karpinskite, Ni-Krp = Ni-karpinskite, Lz = lizardite, Nep = népouite, Ctl = chrysotile, Pec = pecoraite.

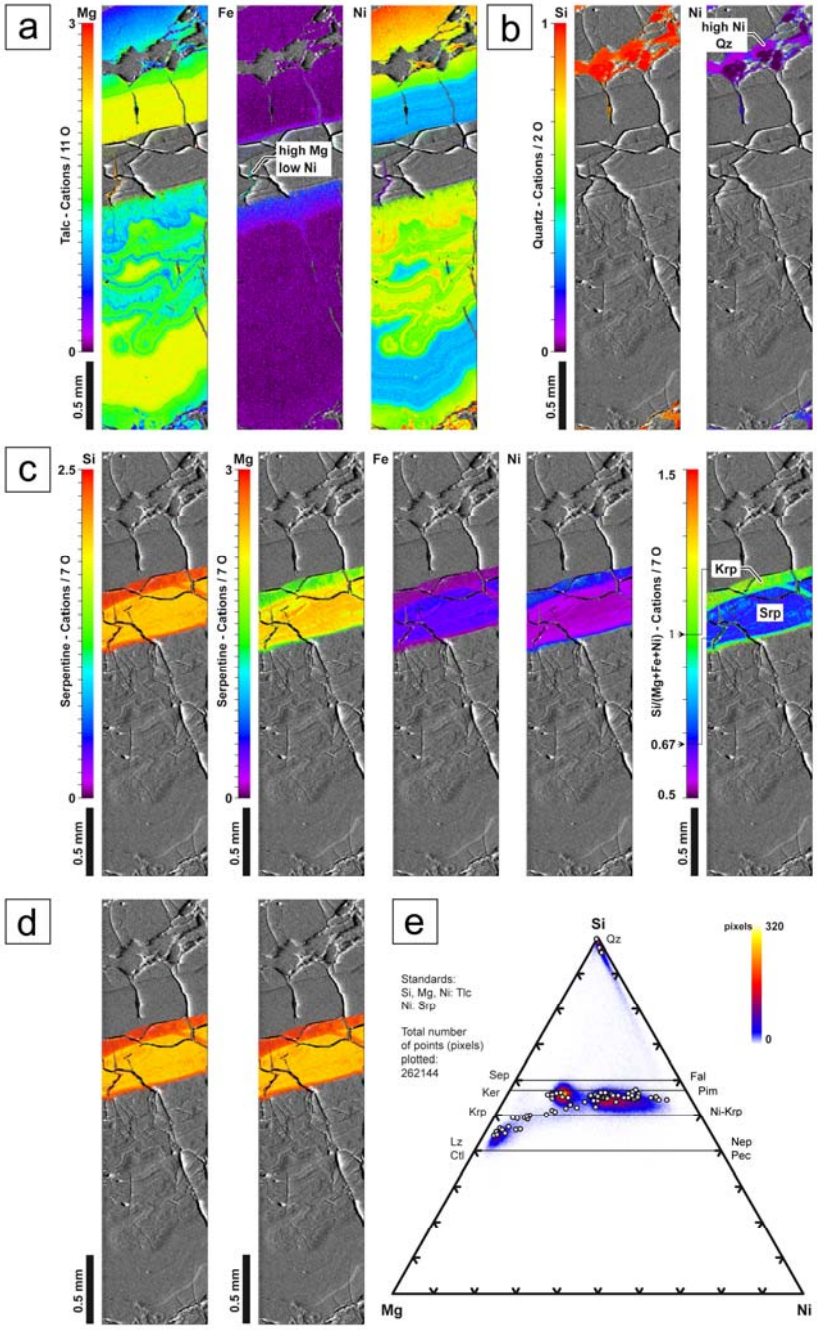

FIGURE 4.7. Quantitative element X-ray map of sample GAR-4a (200 nA). Textural and compositional features of **a**) Ni-bearing talc-like, **b**) quartz, and **c**) serpentine with the intermediate phase, **d**) photomicrograph of the selected area, and **e**) triangular diagram showing the spot analyses and the quantified pixels of the scanned area expressed as absolute frequency (colour scale). In the X-ray maps the scaled (colour code) distribution of elements and elemental ratio is expressed in cations per fixed number of oxygens (i.e., charges) in the respective formula units. Mg, Fe and Ni are scaled uniformly in order to better compareminеral compositions. The mineral formulae were calculated using an internal standard of the same mineral analysed in the scanned area (talc-like or serpentine-like), except for the intermediate phase that was quantified using the same internal standard as serpentine-like. All pixels were quantified using a spot analysis of talc as internal standard. Stoichiometric Mg and Ni end members of the solid solutions of interest are indicated for reference. Legend: Qz = quartz, Srp = serpentine, Sep = sepiolite, Fal = falcondoite, Ker = kerolite, Pim = pimelite, Krp = karpinskite, Ni-Krp = Ni-karpinskite, Lz = lizardite, Nep = népouite, Ctl = chrysotile, Pec = pecoraite.

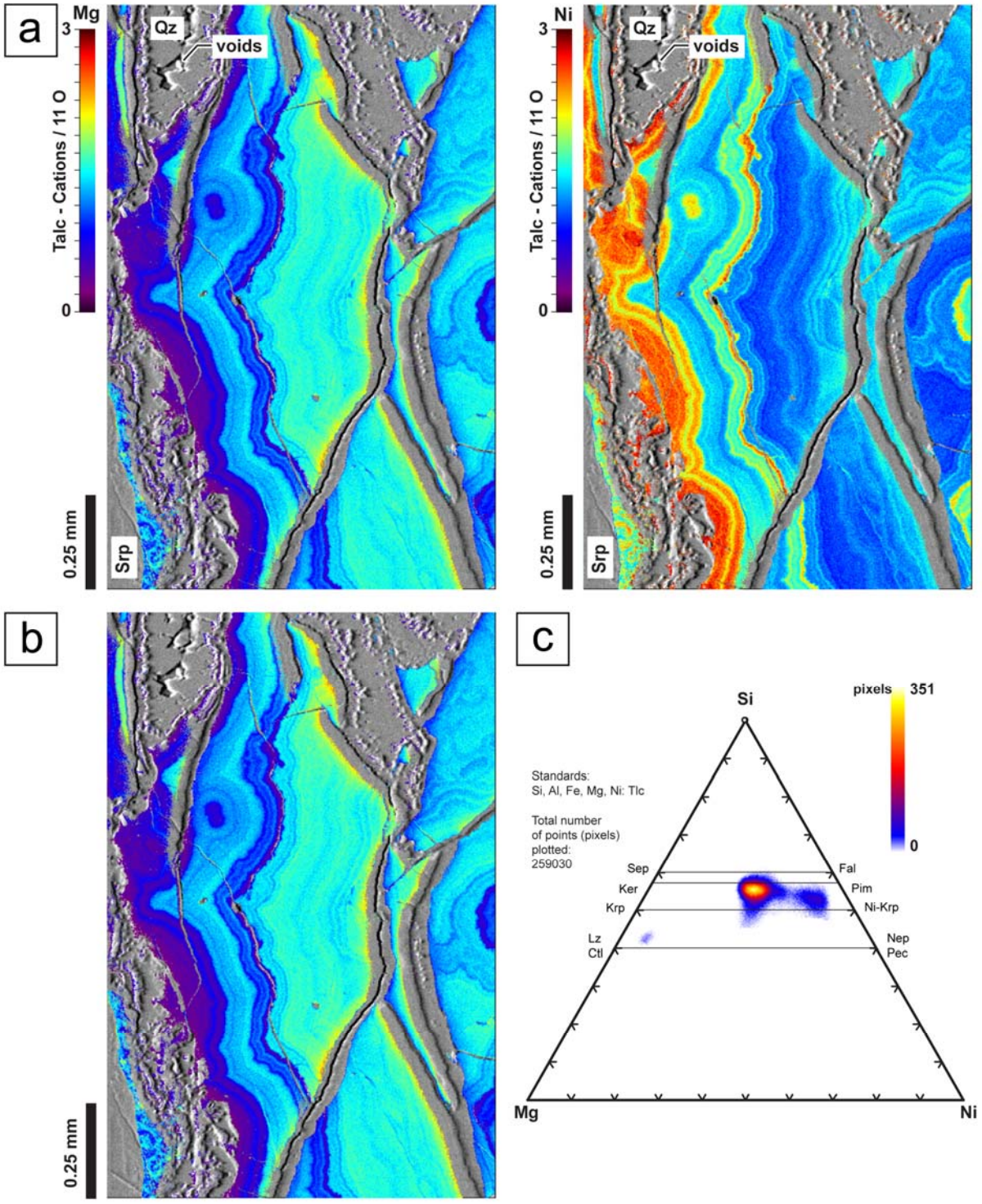

FIGURE 4.8. Quantitative element X-ray map of sample LC-100Bb (200 nA). **a**) Textural and compositional features of Ni-bearing talc-like and quartz, **b**) photomicrograph of the selected area, and **c**) ternary diagram showing the spot analyses and the quantified pixels of the scanned area expressed as absolute frequency (colour scale). In the XR maps the scaled (colour code) distribution of elements and elemental ratio is expressed in cations per fixed number of oxygens (i.e., charges) in the respective formula units. Mg and Ni are scaled uniformly in order to better compare mineral compositions. The mineral formulae were calculated using an internal standard of the same mineral analysed in the scanned area. All pixels were quantified using a spot analysis of talc as internal standard. Stoichiometric Mg and Ni end members of the solid solutions of interest are indicated for reference. Legend: Qz= quartz, Sep = sepiolite, Fal = falcondoite, Ker = kerolite, Pim = pimelite, Krp = karpinskite, Ni-Krp = Ni-karpinskite, Lz = lizardite, Nep = népouite, Ctl = chrysotile, Pec = pecoraite.

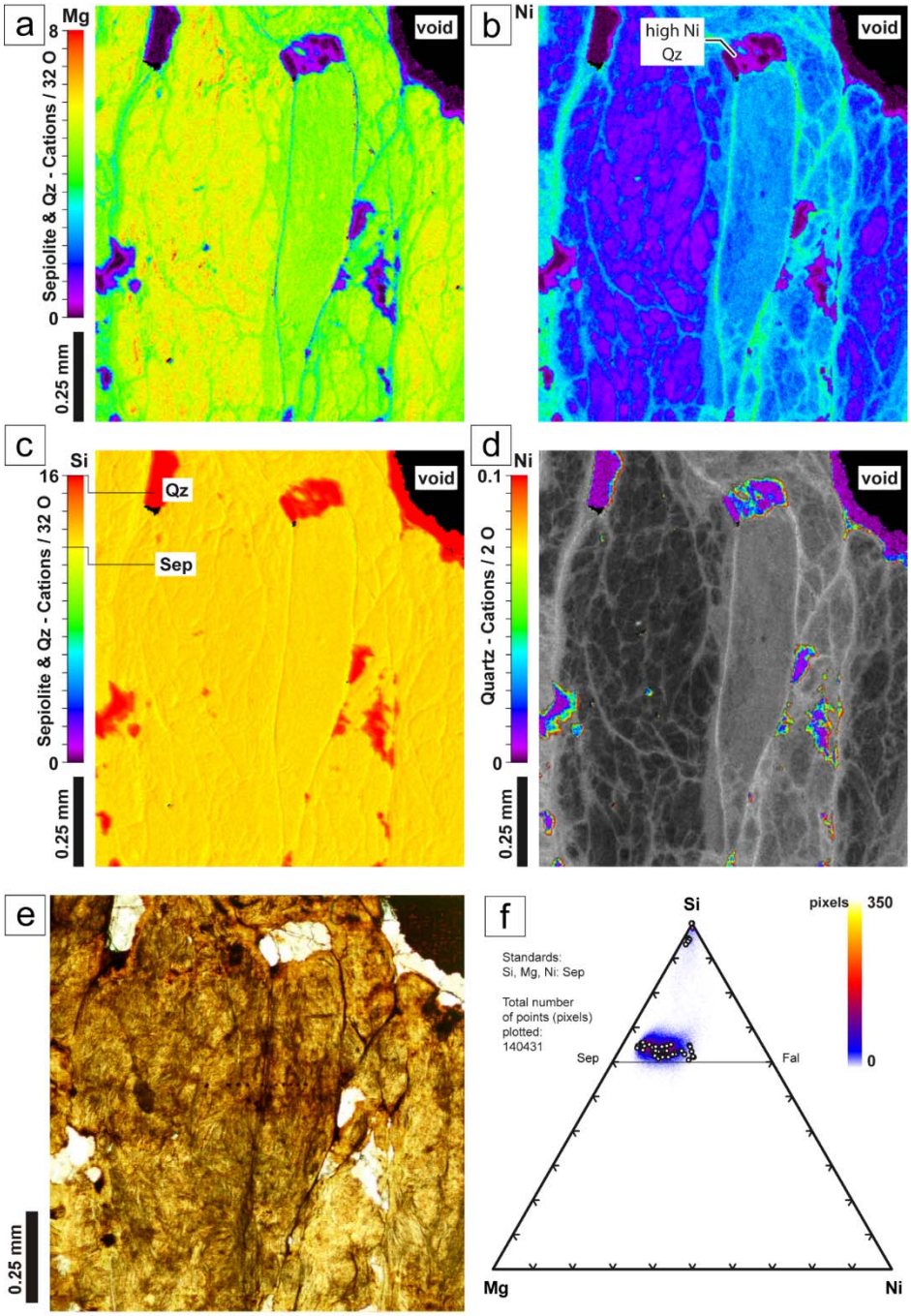

FIGURE 4.9. Quantitative element X-ray map of sample FALC-2 (100 nA). **a–d**) Textural and compositional features of Ni-sepiolite and quartz, **e**) photomicrograph of the selected area, and **f**) ternary plot showing the spot analyses and the quantified pixels of the scanned area expressed as absolute frequency (colour scale). Maps show the distribution of Mg (**a**), Ni (**b**), Si (**c**) in sepiolite and quartz, and Ni in quartz (**d**). In the XRmaps the scaled (colour code) distribution of elements is expressed in cations per fixed number of oxygens (i.e., charges) in the respective formula units. In the upper figures, Mg and Ni are scaled uniformly in order to better compare mineral compositions. The mineral formulae were calculated using an internal standard of sepiolite analysed in the scanned area. The Ni image for quartz is scaled to 0.1 cations/pfu in order to show the chemical zoning of this mineral. The image is set on a greyscale image of Ni to show the basic chemical/textural relations of the scanned area. All pixels were quantified using the same spot analysis of sepiolite. Stoichiometric Mg and Ni end members of the sepiolite solid solution are indicated for reference. Legend: Qz = quartz, Sep = sepiolite, Fal = falcondoite.

botryoidal aggregates of type IV plot continuously in a wide range of compositions between the kerolite–pimelite end members (**Fig. 4.10a**). **Figure 4.10a** also shows that the brown fragments in the microcrystalline quartz matrix have higher Ni contents than the brown botryoidal aggregates they coexist with; and that the talc-like replacements of saprolite fragments and spindle-shaped, talc–like, fine grained envelope in types I and II have similar compositions to those of type IV garnierite. The Ni-sepiolite–falcondoite analyses also plot continuously between sepiolite and falcondoite end members (**Fig. 4.10b**). The sepiolite analyses are, however, slightly enriched in Si probably due to microscopic intergrowths of quartz within sepiolite (Tauler *et al*., 2009). These results suggest the existence of a complete solid solution between Mg and Ni end members.

In general, Ni–Mg hydrous silicates from the Falcondo mine have similar structural and chemical characteristics to garnierite minerals examined in other worldwide Ni-lateritic deposits (**Fig. 4.10d**), except for the Ni dominant serpentine-like phases, which have not been recorded in Falcondo; and falcondoite, which commonly occurs in this deposit.

With regards to the relationships between the different octahedral cations, it is clear that Ni and Fe rarely occur together in large amounts in the same mineral phase (**Fig. 4.11a**), and that there is an almost linear negative correlation close to 1:1 between Mg and Ni, confirming that Ni exchanges for Mg in the octahedral site (**Fig. 4.11b**). However, this correlation is not seen in the Mg-Fe pair, and Fe is mostly concentrated in the serpentine phases (**Fig. 4.11c**). In addition, the Ni versus talc fraction binary diagram displays two groups of points (**Fig. 4.11d**). On one hand, the negative correlation displayed by type III garnierites and all the talc-like phases plotted in **Fig. 4.10a**; and on the other hand, the cloud of saprolite serpentine and serpentine-dominant garnierites (types I and II). It must be noted that this diagram reveals a situation more complex than the linear correlation observed by Soler *et al*. (2008) and Galí *et al*. (2012).

4.4. DISCUSSION

4.4.1. Garnierite mineralisation and brittle tectonic structures

In general, unweathered serpentinised peridotites are massive and do not allow fluids to circulate except along fractures (Cluzel & Vigier, 2008; Genna *et al*., 2005). The creation of open spaces enables water circulation and Ni mobility, thus fracturing and faulting promote weathering and preferential Ni concentration. Garnierite mineralisations follow previous structures such as joints and shear zones in serpentinised peridotites (Freyssinet *et al*., 2005). Ore thickness, grade and type of Ni-laterite deposits are controlled by fractures, faults and shear zones in bedrock and regolith (Butt & Cluzel, 2013; Leguéré, 1976). Unfortunately, little attention has been placed on the effect of brittle tectonics on the formation of garnierites (Cluzel & Vigier, 2008).

In the Falcondo Ni-laterite deposit, evidences of garnierite precipitation during deformation are common. Striations on coated fault surfaces (**Fig. 4.1k, l**) and fault breccias containing garnierite clasts cemented by garnierite (**Fig. 4.2d**) indicate that the precipitation of the ore minerals was synchronous with brittle tectonics affecting the evolving weathering profile. Haldemann *et al*. (1979) and Mann *et al*. (1991) considered these types of faults as evidence of continuous tectonic uplift since at least the Miocene. The tectonic uplift controlled much of the evolution of the profile by allowing the exposure of deeper levels concomitant with erosion at the surface. Cluzel and Vigier (2008) documented similar relationships between brittle tectonics and synchronous precipitation of garnierites in the New Caledonian lateritic weathering profile.

Although the majority of garnierite mineralisations in the Falcondo deposit occur as infillings and coatings on fracture surfaces, their textures/structures suggest that they precipitated in an active tectonic environment. The fault structures in which garnierites precipitated were formed during uplift and weathering of the serpentinised peridotite body. Thus, garnierite-containing fractures hosted in unweathered protolith (**Fig. 4.1d**) document tectonic rupture and uplift of the country ultramafic rock before it could be altered to saprolite, suggesting rapid uplift tectonics compared to weathering rates. Also, the botryoidal habit of type IV garnierite (**Fig. 4.2g**), which represent precipitation from a colloidal solution in open spaces, is commonly fractured and brecciated (**Fig. 4.2g, h**), and the fragments are cemented by a second generation of garnierite and rounded quartz grains. These textures suggest multiple precipitation and deformation events, which may explain the

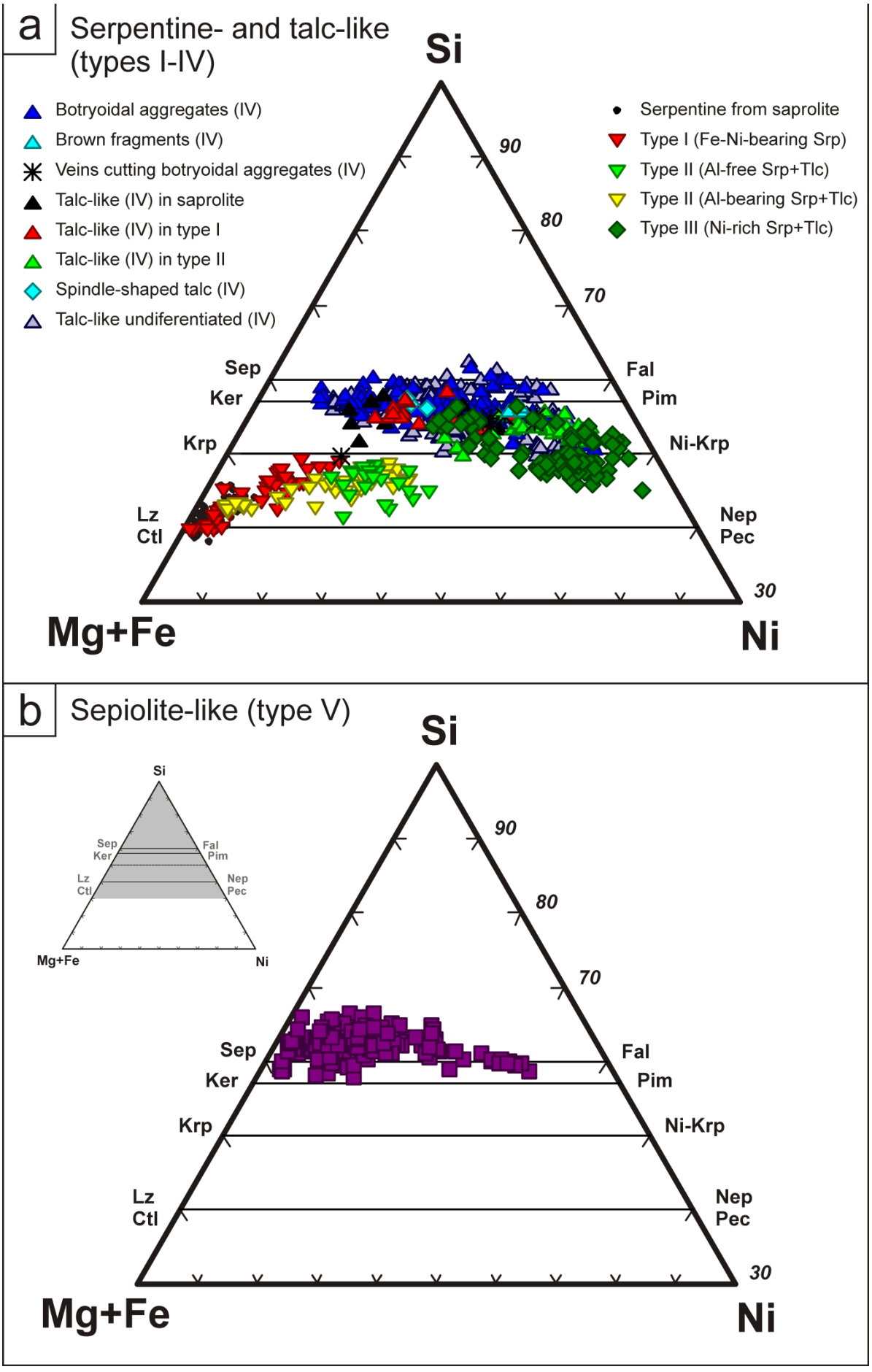
a
Serpentine- and talc-like (types I-IV)
Si
Botryoidal aggregates (IV)
Brown fragments (IV)
Veins cutting botryoidal aggregates (IV)
Talc-like (IV) in saprolite
Talc-like (IV) in type I
Talc-like (IV) in type II
Spindle-shaped talc (IV)
Talc-like undiferentiated (IV)
Serpentine from saprolite
Type I (Fe-Ni-bearing Srp)
Type II (Al-free Srp+Tlc)
Type II (Al-bearing Srp+Tlc)
Type III (Ni-rich Srp+Tlc)
90
80
70
30
Sep
Ker
Krp
Lz
Ctl
Fal
Pim
Ni-Krp
Nep
Pec
Mg+Fe
Ni
b
Sepiolite-like (type V)
Si
Sep
Ker
Fal
Pim
Lz
Ctl
Nep
Pec
Mg+Fe
Ni
90
80
70
30
Sep
Ker
Krp
Lz
Ctl
Fal
Pim
Ni-Krp
Nep
Pec
Mg+Fe
Ni

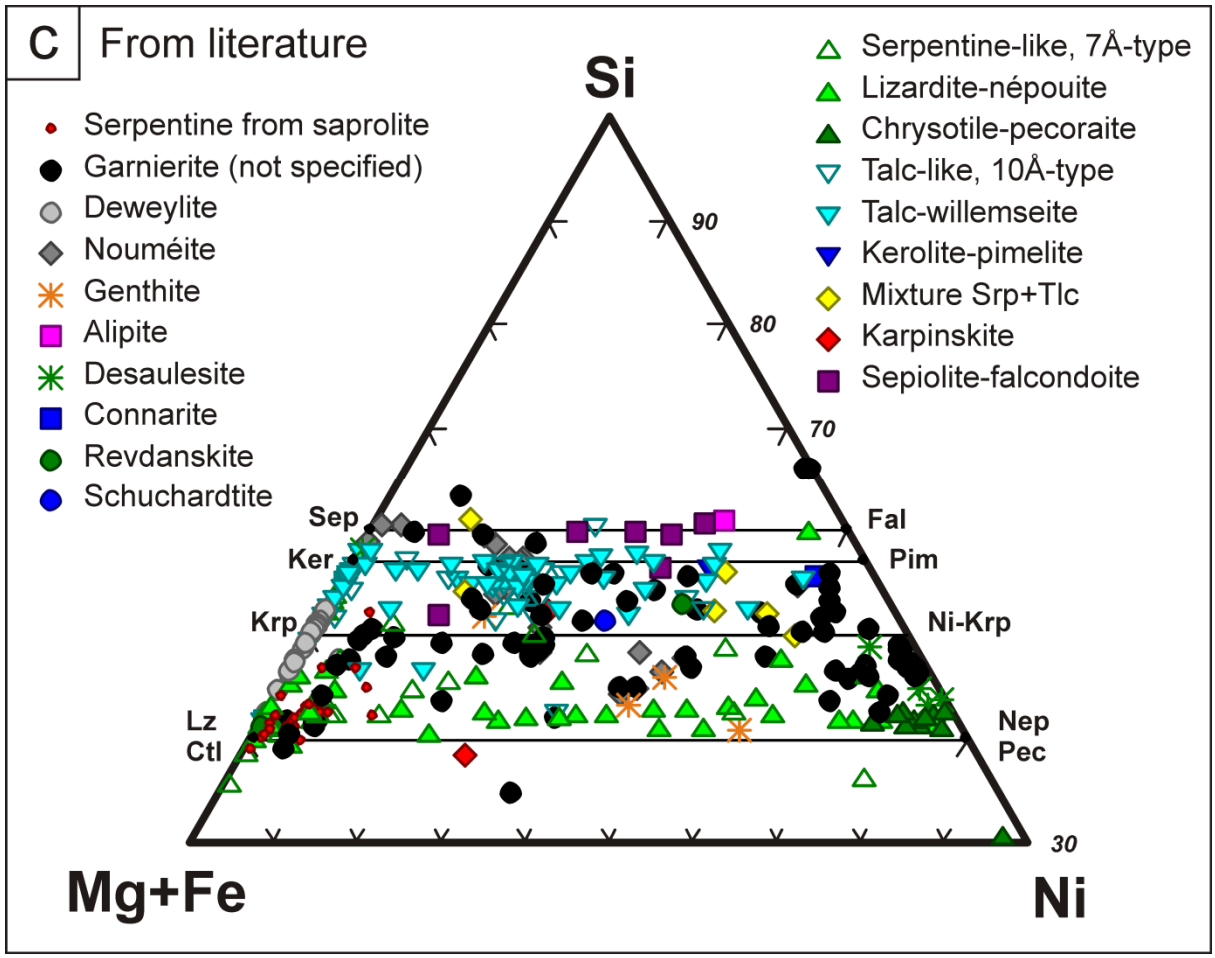

FIGURE 4.10. Ternary plots showing the compositions of the analysed garnierites compared to the data from other localities, plotted as normalised to 100 (instead of to 7, 11 and 32 oxygens for serpentine, talc and sepiolite). **a**) serpentine- and talc-like garnierites, **b**) garnierites of the sepiolite–falcondoite series (including data from Tauler *et al*., 2009 and this study), **c**) garnierite compositions from the literature, according to the description of the author(s) in the corresponding paper. Literature data: Klaproth (1788), Genth (1874), Liversidge (1874a, 1874b), Typke (1876), Des Cloizeaux (1878), Hood (1883), Liversidge (1888), Clarke (1890), Kay (1906), Glasser (1907), Ross & Shannon (1925, 1926), Ross *et al*. (1928), Palache (1937), Pecora & Hobbs (1942), Sudo & Anzai (1942), Pecora *et al*. (1949), Rukavishnikova (1956), Kato (1961), Lapham (1961), Wilkerson (1962), Montoya & Baur (1963), Faust (1966), Naganna & Phene (1968), Vitovskaya & Berkhin (1968), Faust *et al*. (1969), DeWaal (1970a,b), Vitovskaya & Berkhin (1970), Brindley & Hang (1973), Faust *et al*. (1973), Maksimović (1973), Nickel (1973), Springer (1974), Bosio *et al*. (1975), Brindley *et al*. (1975), Brindley & Wan (1975), Nickel & Bridge (1975), Wiewióra & Szpila (1975), Springer (1976), Brindley *et al*. (1977), Bish & Brindley (1978), Esson & Carlos (1978), Maksimović & Bish (1978), Wiewióra (1978), Brindley *et al*. (1979), Golightly & Arancibia (1979), Poncelet *et al*. (1979), Gerard & Herbillon (1983), Manceau & Calas (1985), Ogura (1986), Decarreau *et al*. (1987), Ducloux *et al*. (1993), Song *et al*. (1995), Pelletier (1996), Dubińska *et al*. (2000), Gaudin *et al*. (2004), Gleeson *et al*. (2004), Talovina *et al*. (2008), Wells *et al*. (2009), Suárez *et al*. (2011). Stoichiometric Mg and Ni end members of the sepiolite solid solution are indicated for reference. Legend: Sep = sepiolite, Fal = falcondoite, Ker = kerolite, Pim = pimelite, Krp = karpinskite, Ni-Krp = Ni-karpinskite, Liz = lizardite, Nep = népouite.

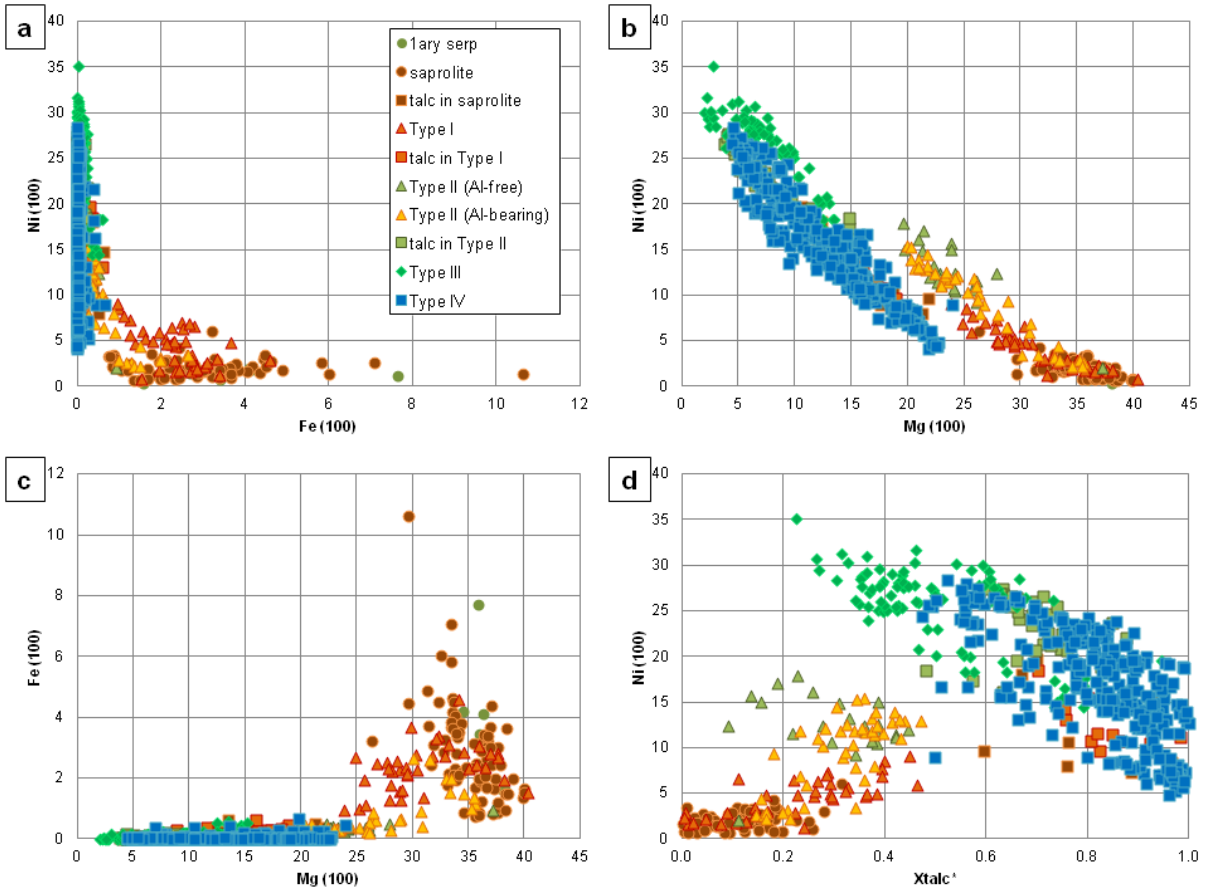

FIGURE 4.11. Binary diagrams relating the **a-c)** Ni, Fe and Mg content of Falcondo garnierite types following the same criteria used in **Fig. 4.10a**, calculated as atomic percent (normalised to 100, instead of to 7 and 11 for serpentine and talc respectively), and **d)** Ni with respect to Xtlc calculated according to **Section 3.6.2** (721 analyses plotted).

origin of the bimodal composition of the botryoidal talc-like phase (**Figs. 4.7**, **4.8**). Similarly, garnierite clasts within breccias (**Fig. 4.2d**) indicate a mineralisation stage prior to a brittle deformation. The fracturing formed tectonic porosity that enhanced the circulation of solutions and the precipitation of a second generation of garnierite, namely type III.

In summary, our observations suggest a regional syn-tectonic environment for the generation of the Ni–ore garnierite deposits in Falcondo, even if the precipitates are pre-, syn- or post-kinematic with respect to the activity of a particular fault. This brittle syn-tectonic environment has played an important role in the formation of hydrous silicate Ni-laterites, since it triggered cyclic, recurrent processes of weathering and erosion. These processes allowed the draining of fluids and reworking of previously formed ore, thus favouring remobilisation and reconcentration of ore minerals.

4.4.2. Garnierites and garnierites

Different greenish colours have been observed in the garnierite samples, which correspond to different mineral assemblages as demonstrated by XRD and EMP analyses. The various phases have been classified as type I to V garnierites. These garnierites show characteristic patterns of serpentine-like (type I), talc-like (type IV) and sepiolite-like minerals (type V). Also, mix phases with different proportions of serpentine and talc-like phases (types II and III) are also common. The different colours of the studied garnierites (**Fig. 4.2**) are not an indication of the Ni content in the minerals as shown in **Figure 4.10**. This is contrary to the observation of Brindley & Hang (1973). However, in the sepiolite–falcondoite series, the greenness of the sample is directly correlated with the Ni concentration. The characteristic colour of type I to IV garnierites gives information on the dominant mineral phase present in the sample

(serpentine-like, talc-like or mixtures), which is useful for a field mineral identification with the naked eye.

The following sections illustrate the complex mineralogical and compositional relations of garnierites. First, saprolite serpentine and type I serpentine-like garnierite compositions mainly display a lizardite [$Mg_3Si_2O_5(OH)_4$] stoichiometry (**Fig. 4.10a**). Deviations from the lizardite–népouite line toward the kerolite–pimelite line (types II and III) are due to mixing or interstratifications of 1:1 and 2:1 layers to form a mix phase (Faust, 1966; Vitovskaya & Berkhin, 1968, 1970). According to Brindley & Hang (1973), however, the same observations can be interpreted as deficiencies of octahedral cations in the 7 Å-type and of tetrahedral cations in the 10 Å-type garnierites. These mixtures (type II and III) show similar tetrahedral versus octahedral cation (T/O) ratios to that of the intermediate series karpinskite-Ni-karpinskite (T/O = 1; **Figs. 4.7e**, **4.10a**). However, the existence of karpinskite as a mineral species is debatable. Although EMP analyses and XR-maps show discrete homogenous regions with a composition similar to karpinskite, its presence is not supported by the X-ray diffractograms. More work is required in order to validate its existence.

Second, the type IV (talc-like) and type V (sepiolite-like) garnierites cover a wide range of composition and plot near the kerolite [$Mg_3Si_4O_{10}(OH)_2{\cdot}(H_2O)$]-pimelite [$Ni_3Si_4O_{10}(OH)_2{\cdot}(H_2O)$] and sepiolite [$Mg_4Si_6O_{15}(OH)_2{\cdot}6(H_2O)$]-falcondoite [$Ni_4Si_6O_{15}(OH)_2{\cdot}6(H_2O)$] lines respectively. The observed excess in Si in sepiolite– falcondoite series (**Fig. 4.10c**) may be due to contamination of silica nanorods observed under Transmission Electron Microscope, as reported by Tauler *et al*. (2009).

The lack of iron is a chemical characteristic of garnierite minerals (Troly *et al*., 1979). Manceau & Calas (1985) suggested that serpentine-like garnierites may have small amounts of iron (systematically below 1.5 wt.% Fe_2O_3), compared to talc-like garnierites, which are iron-free. It is generally accepted that the lack (or very low content) of iron confirms the secondary (neoformed) origin of garnierites, since Fe is largely not soluble under common weathering conditions. In the case of Falcondo, all garnierites fulfil this condition except type I, which display significant Fe values (1.8–6.8 wt.% Fe_2O_3) similar to those of saprolite serpentine (1.5–8.6 wt.% Fe_2O_3). This observation indicates that neoformed serpentine-like garnierite of the lateritic profile can be Fe-rich.

In the Falcondo deposit, this Fe-bearing Ni-phyllosilicate was the first garnierite to be precipitated. In this deposit the predominant garnierite is kerolite– pimelite (type IV), the 10 Å phase, having one of the highest Ni contents (up to 2.83 apfu). Also, Falcondo is the only locality in the world where the Ni-dominant sepiolite (falcondoite) occurs (Springer, 1976; Tauler *et al*., 2009). However, the Ni-dominant serpentine (népouite) has not been described yet. Possibly it only occurs as a mixture with Ni-kerolite–pimelite at the nanoscale. Mixtures of lizardite–népouite and kerolite and of lizardite–népouite and smectite are also described in NewCaledonia (Fig. 20 in Pelletier, 1996; Wells *et al*., 2009). In contrast, in New Caledonia, the presence of a serpentine-like (népouite) garnierite is well documented (e.g. Brindley & Wan, 1975; Glasser, 1907; Maksimović, 1973). The difference among these two Ni-laterite localities may be explained by the lithology of the primary ultramafic rocks. In New Caledonia, the protolith is mainly harzburgite and dunite (e.g. Dublet *et al*., 2012; Pelletier, 1983, 1996; Perrier *et al*., 2006; Troly*et al*., 1979) and lherzolite is rare (Cluzel *et al*., 2012), whereas in the Dominican Republic the protolith is mostly clinopyroxene-rich harzburgite and lherzolite (e.g. Marchesi *et al*., 2012). The higher content in pyroxenes suggests higher activity of silica in the Dominican than in the New Caledonian, leading to the preferential formation of talc rather than serpentine during weathering.

As pointed out by many authors and summarised by Galí *et al*. (2012), the results of this study suggest complete miscibility along the lizardite–népouite, kerolite–pimelite and the sepiolite–falcondoite lines under atmospheric temperature conditions. However, few data exist on the mechanism of Ni–Mg substitution in Ni-phyllosilicates (Manceau & Calas, 1985).

The distribution and speciation of nickel in Ni-bearing Mg-phyllosilicates have been studied, and EXAFS results suggest a heterogeneous distribution of Ni in the octahedral sheets of the Ni-phyllosilicates, forming discrete domains (clustering). However, due to the complexity of

these mineral phases a detailed XAS investigation is needed to define the distribution of Ni in garnierite minerals (see **Chapter 7**).

4.4.3. Water content in talc-like garnierites

First, the rapid weight loss at low temperatures (near 100ºC) is related to the loss of hygroscopic (adsorbed) water (Brindley *et al*., 1973). The loss at higher temperatures, around 600ºC in serpentine-containing garnierites (types I to III) and around 900ºC in garnierites with remarkable amounts of a talc-like fraction (types III to IV), corresponds to the loss of structural water (Caillère & Hénin, 1957; Brindley *et al*., 1973).

The large initial weight loss of type IV garnierite near 200ºC (compared to that of talc in Caillère & Hénin, 1957) which suggest that the mineral contains extra water in the structure. This is coherent with the low oxide totals observed in type IV garnierite, suggesting that it consists of hydrated talc (kerolite-pimelite series) rather than of a standard talc (talc-willemseite series).

In addition, as stated by Brindley *et al.* (1973), the separation between dehydroxylation water (structural water) loss and the monohydrate water (the extra water in the kerolite-pimelite structure) loss is unclear. According to these authors, monohydrate water is lost from 110 to 700ºC.

At first, the additional water, so-called "monohydrate water", was thought to occupy interlayer positions based on $d_{(001)}$ ~10 Å (like cations in micas) (Brindley & Hang, 1973). However, afterwards some data stated that $d_{(001)}$ ~ 9.5-9.6 Å, so the last explanation is either invalid or incomplete. Much of the excess water is removable at temperatures up to 300ºC and probably occupies external positions (Brindley *et al*., 1979). The presence of molecular water in kerolite and pimelite was proven by IR spectrometry with the absorption in the 1900 nm band (Brindley *et al*., 1979). The large surface area of these minerals and the small crystal size are coherent with a large amount of adsorbed water (Brindley, 1978). The slightly increased spacing with respect to that of talc (9.35 Å) may account for random layer stacking in kerolite-pimelite, compared to close packed talc layers (Brindley, 1978).

Hence, for this type of phase, the terms kerolite and pimelite are more appropriate than talc and willemseite. Despite kerolite and pimelite were discredited by CNMMN-IMA (Nickel & Nichols, 2009, http://www.materialsdata.com), they are included in the recommendations for the nomenclature of phyllosilicates by the Association Internationale Pour l'Étude des Argiles (AIPEA; Guggenheim *et al*., 2006) and these names are still used nowadays (Tauler *et al*., 2009; Wells *et al*., 2009; Galí *et al*., 2012; Villanova-de-Benavent *et al*., 2014a, b; Cathelineau *et al*., 2015).

Both kerolite and pimelite have been historically classified as either members of the talc group or of the smectite group by different authors. Faust (1966) reported that pimelite behaved as a montmorillonite group-mineral under the optical microscope as seen in Beyschlag & Krusch (1913) in terms of birefringence, and X-ray powder diffraction confirmed that this phase was comparable to montmorillonite (Spangenberg, 1938). However, many studies misidentified the starting material as "pimelite" and reached erroneous conclusions. A significant literature exists verifying that pimelite has a structure with talc affinity. Many authors proved that kerolite and pimelite do not exhibit intracrystalline swelling (e.g. Slansky, 1955; Maksimović, 1973; Brindley & Hang, 1973). In addition, according to Guggenheim *et al.* (2006), these mineral phases are 2:1 layer trioctahedral phyllosilicates without interlayer positions, so they belong to the talc-pyrophillite group. However, according to Brindley (1978), 2:1 phyllosilicates with small particle size cannot be classified sharply as swelling or non-swelling minerals, because this feature depends on the amount of swelling and non-swelling layers interstratified.

In addition, kerolite and pimelite have been described in other laterite deposits, for example in New Caledonia (e.g. Dublet *et al*., 2012; Wells *et al*., 2009), Poland (e.g. Dubińska *et al*., 2000; Wiewióra, 1978) and India (e.g. Som & Joshi, 2002). In the Cerro Matoso in Colombia Ni-laterite, pimelite is one of the main garnierite-forming minerals (Gleeson *et al*., 2004; Lopez-Rendon, 1986). Also, kerolite has been reported in other settings including karst environments (e.g. Ducloux *et al*., 1993), palustrine-lacustrine (e.g. Martín de Vidales *et al*., 1991; Pozo & Casas, 1999) and in oceanic sediments (e.g. Cole & Shaw, 1983). Therefore, kerolite and pimelite are important components in not only hydrous silicate Ni-laterites but also in other deposits worldwide.

As a conclusion, given the DTA-TG and EMP results presented in this work, the garnierite type IV might actually be a mineral of the kerolite-pimelite series.

4.4.4. Origin of Falcondo garnierites

Similar to other hydrous silicate-type laterites, the Falcondo deposit in the Dominican Republic was formed by tropical weathering of ultramafic rocks undergoing continuous tectonic uplift. Coupled with a low water table, these conditions resulted in the development of a thick saprolite horizon, and a thin ferruginous oxide horizon (Golightly, 1981; Brand *et al*., 1998; Elias, 2002; Gleeson *et al*., 2003; Lewis *et al*., 2006; Butt & Cluzel, 2013).

During laterisation, the main Ni-containing primary silicates are altered to secondary phases which are more stable under the oxidising ambient conditions. Under these conditions, Mg contained in the primary ferromagnesian silicate minerals is solubilised and leached out of the weathering profile. Ferrous Fe originally contained in the silicates is oxidised to the insoluble Fe^{3+}, which is residually concentrated as goethite in the limonite horizon. The Ni released by the silicates is retained in goethite. The retention of Fe in the limonite explains the low Fe content of the garnierites in the Falcondo deposit (Tauler *et al*., 2009; and references therein). The Ni in goethite from the limonite may subsequently be leached by percolating acidic solutions to deeper levels in the profile where it may be co-precipitated with hydrous Mg silicates around water table (e.g. Avias, 1978; Brand *et al*., 1998; Freyssinet *et al*., 2005; Golightly, 1981; Trescases, 1979). This interpretation is supported by the negative correlation of Mg with Ni and Fe in saprolite serpentines, where Ni increases more rapidly than Fe (Golightly & Arancibia, 1979). The Fe in saprolite serpentines is residual, and the Ni is imported from the upper lateritic levels (Avias, 1978; Trescases, 1973, 1979). The Ni is incorporated first in the saprolite Ni-bearing serpentines (Pelletier, 1996). Once the Ni-serpentines are saturated, the excess Ni is precipitated as hydrous Mg silicates (garnierites) in open spaces including cracks and faults. The precipitation is caused by a sudden change in Eh/pH of the solution. The high stability of the octahedrally coordinated Ni^{2+} ion (Burns, 1970) favours the formation of nickeliferous trioctahedral phyllosilicates (e.g. Trescases, 1975).

In general, the stability of Ni-bearing minerals in lateritic environments is determined by the Eh, pH, and chemical composition of permeating groundwater (e.g. Trescases, 1973). In an Al-free system, such as in the Falcondo profile, the stability of lizardite–népouite, kerolite– pimelite or sepiolite–falcondoite is controlled by the silica activity (Galí *et al*., 2012). The ideal formation of the Ni ore occurs as a succession of precipitation of mineral phases progressively enriched in Ni and with higher Si, because silica activity increases with time and through the profile. Thus, the first garnierite to precipitate is lizardite–népouite, followed by kerolite–pimelite, sepiolite–falcondoite and Ni-free sepiolite with quartz (Galí *et al*., 2012). This mineral sequence is coherent with field observations and textural relationships between types I–II and type IV. In this mineral sequence the silica activity increases progressively, as well as pH decreases and Eh becomes more oxidising (Gleeson *et al*., 2004; Golightly, 1981, 2010). In alkaline conditions (pH ~ 8) garnierite minerals are the least-soluble Mg–Ni phyllosilicates, whereas at lower pH quartz may precipitate. The occurrence of later quartz indicates subsequent acidification conditions as a result of rapid access of meteoric surface waters (acidic) to deeper levels (e.g. Golightly, 1981).

According to these results, the first supergene Ni-phyllosilicate phase that was formed in the Falcondo deposit was a Fe-bearing, nickel enriched, serpentine-like garnierite (type I). Its Fe content is similar to that of saprolite serpentine and suggests that type I garnierite precipitated in a Ni-saturated, rock-dominated system under more alkaline and reducing conditions. On the other hand, the other types of garnierite (types II–V) were precipitated under conditions in which Fe was insoluble as suggested by their low Fe content. Furthermore, the mix serpentine- and talc-like phases (types II and III) may have precipitated under an intermediate stage between the stability fields of Ni-serpentine and kerolite–pimelite (see Fig. 6 in Galí *et al*., 2012). These interpretations are coherent with the textures observed in the Falcondo garnierites, where talc-like phases frequently envelop type I and II garnierites (**Fig. 4.2a, b**), and the remaining porosity is finally filled by quartz and/or silica. However, the mineral sequence may be more complex. For example, the polyphase infilings containing serpentine- and talc-like garnierite shown in **Fig. 4.2a, b** suggest that the conditions of

the system allowed the formation of serpentine followed by talc-like phases in the same vein, when the fracture was open. Also, textural–chemical features revealed by the X-ray maps indicate several stages of growth with strong oscillatory changes in Ni content in type IV (**Figs. 4.7**, **4.8**), and progressive Ni enrichment in type V (**Fig. 4.9**). These observations point to recurrent variations in the physical–chemical conditions during garnierite precipitation–dissolution in an aqueous medium.

4.4.5. Metallurgical implications

Variations in the chemical composition of garnierites imply changes in the behaviour of the laterite ore during mineral processing. The laterite ore is a mixture composed mainly of Ni-bearing saprolite serpentine with variable amounts of garnierite, Fe-oxyhydroxides from the limonite horizon, and fresh, unserpentinised and serpentinised peridotite. Due to the high water content of the laterite ore, in the form of free moisture or combined as hydroxyl/molecular water in the mineral structures, it must be first dehydrated by calcination at about 900 °C. The calcination product is later briquetted and partly reduced to transform Ni and Fe oxides into metallic Ni and Fe in the solid state. The ore is then smelted to forma slag at about 1600 °C in an electric furnace in the presence of carbon (Dalvi *et al*., 2004; and references therein).

The garnierites characterised in this paper present different water contents. Judging from the mass deficiency of the EPM analyses, the H_2O contents are about 15 wt.% in the serpentine-like (garnierite types I and II, also in saprolite serpentine, the main component of the laterite ore), 11 wt.% in garnierite mixtures (type III), 10 wt.% in the "hydrated" talc-like (type IV) and 17 wt.% in the sepiolite-like (type V).

In the case of Falcondo, in order to produce ferronickel containing ca. 40% nickel and 60% iron, operation in a conventional electric furnace requires high SiO_2/MgO ratios (~2; wt.% units) and low FeO (~20 wt.% FeO) (Dalvi *et al*., 2004). This ratio acts as a flux in the smelting process. Thus a low SiO_2/MgO leads to an increase of the temperature in the furnace, and to higher energy consumption. The garnierite typologies reported in Falcondo display different SiO_2/MgO ratios: the highest average silica/magnesia is found in types III (6.5), IV (4.6) and V (3.2), followed by type II (2.3) and type I (1.5). The ratio of type I is similar to that of saprolite Ni-serpentine (1.5). In addition, in all cases, the Ni content and the SiO_2/MgO ratio correlate fairly well because Ni substitutes for Mg in the octahedral position. As a result, processing ore containing remarkable amounts of type III or IV garnierites (with relatively high Si and Ni, thus high SiO_2/MgO ratios) requires a lower temperature than processing saprolite serpentine with or without serpentine-like garnierites (with less Si than type III and IV and lower Ni, thus low SiO_2/MgO ratios).

In summary, these variations in water content, Ni and SiO_2/MgO ratio should be taken into account for the preparation of the laterite ore mixture prior to calcination and smelting. Therefore, an accurate mineralogical characterisation of garnierite-forming minerals is important from a metallurgical point of view.

4.5. FINAL REMARKS

This first characterisation of garnierites and related rocks from the Falcondo Ni-laterite deposit by means of XRD, DTA-TG, optical microscopy, SEM and EMP leaded to the following conclusions:

The garnierites in the Falcondo weathering profile were precipitated in a tectonically active regime in which Ni was reconcentrated through recurrent weathering–uplift–erosion cycles. In some cases, the precipitation was syn-kinematic.

The garnierites in the Falcondo weathering profile occur in various shades of greenish colour which, in addition to textural features, characteristic XRD patterns and chemical composition, have been used to classify the minto five groups. The end member phases identified include serpentine-like, talc-like, and sepiolite-like phases. In addition, intermediate phases with mixed serpentine- and talc-like end members were also observed and interpreted as mixtures at nanoscale. The mole fractions of the end members in the mixed phases were calculated from EMP analyses. XR element maps showed complex textures and variable compositions. It isworth noting that the intensity of the greenish colour is not a direct indicator of theNi amount in the sample (except for sepiolite–falcondoite series), but gives information on the dominant mineral phase present in the garnierite.

The formation of the ore occurred in successive stages becoming progressively enriched in Ni and Si. The precipitation sequence was as

follows: iron-bearing Ni-enriched serpentine (Type I), iron-free mixtures between serpentine and kerolite–pimelite (types II and III), kerolite–pimelite (type IV), and sepiolite–falcondoite (type V), being quartz the final product.

Both the low oxide totals obtained by EMP and the large water loss at low temperatures of the talc-like garnierite confirm the presence of extra water in their structure, and therefore the use of the names “kerolite” and “pimelite” to refer these phases seems appropriate. Although these are also not accepted by the IMA-CNMMN, those terms have been used widely in the recent literature for Mg-Ni-bearing minerals with talc-like structures and additional water.

The talc-like phase (10 Å-type), which shows one of the highest Ni contents, is the dominant garnierite phase in the profile. This contrasts with the New Caledonian Ni-laterites, where the serpentine-like garnierite is the most common phase. This difference is probably due to the lower silica activity in the profile imposed by a harzburgite/dunite protolith, as opposed to a clinopyroxene-rich harzburgite/lherzolite protolith in the Loma Caribe peridotite.

The wide variation in the garnierite mineralogy has important implication on ore processing due to variation in the SiO2/MgO ratio which requires careful blending before feeding the ore into the smelter.

5. MINERALOGY, TEXTURES AND MINERAL CHEMISTRY AT THE NANOMETRE SCALE: A TEM-AEM APPROACH

This part of the study presents a textural and chemical characterization by TEM of the different garnierites described in the Falcondo Ni-laterite deposit. The aim is to give evidences of the textural relationships between the different garnierite-forming minerals and to unravel the distribution of Ni among them at the nanometre scale based on High Resolution TEM (HRTEM) and Analytical Electron Microscopy (AEM).

The selected samples for this study are listed in **Table 5.1**. TEM imaging results of the five garnierite types described in **Chapter 4** are presented in **Figures 5.1-5.5**, including a photograph of the selected sample (**Figs. 5.1a-5.5a**), a photomicrograph of the ion thinned specimen (**Figs. 5.1b-5.5b**), low magnification and high resolution images, and electron diffraction patterns. The chemical composition of the Falcondo garnierites obtained by AEM is plotted in **Figure 5.6**, in addition to the previous EMP results for comparison. Representative AEM analyses are shown in **Table 5.2**. Finally, the high resolution images in **Figure 5.7** summarise the textural relationships among the garnierite-forming minerals and **Figure 5.8** presents a proposed model of formation of these mineral phases.

5.1. MINERALOGY AND TEXTURES

5.1.1. Type I garnierite

Type I garnierite consists of serpentine particles and minor talc-like bent thin lamellae with very little porosity (**Fig. 5.1c**). Serpentine occurs as tubes of various sizes which are randomly oriented, as basal and longitudinal sections are observed in low magnification images. There are two groups of serpentine tubes: i) thick, short tubes up to 5000 Å long and about 3000 Å in diameter, with 85 Å in diameter hollow cores; ii) less abundant, narrow, long tubes up to 3000 Å in length and around 750 Å in diameter, with ~50 Å hollow cores (**Fig. 5.1d**). These nanostructures together with the particle size indicate that this sample is formed mostly by polygonal serpentine in relatively short fibres, finely intermixed with talc-like lamellae. Uyeda *et al*. (1973) also reported short stubby tubes with central holes in serpentine-like garnierites from Brazil, with an average width of 740 Å (4.4 wt.% NiO, talc fraction = 10.3), with less abundant ill-defined platy fragments, which may resemble the talc-like particles in type I garnierite (**Fig. 5.1c, d**).

As seen in Fig. 2d, the short tubes display bending at the fibre tip. These features have also been observed in polygonal serpentines coexisting with polyhedral serpentines by Andréani *et al*. (2008). In the high resolution images of the short tubes longitudinal sections 7.3 Å spacings are observed, in some cases presenting dislocations (**Fig. 5.1e**). The 7.3 Å spacings were confirmed in both the electron diffraction patterns and the Fast Fourier Transform obtained for the same short tubes, which displayed few reflections of the *h0l* plane that can be indexed with the clinochrysotile-$2M_{c1}$ 14 Å structure (Brindley & Brown, 1980) (**Fig. 5.1f**). However, no high resolution images of the long tubes could be obtained due to electron beam damage. According to the total diameters and the measured spacings, the short, thick ones have approximately 200 layers and the long, thin ones have 50 layers.

5.1.2. Type II garnierite

In the specimen of type II garnierite, serpentine particles, with characteristic 7.2 Å spacings, display various shapes and sizes and are found scattered in a matrix of talc-like bundles (**Fig. 5.2c-g**). Some serpentine basal sections have diameters around 5000 Å with tiny hollow cores, and are divided in 15 equidimensional sectors with an angle of 24º between adjacent (001) lattice planes, so-called polygonal serpentine (**Fig. 5.2g-h**). In some cases, polygonal sections are kidney-shaped, resembling the polyhedral serpentine of Andréani *et al*. (2008) (**Fig. 5.2d**). The inner diameter of some polygonal serpentines is similar to the outer diameter of the chrysotile basal sections in type I (**Fig. 5.2e**). Other serpentine particles display less rounded cylindrical

TABLE 5.1. Summary of the studied garnierite samples from the Falcondo Ni-laterite (Dominican Republic). Xtlc calculated according to Brindley & Hang (1973).

Samples	Type	Mineralogy (XRD)	Structural formula (EMP)	Xtlc
LC-101	TYPE I	serpentine + traces kerolite-pimelite (type I)	$(Mg_{3.11}Ni_{0.31}Fe_{0.24})Si_{2.86}O_{5.87}(OH)_{3.65}\cdot 0.17H_2O$	0.17
09GAR-2	TYPE I	serpentine + traces kerolite-pimelite (type I)	$(Mg_{2.94}Ni_{0.50}Fe_{0.21})Si_{2.91}O_{6.00}(OH)_{3.60}\cdot 0.20H_2O$	0.2
LC-100B, LC-100AB	TYPE II	serpentine + minor kerolite-pimelite (type II)	$(Mg_{2.37}Ni_{1.22}Fe_{0.04})(Si_{3.07}Al_{0.10})O_{6.58}(OH)_{3.37}\cdot 0.32H_2O$	0.32
GAR-1	TYPE III	serpentine + kerolite-pimelite (type III)	$(Ni_{2.92}Mg_{0.65})Si_{3.28}O_{6.91}(OH)_{3.24}\cdot 0.38H_2O$	0.38
GAR-2	TYPE III	serpentine + kerolite-pimelite (type III)	$(Ni_{2.89}Mg_{0.67}Fe_{0.01})Si_{3.24}O_{6.84}(OH)_{3.27}\cdot 0.37H_2O$	0.37
LC-101	TYPE IV	kerolite-pimelite (type IV)	$(Mg_{1.83}Ni_{1.45}Fe_{0.03})Si_{4.15}O_{9.40}(OH)_{2.24}\cdot 0.88H_2O$	0.88
09GAR-2	TYPE IV	kerolite-pimelite (type IV)	$(Mg_{1.85}Ni_{1.43}Fe_{0.01})Si_{4.25}O_{9.70}(OH)_{2.12}\cdot 0.94H_2O$	0.94
LC-100B, LC-100AB	TYPE IV	kerolite-pimelite (type IV)	$(Ni_{2.19}Mg_{1.15})(Si_{4.06})O_{9.11}(OH)_{2.36}\cdot 0.82H_2O$	0.82
GAR-7	TYPE V	sepiolite-falcondoite (type V)	$(Mg_{4.60\text{-}7.05}Ni_{1.01\text{-}2.39}Fe_{0\text{-}0.05})(Si_{11.75\text{-}12.75}Al_{0\text{-}0.02})O_{15}(OH)_2\cdot 6H_2O$	-
FALC-3	TYPE V	sepiolite-falcondoite (type V)	$(Mg_{3.42\text{-}5.15}Ni_{2.29\text{-}5.24}Fe_{0\text{-}0.02})(Si_{11.57\text{-}12.55}Al_{0\text{-}0.15})O_{15}(OH)_2\cdot 6H_2O$	-
FALC-4	TYPE V	sepiolite-falcondoite (type V)	$(Mg_{6.51\text{-}7.94}Ni_{0.34\text{-}0.58}Fe_{0.01\text{-}0.27})(Si_{11.46\text{-}12.32}Al_{0.01\text{-}0.03})O_{15}(OH)_2\cdot 6H_2O$	-

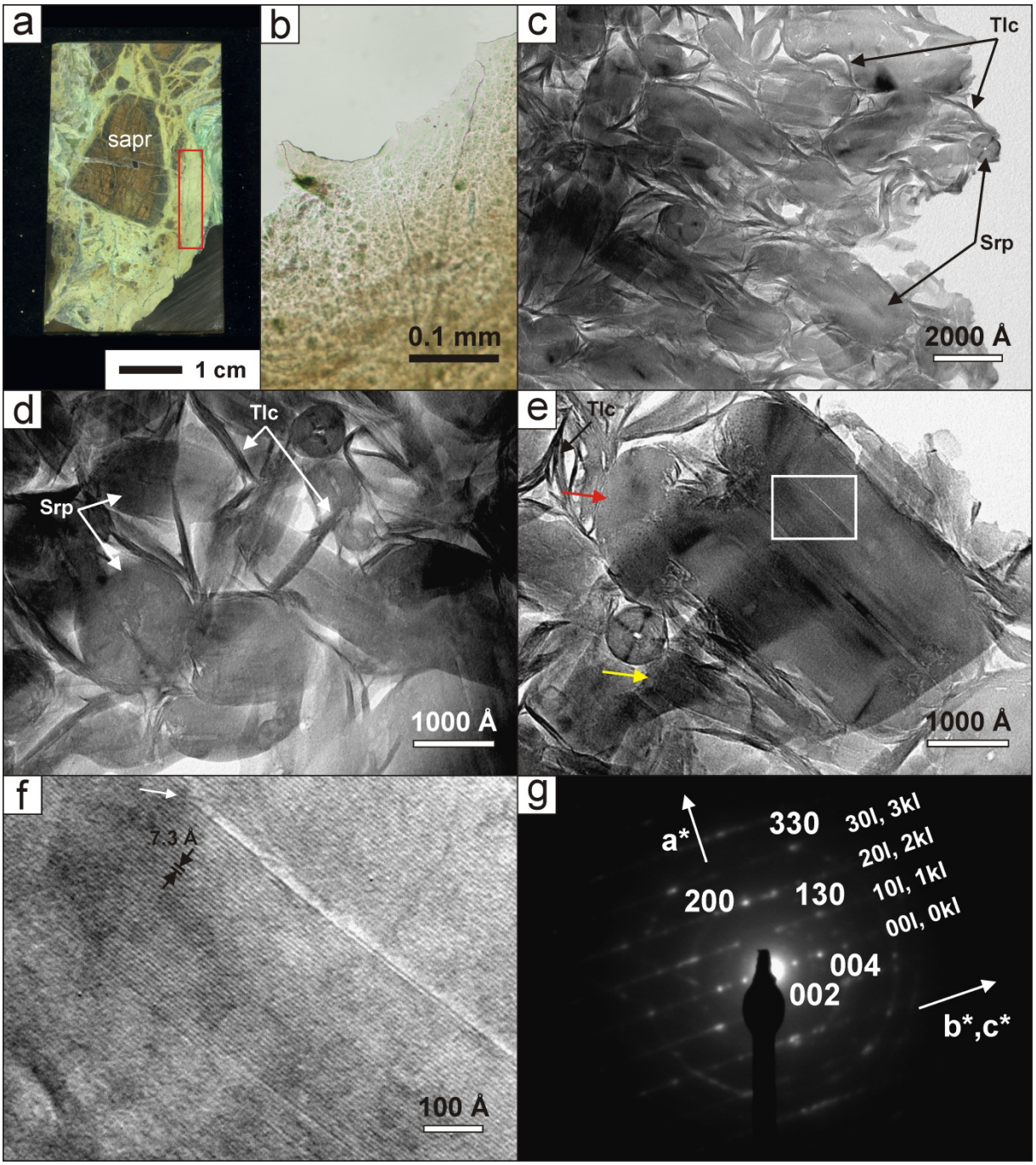

FIGURE. 5.1. Type I garnierite as seen under the TEM (specimen LC-101): **a**) image of the sample, the specimen was detached from the area in the red rectangle; **b**) detail of the hole in the grid under the optical microscope (plane polarised light); **c-d**) low magnification images of the specimen showing short serpentine tubes (Srp) and minor talc-like lamellae (Tlc); **e**) detail of a short serpentine tube with a hollow core (red arrow), next to a long serpentine tube (yellow arrow); **f**) high resolution image of the area in the rectangle in d) showing the typical basal spacings of serpentine minerals of 7.3 Å, and a dislocation marked with a white arrow; **g**) electron diffraction pattern of the serpentine tubes. All images were obtained in a CM20 (CIC-UGR).

fibres, probably corresponding to oblique sections of serpentine tubes, smaller than the polygonal fibres (up to 3000 Å in diameter), which are hollow-cored or contain disordered layers in the centre, probably of a talc-like phase (**Fig. 5.2f**). Uyeda *et al*. (1973) also observed those features and mentioned that this material in the cores could be amorphous. Talc-like lamellae were also

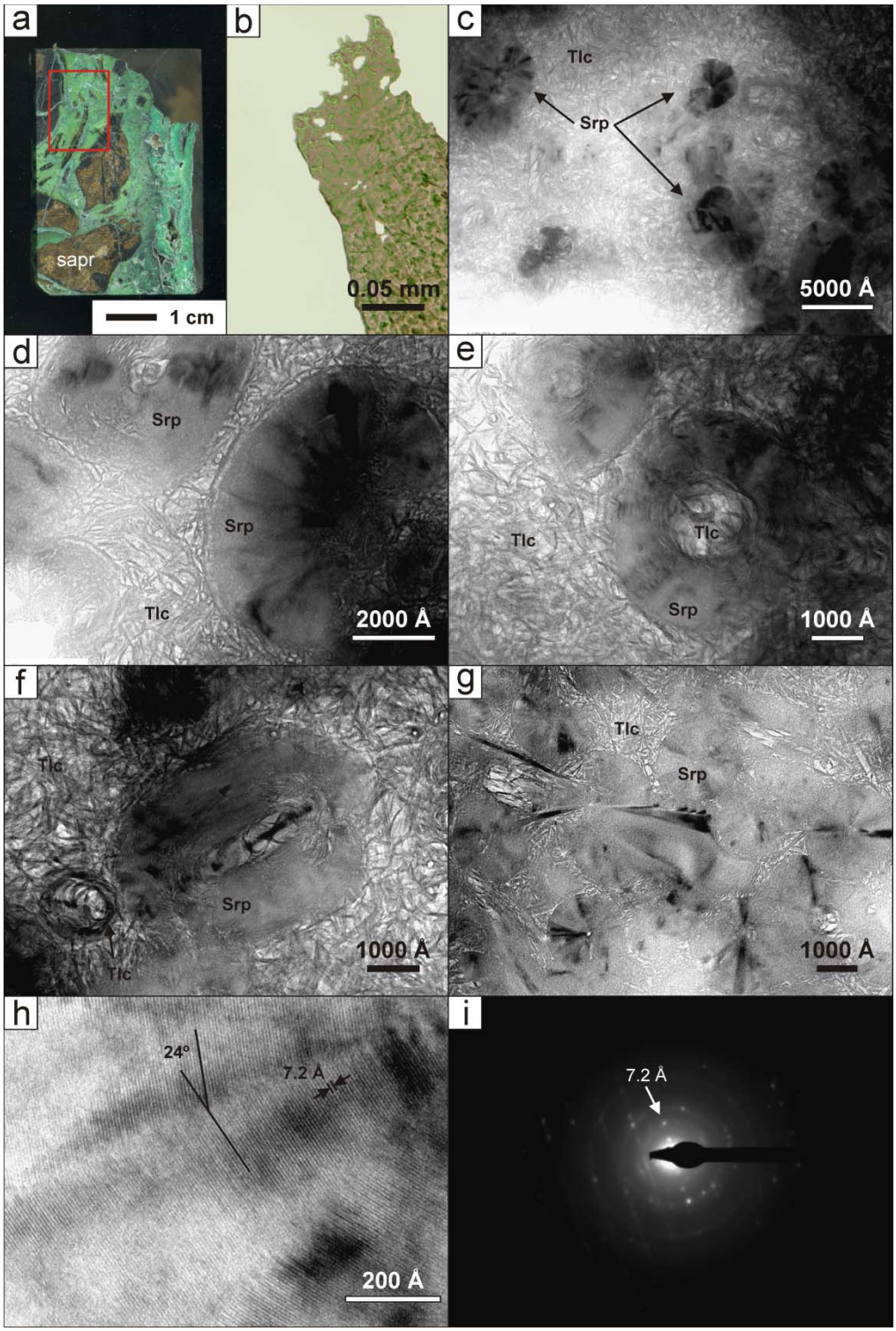

FIGURE. 5.2. Type II as seen under the TEM (specimen): **a**) image of the sample LC-100B, the specimen LC-100B2 was detached from the area in the red rectangle; **b**) detail of the LC-100B2 hole in the grid under the optical microscope (plane polarised light); **c-f**) low magnification images of the specimen LC-100B2 showing circular sections of serpentine (Srp) within a matrix of talc-like lamellae (Tlc), including: **d**) kidney-shaped sectored serpentine; **e**) serpentine tubes with large holes filled with talc-like lamellae; **f**) oblique section of serpentine tube, the central hole being altered to talc, with curled up talc-like lamellae aggregate (lower left); **g)** polygonal serpentine (Srp) embedded in a talc-like (Tlc) matrix in specimen LC-100B3b; **h**) high resolution image of polygonal serpentine in LC-100B2, showing the angle between sectors and the basal spacings; **i**) electron diffraction pattern with distinctive 7.2 Å spots and a less crystalline phase in LC-100B-2. All images were obtained in a CM20 (CIC-UGR).

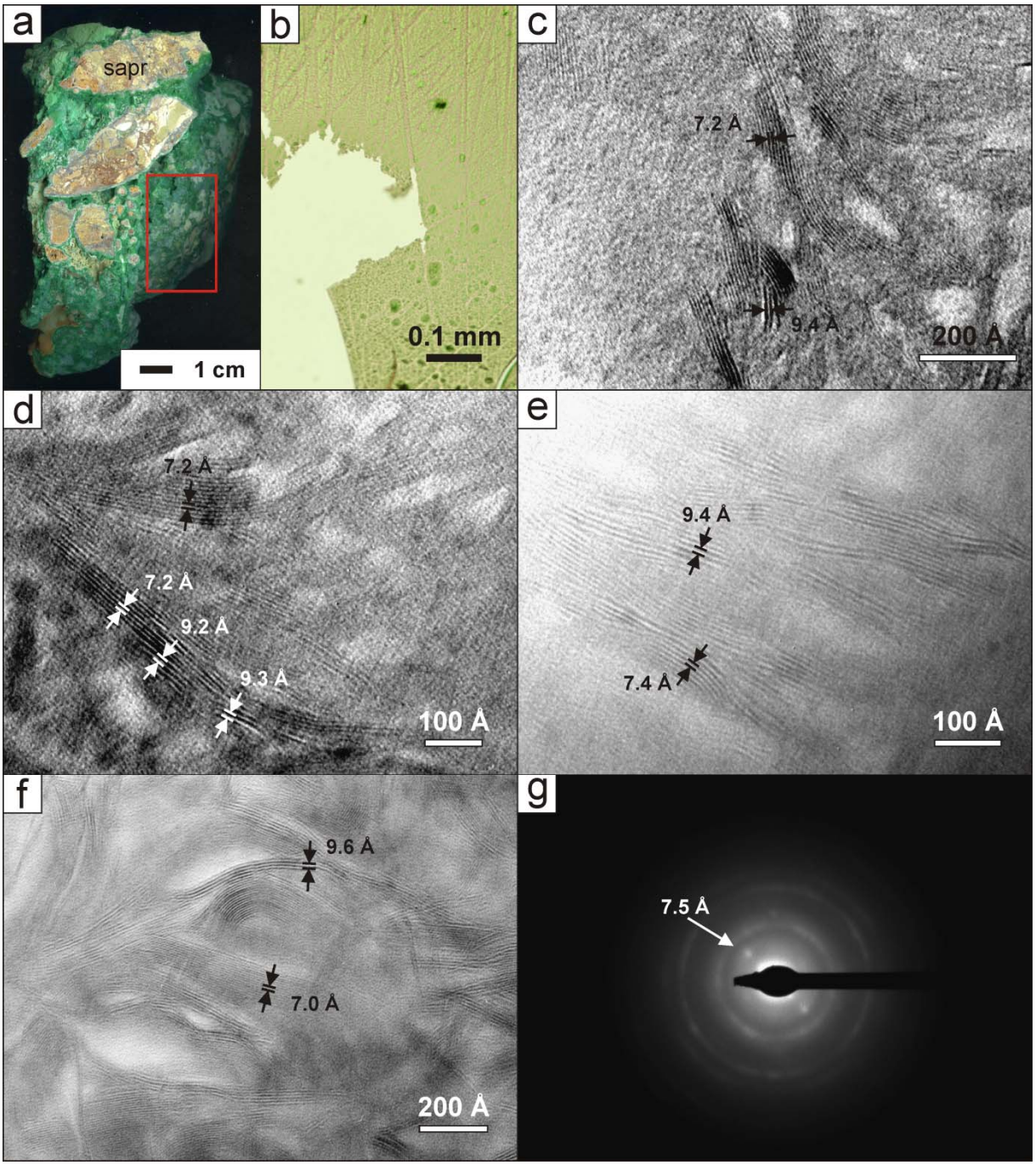

FIGURE 5.3. Type III as seen under the TEM: **a**) image of the sample GAR-2, the specimen was detached from the area in the red rectangle; **b**) detail of the hole in the GAR-2.2 grid under the optical microscope (plane polarised light); **c-e**) high resolution images of GAR-2.2 showing the presence of 7.2-7.4 Å and 9.2-9.4 Å basal spacings (Philips CM20, CIC-UGR); **f**) high resolution image of thick, bent lizardite (Lz) lamellae with talc-like (Tlc) lamellae in sample GAR-1.2 (Jeol 2010,UniSi); **g**) electron diffraction pattern of GAR-2.2 showing a higher crystallinity 7.5 Å spacing coexisting with a less crystalline material (Philips CM20, CIC-UGR).

observed to concentrate in curved aggregates (**Fig. 5.2h**). The selected area electron diffraction patterns show a well defined 7.2 Å spacing and diffuse concentric circles (**Fig. 5.2i**).

5.1.3. Type III garnierite

Type III garnierites display long and bent lamellae with basal spacings of 9.2-9.6 Å and 7.0-7.4 Å (**Fig. 5.3c-e**), which are frequently parallel to each other (**Fig. 5.3d-e**). Lamellae of 7.0-7.4 Å spacings are

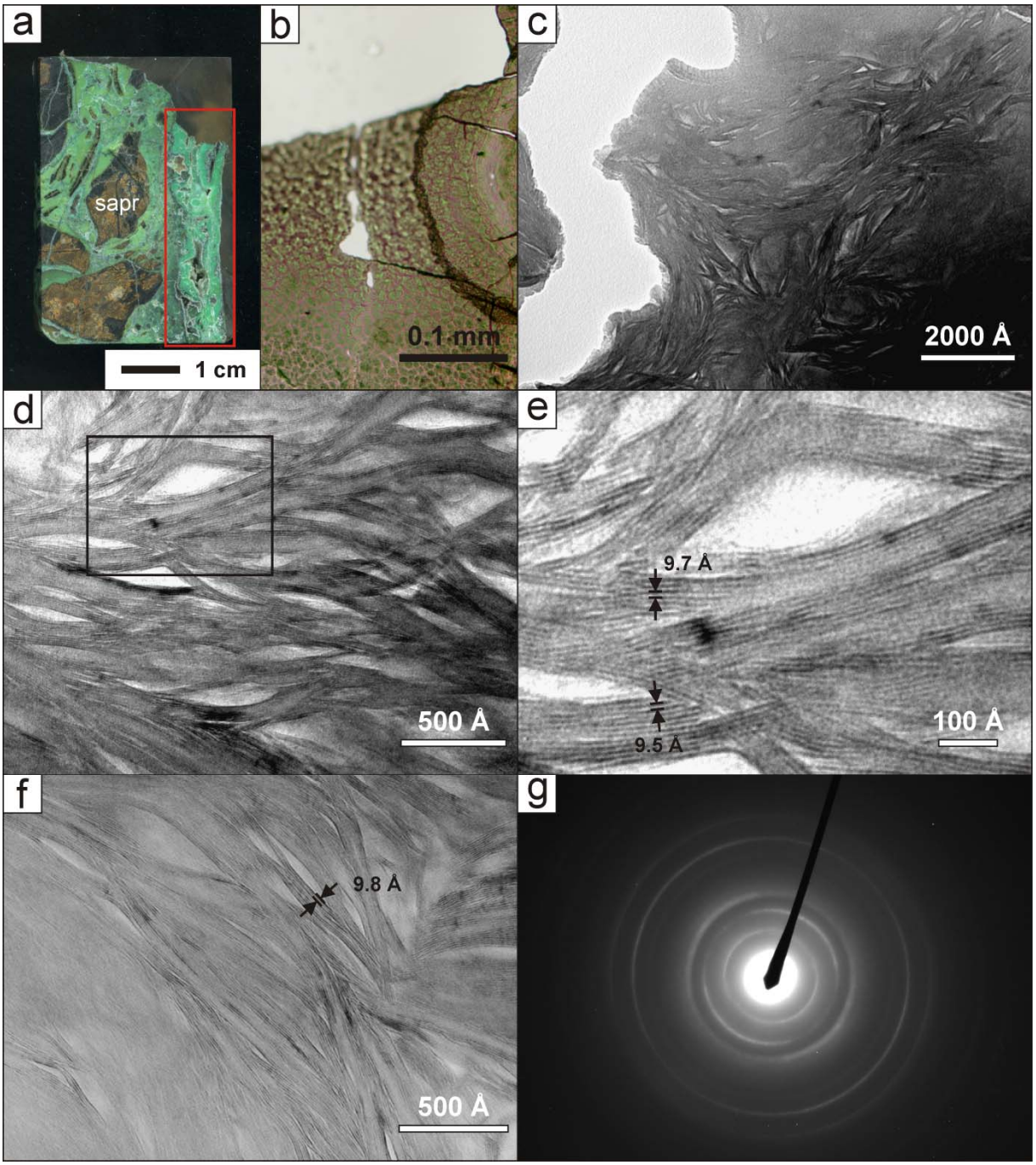

FIGURE. 5.4. Type IV (kerolite-pimelite) as seen under the TEM: **a**) image of the sample LC-100B, the specimen was detached from the area in the red rectangle; **b**) detail of the hole in the LC-100B4 grid under the optical microscope (plane polarised light); **c**) low magnification images of LC-100B4 showing bundles of talc-like lamellae (Philips CM20, CIC-UGR); **d**) high resolution image of talc-like lamellae in LC-100B4 and **e**) close-up displaying the typical basal spacings of talc-like minerals (obtained in a Philips CM20, CIC-UGR); **f**) high resolution image and **g**) electron diffraction pattern of talc-like lamellae in sample LC-100B4s (obtained in a Jeol 2010,UniSi).

curved, more regular and thicker (from six to sixteen 7.0-7.4 Å spacings) when compared to the 9.2-9.6 Å lamellae (four fringes mostly, and up to six) (**Fig. 5.3f**). This is supported by electron diffraction patterns, showing that the sample is composed of crystalline lizardite with a 7.0 Å spacing, coexisting with a lower crystallinity talc-like phase (**Fig. 5.3g**). No polygonal serpentine was

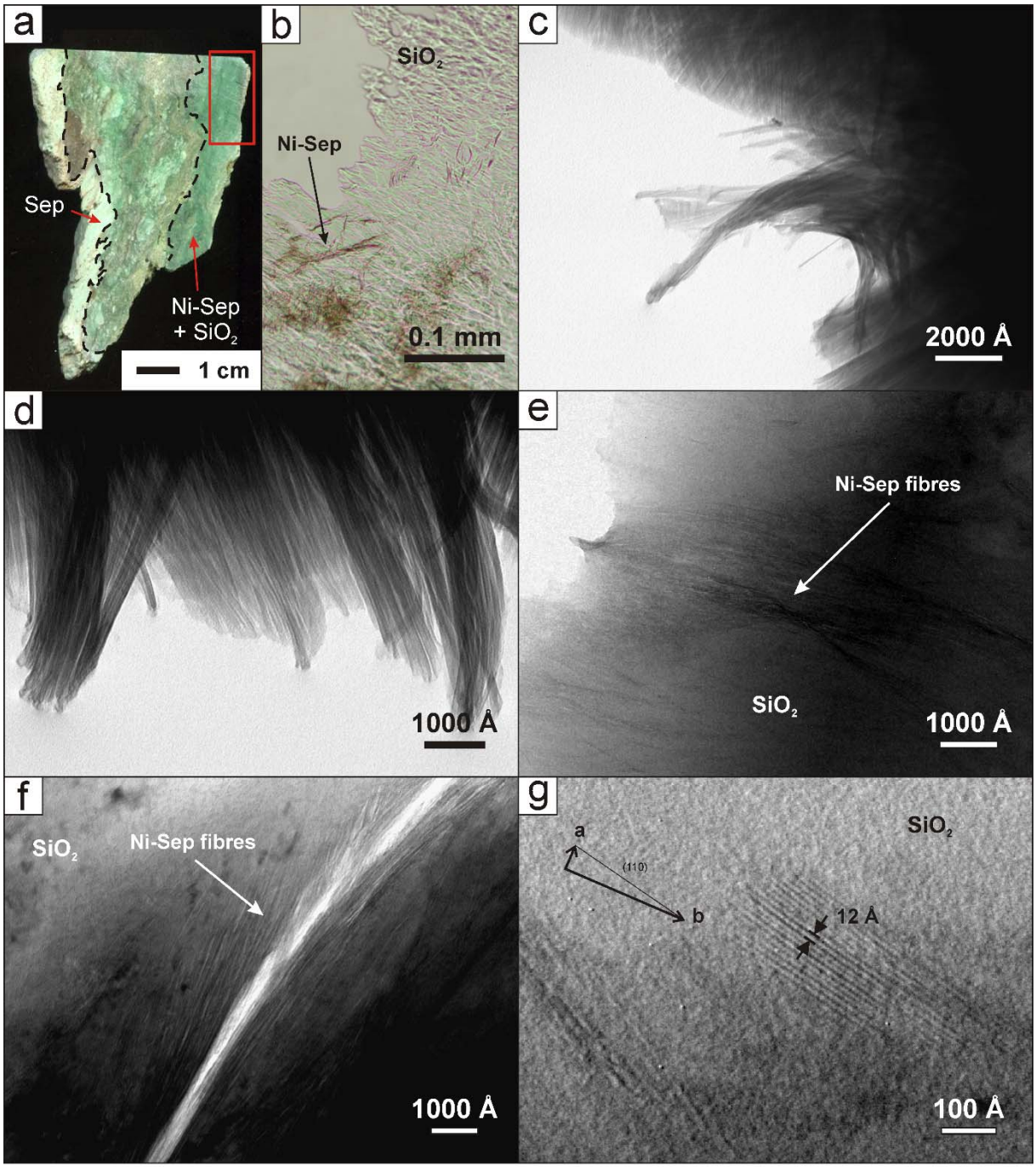

FIGURE. 5.5. Sepiolite-falcondoite (type V) as seen under the TEM (specimen GAR-7v): **a**) image of the sample, the specimen was detached from area in the red rectangle; **b**) detail of the hole in the grid under the optical microscope (plane polarised light); **c-d**) detailed view of criss-cross sepiolite ribbons of the sample (in a Philips CM20, CIC-UGR); **e-f**) low magnification image of the specimen showing sepiolite ribbons in a matrix of amorphous silica (**e:** obtained in a Jeol 2010, CCiT-UB; **f:** in a Philips CM20, CIC-UGR); **g**) detail of 12 Å fringes of a Ni-sepiolite ribbon oriented normal to the beam, in the matrix of amorphous silica (Philips CM20, CIC-UGR).

found and only one basal and one longitudinal sections of chrysotile tubes were observed in the specimen. Similar features involving ~7 Å and ~10 Å structures were observed in a garnierite from Oregon (18.6 wt.% NiO, talc fraction = 27 %) by Uyeda *et al*. (1973). These values differ from those of the type III garnierite (29–50 wt.% NiO and average talc fraction of 47 %, Villanova-de-

Benavent *et al*., 2014a). Garnierites from New Caledonia shown by Pelletier (1983) and references therein also displayed comparable features.

5.1.4. Type IV garnierite

The specimen containing Ni-kerolite-pimelite garnierites is very homogeneous, as it consists uniquely of sets of superimposed and/or plaited, thin, apparent lamellae with two to six basal spacings of 9.5-9.8 Å (**Fig. 5.4c-f**), confirmed by the absence of ~7 Å fringes in this specimen. Identical textures were observed in 10 Å-type garnierites from Brazil by Esson & Carlos (1978), in which no other crystalline phases were detected either. These Brazilian garnierites under the optical microscope display botryoidal features and coexist with silica, like type IV garnierites (Villanova-de-Benavent *et al.*, 2014a). The small particle size, together with the wide and diffuse rings observed in the electron diffraction patterns (typical of a random polycrystalline pattern), suggest that the sample may have low crystallinity (**Fig. 5.4g**).

5.1.5. Type V garnierite

The obtained TEM bright field images demonstrate the presence of Ni-rich sepiolite roughly oriented in fine ribbons with lengths above several hundreds of nanometres (**Fig. 5.5c-d**) and frequently enclosed within an amorphous silica matrix (**Fig. 5.5e-f**). The high magnification image in **Fig. 5.5g** shows a normal section of the fibre with the well defined (110) crystalline planes. This image allows measuring the 12 Å spacing typical of sepiolite-falcondoite (Post *et al*., 2007; Tauler *et al*., 2009).

5.2. MINERAL CHEMISTRY (AEM)

The composition of garnierite-forming minerals obtained by AEM is represented in **Figure 5.6**, compared to previous analyses obtained by EMP (Villanova-de-Benavent *et al*., 2014a), and in **Table 5.2**. The identification of the mineral species based on the lattice fringe spacing and that from the chemical composition were coherent. In addition, to increase the number of analysis of each mineral species, additional analyses were obtained on particles deposited on copper grids (e.g. López Munguira & Nieto, 2000; Abad *et al*., 2001).

In general, Al is virtually absent in the Falcondo garnierites. Serpentine particles have low Ni, up to 0.2 apfu in type I and 0.6 apfu in type II; and yield remarkable amounts of Fe, 0.1-0.4 apfu in type I and up to 0.3 in type II garnierites. Type III compositions are actually mixed analyses of lizardite lamellae and the talc-like phase, with Ni contents ranging from 2.7 to 3.3 apfu and Al and Fe below detection limits. Talc-like analyses from all the studied garnierite types yield highly variable Ni contents, between 1.2 to 2.3 apfu (1.7 on average), and Al and Fe are generally low (up to 0.13 apfu Al, 0.03 on average; and up to 0.04 apfu Fe, <0.01 on average). In addition, Ni content in talc-like particles increases gradually from type I to type IV garnierites (**Fig. 5.6**).

AEM results plot within or near the compositional fields previously obtained through EMP in the same samples (Villanova-de-Benavent *et al*., 2014a), although type III mixtures and some analyses of type II serpentines still deviate towards the kerolite-pimelite series. Even if in most cases it was impossible to obtain pure analysis of the constituent phases of the mixture due to the very small size of the individual packets (e.g. **Fig. 5.3c, d, e**), the AEM spot size of tens of nanometres versus the EMP spot size of one micrometre gives unique results of the preferential partitioning of Ni in talc-like particles rather than in the associated serpentines. In summary, the higher spatial resolution of AEM analyses allowed better discrimination than EMP analyses, with slight deviations from the average composition obtained by EMP toward the respective constituent end-members (**Fig. 5.6**).

Finally, the EDS spectra in type V garnierite enabled distinction of Ni-sepiolite ribbons from the surrounding matrix. The Ni-sepiolite fibres show a distinctive Ni and Mg content in addition to Si and O, and the presence of Si seems to be related not only with sepiolite but also with amorphous SiO_2 matrix. Ni contents varied from 1.2 to 2.2 apfu and Al and Fe were below detection limits.

5.3. DISCUSSION

5.3.1. Nanotextural variability of garnierite from the Falcondo Ni-laterite

As stated by Brindley (1978), most garnierites are a mixture of serpentine-like and talc-like phases, and previous TEM imaging studies reported the occurrence of some garnierites as intimate mixtures of ~7 and ~10 Å phases at the nanometre scale (e.g. Uyeda *et al*., 1973; Poncelet *et al*., 1979; Soler *et al*., 2008). Most garnierites from the Falcondo Ni-laterite deposit consist actually of mixtures of different relative proportions of serpentine (7.2-7.4

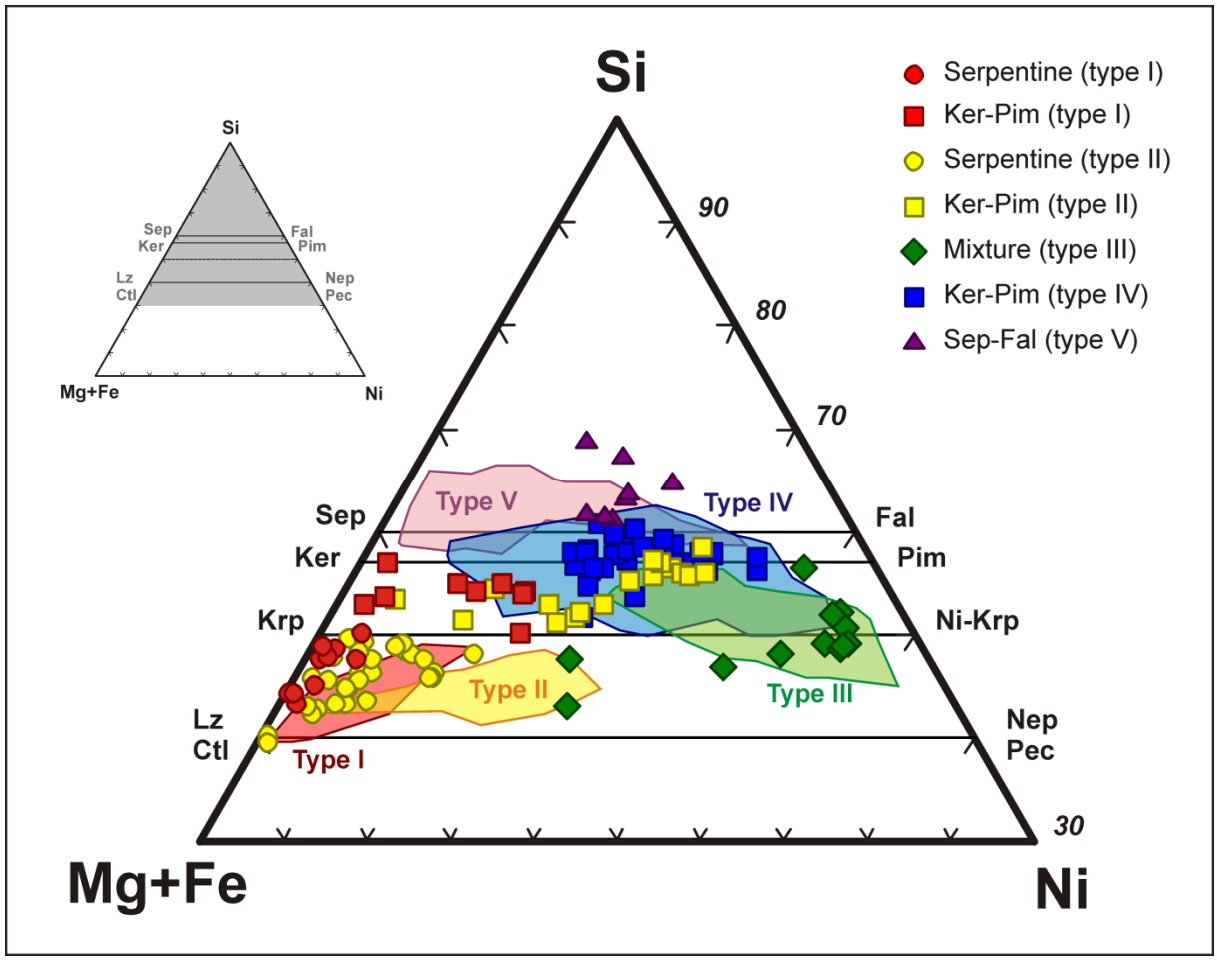

FIGURE. 5.6. Triangular diagram comparing AEM (circles, squares and triangles) with previous EMP (fields). Compositional fields from **Chapter 4**. Abbreviations from Whitney & Evans (2010) except falcondoite (Fal), kerolite (Ker), pimelite (Pim), pecoraite (Pec). Both the AEM on ion-thinned grids and grids with suspended powders are plotted, with no significant differences.

Å) and talc-like (9.2-9.7 Å) phases (kerolite-pimelite) (**Figs. 5.1-5.5**). TEM imaging distinguished a wide variety of textures and mineral species of the serpentine minerals in the different garnierite mixtures (chrysotile tubes in type I, polygonal serpentine in type II, lizardite lamellae in type III). In addition, TEM revealed the presence talc-like particles in all the serpentine-bearing garnierites even when these had not been detected by XRD, as in type I, probably due to their small quantity and low crystallinity.

Another characteristic feature is that 7.2-7.4 Å fringes occurred in large numbers, whereas 9.2-9.7 Å occurred in smaller sets (as stated by Uyeda *et al.* 1973), suggesting a lower crystallinity of talc-like phases, which is coherent with their broad peaks, or absence of them, in powder X-ray diffraction (Villanova-de-Benavent *et al.*, 2014a) and with the diffuse and weak ring-shaped electron diffraction patterns in this study. Kato (1961) also reported that talc-like garnierites from New Caledonia produced ring-shaped SAED patterns whereas serpentine-like phases gave single crystal diffraction patterns with well-defined spots. Furthermore, Pelletier (1983) (and references therein) distinguished the electron diffraction pattern of the talc-willemseite, with a regular structure, from the kerolite-pimelite, showing concentric circles. Other studies reported unspecified disordered regions in the TEM photomicrographs as well (e.g. Uyeda *et al.*, 1973; Brindley, 1978; Esson & Carlos, 1978).

Such low crystallinity of the talc-like phase could be related to specific conditions, such as very low temperature, high water availability and/or high growth rate during crystallization. The fact that the 10 Å fringes are less regularly defined than the 7 Å ones, could be also explained by a variable degree of hydration of their interlayers (Brindley & Hang,

TABLE 5.2. Representative normalised AEM analyses performed on Falcondo garnierites in atoms per formula unit (apfu).

Sample	Type I (Srp) LC-101 serp 1-2	Type I (Srp) LC-101 serp 1-5	Type I (Srp) LC-101 serp 1-8	Type I (Tlc) LC-101 serp 1-10	Type I (Tlc) LC-101 serp 1-11	Type II (Srp) LC-100B-Serp-6	Type II (Srp) LC-100B-Serp-7	Type II (Srp) LC-100B-Serp-8	Type II (Tlc) LC-100B-2 (SERP)-4	Type II (Tlc) LC-100B-2 (SERP)-14
Oxygens formula	14	14	14	22	22	14	14	14	22	22
Mg	2.814	2.050	2.538	2.391	2.117	2.117	2.391	2.440	1.484	1.009
Al	0	0	0	0	0	0.506	0.418	0.405	0	0.054
Si	1.876	2.251	2.109	3.897	3.858	1.887	1.904	1.893	3.908	3.910
K	0	0	0	0	0	0.012	0	0	0	0
Ca	0	0	0	0	0	0	0	0	0	0
Cr	0	0	0	0	0	0	0	0	0	0
Mn	0	0	0	0	0	0	0	0	0	0
Fe2+	0.397	0.235	0.162	0.159	0.072	0.023	0.012	0.012	0.018	0.018
Ni	0.036	0.213	0.081	0.655	1.095	0.322	0.163	0.155	1.683	2.072
∑Octa	3.247	2.498	2.781	3.206	3.284	2.462	2.566	2.607	3.184	3.099
∑Tetra	1.876	2.251	2.109	3.897	3.858	2.393	2.322	2.298	3.908	3.964

Sample	type III GAR-2.3B-1	type III GAR-2.3B-2	type III GAR-2.3B-6	type IV LC-100B-4 (TLC)-2	type IV LC-100B-4 (TLC)-5	type IV LC-100B-4 (TLC)-12	type V GAR-7v-1	type V GAR-7v-5	type V GAR-7v-8
Oxygens formula	22	22	22	22	22	22	32	32	32
Mg	1.273	0.590	0.438	1.440	1.494	1.725	1.744	1.158	1.739
Al	0	0	0	0	0	0	0	0	0
Si	3.509	3.611	3.612	3.997	4.015	4.026	6.193	6.277	6.509
K	0	0	0	0	0	0	0	0	0
Ca	0	0	0	0	0	0	0	0	0
Cr	0	0	0	0	0	0	0	0	0
Mn	0	0	0	0	0	0	0	0	0
Fe2+	0.036	0	0	0	0	0	0	0.103	0	0
Ni	2.673	3.188	3.338	1.566	1.476	1.222	1.870	2.186	1.242
∑Octa	3.982	3.777	3.776	3.007	2.971	2.948	3.615	3.447	2.981
∑Tetra	3.509	3.611	3.612	3.997	4.015	4.026	6.193	6.277	6.509

1973; Uyeda *et al*., 1973) and/or possible volatilization phenomena under the TEM vacuum.

Finally, sepiolite-falcondoite occurs as an independent phase, never mixed with serpentine nor talc-like garnierites. It displays the characteristic elongated ribbon shape of sepiolite, commonly related to amorphous silica and/or quartz, but has a remarkably higher Ni content (26.82 wt.% NiO) when compared to sepiolites examined under TEM in other localities (maximum 3.28 wt.% NiO in Indonesia; Kuhnel *et al*., 1978).

5.3.2. Preferential Ni concentration in the talc-like structure

According to AEM, talc-like phases yield higher Ni concentrations than serpentine, which is coherent with the good correlation between Ni content and the talc fraction in the garnierites from Falcondo, as suggested by Galí *et al*. (2012) and Villanova-de-Benavent *et al*. (2014a), and by Soler *et al*. (2008), in the Loma de Hierro Ni-laterite (Venezuela). The higher resolution of the AEM with respect to EMP allowed distinguishing the serpentine particles from the kerolite-pimelite lamellae (**Fig. 5.6**), despite being difficult to obtain pure, single-phase analyses of talc-like or serpentine in type III. Therefore, the distribution of Ni between serpentine- and talc-like in type III could not be well established because of its finer particle size.

Despite Uyeda *et al*. (1973) stating that there was no correlation between Ni content and morphology of the particles under TEM, and between proportions of platy and elongated particles and the number of serpentine-like and talc-like layers (equivalent to serpentine or talc fraction, respectively), other studies reported that Ni is mostly concentrated in talc-like phases (e.g. Esson & Carlos, 1978; Poncelet *et al*., 1979). Besides, Vitovskaya & Berkhin (1968) also showed some low-magnification images and electron diffraction patterns of what they described as Mg- and Ni-bearing "kerolites" (actually garnierite mixtures). They identified typical tiny clinochrysotile tubes in Mg-"kerolite" (consisting predominantly of serpentine with Ni below detection limit), and scales with tiny tubes of clinochrysotile in the Ni-"kerolite" (mostly a 10 Å mineral with 11.32 wt.% NiO). Consequently in this case Ni was also related to a 10 Å phase. Furthermore, Poncelet *et al*. (1979) showed by EMP analyses and by heating experiments that most of the nickel was concentrated in the octahedral layer of the 10 Å phase, and not homogeneously distributed in the octahedral layer of both the 7 Å and 10 Å. During these experiments, metallic Ni particles were deposited onto the 10 Å flakes and rarely onto the serpentine fibres after heating the sample. In addition to these observations and interpretations, our AEM data confirm that the Ni is preferably contained in the talc-like phase. Possibly, the TOT talc structure is more likely to host Ni than the TO serpentine structure, as demonstrated by the equilibrium constants of the simultaneous precipitation of Ni-serpentine and kerolite-pimelite (Galí *et al*., 2012).

AEM results of garnierites from the Falcondo Ni-laterite showed that Ni concentration in serpentine is lower than in the talc-like particles, and always below the 50% of the total elements in octahedra coordination. Therefore, neither népouite nor pecoraite, the Ni analogues of lizardite and chrysotile respectively, are found in the garnierites from the Falcondo Ni-laterite deposit. However, the presence of népouite and pecoraite is widely reported in other localities. In particular, népouite has been extensively studied in New Caledonia (e.g. Brindley & Wan, 1975; Wells *et al*., 2009 and references therein). One possible explanation for the different mineralogy between New Caledonian and Dominican Ni-laterites is the lithology of the primary ultramafic rocks. In New Caledonia, the protolith is mainly harzburgite and dunite (e.g. Pelletier, 1983, 1996), whereas in the Dominican Republic the protolith is mostly clinopyroxene-rich harzburgite and lherzolite, commonly intruded by microgabbro and dolerite dykes (e.g. Marchesi *et al*., 2012). The higher pyroxene content may imply a greater availability of silica in the Falcondo Ni-laterite deposit, leading to the preferential formation of talc rather than serpentine during weathering.

When examined under TEM, népouite usually occurs as highly crystalline plates (34.8 wt.% NiO, Montoya & Baur, 1963; 47.6 wt.% NiO, Manceau & Calas, 1985), whereas pecoraite develops coils and spiral shapes with three to five revolutions about the spiral axis (Faust *et al*., 1969, 1973; Milton *et al*., 1983). In contrast, the serpentine particles in Falcondo present larger diameters and lengths than the Ni-dominant counterparts described in the literature. Roy & Roy (1954) and Milton *et al*. (1983) suggested that the substitution of Mg by Ni in chrysotile gives rise to non-tubular but also not well formed, platy crystals. The Ni

substitution probably prevents the tubes to grow up to several hundreds of Å and to develop well rounded spirals or concentric tubes. Accordingly, despite that the serpentine particles in type III were not analysed by AEM due to the small particle size, the possibility of these serpentine lamellae yielding higher Ni contents than the chrysotile tubes and polygonal serpentine in types I and II cannot be discarded.

5.3.3. The formation of garnierites in the Falcondo Ni-laterite

Low magnification and high resolution images are fundamental to understand the genetic relationships between serpentine (in most cases, polygonal fibres) and Ni-rich talc-like phases. The talc-like lamellae are observed inside the serpentine central hole (**Fig. 5.7a, b, e**), surrounding the serpentines, forming at the very edges of the particles (**Fig. 5.7a, c, d, f**) and at the boundaries between adjacent sectors of the largest polygonal serpentines (**Fig. 5.7e, f**). In addition, HRTEM details indicate that, at the reaction front, the (001) talc-like planes are parallel to the 001 serpentine ones. All these textural evidences suggest that the talc-like phase forms after serpentine, taking advantage of high stress sites, such as the outer rims (where the (001) basal planes of serpentine are bent), the fibre cores (highest layer curvature), and the intersector boundaries. When replacement of serpentine by talc is more advanced, sectors become fully pseudomorphed by talc-like lamellae (**Fig. 5.7g, h**) and talc-like lamellae may develop rounded aggregates, mimicking the rounded shapes of former serpentine particles (**Fig. 5.7i, j**). It is worth noting that these poorly crystalline, talc-like layers are bent and characterized by extremely wide interlayer partings, giving rise to a highly porous nanotexture (**Fig. 5.4d, e; 5.7h**).

The overall data indicates that the formation of the successive phases in the garnierite mixtures may be explained by an early formation of serpentine tubes. The diameter of the serpentine cores in type II is comparable to the outer diameter of narrow chrysotile tubes in type I. This may indicate that the diameter of the chrysotile increases in size until its curled structure is unstable. Then it is transformed into polygonal serpentine while preserving a cylindrical core, which may more likely be altered by later dissolution-precipitation than polygonal sectors. The serpentine particles are subsequently replaced by kerolite-pimelite, starting from high stress sites and structural discontinuities, such as cores, rims and contact between sectors. The final product is possibly a garnierite formed exclusively by talc-like lamellae (**Fig. 5.8**).

The later formation of kerolite-pimelite from serpentine particles is in accordance to the garnierite precipitation model proposed by Galí *et al*. (2012). This model is based on that, in an Al-free system such as the Falcondo laterite profile, the stability of serpentine, kerolite–pimelite or sepiolite–falcondoite is mainly controlled by the silica activity. As a result, the ideal formation of the Ni ore occurs as a successive precipitation of mineral phases progressively enriched in Ni and Si, because silica activity increases with time and through the profile. Thus, the first garnierite-forming phase to precipitate is serpentine, then followed by kerolite–pimelite, and eventually by sepiolite–falcondoite and sepiolite–falcondoite with amorphous silica and/or quartz (Galí *et al*. 2012).

5.4. FINAL REMARKS

This TEM study including low magnification and high magnification imaging, electron diffraction, and AEM chemical analyses concluded that:

The five types of garnierites present distinctive characteristic features at the nanometre scale, as seen under TEM. Most garnierites consist of an ultrafine mixture of serpentine and a talc-like phase, but nanotextures and the relative amounts of serpentine and talc-like particles are variable from sample to sample.

Serpentine occurs as chrysotile tubes, polygonal serpentine and lizardite lamellae, and in general is more crystalline than the associated talc-like particles. It is remarkable that all garnierite samples contained at least a small portion of talc-like lamellae, even when this phase was not detected by XRD, due to its low crystallinity and low abundance. These particles, which may be the only component of garnierites, are in fact minerals of the kerolite-pimelite series, a talc-like phase with extra water in their structure and showing an expansion of d_{001} spacing from 9.2 (talc) to 9.7 Å.

AEM data confirm that Ni is mostly concentrated in kerolite-pimelite instead of in serpentine particles. Low magnification and HRTEM images established an insight of the mechanisms by which Falcondo garnierites are formed, showing the preferential replacement of

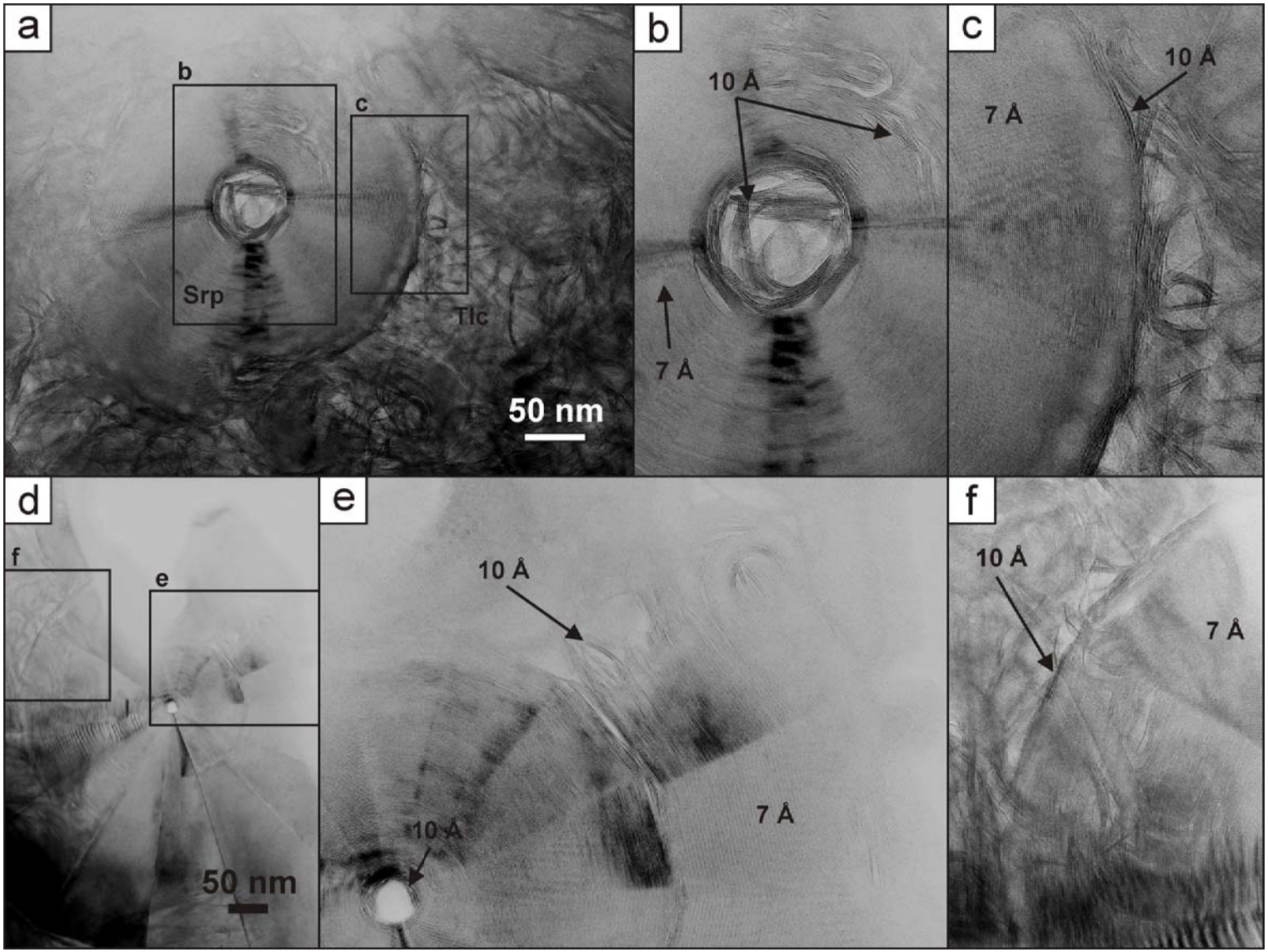

FIGURE 5.7. Replacement textures between Ni-phyllosilicates: **a**) sectored serpentine being replaced by talc-like lamellae, with talc-like lamellae inside the serpentine core (**b**) and growing from the serpentine edges (**c**) (sample LC-100AB-5); **d**) large 15-sectored polygonal serpentine, showing talc-like lamellae inside the core and at the edges of sectors (**e**), and at the border (**f**) (sample LC-100AB-5). All these images were obtained in a Jeol 2010 (UniSi).

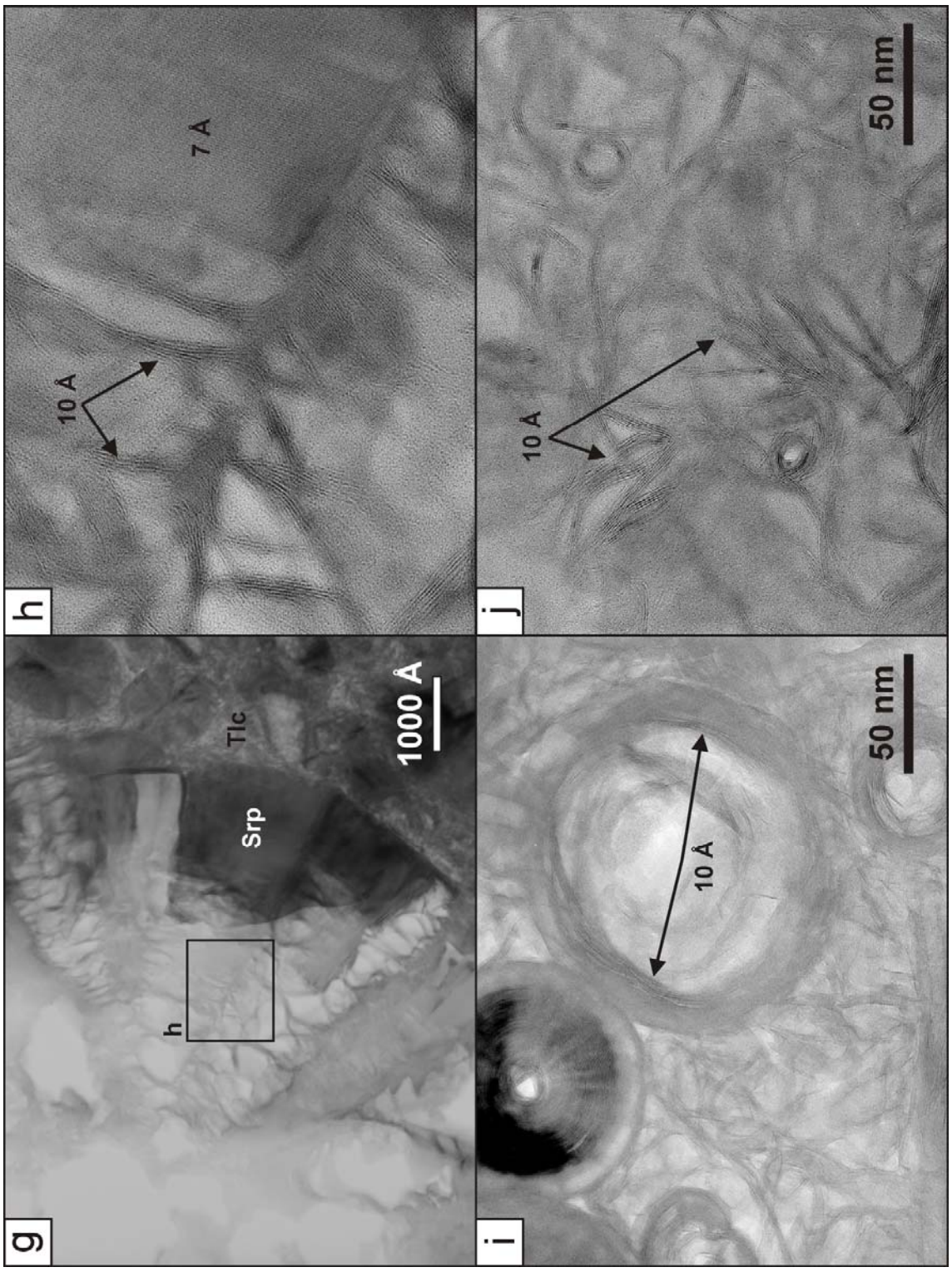

FIGURE 5.7. (CONTINUED). **g)** polygonal serpentine being altered to talc-like lamellae; **h)** detail of **(g)** (sample 09GAR-2.1); **i-j)** rolled talc-like lamellae recording textures of former serpentine particles (**i**: sample 09GAR-2.1; **j**: LC-100AB-5). All these images were obtained in a Jeol 2010 (UniSi).

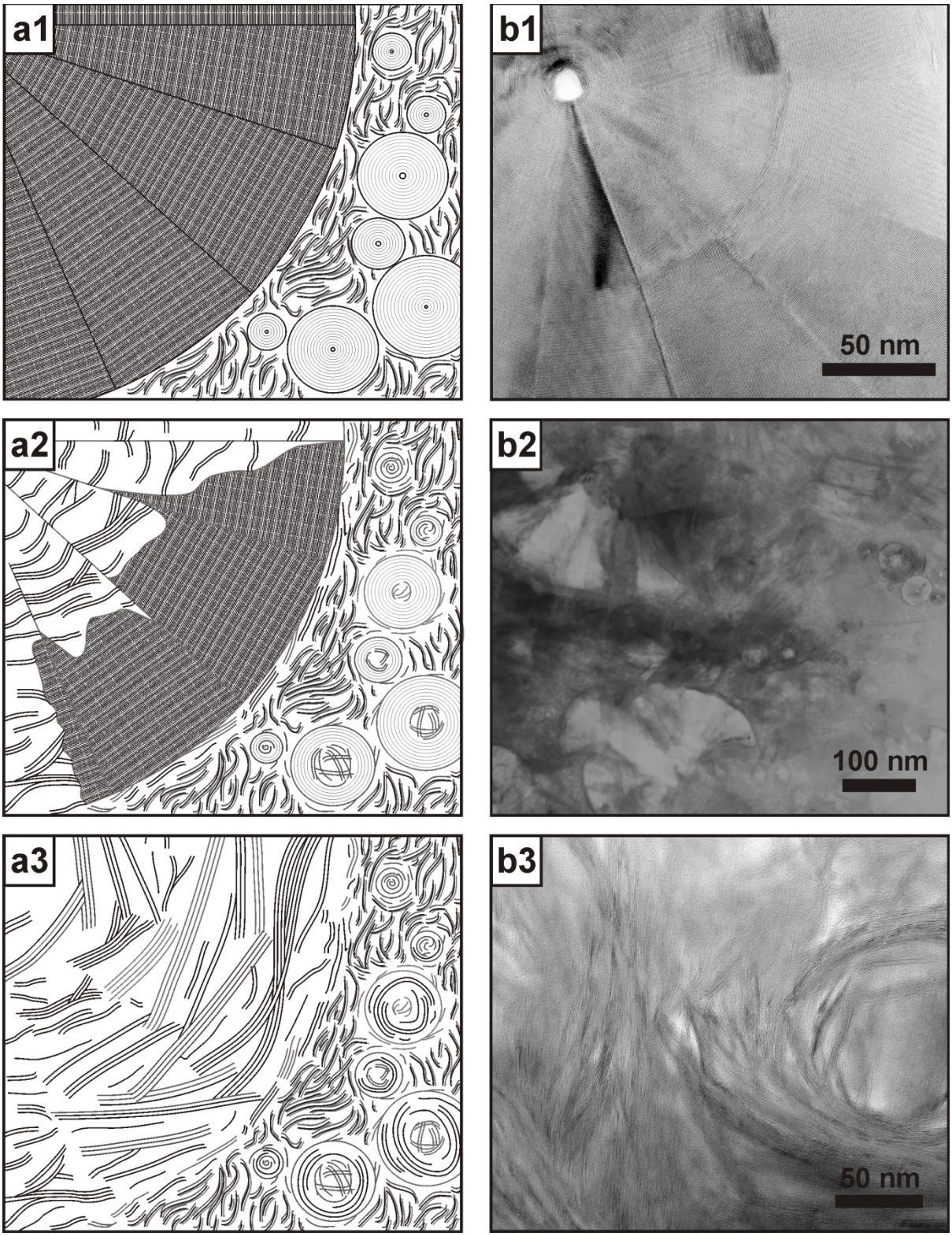

FIGURE 5.8. Replacement model which may explain the formation of Ni-enriched talc-like (kerolite-pimelite) lamellae from the alteration of Ni-poor serpentine particles (**a1-a3**) and HRTEM images representative of each precipitation stage (**b1-b3**): early formation of polygonal serpentine and chrysotile tubes (**a1, b1**), which are subsequently replaced by talc-like lamellae mainly in the higher stress sites (inner cores, outer rims, borders between sectors) (**a2, b2**), leading to a complete replacement of serpentine particles by talc-like, leaving some rolled and curved talc-like lamellae as remnants of the former serpentine features (**a3, b3**). The HRTEM images were obtained in a Jeol 2010 (UniSi): sample LC-100AB-5 (**b1**), sample 09GAR-2.1 (**b2)**, sample LC-100AB-4 (**b3**).

serpentine by kerolite-pimelite at high-stress sites in the serpentine structure, such as the inner walls of cores, outer rims and inter-sector boundaries.

The fact that Ni-enriched kerolite-pimelite lamellae replace Ni-poor serpentine particles is coherent with previous mineralogical, textural, geochemical and thermodynamical studies, and may explain the process of progressive Ni-enrichment within garnierites and along the profile.

6. CHARACTERISATION BY MICRO-RAMAN SPECTROSCOPY

Micro-Raman spectroscopy represents an easy, trustworthy and non-destructive method that can be used to distinguish the different garnierite-forming minerals *in situ*, and therefore, to differentiate the various garnierite types described in the previous chapters, even when samples are very fine grained, consist of intimate mixtures at the nanometre scale and/or are poorly crystalline. This Chapter presents the analyses obtained by micro-Raman spectroscopy performed on Falcondo garnierites with well constrained mineralogy and chemistry (see **Chapters 4** and **5**). In the discussion, the resulting Raman spectra were compared to those obtained in the Mg-end members of the garnierite-forming minerals (namely lizardite, chrysotile, talc and sepiolite, see **Appendix A2**), as well as to a collection of data from the literature.

The samples were analysed using four laser wavelengths: 325 nm (near ultraviolet), 532 nm (green), 785 nm (red) and 1064 nm (near infrared). The use of the near infrared laser reduced the fluorescence and sample heating effects (Colthup *et al*., 1990; Groppo *et al*., 2006), and the 532 nm laser also produced satisfactory results in most samples. Therefore, only the patterns obtained at 532 and 1064 nm will be included.

In this chapter the description and discussion of the Raman spectra is divided into: a) the low spectral region (100-1000 cm^{-1}) and ii) the high spectral region (>3000 cm^{-1}). The first is mostly associated to the vibration of Si-O and metal-O bonds, whereas the second is related to the stretching mode of OH and water in the phyllosilicate structures (e.g. Wang *et al.*, 2002).

A list of the studied samples is presented in **Table 6.1**, which includes the mineralogy obtained by XRD and TEM, as well as their average structural formulae calculated from EMP analyses. **Figure 6.1** shows the Raman spectra of the five garnierite types described in **Chapters 4** and **5**, obtained with the 1064 nm laser; whereas **Figure 6.2** presents the spectra of the different garnierite types compared to those obtained in Ni-free phyllosilicates both obtained with the 532 nm laser. **Figure 6.3** is a Raman map performed in a representative area containing serpentine- and kerolite-dominant garnierites and saprolite fragments. The Raman bands detected in this study and their respective assignments found in literature are displayed in **Table 6.2**, an extended version of this table being included in the **Appendix A3**.

6.1. MICRO-RAMAN SPECTRA OF GARNIERITES IN THE LOW SPECTRAL REGION (100-1000 cm^{-1})

6.1.1. Type I garnierite

Type I garnierite presents strong bands at 226-231 cm^{-1} 383-386 and 687-689 cm^{-1} and weak bands at 343, 619 cm^{-1}. In addition, two shoulders were observed at 364 and 668 cm^{-1} using the 1064 nm laser (**Fig. 6.1a, 6.2a**, **Table 6.2**).

6.1.2. Type II garnierite

This Ni-bearing mixture of serpentine and minor kerolite-pimelite displays intense bands at 383-384 and 687-689 cm^{-1}. The strong bands at 186 and 231 cm^{-1} with the 1064 nm laser are observed as weak bands at 179 and 230 cm^{-1} with the 532 nm laser, respectively. The shoulders at 345 and 368 cm^{-1} are only found with the 1064 nm laser, and the band at 271 cm^{-1} is exclusive of the 532 nm laser pattern (**Fig. 6.1b, 6.2b**, **Table 6.2**).

6.1.3. Type III garnierite

This high Ni mixture of serpentine and kerolite-pimelite shows very strong bands at 183-184, 679-680 cm^{-1}; and a less intense band at 366-368 cm^{-1}. Another peak at 209 cm^{-1} was produced by the 1064 nm laser and at 271 cm^{-1} by the 532 nm laser (**Fig. 6.1c, 6.2c**, **Table 6.2**).

6.1.4. Type IV garnierite

In kerolite-pimelite, strong bands were observed at 184-187 and 674-676 cm^{-1}, and less intense bands at 383-385 cm^{-1}. Additional weaker bands at 364, 640 and 823 cm^{-1} were observed using the 1064 nm laser (**Fig. 6.1d, 6.2d**, **Table 6.2**).

6.1.5. Type V garnierite

In general, the Raman spectra of Ni-poor sepiolite and falcondoite are similar and do not display major

TABLE 6.1. List of samples analysed by micro-Raman spectroscopy, including their mineralogy, and mineral chemistry obtained by means of XRD; EMP and TEM. For the XRD characterisation of the Ni-free phyllosilicates see **Appendix A2**.

Type / mineral	Locality	Sample	Mineralogy		Structural formula [number of analyses averaged]
			XRD	TEM	EMP
Type I	Falcondo	LC-101 09GAR-2	serpentine (7.26-7.32 Å)	chrysotile tubes with minor short kerolite-pimelite lamellae	$(Mg_{2.31}Ni_{0.24}Fe_{0.18})Si_{2.16}O_{5.51}(OH)_{3.29}\cdot 0.19H_2O$ [24] $(Mg_{2.34}Ni_{0.48}Fe_{0.15})Si_{2.48}O_{6.27}(OH)_{3.49}\cdot 0.26H_2O$ [16]
Type II	Falcondo	LC-100	serpentine (7.30 Å) + talc (10.20-10.54 Å)	polygonal serpentine and chrysotile tubes in a kerolite-pimelite lamellae matrix	$(Mg_{2.12}Ni_{0.82}Fe_{0.06})(Si_{2.49}Al_{0.08})O_{6.51}(OH)_{3.40}\cdot 0.29H_2O$ [71]
Type III	Falcondo	GAR-2	serpentine (7.40 Å) + talc (10.56 Å)	thick lizardite lamellae and thin kerolite-pimelite lamellae	$(Ni_{2.42}Mg_{0.56}Fe_{0.01})Si_{2.71}O_{6.81}(OH)_{3.28}\cdot 0.36H_2O$ [4]
Type IV	Falcondo	GAR-6 LC-100	talc (9.94-10.14 Å ± 7.34 Å)	kerolite-pimelite lamellae	$(Ni_{1.90}Mg_{1.10})(Si_{3.61}Al_{0.01})O_{9.06}(OH)_{2.40}\cdot 0.81H_2O$ [17] $(Ni_{1.95}Mg_{1.04})Si_{3.69}O_{9.24}(OH)_{2.30}\cdot 0.85H_2O$ [109]
Type V (Ni-sepiolite)	Falcondo	FALC-4	sepiolite (12.07 Å)	sepiolite ribbons	$Mg_{7.02}Ni_{0.51}Fe_{0.12}Si_{12.11}Al_{0.02}O_{15}(OH)_2\cdot 6H_2O$ [16]
Type V (falcondoite)	Falcondo	FALC-3	sepiolite (12.15 Å)	sepiolite ribbons	$Mg_{4.07}Ni_{3.90}Fe_{0.01}Si_{11.91}Al_{0.12}O_{15}(OH)_2\cdot 6H_2O$ [4]
Lizardite	Cornwall, UK	Liz-1	serpentine (7.29 Å)	-	
Lizardite	Elba Island, Italy	Liz-2	serpentine (7.26 Å)	-	$Mg_{2.74}Al_{0.16}Fe_{0.15}Si_{1.90}O_5\ (OH)_4$ [20]
Chrysotile	Huelva, Spain	Cris	serpentine (7.29 Å)	-	$Mg_{2.79}Fe_{0.11}Si_{2.02}O_5\ (OH)_4$ [15]
Talc	León, Spain	Tlc	talc (9.35 Å)	-	$Mg_{2.94}Al_{0.01}Fe_{0.01}Si_{4.01}O_{10}\ (OH)_2$ [8]
Sepiolite	Setcases, Spain	Sep	sepiolite (11.94 Å)	-	$Mg_{3.82}Fe_{0.04}Si_{6.04}O_{15}(OH)_2\cdot 6H_2O$ [15]

differences. Falcondoite presents strong peaks at 196, 673 cm^{-1} and weaker peaks at 334, 385, 640 cm^{-1} (1064 nm; **Fig. 6.1e**; **Table 6.2**). Ni-sepiolite and falcondoite show an intense band at 670-674 cm^{-1} and a weaker one at 193-196 cm^{-1} (532 nm; **Fig. 6.2e,f**; **Table 6.2**). The only remarkable difference between Ni-sepiolite and falcondoite is the band at 482 in Ni-sepiolite, which may correspond to that at 482 cm^{-1} in falcondoite (**Table 6.2**).

It is worth noting that all sepiolite spectra were more resolute at 1064 nm than those obtained at 532 nm, due to the fluorescence effects produced by the use of the green laser (**Figs. 6.1e, 6.2e,f**).

6.2. MICRO-RAMAN SPECTRA OF GARNIERITES IN THE HIGH SPECTRAL REGION (> 3000 cm^{-1})

The high spectral region was measured with the 532 nm laser. A band was detected near 3680 cm^{-1} in most garnierite types, being strong in types I and II and weak in sepiolite-falcondoite. Type III showed two strong bands at 3647 and 3667 cm^{-1}; and type IV a medium intensity band at 3629 and a weak one at 3674 cm^{-1}. As in the low spectral region, Ni-poor sepiolite and falcondoite do not display significant differences at the high spectral region showing consistently a band near 3680 cm^{-1} (**Fig. 6.2**, **Table 6.2**).

6.3. MICRO-RAMAN MAP

The micro-Raman map was performed in an area containing type II and IV garnierites, saprolite serpentine and quarz (**Fig. 6.3a-e**), according to the conditions in **Section 3.8.2**.

Two Raman spectra associated to serpentine were distinguished, one corresponding to the saprolite fragments (in red) and the other to the type II garnierite (in navy blue) (**Fig. 6.3d-e**). Type IV garnierite (kerolite-pimelite) was easily identified as well (in green) (**Fig. 6.3d-e**), with its characteristic zoning visible in the integrated intensity image (**Fig. 6.3c-e**).

6.4. DISCUSSION

6.4.1. Micro-Raman spectra of garnierites in the the low spectral region (100-1000 cm^{-1})

Serpentine bands

The serpentine-dominant garnierites (types I and II) are characterised by the presence of strong bands at ~230, ~385 and ~680 cm^{-1}, and weaker bands and/or shoulders at 343-345, 364-368 and ~620 cm^{-1} (**Figs. 6.1a-b, 6.2a-b**, **Table 6.2**). The peaks at 230 and 385 cm^{-1} can be assigned to either serpentine group minerals or talc, although they are less intense (or even absent) when the garnierite mixtures contain higher amounts of kerolite-pimelite (or when the sample consists uniquely of this phase) (**Figs. 6.1a-d, 6.2a-d**, **Table 6.2**). These two bands are observed in the lizardite and chrysotile reference samples (**Fig. 6.2g-i**), and absent in talc and sepiolite (**Fig. 6.2j-k**, **Table 6.2**). Therefore, the band at 230 is attributed to metal-oxygen (M-O) or O-H-O vibrations, the peak at 343-345 to M-O or SiO_4 bending, the band at 385 to M-O or symmetric SiO_4 vibrations, the peak at 620 to M-O or Si-O or OH-Mg-OH vibrations and the one at 680 to Si-O vibrations, all in serpentine minerals (**Table 6.2**). Apart from this, the band at ~345 cm^{-1} in types I and II could be related to that at 356 cm^{-1} of chrysotile, which is coherent with the mineralogy of these garnierite types observed under TEM (see **Chapter 5**).

The shifted position of the serpentine M-O band to lower wavelengths from 231 cm^{-1} down to 209 cm^{-1} may be correlated with the disappearance of the polygonal serpentines present in types I and II and the development of bended lamellae of serpentine present in type III in agreement with the results obtained by means of HRTEM on equivalent samples (see **Chapter 5**).

In conclusion, the presence of serpentine minerals in the garnierite types I, II and III is shown by the bands at ~230, 340, 620 and 680 cm^{-1}, and when the garnierite consists only of kerolite-pimelite (type IV), all those bands are lacking (**Figs. 6.1a-d**, **Table 6.2**).

Talc-like bands

The occurrence of talc-like particles in the garnierites is stated by the bands at ~185 and ~365 cm^{-1} (**Figs. 6.1b-d, 6.2b-d**, **Table 6.2**). The former is also found in the talc reference sample (**Fig. 6.2j**, **Table 6.2**). Therefore, even though the talc-like was not identified by XRD in type I garnierite, the particles were observed by TEM and can be detected by Raman spectroscopy (shoulder at 364 cm^{-1} in **Fig. 6.1**). Furthermore, two Si-O bands are observed in the range between 668 and 687 cm^{-1}, which are present in all five garnierite types. Both 668-674 and 687 cm^{-1} peaks are observed in type I and II garnierites, the later being more intense in type I.

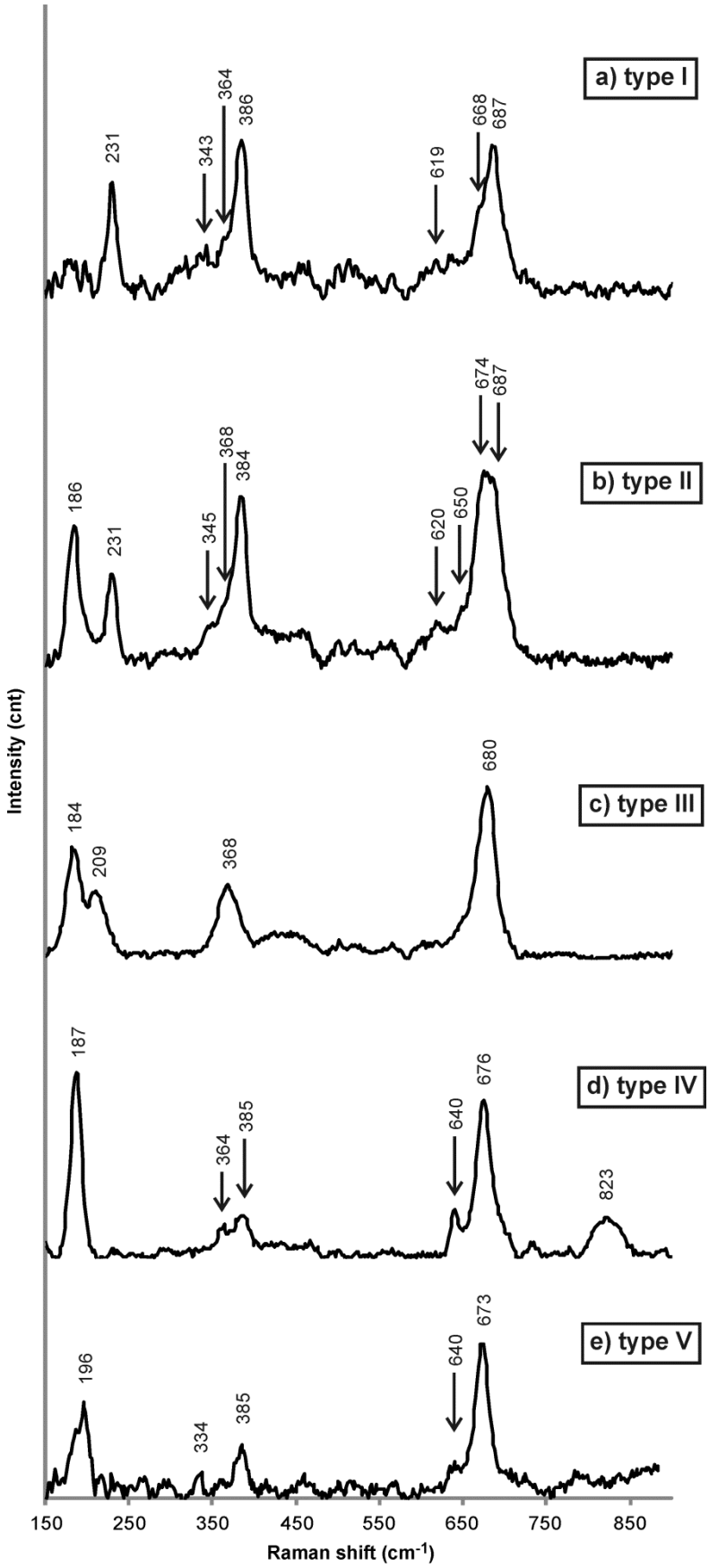

FIGURE 6.1. Micro-Raman spectra of the Falcondo garnierite types described in **Chapter 4** and **5** obtained with the 1064 nm laser: **a**) type I (sample 09GAR-2), **b**) type II (sample LC-100), **c**) type III (sample GAR-2), **d**) type IV (sample GAR-6), **e**) type V (sample FALC-3).

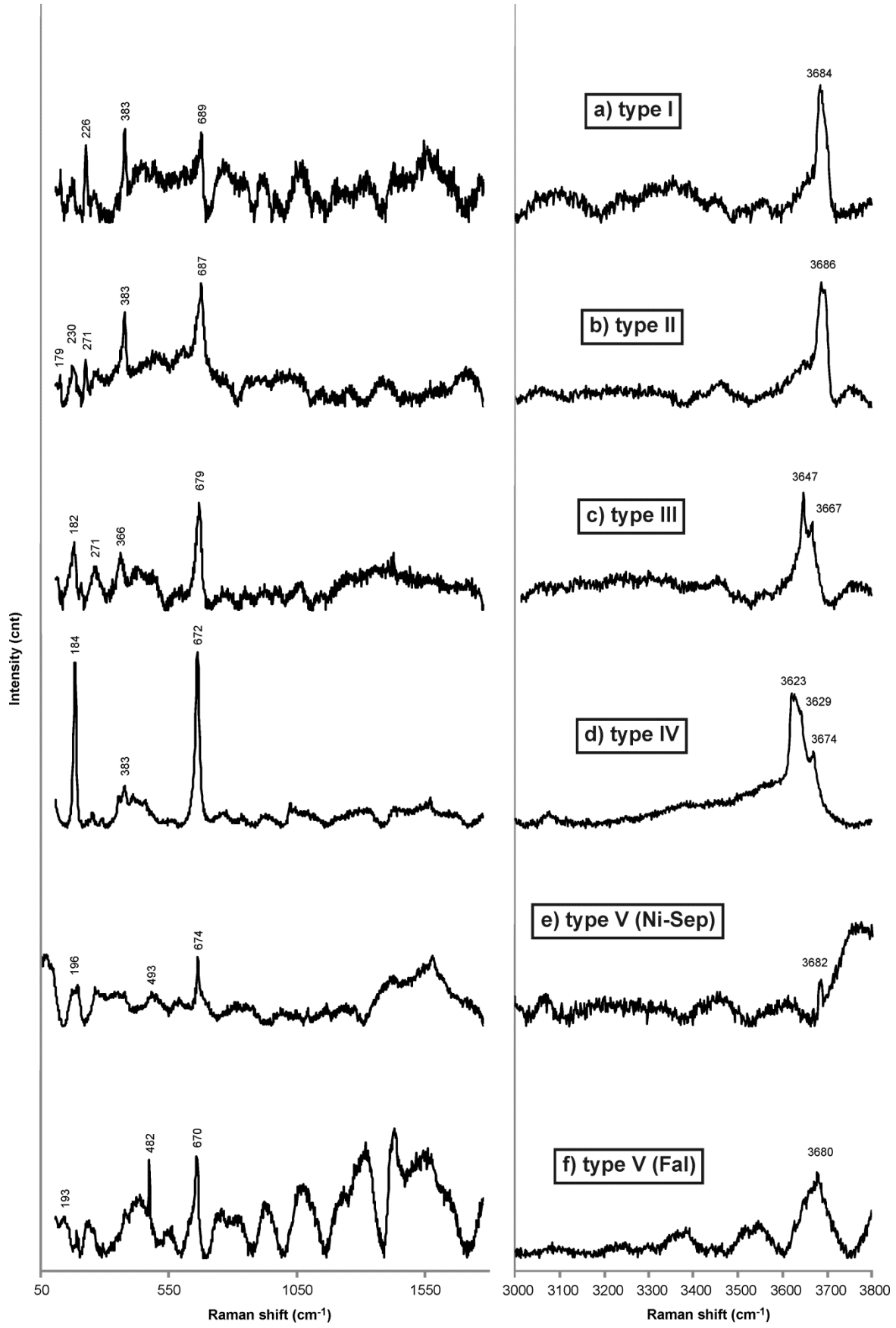

FIGURE 6.2. Micro-Raman spectra of the Falcondo garnierite types described in **Chapter 4** obtained with the 532 nm laser: **a**) type I (sample 09GAR-2), **b**) type II (sample LC-100), **c**) type III (sample GAR-2), **d**) type IV (sample LC-100), **e**) type V Ni-sepiolite (sample FALC-4), **f**) type V falcondoite (sample FALC-3).

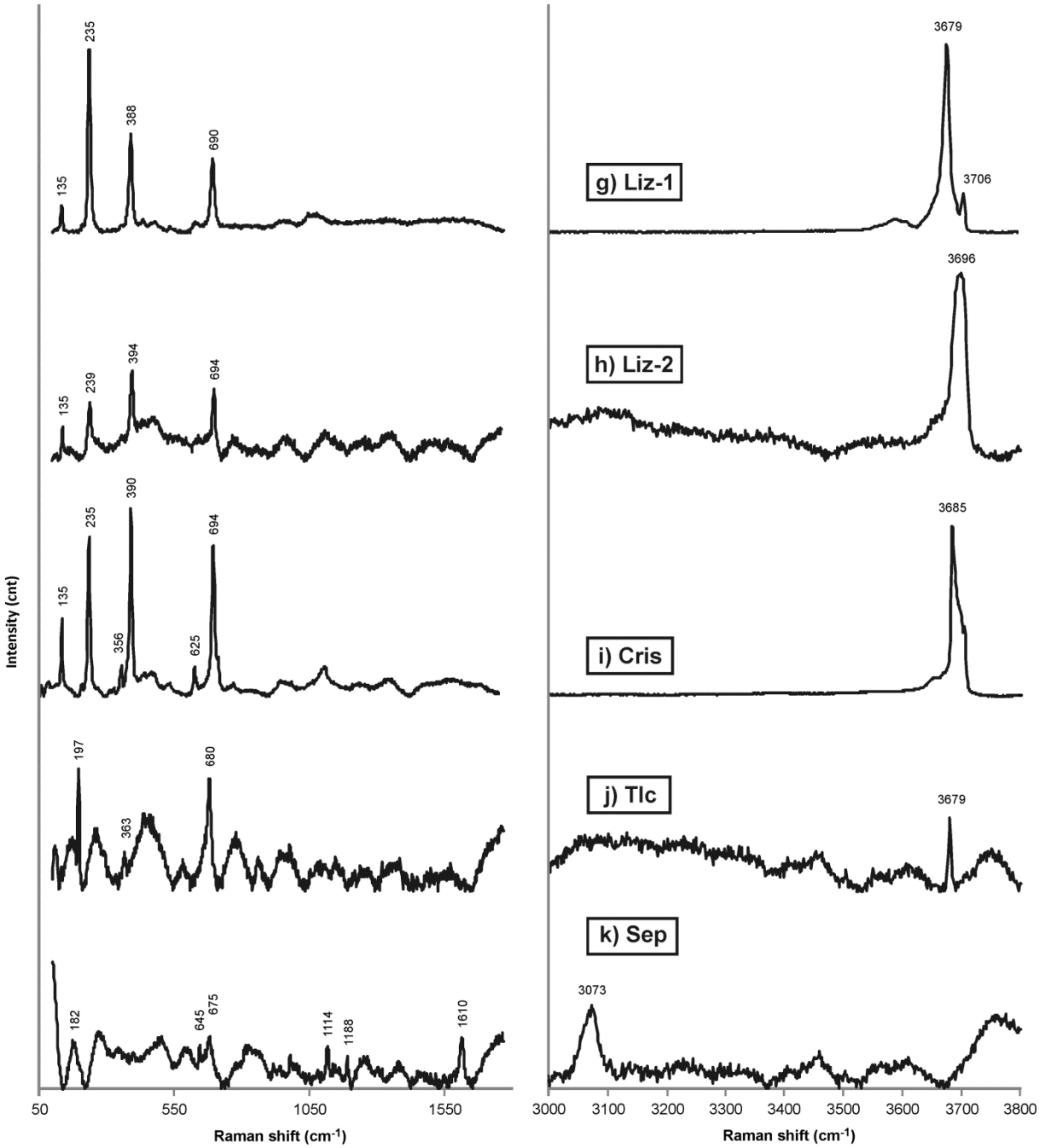

FIGURE 6.2. (CONTINUED). Micro-Raman spectra of the Ni-free phyllosilicate analysed for comparison, obtained with the 532 nm laser: **g**) Liz-1 (lizardite from Lizard, Cornwall), h) Liz-2 (lizardite from Elba Island), i) Cris (chrysotile from Huelva), **j**) Tlc (talc from León), **k**) Sep (sepiolite from Setcases). For the XRD mineral identification of these samples see **Appendix A2**.

However, the peak at 675 cm^{-1} is the only one of this range found in type IV garnierites; and a band halfway, at 680 cm^{-1}, is shown in type III garnierites, the mixture with lower serpentine content (**Figs. 6.1c, 6.2c**), as well as in the talc reference sample (**Fig. 6.2j**, **Table 6.2**). Therefore, the higher Raman band shifts may be characteristic of serpentine minerals, whereas bands at lower Raman shifts may be related to talc-like phases. This is coherent with most of the literature (Blaha & Rosasco, 1978; Rosasco & Blaha, 1980; Kloprogge *et al*., 1999; Rinaudo *et al*., 2003; Groppo *et al*., 2006; RRUFF) (**Table 6.2**).

In contrast to serpentine-dominant garnierites, kerolite-pimelite (type IV garnierite) presents high intensity bands at ~180 and 675 cm^{-1}, and less

intense bands at ~365, 385, 640 and 823 cm^{-1} (**Figs. 6.1d, 6.2d**). The band at ~180 is typical of talc, as reported in the literature (**Table 6.2**). The peak at 365 is assigned to the M-O vibrations and 675 corresponds to O-Si-O bridging/Si-O-Si symmetric stretching in talc. Finally, the broad 823 band may be attributed to Ni-OH deformation (**Table 6.2**). These characteristic talc bands were also observed in type I, II and III garnierites, like the weak bands at 364-368, typical M-O bands for talc, the non-hydrated Mg analogue of kerolite, confirming the presence of low amounts of talc-like particles in the samples. In type II, the new appearing band at 179-186 cm^{-1} is more intense than the band at 230-231 cm^{-1}, and the former decreases slightly in intensity when compared to the same band in type I. This can be indicative of a higher amount of talc than serpentine in the sample for the analysed spot, and a decrease of serpentine in type II when compared to type I (**Figs. 6.1b, 6.2b**). In type III garnierites, the mixture with more kerolite-pimelite than types I and II, the bands are comparable to those detected in the other garnierite types, except for the band at 209 cm^{-1}, which is exclusively related to serpentine (**Fig. 6.2c**, **Table 6.2**).

Sepiolite bands

Finally, sepiolite-falcondoite is easily identifiable by the band at 193-196 cm^{-1} which is lacking in the other garnierite types. The bands at 385, 640 and 673 cm^{-1} in falcondoite are also observed in the other garnierites (**Figs. 6.1e, 6.2e,f**), and the Si-O band (673 cm^{-1}) is present at even lower Raman shifts than in type IV garnierite (675 cm^{-1}) (**Fig. 6.1d**, **Table 6.2**).

In addition, the Ni-bearing sepiolite and falcondoite patterns are similar to that of the Ni-free sepiolite, with bands at 182, 645, 675 cm^{-1} (**Fig. 6.2k**, **Table 6.2**). Bands at about 200, 650 and 1100 cm^{-1} have also been observed in sepiolite by McKeown *et al*. (2002), and a broad peak at around 670 is also seen in the RRUFF database (sepiolite, ID R070311). However, a band at ~250 cm^{-1} is present in both references, but not in any of the samples analysed in this study (**Table 6.2**).

General remarks in the low spectral region

It is difficult to unravel the effect of the Ni content in the Raman spectra of Ni-bearing phyllosilicates in this spectral region. Wang *et al*. (2002) explained the influence of the cations in the octahedral site and the position of the bands in the range <600 cm^{-1} in phyllosilicates. Most Fe-bearing phyllosilicates show a wide, strong band at ~550cm^{-1}, most Al-bearing have a wide, strong peak at ~420, and most Mg-bearing show a strong peak at ~350 cm^{-1}. Therefore, the Ni content in pyllosilicates may have a characteristic Raman effect on the garnierite patterns. However, by comparing the garnierite spectra with the Ni-free serpentine, talc and sepiolite patterns, no significant differences were found which could be attributed to the presence of Ni in the minerals.

Moreover, some conclusions can be extracted from the preliminary results obtained in other Ni-bearing Mg-phyllosilicates, such as the Ni-bearing mineral of the chlorite group, nimite (Villanova-de-Benavent *et al*., 2014d). By comparing the Raman spectrum of nimite with its Mg and Fe equivalents (clinochlore and chamosite, respectively), we observed that peaks in nimite are slightly shifted between the values of clinochlore (higher cm^{-1}) and chamosite (lower cm^{-1}) from the RRUFF database available. Therefore in this case the position of certain Raman bands is a good indicator of the elements in the octahedral site.

Nevertheless, as demonstrated by some specific characteristic bands in the Raman spectra as well as by the Raman map, the five garnierite types could be distinguished.

6.4.2. Micro-Raman spectra of garnierites in the high spectral region (> 3000 cm^{-1})

This region is often assigned in the literature to the OH-stretching in phyllosilicates (Rosasco & Blaha, 1980; Kloprogge *et al*., 1999; Wang *et al*., 2002; Frost et al., 2008). The number of OH peaks, their positions and their relative intensities are controlled by the number and types of OH sites and the types of cation occupancies around OH groups (Wang *et al*., 2002). In particular, the band at ~3640 cm^{-1} was identified in chrysotile (Kloprogge *et al*., 1999; Frost *et al*., 2008), pecoraite (Frost *et al*., 2008). The band at ~3670 cm^{-1} was found in the lizardite from Cornwall (this study), in chrysotile (Kloprogge *et al*., 1999) and talc (Blaha & Rosasco, 1978; Rosasco & Blaha, 1980; this study). The band at ~3680 cm^{-1} was observed in chrysotile (Kloprogge *et al*., 1999; this study). Finally, a band at 3700 cm^{-1} was identified in lizardite (this study), chrysotile and pecoraite (Frost *et al*., 2008) and kerolite (Cathelineau *et al*., 2015) (**Table 6.2**, **Fig. 6.2**).

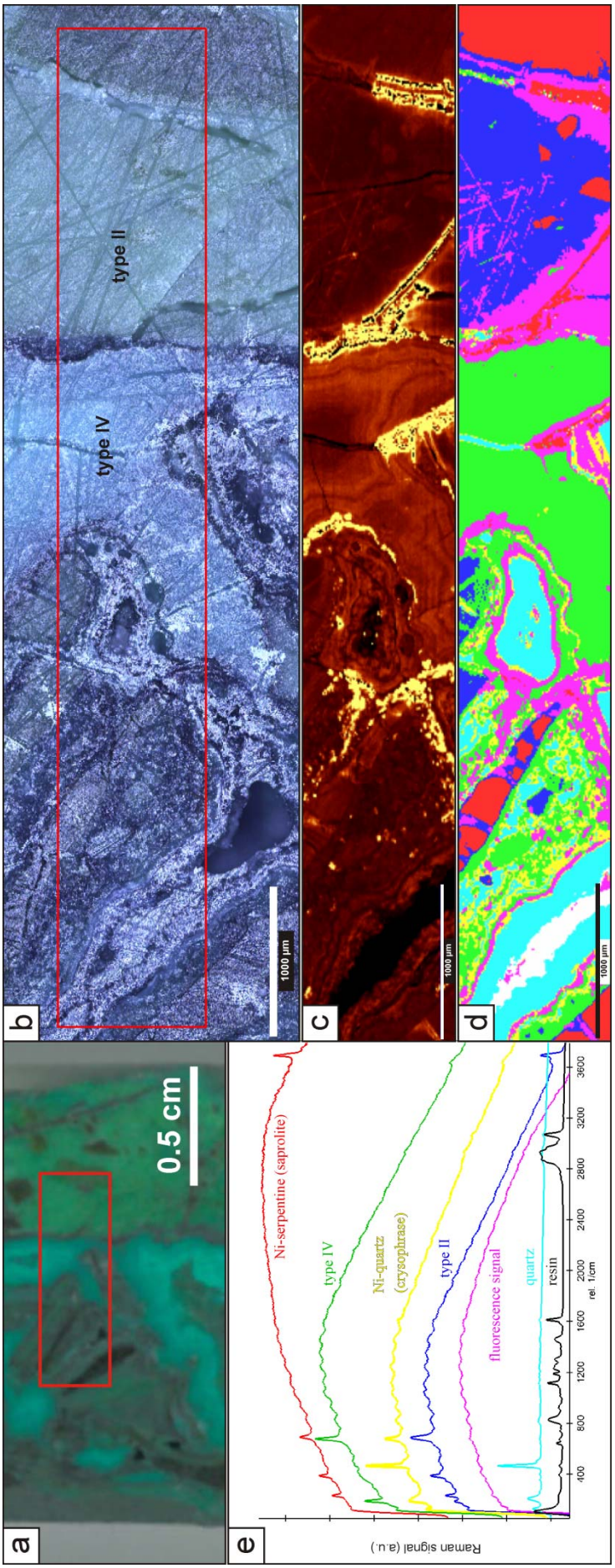

FIGURE 6.3. Micro-Raman map: **a)** image and **b)** reflected light photomicrograph of the selected sample; **c)** false colour integrated intensity micro-Raman image in the range 150-750 cm^{-1}; **d)** micro-Raman map; **e)** corresponding colour-coded spectra of each characteristic zone in d). Red rectangles indicate the scanned area.

However, the sepiolite-falcondoite bands at ~3680 cm^{-1} were not found in the literature for sepiolite neither detected in the sepiolite analysed in this study (**Table 6.2**, **Fig. 6.2**).

Therefore, when the values are compared with Ni-free phyllosilicates analysed in the same instrument using the same laser wavelength, and with those present in the literature, no correlation between band position and mineralogy is observed.

However, some authors use this spectral region to distinguish among species of the serpentine group (Petriglieri *et al*., 2014) and different Ni contents within the kerolite-pimelite series (Cathelineau *et al*., 2014, 2015). On one hand, Petriglieri *et al*. (2014) found that chrysotile and polygonal serpentine have similar Raman curves in this region, characterised by a very strong peak (at 3698 in chrysotile and at 3697 in polygonal serpentine) and a shoulder (at 3691 and 3689, respectively), preceded by a very weak peak (at 3651 cm^{-1} and 3646 cm^{-1}). In contrast, lizardite had a weak band at 3660 preceding a strong band at 3683 with a shoulder at 3703 cm^{-1}. The bands in type I and II garnierites are comparable to those of chrysotile reported by Petriglieri *et al*. (2014), which is coherent with the mineralogy of these garnierites observed at the nanometre scale by TEM (**Table 6.1**, **Chapter 5**), despite not being similar to the chrysotile analysed in this study. It is worth noting that the spectrum of lizardite from Cornwall ressembles that of lizardite in Petriglieri *et al*. (2014), whereas the spectrum of lizardite from Elba Island is similar to that of polygonal serpentine in the same article (**Table 6.2**, **Fig. 6.2**).

On the other hand, Cathelineau *et al*. (2014, 2015) established that the position and intensity of the Raman bands in the high region was sensitive to the Ni content in the kerolite-pimelite series: the lower Ni contents are related to intense bands at higher positions (3670, 3685 and 3700 cm^{-1}, being the former the only band present when Ni is absent), and the higher Ni contents are associated to lower positions (3650, 3660 and a shoulder at 3625 cm^{-1}); being the intermediate Ni contents related to a complex band cluster with three major peaks at 3649, 3670 and 3700 cm^{-1}. On this basis, the bands observed in the Raman spectrum of type IV garnierite indicate that the point analysis may have been performed on an area with a remarkably high Ni content (**Fig. 6.2**). In contrast, the bands in type III could be explained by the presence of a kerolite-pimelite with less Ni (**Fig. 6.2**).

6.5. FINAL REMARKS

The analysis of Ni-bearing Mg-phyllosilicates from the Falcondo Ni-laterite deposit, compared to data from Ni-free Mg-phyllosilicates as well as from previous data from the literature gave the following conclusions:

Despite the limited occurrence of Raman spectra of Ni-phyllosilicates in the literature, each garnierite type described in this work is distinguishable by means of a characteristic Raman pattern. Knowledge of characteristic Raman vibrations of different garnierites with well constrained structure and composition is a significant improvement for the evaluation of the reliability of this technique to characterise the mineral phases contained in the garnierites.

Some Raman bands can be related to serpentine group minerals, talc or sepiolite from the literature or from the analysed reference samples. However, the low spectral region results were not conclusive in distinguishing among the serpentine "polymorphs", but the presence of chrysotile and polygonal serpentine was confirmed by analysing the high spectral region of the Raman pattern of some garnierites.

In the particular case of kerolite-pimelite, the bands present in the high spectral region could be used to determine the amount of Ni in the probed area by comparing the results obtained in this work with the literature.

TABLE 6.2. Micro-Raman bands obtained in the garnierites from Falcondo at 1064 and 532 nm, and in Ni-free phyllosilicates from other localities at 532 nm, with possible assignments from the literature (Blaha & Rosasco, 1978; Rosasco & Blaha, 1980; Lewis *et al*., 1996; Bard *et al*., 1996; Kloprogge *et al*., 1999; McKeown *et al*., 2002; Rinaudo *et al*., 2003; Groppo *et al*., 2006; Frost *et al*., 2008; Cathelineau *et al*., 2015). Legend: s = strong, m = medium, w = weak, sh = shoulder, d = doubtful. The extended table is in the **Appendix A3**.

This study - 1064 nm					**This study - 532 nm**						**This study - 532 nm**					**Kloprogge et al. (1999) - 633 nm**	**Rinaudo et al. (2003) - 1064 nm**	**Groppo et al. (2006) - 632.8 nm**	**Frost et al. (2008) - 633 nm**	**Blaha & Rosasco (1978) - 514.5 nm**	**Rosasco & Blaha (1980) - 514.5 nm**	**Cathelineau *et al*. (2015) - 514.5 nm**	**McKeown *et al*. (2002) - 1064 nm**	**RRUFF**
Type I (09GAR-2)	**Type II (LC-100)**	**Type III (GAR-2)**	**Type IV (GAR-6)**	**Type V (FALC-3)**	**Type I (09GAR-2)**	**Type II (LC-100)**	**Type III (GAR-2)**	**Type IV (LC-100)**	**Type V-Sep (FALC-4)**	**Type V-Fal (FALC-3)**	**lizardite (LIZ-1)**	**lizardite (LIZ-2)**	**chrysotile (CRIS)**	**talc (TLC)**	**sepiolite (SEP)**	chrysotile	chrysotile (Ctl), antigorite (Atg), lizardite (Lz), [all=Srp]	antigorite (Atg), lizardite (Lz), chrysotile (Ctl), [all=Srp]	pecoraite (Pec), chrysotile (Ctl)	talc (Tlc)	talc (Tlc)	kerolite (Ker)	sepiolite (Sep)	bands (laser wavelength listed with the reference)
					127.6**w**											-	-	-	-	-	-	-	-	-
				131.7**s**							135.1**w**	135.1**w**	135.1**m**			-	-	-	-	-	-	Ker	-	-
	186.1**s**	183.6**s**	186.7**s**			178.8**w**	182.4**w**	184.3**s**							182.0**d**		-	-	-	-	-	Ker	-	talc R080080(514), R050050(532)
				195.5**s**					195.5**w**	193.4**w**				196.6**s**		M-O	A1g mode of Mg(O,OH)6 in Ctl (Kloprogge *et al*., 1999)	Mg(O,OH)6 groups vibrations in Srp	Pec	Metal-O	perpendicular "brucite"	-	silicate sheet and Mg octahedra deformations	lizardite R060006, talc R040137(514), R050058(514, 532), willemseite R061112(532)
		209.3**m**														-	-	vibrations of O-H-O groups in Lz, Ctl	-	-	-	-	-	-
230.6**s**	230.5**s**				226.1**m**	229.7**w**					234.7**s**	239**m**	235.3**s**			M-O	vibrations of O-H-O groups in Srp (also Kloprogge *et al*., 1999)	vibrations of O-H-O groups in Srp	OSiO bend in Pec	Metal-O	Tlc	Ker	-	chrysotile R070088, R070355
						271.3**w**	271.3**w**									-	-	-	-	-	-	-	silicate sheet and Mg octahedra deformations	sepiolite R070311(532)
				333.8**w**													-	-	-	Metal-O	-	-	silicate sheet and Mg octahedra deformations	-
343.0**w**	344.6**sh**												355.9**w**			M-O	bending of SiO4 in Ctl, Lz (also Kloprogge *et al*., 1999)	bending of SiO4 in Ctl	-	-	Tlc	-	-	chrysotile R070088, R070355
364.4**sh**	367.7**sh**	368.4**m**	363.9**w**			366.4**w**								363.4**w**			-	-	-	Metal-O	Tlc	-	-	talc R040137(514), R050050(514, 532), R050058(514, 532)
385.8**s**	384.2**s**		385.1**w**	384.9**w**	382.5**m**	382.5**m**		382.5**w**			388.3**m**	394.2**s**	389.8**s**			M-O	symmetric v5(e) SiO4 in Srp (also Kloprogge *et al*., 1999)	symmetric v5(e) SiO4 in Srp	-	Metal-O	Tlc	-	silicate sheet and Mg octahedra deformations	chrysotile R070088, R070355
								492.5**w**	481.7**s**							-	-	-	-	-	-	-	-	-
																-	Atg	-	-	Tlc	vs A1	-	-	lizardite R060006
618.8**w**	620.3**w**												625.2**w**			-	antisymmetric OH-Mg-OH translation modes in Ctl (Kloprogge *et al*., 1999)	-	-	-	-	-	-	-

TABLE 6.2. (CONTINUED).

This study - 1064 nm					This study - 532 nm						This study - 532 nm					Kloprogge *et al.* (1999) - 633 nm	Rinaudo *et al.* (2003) - 1064 nm	Groppo *et al.* (2006) - 632.8 nm	Frost *et al.* (2008) - 633 nm	Blaha & Rosasco (1978) - 514.5 nm	Rosasco & Blaha (1980) - 514.5 nm	Cathelineau *et al.* (2015) - 514.5 nm	McKeown *et al.* (2002) - 1064 nm	RRUFF
Type I (09GAR-2)	**Type II (LC-100)**	**Type III (GAR-2)**	**Type IV (GAR-6)**	**Type V (FALC-3)**	**Type I (09GAR-2)**	**Type II (LC-100)**	**Type III (GAR-2)**	**Type IV (LC-100)**	**Type V-Sep (FALC-4)**	**Type V-Fal (FALC-3)**	**lizardite (LIZ-1)**	**lizardite (LIZ-2)**	**chrysotile (CRIS)**	**talc (TLC)**	**sepiolite (SEP)**	chrysotile	chrysotile (Ctl), antigorite (Atg), lizardite (Lz), [all=Srp]	antigorite (Atg), lizardite (Lz), chrysotile (Ctl), [all=Srp]	pecoraite (Pec), chrysotile (Ctl)	talc (Tlc)	talc (Tlc)	kerolite (Ker)	sepiolite (Sep)	bands (laser wavelength listed with the reference)
	649.7**sh**		639.6**m**	639.5**w**											644.5**d**	-	-	antisymmetric OH-Mg-OH translation modes in Srp	-	-	-	**-**	**-**	sepiolite R070311(532)
668.2**sh**	674.3**s**	680.4**s**	675.9**s**	673.4**s**			678.6**s**	671.7**s**	673.6**s**	670.0**s**				679.6**s**	675.2**d**	-	-	-	OSiO bridge in Pec	Si-Ob-Si symmetric stretching mode	vs E2 Si-O-Si	**-**	silicate sheet and Mg octahedra deformations	talc R040137(514), R050050(514, 532), R050058(514, 532), willemseite R061112(532)
686.5**s**	686.5**s**				688.9**m**	687.2**m**					689.8**m**	694.2**m**	694.2**s**			Si-O bridging or stretching, also 692 Lewis (1996) and 622 Bard (1997)	vs Si-Ob-Si in Srp (also Kloprogge *et al.*, 1999)	vs Si-Ob-Si in Srp	OSiO bridge in Ctl	-	-	**-**	**-**	chrysotile R070088, R070355
			822.9**w**													-	-	-	NiOH deformation in Pec	-	-	**-**	**-**	-
															1114.3**d**	-	-	-	-	-	-	**-**	**-**	talc R050050(514)
															1187.5**d**	-	-	-	-	-	-	**-**	**-**	-
																-	-	-	Pec	-	-	**-**	**-**	-
															1610.4**d**	-	-	-	-	-	-	**-**	**-**	-
																-	-	-	Pec	-	-	**-**	**-**	-
															3072.6**d**	-	-	-	-	-	-	**-**	**-**	-
																-	-	-	-	-	-	**-**	**-**	-
																inner OH stretch	-	-	inner OH stretch (Pec, Ctl), inner surface OH stretch (Pec)	-	-	**-**	**-**	-
																OH stretch, also 3685 Bard (1997)	-	-	-	Tlc	OH stretch	**-**	**-**	-
																OH stretch or external OH stretch, also 3700 Bard (1997)	-	-	-	-	-	**-**	**-**	-
																-	-	-	inner surface OH stretch in Pec, Ctl	-	-	OH stretching	**-**	-

7. CRYSTALLOCHEMISTRY OF Ni AND Fe IN GARNIERITES AND RELATED ROCKS: LOCAL ENVIRONMENT AND SPECIATION BY SYNCHROTRON RADIATION

This part of the study highlights the importance of the application of μXAS in ore deposits and, in particular, provides for the first time detailed synchrotron data of garnierites and related rocks from Caribbean Ni-laterites.

Five samples from the saprolite horizon of the Falcondo Ni-laterite deposit were selected as the most representative from each one of the five garnierite types previously described and studied in detail by means of powder X-ray diffraction, differential thermal analysis coupled to thermogravimetry, optical microscopy, scanning electron microscopy, electron microprobe (**Chapter 4**; Villanova-de-Benavent *et al*., 2014b), transmission electron microscopy (**Chapter 5**; Villanova-de-Benavent *et al*., 2011a; 2011b; *submitted*) and micro-Raman spectroscopy (**Chapter 6**; Villanova-de-Benavent *et al.,* 2012) (**Table 7.1**).

The samples consist of saprolite fragments crosscut by millimeter- to centimeter-thick garnierite veins, labeled L101A (type I), LC100B (type II) and GAR2C (type III) (**Figs. 7.1a1-2, b1-2, c1-2**); or are uniquely composed of massive garnierite aggregates, labeled GAR6 (type IV) and FALC3 (type V) (**Figs. 7.1d1-2, e1-2**). In order to select the representative regions of interest (ROI) to be studied by means of synchrotron radiation (**Figs. 7.1a3-e3, 7.1.4, 7.1a5-c5**), these samples were prepared as polished thin sections and examined through optical microscopy (**Figs. 7.1a2, b2, c2, d2, e2**) and electron microprobe (**Fig. 7.1.6**), These ROIs were analysed by micro X-ray fluorescence (μXRF) and microfocus X-ray absorption spectroscopy (μXAS) in an attempt to correlate the mineralogy, texture, mineral chemistry and textures at the nano scale with the distribution of Ni and the speciation of Fe, both in the saprolite Ni-serpentine

TABLE 7.1. Summary of the samples selected for the synchrotron radiation study, including the mineralogy obtained by XRD and TEM, and their corresponding average structural formulae from EMP analyses (numbers in brackets indicate the amount of averaged analyses).

Type	Sample	Mineralogy		Structural formula [number of analyses averaged]
		XRD	TEM	EMP
Type I	LC-101	serpentine (7.28 Å)	chrysotile tubes with minor short kerolite-pimelite lamellae	$(Mg_{2.31}Ni_{0.24}Fe_{0.18})Si_{2.16}O_{5.51}(OH)_{3.29}\cdot 0.19H_2O$ [24]
Type II	LC-100B	serpentine (7.30 Å) with minor talc-like (10.20-10.54 Å)	polygonal serpentine and chrysotile tubes in a kerolite-pimelite lamellae matrix	$(Mg_{2.12}Ni_{0.82}Fe_{0.06})(Si_{2.49}Al_{0.08})O_{6.51}(OH)_{3.40}\cdot 0.29H_2O$ [71]
Type III	GAR-2	serpentine (7.40 Å) + talc (10.56 Å)	thick lizardite lamellae and thin kerolite-pimelite lamellae	$(Ni_{2.42}Mg_{0.56}Fe_{0.01})Si_{2.71}O_{6.81}(OH)_{3.28}\cdot 0.36H_2O$ [4]
Type IV	GAR-6	talc (10.14 Å) and traces of serpentine (7.34 Å)	kerolite-pimelite lamellae	$(Ni_{1.90}Mg_{1.10})(Si_{3.61}Al_{0.01})O_{9.06}(OH)_{2.40}\cdot 0.81H_2O$ [17]
Type V	FALC-3	sepiolite (12.15 Å)	sepiolite ribbons	$Mg_{4.07}Ni_{3.90}Fe_{0.01}Si_{11.91}Al_{0.12}O_{15}(OH)_2\cdot 6H_2O$ [4]

and within the different garnierite types of the Falcondo Ni-laterite deposit. The μXRF multi energy map on each ROI has been acquired to study the distribution of Fe, Ni and Cr (**Figs. 7.1a3, b3, c3, d3, e3**), and a scatter plot of the fluorescence intensities of Ni and Fe from each pixel has been obtained to correlate the distribution of Ni and Fe in the selected areas to understand the relationships between the weathered protolith fragments and the garnierite precipitates (**Fig. 7.2**). When these points are aligned with a positive slope it is indicative of cross-correlation, whereas when the slope is negative it indicates that one of the elements is excluding the other showing anti-correlation.

μXAS was deployed in order to acquire Fe K-edge micro X-ray absorption near edge structure (μXANES) and the Ni K-edge micro Extended X-Ray Absorption Fine Structure (μEXAFS). These techniques were used to elucidate the chemistry of Ni and Fe, and the local environment of Ni within the garnierites and the Ni-serpentines from the host saprolite. To precisely identify the Fe-rich phases, Fe K-edge XANES has been acquired on single representative spots of the reduced and the oxidised Fe-bearing phases. Subsequently, these spectra have been fitted by means of PCA with selected representative standards of forsterite, maghemite and serpentine (**Fig. 7.3**). Each representative Fe K-edge XANES has been fit with known Fe-bearing standards and then the spectra have been used to plot the distribution of each phase within the ROIs (**Figs. 7.1a5-c5**). To unravel the local environment of Ni in the saprolite and the different garnierites, Ni K-edge μEXAFS spectra have been acquired and the Fourier transforms (FT($\chi(k)$)) of these spectra were obtained (**Figs. 7.4-7**; **Tables 7.3-5**).

7.1. DESCRIPTION OF THE SELECTED SAMPLES AND ROIS.

The ROI selected in sample LC101A contains yellowish green type I garnierite and thin quartz veinlets crosscutting brown saprolite fragments (**Figs. 7.1a1-2**). The brown saprolite fragments consist mostly of Ni-Fe-bearing serpentine and minor Fe-oxyhydroxides and relict chromian spinel. They yield variable Ni and Fe contents, with an average structural formula of $Mg_{2.32}Ni_{0.20}Fe^{3+}_{0.19}Al_{0.05}Si_{2.00}O_5(OH)_4$ (**Table 7.1**; **Fig. 7.1.6**). Type I garnierite is yellowish pale green in color, which consists of serpentine, according to XRD and is the garnierite with highest Fe (2.7-8.9 wt.% Fe_2O_3) and lowest Ni (1.2-8.9 wt.% NiO) contents of Falcondo, according to EMP (**Fig. 7.1.6**; see **Chapter 4**, Villanova-de-Benavent *et al*., 2014b). However, from calculations based on the EMP analyses, a contribution of a talc-like fraction was found (about 0.14). In agreement with this result, TEM investigations determined that type I garnierite consists of randomly oriented serpentine tubes of various sizes surrounded by minor kerolite-pimelite fibres with very little porosity, even when this talc-like phase was not detected by XRD (**Table 7.1**).

The selected area in sample LC100B contains greenish type II garnierite surrounding saprolite fragments and with the resulting voids being filled by euhedral quartz (**Figs. 7.1b1-2**). Type II garnierite displays a characteristic apple green color. XRD identified that this garnierite is a mixture of serpentine and a minor talc-like phase (kerolite-pimelite). The EMP analyses indicate that type II garnierites are a mixture of a serpentine mineral and kerolite-pimelite, with higher Ni than type I (21.6-25.2 wt.% NiO) and Fe around 0.5 wt.% Fe_2O_3, and the calculated talc fraction is 0.27 (**Fig. 7.1.6**). Therefore type II shows an increase of the content of Si and Ni at expenses of Fe and Mg and is closer to the kerolite-pimelite series than type I, following the trend described in **Chapter 4** and Villanova-de-Benavent et al. (2014b). Under TEM, this garnierite occurs as large polygonal serpentines and smaller weakly round cylindrical fibres, all scattered in a matrix of kerolite-pimelite (**Table 7.1**).

The GAR2C ROI is composed by two fragments of weathered protolith cemented by euhedral quartz which is in turn cemented by dark green type III garnierite (**Figs. 7.1c1-2**). Type III garnierite is dark green in color. According to the XRD diffractograms, this is also a mixture between serpentine and kerolite-pimelite. EMP results determine a composition halfway between the serpentine (lizardite/chrysotile-népouite/pecoraite) and the talc-like (kerolite- pimelite) series, closer to the Ni-dominant end members, with a Ni content ranging from 29.0 to 41.0 wt.% NiO and a talc fraction of 0.47 (**Table 7.1**, **Fig. 7.1.6**). Under TEM, type III garnierite is composed by long, thick, bended serpentine lamellae coexisting with less crystalline kerolite-pimelite thin fibres.

In sample GAR6 the turquoise-colored type IV garnierite is cementing light brown saprolite

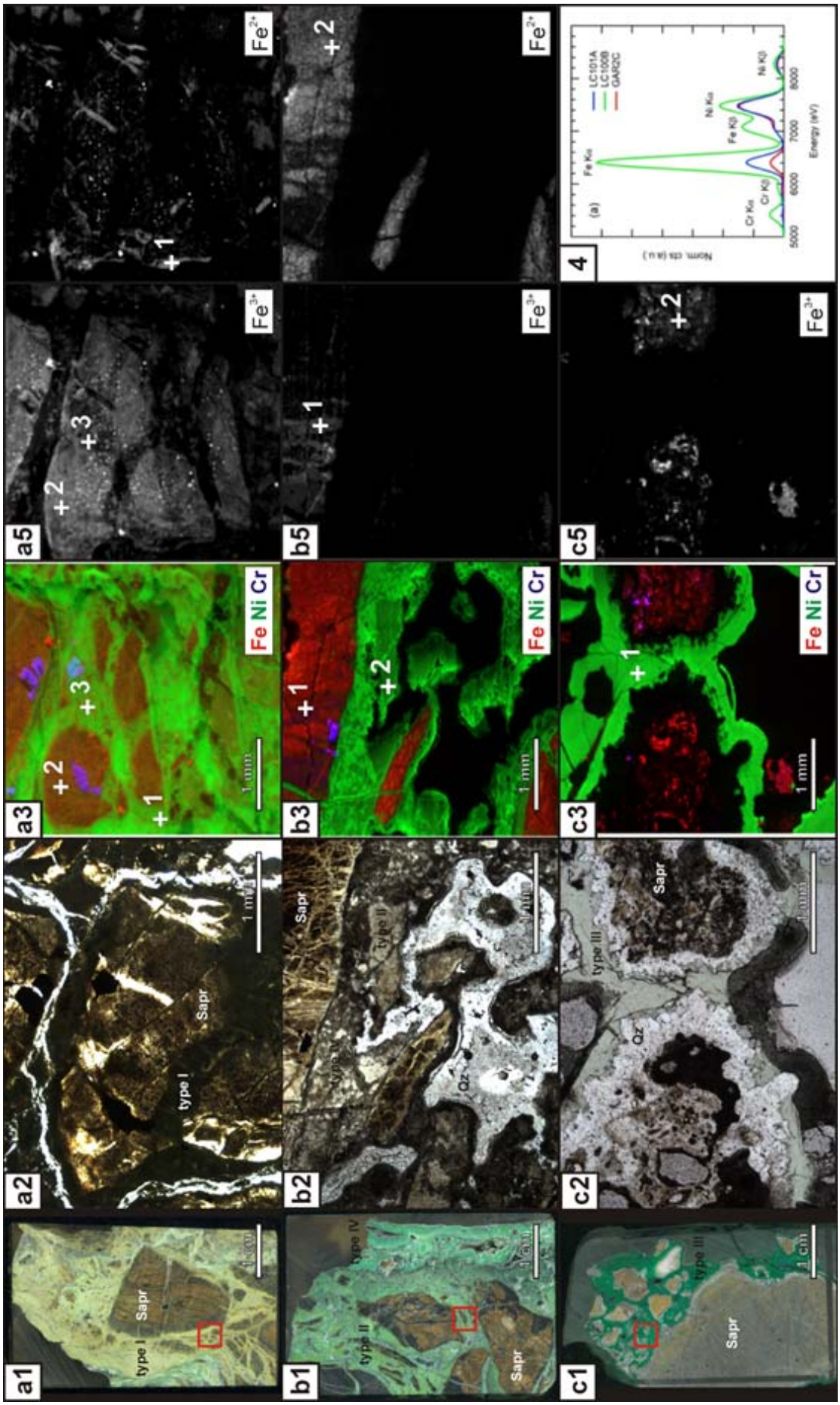
a1
type I
Sapr
1 cm
a2
type I
Sapr
1 mm
a3
+1
+2
+3
Fe Ni Cr
1 mm
a5
+1
+2
+3
Fe2+
Fe3+
b1
type IV
type II
Sapr
1 cm
b2
Sapr
type II
Qz
1 mm
b3
+1
+2
Fe Ni Cr
1 mm
b5
+1
+2
Fe2+
Fe3+
c1
type III
Sapr
1 cm
c2
type III
Sapr
Qz
1 mm
c3
+1
Fe Ni Cr
1 mm
c5
+2
Fe3+
4
LC101A
LC100B
GAR2C
Fe Kα
Fe Kβ
Ni Kα
Ni Kβ
Cr Kα
Cr Kβ
(a)
Norm. cts (a.u.)
5000
6000
7000
8000
Energy (eV)

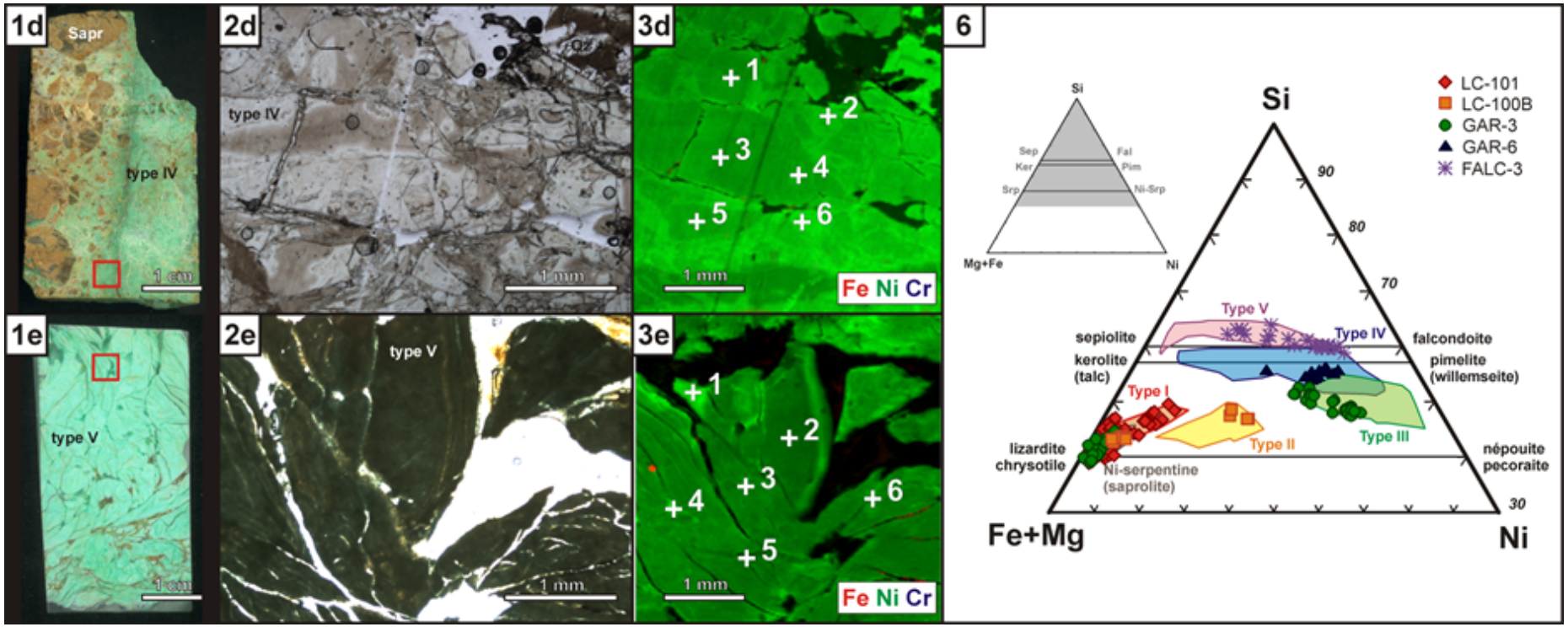

FIGURE 7.1. Hand specimen images (**1**), optical photomicrographs under plane polarized light, corresponding to the areas inside the red squares in (1) (**2**), and µXRF maps of the regions of interest (**3**), inset graph showing the integrated XRF intensities at 10keV for samples LC101A, LC100B and GAR2C (**4**), greyscale chemical maps of the Fe K-edge µXANES (**5**), and ternary plot showing the composition of the analysed garnierites and related saprolite serpentines (**6**) of the selected samples: **a)** LC101A (saprolite and type I garnierite), **b)** LC100B (saprolite and type II garnierite), **c)** GAR2C (saprolite and type III), **d)** GAR6 (type IV garnierite) and **e)** FALC3 (type V garnierite). In the µXRF maps, the red channel corresponds to Fe Kα, the green channel to Ni Kα and the blue channel to Cr Kα. In the triangular diagram, the composition of the garnierite samples selected for the synchrotron radiation study is compared to the fields representing the composition of all garnierite types analysed by EMP (see **Chapter 4**). Abbreviations are after Whitney & Evans (2010), Tauler *et al.* (2009) and Villanova-de-Benavent *et al.* (2014b), except Pec for pecoraite. White crosses in Figs. **7.1a3-e3** indicate the Ni K-edge µEXAFS analysed points, and the white crosses in **Figs. 7.1a5-c5**, the Fe K-edge µXANES.

fragments, and the selected ROI consists uniquely of type IV garnierite and minor quartz (**Figs. 7.1d1-2**). Under the optical microscope this ROI is formed by banded and/or botryoidal aggregate fragments cemented by a later garnierite precipitate. Type IV garnierite, with a characteristic bluish green color, consists uniquely of a talc-like phase as inferred by a broad XRD peak near 10 Å. The composition of this garnierite obtained by EMPA yields between the kerolite-pimelite series, with a variable Ni content, ranging from 24.2 to 31.8 wt.% NiO (**Table 7.1**, **Fig. 7.1.6**). This is confirmed by TEM, showing that this garnierite is very homogeneous, it consists only of sets of plaited thin fibres with basal spacings of 9.5-9.7 Å and it shows low crystallinity. In addition to the EMP low oxide totals, DTA-TG confirms the presence of extra water in the structure and therefore justifies the use of the names kerolite-pimelite instead of talc-willemseite. This garnierite type may coexist in other samples with all the other garnierite types described above.

Ni-sepiolite-falcondoite is the major constituent of the selected ROI and of sample FALC3, occurring as light green undulated bundles of fibers, accompanied only by tiny quartz veinlets and some oxide impurities (**Figs. 7.1e1-2**). It is identified as sepiolite by XRD and EMP gave compositions in the range between sepiolite and falcondoite, closer to the Ni end member falcondoite with a Ni content of 12.3-26.8 wt.% NiO (**Table 7.1**, **Fig. 7.1.6**). The particularity of this material is that such a high Ni concentration in sepiolite has not been described in the literature in other places outside the Falcondo Ni-laterite deposit. This sample is thought to correspond to the later stages of garnierite precipitation in agreement with Galí *et al*. (2012) and Villanova-de-Benavent *et al*. (2014b), since the silica content increases with time along the profile. As seen under TEM, Ni-bearing sepiolite-falcondoite develops roughly oriented, long, thin ribbons.

7.2. DISTRIBUTION OF Fe, Ni AND Cr (μXRF,)

The distribution of Ni, Cr and Fe within the LC101A ROI shows that Fe is associated to the saprolite fragments, Ni is localised mostly in the type I garnierite veins and Cr is found concentrated in small scattered regions within the saprolite fragments, probably representing chromian spinel relicts (**Fig. 7.1a2-3**). The obtained Ni:Fe scatter plot from LC101A in **Figs. 7.2a, b** displays various clouds of pixels: i) two with high Fe Kα fluorescence intensities and low Ni Kα fluorescence intensities (Fe Kα not related to Ni Kα), ii) a group of pixels where the fluorescence of Ni Kα is anti-correlated to the fluorescence of Fe Kα, and iii) one cloud with low Fe Kα fluorescence intensities and high Ni Kα fluorescence intensities (Ni Kα not related to Fe Kα).

The first two may correspond to the chromium spinel relict grains observed in **Fig. 7.1a3** and to a primary serpentine veinlet of hydrothermal origin. The third cloud with Ni negatively correlated to Fe may correspond to the Fe-Ni-bearing serpentine from the saprolite fragments and the Fe-Ni-bearing serpentine-dominant type I garnierite, in which Fe and Ni occupy the same position in the structure, in the octahedral layer (**Figs. 7.2a, b**). The serpentine from the saprolite is distinguished from the type I garnierite by its lower Ni content, and therefore may be represented by a round-shaped denser cloud of points (**Fig. 7.2b**). Finally, the third may represent an Fe-free garnierite (possibly type IV), which occurs frequently as veinlets crosscutting the saprolite fragments associated to type I garnierite. (**Figs. 7.2a, b**, see **Chapter 4**).

As in LC101A, the distribution of Ni, Cr and Fe within the LC100B ROI shows that Fe is principally associated to the saprolite fragments, Ni is found in the garnierite veins and that Cr is also present as chromian spinel relicts (**Figs. 7.1b2-3**). The map on LC100B displays some dark areas, representing voids and secondary precipitated quartz. The Ni:Fe scatter plot obtained from LC100B displays two major clouds of pixels: i) one with fluorescence intensities of Ni Kα not related to Fe Kα, and ii) another with higher fluorescence intensities of Fe Kα and relatively lower Ni Kα fluorescence intensities (**Figs. 7.2a, c**). In addition, the inset graph shows that there is still a minor third group of pixels where the fluorescence of Ni Kα is anti-correlated to the fluorescence of Fe Kα, but being much less significant than in LC101A (**Fig. 7.2c**). The first cloud represents the sum of Fe-free, Ni-bearing, serpentine-dominant type II garnierite and the Ni-bearing hydrated talc-like (kerolite-pimelite) type IV garnierite matrix surrounding type II (**Fig. 7.1b2**); whereas the second cloud corresponds to the Ni-Fe-bearing serpentine from the saprolite fragments (**Fig. 7.2c**).

The distribution of Fe, Cr and Ni within the GAR2C ROI shows a heavily weathered and fragmented saprolite that concentrates most of the

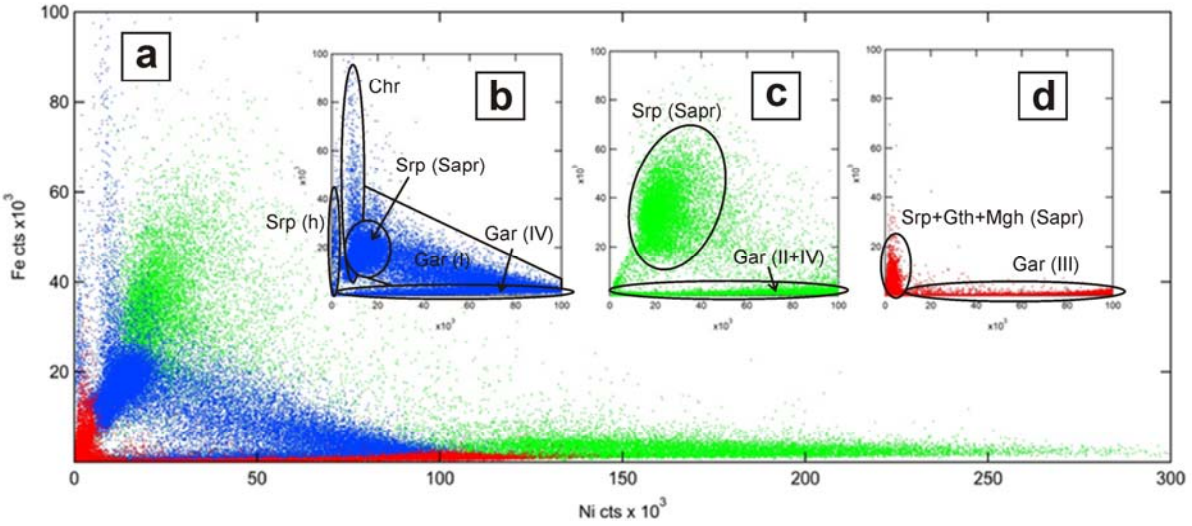

FIGURE 7.2. Ni Kα vs Fe Kα scatter plots (**a**) for sample LC101A in blue (**b**), LC100B in green (**c**) and GAR2C in red (**d**). Legend: Chr = chromium spinel; Srp (h) = Ni-poor primary hydrothermal serpentine; Srp (Sapr) = Ni-enriched secondary serpentine; Gar (I-IV) = garnierite type I-IV; Gth = goethite; Mgh = maghemite.

Fe, coated by the high Ni type III garnierite (**Figs. 7.1c2-3**). No Cr spots were observed as in the previously described ROIs. The element map displays a complete separation between Fe and Ni-bearing phases, which is also confirmed by the Ni versus Fe scatter plot (**Figs. 7.2a,d**). Unlike LC101A and LC100B ROIs, no negative correlation between Ni Kα and Fe Kα has been observed. In the GAR2C scatter plot there are only two groups of pixels: i) one with high fluorescence intensities of Fe Kα and low Ni Kα, and ii) another with high fluorescence intensities of Ni Kα and no Fe Kα. The first cloud represents the heavily weathered saprolite fragments and the second cloud is related to the presence of type III garnierite (**Figs. 7.2a,d**).

The distribution of Ni, Cr and Fe within the saprolite free ROIs GAR6 and FALC3 is shown in **Figs. 7.1d3, e3**. Both ROIs show a high content of Ni across the mapped area with no detectable amounts of Fe or Cr. However, in GAR6 some variations in Ni concentrations can be seen in the elemental map, depicting a garnierite breccia with lower Ni content garnierite fragments (in dimmer green color) surrounded by a garnierite cement with higher Ni content (in a brighter green color) (**Fig. 7.1d3**). Differently to GAR6, in FALC3 the Ni is mostly uniformly distributed across the entire ROI, except for the rims of some fibrous aggregates, which yield higher Ni concentrations. The element map on FALC3 shows a Ni distribution matching a distinctive elongated texture consistent with the crystalline habit of a mineral from the sepiolite-falcondoite series (**Fig. 7.1e3**).

7.3. SPECIATION OF FE (μXANES)

The Fe-bearing mineral phases identified (primary hydrothermal serpentine, serpentine from the saprolite and type I garnierite) have been analysed by μXANES in order to study the speciation of Fe, and Fe^{2+} and Fe^{3+} distribution maps were performed on the selected ROIs (**Figs. 7.1a4-5, b4-5, c4-5**). To gather more information on the main Fe-bearing phases, Fe K-edge μXANES have been acquired on selected points of these ROIs. The Fe K-edge μXANES spectra have been fitted with forsterite, serpentine, maghemite and goethite standards as shown in **Fig. 7.3**, and the corresponding fitting values are given in **Table 7.2**.

The Fe μXANES map on the LC101A ROI (**Figs. 7.1a5**) demonstrates that the reduced fraction of Fe is confined into veinlets within the saprolite and that the oxidised fraction of Fe constitutes the rest of the saprolite fragments and the surrounding type I garnierite. In addition, the vein-like texture displayed by the areas with Fe^{2+} indicates that they probably correspond to relicts of primary serpentine of hydrothermal origin, formed prior to the exhumation and weathering of the saprolite, as observed by Andréani *et al.* (2008, 2013). According to the Fe K-XANES fittings (**Table 7.2**), the more oxidised Fe corresponding to the bulk of the saprolite corresponds to 65.7 % serpentine, 28.2 % maghemite and 6.3 % fosterite (**Fig. 7.3a**), and

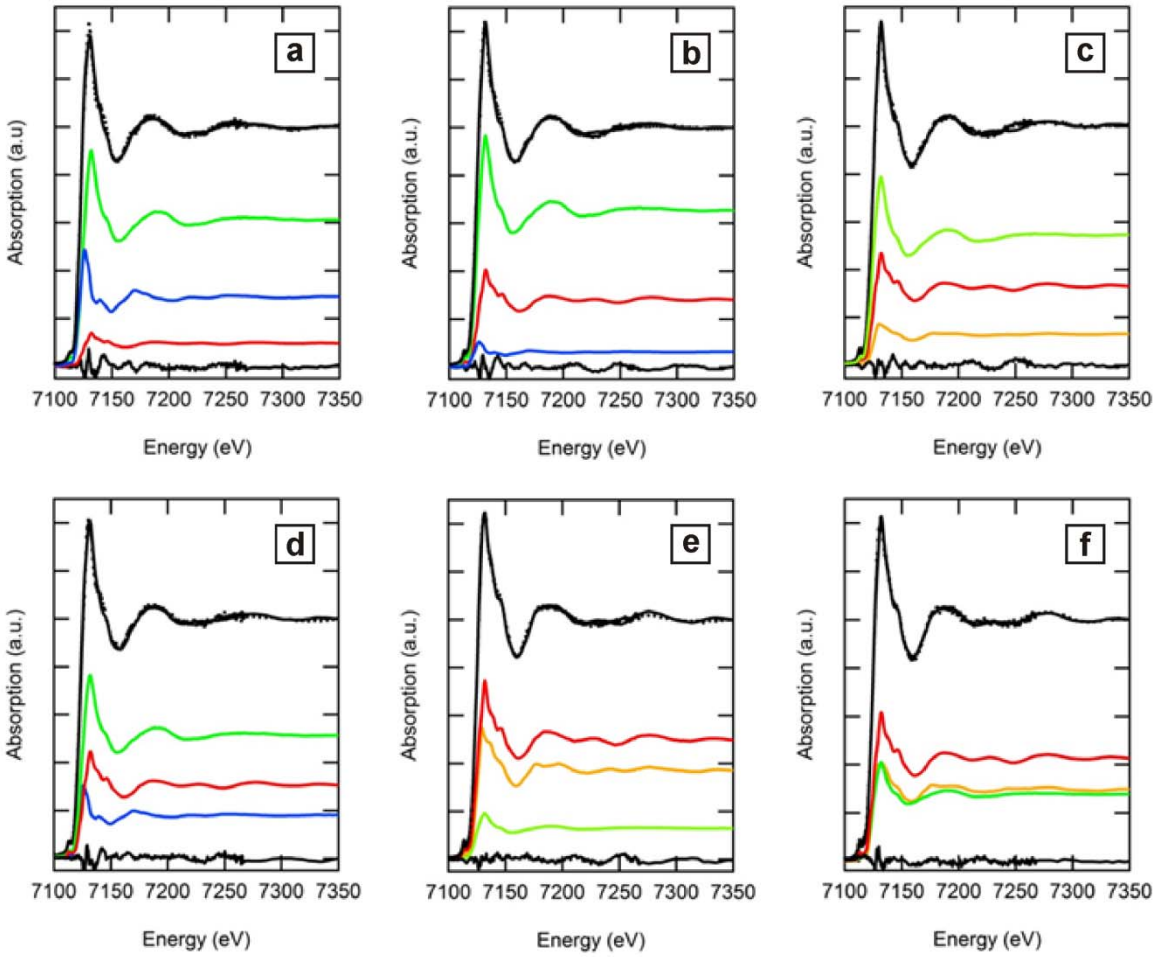

FIGURE 7.3. Fe K-edge μXANES (black) and the resulting fits with goethite (yellow), maghemite (red), serpentine (green) and forsterite (blue) of: (**a**) LC101A_02 (saprolite fragment), (**b**) LC101A_01 (primary hydrothermal serpentine), (**c**) LC101A_3 (type I garnierite), (**d**) LC100B_01 (saprolite fragment), and (**e**) LC100B_02 (saprolite fragment), (**f**) GAR2C (saprolite fragment). The probed points are marked in **Figs. 7.1a5, b5, c5**.

TABLE 7.2. Phases contributing to the Fe-K XANES and their respective fittings.

Sample	LC101A_2	LC101A_1	LC101A_3	LC100B_1	LC100B_2	GAR2C_1
Type	saprolite	saprolite	type I	saprolite	saprolite	saprolite
Fo(%)	29	6.3	-	18.2	-	-
Srp(%)	61.3	65.7	54	51.9	13.2	27.8
Mgh(%)	9.7	28.2	32.5	30.9	51	42.8
Gt(%)	-	-	12.7	-	37.7	29.6
Norm. Sum. Sq.	2.40E-04	2.12E-04	2.10E-04	2.72E-04	1.21E-04	1.96E-04

the more reduced Fe can be associated to the primary hydrothermal serpentine that fits with 61 % serpentine, 9.7 % maghemite and 29 % forsterite (**Fig. 7.3b**). The Fe-K edge XANES fitting in type I garnierite confirms that Fe is completely oxidized with a content of 57 % serpentine, 39.6 % maghemite and 1.9 % goethite (**Fig. 7.3c**).

The distribution of Fe^{2+} and Fe^{3+} in LC100B shows that the oxidised Fe fraction is found widespread in the saprolite fragment and that some areas of the saprolite fragments have reduced Fe as well (**Figs. 7.1b5**). Two Fe K-edge XANES have been acquired to identify the main phases constituting the Fe^{2+} rich vein and the bulk of the saprolite fragment with a high content of Fe^{+3}. According to

the fittings in **Table 7.2**, a point measured in an area with Fe^{2+} and Fe^{3+} in the saprolite fragment gives 60 % serpentine, 30.9 % maghemite and 18.2 % forsterite (**Fig. 7.3d**), whereas a point measured in the saprolite fragment with mostly Fe^{3+} fits with 13.2 % serpentine, 51 % maghemite and 37.7 % goethite (**Fig. 7.3e**)

In the GAR2C ROI, the distribution of Fe^{2+} and Fe^{3+} rich phases shows that the oxidized fraction of Fe constitutes the overall of the saprolite remains and no unweathered primary hydrothermal serpentine relicts with reduced Fe are detected (**Fig. 7.1c4**). A Fe K-edge μXANES has been acquired in one representative point of the protolith fragment (**Fig. 7.3f**), and according to the fitting data in **Table 7.2** the Fe is mostly as Fe^{3+} and correspond to 42.8 % maghemite, 27.8 % serpentine and 29.6% goethite. This data confirms that significant amounts of goethite started to develop, suggesting an advanced weathering stage of the saprolite.

7.4. LOCAL ENVIRONMENT OF Ni (μEXAFS)

To study the Ni local environment in the serpentine from the saprolite, the primary hydrothermal serpentine and in the different garnierite types, Ni K-edge μEXAFS have been acquired on representative points of LC101A, LC100B, GAR2C, GAR6C and FALC3 samples (marked in **Figs. 7.1a3, b3, c3, d3, e3).** The Ni local environment has been fitted taking into account the parameters and constraints of Ni within the minerals constituting the saprolite fragments and the garnierites. In order to have accurate fittings, special attention has been given to the second coordination shell. In EXAFS, the phase shift of the scattered photoelectrons depends on the chemical nature of the backscattering atom. This allows distinguishing between Ni and Mg second coordination shells in phyllosilicates if some constraints are applied on Ni-Ni and Ni-Mg distances. According to Manceau and coauthors (Manceau & Calas, 1985a; 1985b; Manceau *et al.*, 1985; Manceau & Calas, 1986; Manceau, 1990) the interatomic distances in the octahedral layer of Ni-bearing phyllosilicates should be close to 3.06 Å, otherwise it cannot be considered a correct second shell fit. This constrain was taken into account across Ni K-edge μEXAFS fittings, and when it did not apply, other Ni local environments were considered which were still consistent with the mineral assemblages in the saprolite horizon of the Falcondo Ni-laterite deposit.

In the sample LC101A, three Ni K-edge μEXAFS have been acquired, corresponding to: i) the primary hydrothermal serpentine veins (LC101A_1); ii) the saprolite fragment (LC101A_2); and iii) the type I garnierite surrounding the saprolite fragments (LC101A_3) (**Figs. 7.1a3**, **7.4**). Qualitatively, the LC101A_1 and LC101A_2 spectra show significant differences when compared to the LC101A_3 spectrum (**Fig. 7.4**). In the FT($\chi(k)$), the second shell peak between ~2 and 3.5 Å is clearly enhanced in LC101A_3. This is strongly indicative of different local environments of Ni within the garnierite veins and the saprolite fragments. (**Fig. 7.4**).

In the primary hydrothermal serpentine (LC101A_1), the FT($\chi(k)$) second shell peak can be fitted with Ni-Mg shells. There is a shell with 4.6 Mg atoms at 3 Å and another shell with 3.1 Si atoms at 3.3 Å (**Table 7.3**), similar to the values presented by Dublet *et al.* (2012) in the Ni-poor serpentine from the saprolite horizon and by Fan & Gerson (2011) in the saprolite. In the saprolite fragment (LC101A_2), the FT($\chi(k)$) peak has an even better fit with a Ni site that has a Ni-Ni shell partially substituted by Mg. The FT($\chi(k)$) peak can be fitted with a 2.9 Ni shell at 3.06 Å partially substituted by 3.1 Mg at 3.06 Å (**Fig. 7.4**, **Table 7.3**). These values are comparable to those obtained in Ni-bearing lizardite by Manceau & Calas (1985), but with lower Ni in the second shell. In contrast, the FT($\chi(k)$) prominent second peak at 2.8-2.9 Å in type I garnierite (LC101A_3) suggests a second atom shell of higher atomic number than for the second shell in LC101A_1 and LC101A_2. The EXAFS fitting values (**Table 7.3**) demonstrate that the second shell peak for LC101A_3 on the garnierite matrix can be fit with 5.2 Ni at 3.04Å and 3.8 Si at 3.17Å. The Ni-Ni distances close to 3.06 Å are consistent with edge-sharing NiO_6 and the Ni-Si distance close to 3.3 Å is coherent with edge-sharing between SiO_4 tetrahedra and NiO_6 octahedra in both the T-O serpentine group minerals and of T-O-T structures of talc-like kerolite-pimelite (Manceau & Calas, 1985a; 1985b; Manceau *et al.*, 1985; Manceau & Calas, 1986; Manceau, 1990).

In the sample LC100B, two Ni K-edge μEXAFS points were obtained: i) one in an area of the saprolite fragment with both Fe^{2+} and Fe^{3+} detected by μXANES (LC100B_1), and ii) the other on the type II garnierite (LC100B_2) (**Figs. 7.1b3**, **7.4**). As in sample LC101A, the spectra of saprolite

serpentine and of garnierite display significant differences of Ni local environment that are visible in the corresponding FT(χ(k)) second shell peaks between ~2 and 3.5 Å. The prominent second peak at 2.8-2.9 Å in the type II garnierite (LC100B_2) suggests a second shell of higher atomic number than for the second shell in the saprolite fragment (LC100B_1) (**Fig. 7.4**). The μEXAFS fitting values show that the second shell peak for saprolite serpentine has a better fit with a Ni site with a second Ni-Ni shell partially subtituted by Mg at 3.08Å with 5.7 Ni and 0.3 Mg and 4.24 Si at 3.21 Å. In this site the Ni-Ni and Ni-Mg distances are close to 3.06 Å and the Ni-Si distances are close to 3.3 Å. The interatomic distances are comparable to those of the Ni-rich serpentine from the saprolite horizon in Dublet *et al*. (2012) and in the saprolite in Fan & Gerson (2011), but the shell has more Ni. The second shell of type II garnierite can be fit with a combination of 4.8 Ni at 3.04 Å and 2.9 Si at 3.17 Å (**Table 7.3**). The Ni-Ni distances close to 3.06 Å and the Ni environment are consistent with those of Ni-bearing Mg-phyllosilicates (Manceau & Calas, 1985a; 1985b; Manceau *et al.*, 1985; Manceau & Calas, 1986).

To study the local environment of Ni within the GAR2C ROI a Ni K-edge μEXAFS spectrum was obtained on the type III garnierite coating (GAR2C_1) (**Figs. 7.1c3**; **7.4**). No Ni K-edge μEXAFS were performed on the saprolite fragment since no significant amounts of Ni were detected. Qualitatively the GAR2C_1 spectra displays similar FT(χ(k)) features to those in garnierite types I (LC101A_3) and II (LC100B_2) with a prominent second shell peak between 2.8 and 2.9 Å (**Fig. 7.4**). This peak can be fit with a combination of 3.72 Ni at 3.08 Å and 2.04 Si at 3.24 Å (**Table 7.3**). The Ni-Ni distances close to 3.06 Å are consistent with edge-sharing NiO_6, and the Ni-Si distance close to 3.3 Å is consistent with edge-sharing between SiO_4 tetrahedra and NiO_6 octahedra in Ni-bearing Mg-phyllosilicates (Manceau & Calas, 1985a; 1985b; Manceau *et al.*, 1985; Manceau & Calas, 1986; Manceau, 1990). However, the coordination of Ni-Ni is slightly defective suggesting that local environment may be highly disordered or partly depleted in Ni. This is coherent with the low crystallinity features observed in the abundant kerolite-pimelite particles observed under TEM (see **Chapter 5**; Villanova de Benavent *et al*., 2011a; 2011b; *in press*).

All the analysed spots on GAR6C, regardless of their Ni content (**Fig. 7.1d3**), show FT(χ(k)) prominent second shell peaks between 2.8 and 2.9 Å suggest that the second shell atoms are of Ni, and that they can be fit with a combination of 6 Ni at 3.06 Å and 4 Si at 3.3 Å (**Fig. 7.5**, **Table 7.4).** In type IV the coordination numbers and the interatomic distances obtained are consistent with edge-sharing NiO_6 and with edge-sharing between SiO_4 tetrahedra and NiO_6 octahedra in the kerolite-pimelite series determined by Manceau and coauthors (Manceau & Calas, 1985a; 1985b; Manceau *et al.*, 1985; Manceau & Calas, 1986). However, these FT(χ(k)) show some particular differences when compared to the previous garnierites. μEXAFS in type IV garnierite displays a second shell peak less prominent than those in type I (LC101A_3), type II (LC100B_2) and type III (GAR2C_1) garnierites, but remarkably higher than those of the saprolite fragments (L101A_1-2, LC100B_1).

In the FALC3 ROI four Ni K-edge EXAFS were acquired in the areas with low Ni (FALC3_2, FALC3_3, FALC3_5, FALC_6) and two in the areas with higher Ni (FALC3_1, FALC3_4) (**Fig. 7.1e3**). Their FT(χ(k)) show the distinctive second shell peak at 2.8-2.9 Å with no significant qualitative variations across the analysed points. Although, the sepiolite-falcondoite second shell peaks are slightly less prominent than those obtained in the other garnierite types (**Fig. 7.6**). The height of the FT($\chi(k)$) second shell peaks at 2.8-2.9 Å still suggests that the second shell atoms are of Ni and it has been confirmed with the subsequent EXAFS fittings. This second peak can be fit with a combination of Ni and Si with coordination numbers close to 3 and 4 respectively, and with the Ni-Ni distances close to 3.06 Å and the Ni-Si distances close to 3.3 Å (**Table 7.5**). As in the other garnierite types, the distances obtained in type V garnierite are consistent with edge-sharing NiO_6 and with edge-sharing between SiO_4 tetrahedra and NiO_6 octahedra as described by Manceau and coauthors in Ni-bearing phyllosilicates (Manceau & Calas, 1985a; 1985b; Manceau *et al*., 1985; Manceau & Calas, 1986; Manceau, 1990). However, the low coordination values for the second coordination shell suggests that this second shell may be consistently depleted in Ni within the sepiolite-falcondoite mineral series when compared to the other garnierite types.

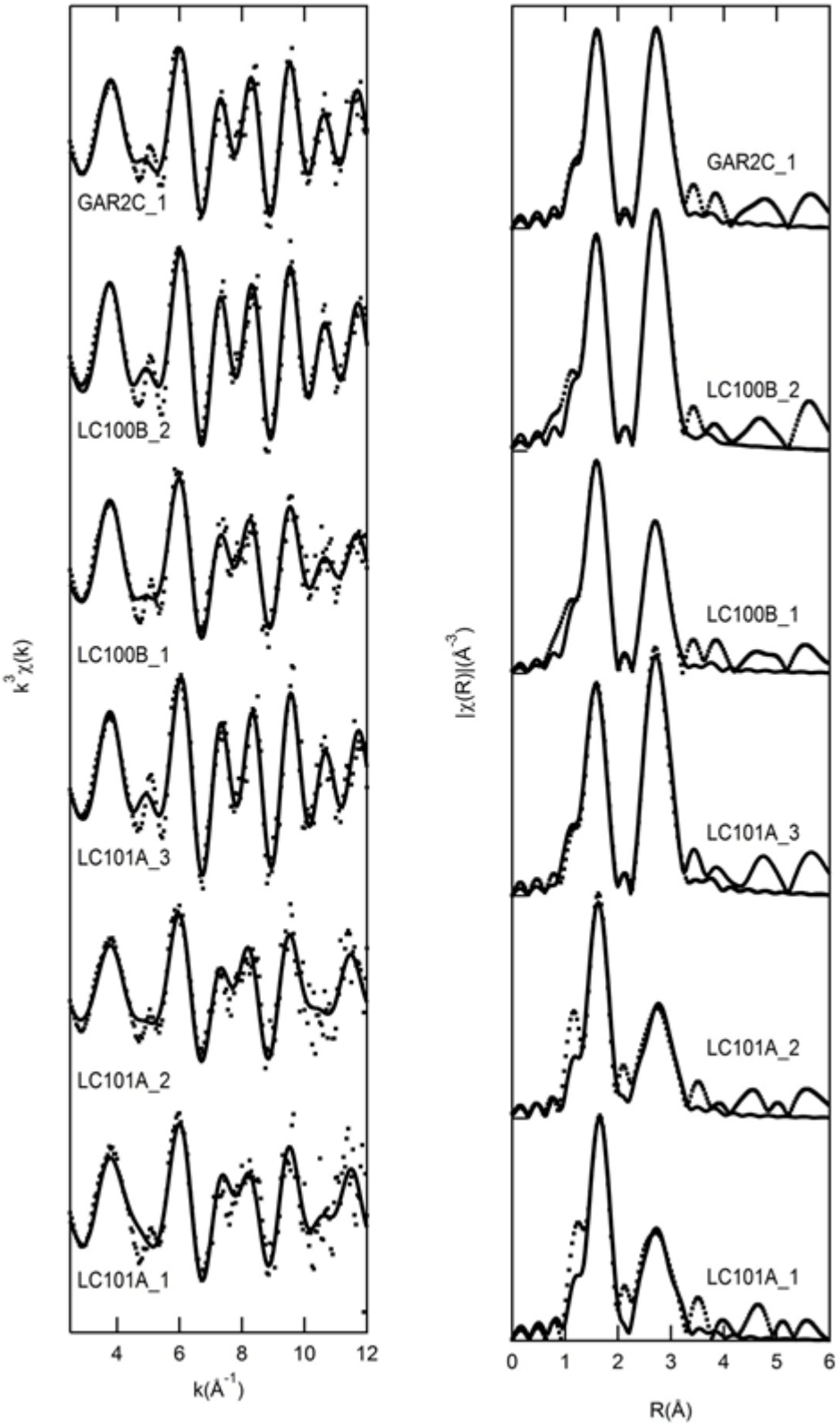

FIGURE 7.4. Ni K-edge μEXAFS, the corresponding FT($\chi(k)$) and the resulting fits from samples LC101A, LC100B and GAR2C. The differences on the second shell peak height at 2.8-2.9 Å are clearly visible.

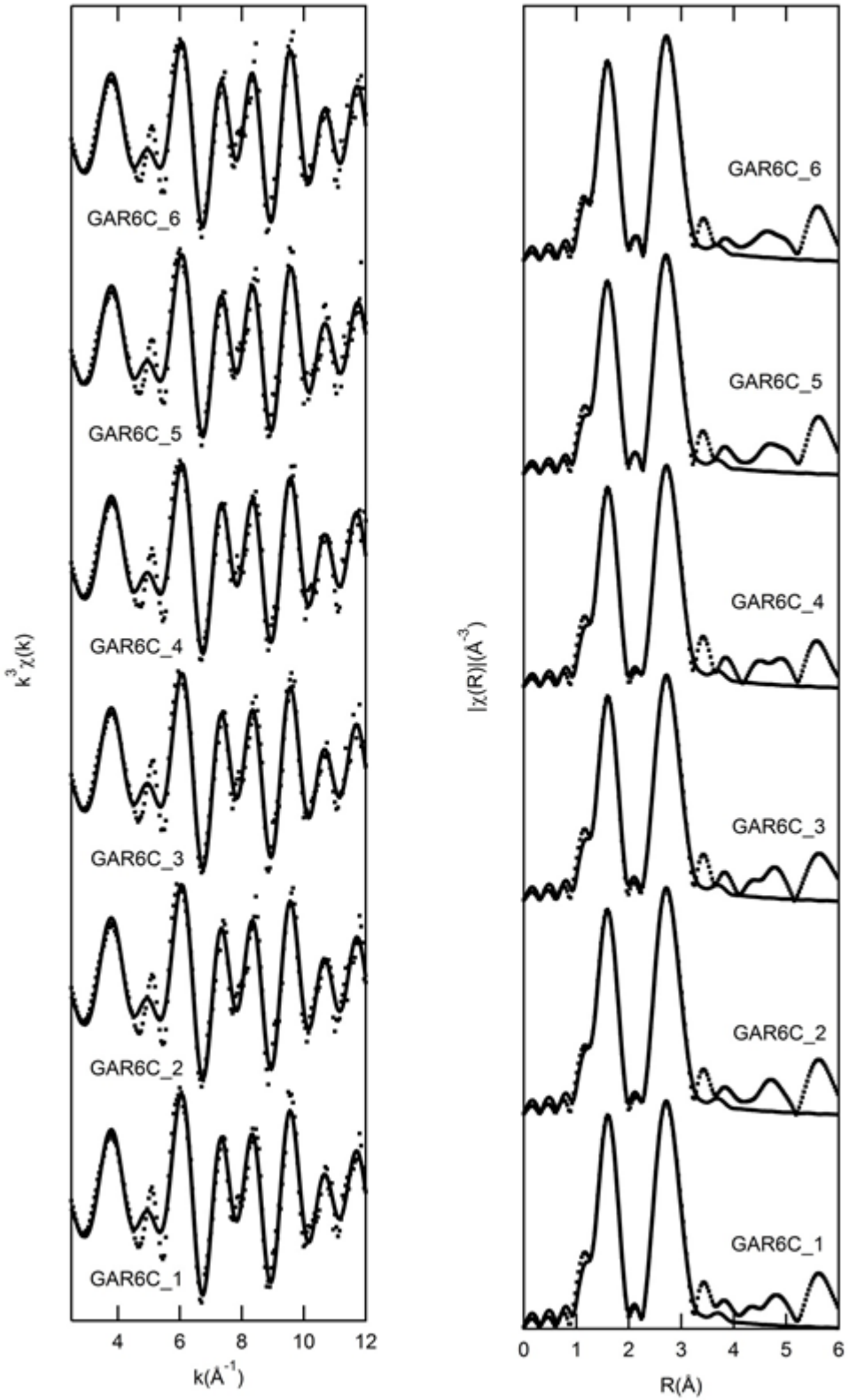

FIGURE 7.5. Ni K-edge μEXAFS, the corresponding FT($\chi(k)$) and the resulting fits from sample GAR6C. No differences on the second shell peak height at 2.8-2.9 Å are visible despite of the different Ni content.

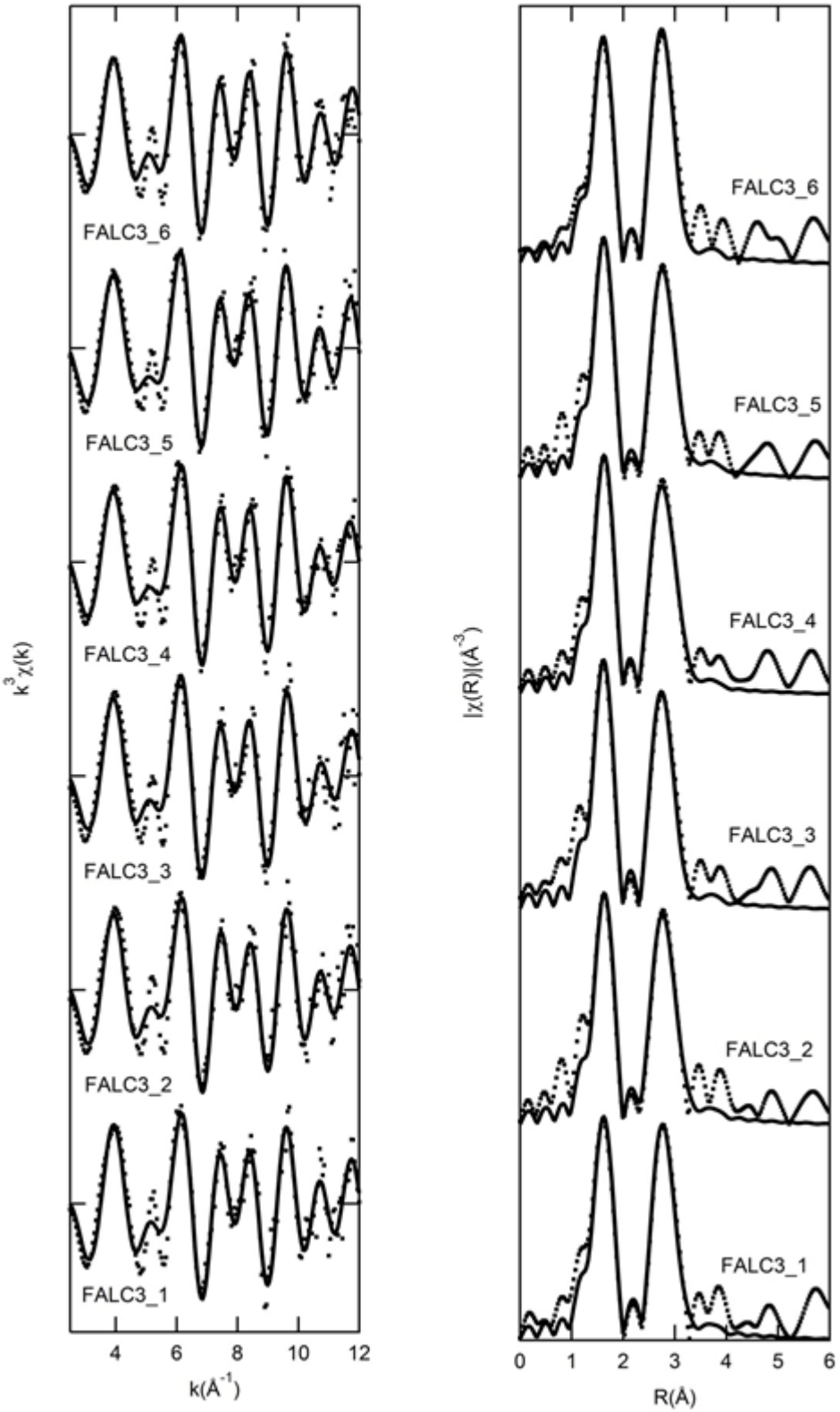

FIGURE 7.6. Ni K-edge μEXAFS, the corresponding FT($\chi(k)$) and the resulting fits from sample FALC3. No major changes on the second shell peak height at 2.8-2.9 Å are visible.

TABLE 7.3. Fitting values for Ni K-edge μEXAFS in LC101A, LC100B and GAR2C. Legend: R(Å) = interatomic distances; N = number of neighboring atoms; ss2 = the Debye-Waller factor; E0 (eV) = the difference between the defined threshold energy and the experimentally determined threshold energy; R-factor = the fit coefficient; RedChi2 = goodness of fit.

Sample	LC101_1 saprolite			LC101_2 saprolite				LC101_3 type I			LC100_1 saprolite				LC100_2 type II			GAR2_1 type III		
shell	Ni-O	Ni-Mg	Ni-Si	Ni-O	Ni-Ni	Ni-Mg	Ni-Si	Ni-O	Ni-Ni	Ni-Si	Ni-O	Ni-Ni	Ni-Mg	Ni-Si	Ni-O	Ni-Ni	Ni-Si	Ni-O	Ni-Ni	Ni-Si
R(Å)	2.08	3	3.3	2.06	3.06	3.06	3.3	2.06	3.04	3.17	2.06	3.08	3.08	3.17	2.06	3.08	3.21	2.06	3.08	3.24
N	4.6	4.6	3.1	4.2	2.9	3.1	2.8	5.2	5.2	3.8	5.8	5.7	0.3	3.9	4.8	5.22	4.24	4.8	3.72	2.04
Ss2	0	0.01	0	0	0.011	0.011	0	0.01	0.01	0.01	0.01	0.01	0.01	0.01	0.01	0.01	0.01	0.01	0.01	0.01
E0	1.23			-3.46				-3.28			-3.46				-3.39			-2.45		
R-factor	3.30E-02			2.00E-02				4.10E-03			2.00E-02				1.00E-03			1.00E-03		
RedChi2	9.22			8.12				6.09			8.12				8.28			3.98		

TABLE 7.4. Fitting values for Ni K-edge μEXAFS in GAR6C (type IV garnierite). Legend: R(Å) = interatomic distances; N = number of neighboring atoms; ss2 = the Debye-Waller factor; E0 (eV) = the difference between the defined threshold energy and the experimentally determined threshold energy; R-factor = the fit coefficient; RedChi2 = goodness of fit.

Sample	GAR6_1			GAR6_2			GAR6_3			GAR6_4			GAR6_5			GAR6_6		
shell	Ni-O	Ni-Ni	Ni-Si	Ni-O	Ni-Ni	Ni-Si	Ni-O	Ni-Ni	Ni-Si	Ni-O	Ni-Ni	Ni-Si	Ni-O	Ni-Ni	Ni-Si	Ni-O	Ni-Ni	Ni-Si
R(Å)	2.06	3.08	3.24	2.06	3.08	3.24	2.06	3.08	3.25	2.06	3.08	3.24	2.05	3.07	3.21	2.06	3.07	3.23
N	5.12	5.05	3.2	5.04	4.68	3.36	4.68	4.68	3.36	5.04	4.68	3.4	4.56	4.99	3.99	4.56	4.08	3.88
Ss2	0.01	0.006	0.01	0.01	0.005	0.007	0.01	0	0.01	0.01	0.01	0.01	0.01	0.01	0.01	0.01	0.01	0.01
E0	-0.05			-3.46			-3.28			-4.63			-3.39			-2.45		
R-factor	2.00E-02			2.00E-02			4.10E-03			1.00E-03			1.00E-03			1.00E-03		
RedChi2	7.47			8.12			6.09			1.27			8.28			3.98		

TABLE 7.5. Fitting values for Ni K-edge μEXAFS in FALC3 (type V garnierite). Legend: R(Å) = interatomic distances; N = number of neighboring atoms; ss2 = the Debye-Waller factor; E0 (eV) = the difference between the defined threshold energy and the experimentally determined threshold energy; R-factor = the fit coefficient; RedChi2 = goodness of fit.

Sample	Falc3_1			FALC3_2			FALC3_3			FALC3_4			FALC3_5			FALC3_6		
shell	Ni-O	Ni-Ni	Ni-Si	Ni-O	Ni-Ni	Ni-Si	Ni-O	Ni-Ni	Ni-Si	Ni-O	Ni-Ni	Ni-Si	Ni-O	Ni-Ni	Ni-Si	Ni-O	Ni-Ni	Ni-Si
R(Å)	2.06	3.09	3.23	2.07	3.07	3.26	2.06	3.07	3.24	2.06	3.07	3.26	2.05	3.08	3.25	2.06	3.08	3.2
N	5.34	3.04	5.08	5.1	2.82	3.72	5.34	3.6	3.56	5.04	3.18	3.36	5.52	3.48	2.72	5.1	5.1	3.44
Ss2	0.01	0.006	0.01	0.01	0.007	0.003	0.01	0.01	0	0.01	0.01	0	0.01	0.01	0	0.01	0.01	0.01
E0	1.69			2.34			1.17			1.88			1.54			1.43		
R-factor	4.80E-03			4.60E-03			5.10E-03			3.60E-03			2.70E-03			7.20E-03		
RedChi2	8.42			8.79			7.15			17.8			8.51			20.05		

In general, the Ni-Mg and Ni-Si distances are coherent with the Mg-Mg and Mg-Si interatomic distances in serpentine group minerals (Dublet *et al*., 2012) and the Ni-Mg, Ni-Ni and Ni-Si distances in Ni-bearing phyllosilicates (Manceau & Calas, 1985a; 1985b).

7.5. DISCUSSION

The results obtained in this chapter provide valuable insights to understand the processes of Ni enrichment in the saprolite horizon and the precipitation of garnierites from a crystallochemical point of view. These results can be compared to those previously obtained in the saprolite serpentine from New Caledonia (Dublet *et al*., 2012) and the Philippines (Fan & Gerson, 2011), in lizardite–népouite and kerolite–pimelite from New Caledonia (e.g. Manceau & Calas, 1985), and the preliminary data on Ni-sepiolite from the Dominican Republic (Roqué-Rosell *et al*., 2011).

7.5.1. The distribution of Ni and Fe among the saprolite serpentines and the garnierites

The chemical compositions of the saprolite fragments mostly remain similar when associated to type I, II and III garnierites, with the only exception of the NiO content that drops significantly to almost disappear in saprolite fragments associated to type III garnierite (**Figs. 7.1a3-c3**; **Table 7.2**). This may indicate that type III garnierites occur at later stages than types I and II, which is coherent with their Ni, and SiO_2 content (see **Chapter 4**). During weathering, the Mg is leached out of the primary ultramafic rock and the saprolite horizon while Fe is concentrated in the limonite horizon, leading to a replacement of serpentine and other primary ferromagnesian silicates by goethite and other Fe-oxyhydroxides (e.g. Freyssinet *et al*., 2005). Simultaneously, the laterite profile is progressively enriched in Ni and Si, which is indicated by the early precipitation of low Ni serpentine-like phases, followed by higher Ni talc-like phases and finally sepiolite-like phases Galí *et al*. (2012) and Villanova-de-Benavent *et al*. (2014b).

In addition, as detected by the X-ray quantified element EMP maps in **Chapter 4**, the variations in Ni content in the garnierite types IV (kerolite-pimelite) and V (sepiolite-falcondoite) related to different textures observed in the µXRF maps may be explained by recurrent changes in the physical–chemical conditions of the Ni and Si saturated aqueous solution that formed the Ni-bearing phyllosilicates (Villanova-de-Benavent *et al*., 2014; **Chapter 4**).

7.5.2. Ferrous (Fe^{2+}) versus ferric (Fe^{3+}) iron in the Ni-laterite profile

The Fe K-edge µXANES maps allowed distinguishing the Ni-enriched secondary serpentine and Fe-bearing garnierite (type I) from the hydrothermal primary serpentine by the oxidation state of iron.

While the primary ferromagnesian anhydrous silicates (mostly olivine and pyroxene) of the peridotitic protolith are likely to be weathered when the ophiolite complex is exposed to the intense rainfall and temperatures of tropical latitudes, the hydrothermal serpentine veins, formed prior to the exhumation, may remain more stable (Golightly, 1981; 2010; Gleeson *et al*., 2003). This hydrothermal serpentine has a small amount of Fe in the form of Fe^{2+}. However, during the formation of the Ni-laterite profile, the primary olivine and pyroxene are altered to the Ni-Fe-bearing serpentine that constitutes the saprolite horizon. This secondary serpentine incorporates Ni from the Ni-saturated aqueous solutions percolating from the upper horizons, and the iron in the structure of the serpentine is oxidised. In the case of type I garnierite, formed by chrysotile tubes and traces of kerolite-pimelite lamellae and precipitated in veins, the iron is thought to be residual (Villanova-de-Benavent *et al*., 2014b).

7.5.3. The local environment of Ni as indicator of weathering

The present study indicates that the local environment of Ni in Ni-bearing phyllosilicates does not depend on the mineralogy (serpentine-like, versus talc-like and sepiolite-like), but on the origin of the phase (inherited/relict and weathered).

The primary hydrothermal serpentine Ni K-edge µEXAFS revealed that Ni is found homogeneously distributed in the octahedral sheet, that is to say that there is solid solution between Mg and Ni. In the secondary serpentine from the saprolite, the steady increase in height of the second shell peak may indicate that Ni is distributed homogeneously but with incipient clustering in the serpentine structure. However, Ni is uniquely found forming clusters inside the crystalline structures of all garnierite types. The Ni atoms are completely surrounded by Ni, and therefore form clusters (heterogeneous distribution) (**Fig. 7.7**).

This different local Ni environment may be explained by the substitution of Mg by Ni to form the Ni-enriched serpentines of the saprolite, as well as by the precipitation of Ni-bearing fine grained phyllosilicates (garnierites) from Ni and Si saturated aqueous solutions in veins. These processes, under atmospheric conditions, lead to an inhomogeneous distribution of Ni atoms in discrete domains in the octahedral layer.

Furthermore, there are some systematic differences from the expected ideal Ni-Ni second shell coordination number and the obtained values by means of Ni K-edge μEXAFS. According to the synchrotron measurements, the second Ni-Ni shell coordination number in kerolite-pimelite (type IV) and sepiolite-falcondoite (type V) is systematically lower when compared to talc and sepiolite theoretical values. These differences are not observed on the measured first Ni-O coordination shells which remain close to the theory. The agreement with the experimental and theoretical coordination values for the Ni-O shells and the discrepancy with the experimental and theoretical coordination values for the Ni-Ni shells are indicative of intrinsic features of the material and discards other explanations affecting the FT(χ(k)) peaks such as overabsorption.

In kerolite-pimelite, the best Ni K-edge μEXAFS fit was obtained with a model of Ni clustered and only surrounded by a defective shell of Ni. This can be justified by the disordered nature of this talc-like phase, as observed under TEM (**Chapter 5**; Villanova-de-Benavent *et al*., 2011a; 2011b; in press).

In sepiolite-falcondoite, Ni is only surrounded by Ni forming clusters and the small decrease of the FT($\chi(k)$) second peak when compared to garnierite types I, II, III and IV is attributed to Ni depleted shells. The depletion of Ni is thought to be related to the important discontinuities of the octahedral layer of the sepiolite structure, consisting of channels along the *c* axis (Post *et al.*, 2007). These channels truncate the horizontal layers of NiO_6 octahedra and thus lower the overall local Ni coordination in Ni-bearing sepiolite. Thus the coordination numbers and the distances in sepiolite-falcondoite are consistent with discontinuous layers of edge-sharing NiO_6 octahedra and with edge-sharing between SiO_4 tetrahedra and NiO_6 octahedra. According to its symmetry the sepiolite structure has 4 Ni atoms in Wyckoff postions, with two Ni positions coordinated with another 6 second shell atoms, one Ni position coordinated with 5 second shell atoms and one last Ni position coordinated with 3 second shell atoms. The overall is an average of 5 second shell atoms for each Ni position in sepiolite (Post *et al.*, 2007). Because of the lower symmetry in the talc structure the Ni atoms in Wyckoff positions in talc are 2 and according to its crystalline structure both are coordinated by another 6 second shell atoms (Gruner, 1934). Thus the differences observed in the FT($\chi(k)$) second peak from type V garnierite when compared to types II, III, and IV are in agreement with ideal second shell coordination for Ni being smaller in sepiolite than in talc.

Manceau and coauthors (Manceau & Calas, 1985a; 1985b; Manceau *et al*., 1985; Manceau & Calas, 1986) found by bulk EXAFS that Ni in Ni-bearing serpentine (particularly of the lizardite-népouite series) is heterogeneously distributed in the octahedral layer, whereas Ni and Mg in hydrated talc (kerolite-pimelite series) can be either i) clustered within the octahedral sheet or ii) be irregularly distributed in the structure, forming mixtures of kerolite and pimelite at the scale of several layers. In addition, the authors determined that Ni is essentially surrounded by heavy atoms (Ni, Fe) even in clay minerals of low Ni and Fe contents, there is clear evidence of the heterogeneous substitution of Mg by transition elements (Manceau & Calas, 1985a; 1985b). From these premises, the authors stated that the Ni-enriched serpentine from the saprolite is formed by the transformation of low Ni-primary serpentines by means of a Ni-enrichment and a subsequent Mg loss and that kerolite-pimelite are precipitated from a solution, pointing out distinct formation conditions.

In the case of the results obtained in the Falcondo Ni-laterite deposit, homogeneously distributed Ni (solid solution) is found in serpentines formed prior to the exhumation and weathering (the primary hydrothermal serpentine relicts), whereas clustering of Ni occurs in all the phyllosilicate structures (serpentine, including saprolite serpentine, talc and sepiolite) and is linked to lateritisation. Dublet *et al*. (2012) already reported that Ni is randomly distributed in the Ni-poor serpentines from the bedrock (peridotite) and clustered in the Ni-rich serpentines from the saprolite.

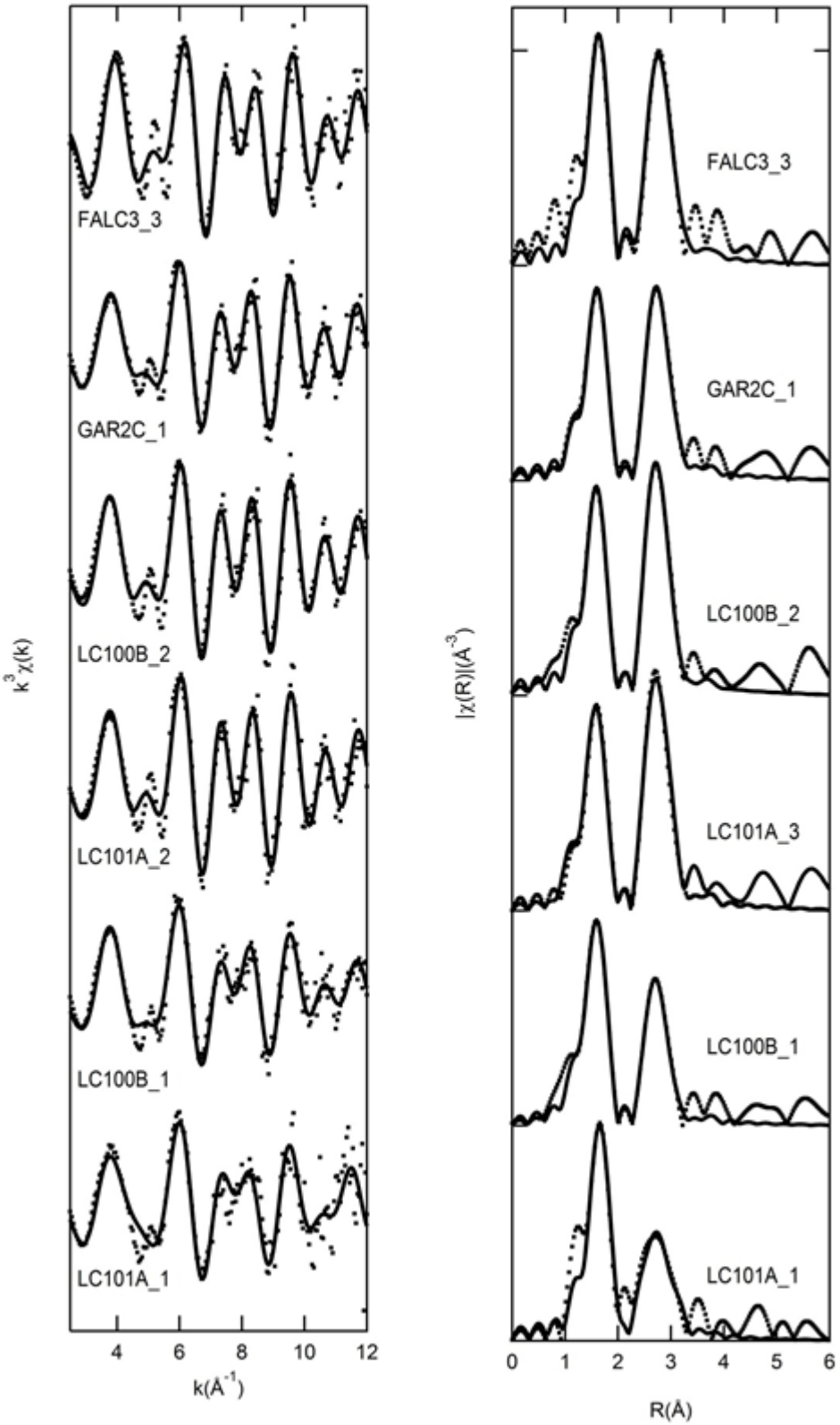

FIGURE 7.7. Ni K-edge μEXAFS from samples LC101A, LC100B, GAR2C and FALC3 highlighting the main differences on Ni local environment between primary hydrothermal and saprolite serpentine (LC101A_1 and LC100B_1, respectively) and garnierite types I (LC101A_3), II (LC100B_2), III (GAR2C_1) and V (FALC3_3).

7.6. FINAL REMARKS

By combining the μXRF maps with the Fe K-edge μXANES and Ni K-edge μEXAFS with the information gathered from the previous chapters, the following conclusions can be extracted:

The saprolite fragments consist mainly of Ni-Fe-enriched serpentines in which Fe is mostly in the ferric form (Fe^{3+}), and Ni is randomly distributed in the octahedral layer (homogeneous distribution). In addition, some relicts of the Ni-poor primary hydrothermal serpentine have been identified within the weathered protolith with a characteristic high fraction of Fe^{2+} and with a distinctive Ni local environment with Ni forming a homogenous solid solution with Mg.

All the garnierite types studied show similarities in the Ni distribution, regardless of the Ni content and the mineralogy. In all garnierites the Ni is found forming clusters (heterogeneous distribution). Within the serpentine and the kerolite-pimelite that constitute the type I, II, III and IV garnierites the Ni is found forming a heterogeneous solid solution where Ni is surrounded exclusively by a second shell of Ni. This has been also the case on the sepiolite constituting the type V garnierite, where Ni is found forming clusters with a depleted second shell which is consistent discontinuous octahedral layers within its structure.

The μXAS results are consistent with the formation of the saprolite Ni-Fe-enriched serpentines from Ni-Mg substitution as a result of the interaction of the primary rock-forming minerals with a Ni-enriched solution; and of garnierites as precipitates from a Ni-Si-saturated aqueous solution at low temperatures.

8. DISSOLUTION KINETICS OF GARNIERITES

In general, the stability of Ni-bearing minerals in lateritic environments is determined by the Eh, pH, and chemical composition of permeating groundwater (e.g. Trescases, 1973). A first study of the dissolution kinetics of a garnierite from Loma de Hierro (Venezuela) was performed by Soler *et al*. (2008). It was found that the garnierite dissolution rate decreases with increasing pH. The dissolution showed to be congruent at pH > 5 and incongruent at pH < 5, indicating different contributions from serpentine and talc to the total dissolution rate (the serpentine component tends to dissolve faster under more strongly acidic conditions).

As deduced from previous chapters, the mineralogy and chemistry of garnierites is complex. For this reason, the overall aim of this chapter is to extend the study of the kinetics of garnierite dissolution in terms of the structures and compositions of the reacting garnierites. The dissolution kinetics of selected garnierite samples with well constrained mineralogical and chemical composition has been studied under acidic conditions (pH~3 and ~5) by means of non-stirred flow-through experiments.

For these experiments, seven samples were selected according to the different garnierite types described previously (**Chapters 4-7**). The mineralogy and mineral chemistry of the seven selected samples is summarised in **Table 8.1**, the average chemical composition of each sample is displayed in the ternary plot in **Figure 8.1**, and the binary diagram in **Figure 8.2** plots the talc fraction (Xtlc) versus the Ni content in all the analysed points.

These samples were prepared as described in **Section 3.8.1** and introduced into a reaction cell with a constant flux of an aqueous solution with pH~3 and ~5 for 1000-3000 hours (see **Section 3.8.2** for further details). The pH of the output solutions was kept around 3 and 6, respectively, although the output solution of the experiment with input pH~5 recorded large variations between 5 and 7. Achievement of steady state was verified by a series of constant Mg, Ni and Si output concentrations that differed by less than 5% during at least 500 h and 4-6 consecutive output samples.

The degree of saturation of the output solutions with respect to Si–Mg–Ni-bearing phases was calculated using the PHREEQC code, version 2.15.0 (Parkhurst & Appelo, 1999) and the LLNL thermodynamic database included in it. Calculations showed that the output solutions were highly undersaturated with respect to Si, Mg and Ni bearing phases (e.g. $Mg(OH)_2$, $Ni(OH)_2$, chrysotile, sepiolite, talc, anthophyllite, antigorite, enstatite, forsterite, Ni_2SiO_4) and slightly undersaturated with respect to quartz in the conditions of the experimental runs.

The output Mg, Ni and Si concentrations are presented in **Figures 8.3a1-2, b1-2, c1-2, d1-2, e1-2, f1-2, g1-2**, from which the molar Mg/Si, Ni/Si, Ni/Mg ratios and octa/tetra (octahedral divided by tetrahedral elements) were calculated and compared to their respective ratios in the mineral (solid molar ratios) in **Figures 8.3a3-4, b3-4, c3-4, d3-4, e3-4, f3-4, g3-4**.

Steady-state dissolution rates (in mol m^{-2} s^{-1}) were normalised with respect to both the final mass and the final specific surface area. As most sheet silicate dissolution rates are expressed in mol m^{-2} s^{-1}, the normalisation with the final BET specific surface area facilitates the comparison with rates reported in the literature (see Nagy, 1995). Both final mass and final specific surface area normalised values are included in **Table 8.2**. In most cases, final BET values were systematically higher (82-194 m^2 g^{-1}) than the initial BET surface area (33-176 m^2 g^{-1}).

Finally, the steady-state, BET normalised, Mg dissolution rate versus pH in the different garnierite types is represented in **Figure 8.4**, including the dissolution rate equation calculated parameters. Only the $\log R_{Mg\ BET}$ was taken into account because Mg is the fastest element to be released. The dissolution reactions of these garnierite types are listed in **Table 8.3**.

8.1. GARNIERITE DISSOLUTION RATES

In general, Mg, Ni and Si output concentrations are higher in a more acidic environment: below 20 μM at pH~5 and mostly between 10 and 200 μM at

TABLE 8.1. List of the selected samples including their mineralogy, average structural formulae, talc fraction (Xtlc, see **Section 3.6.2**), and Mg/Si, (Mg+Ni)/Si, Ni/Si and Ni/Mg ratios.

Label (Fig. 8.1)	Sample	Description	XRD	Structural formula [number of analyses averaged]	Xtlc	∑octa/∑ tetra	Mg/Si	Ni/Si	Ni/Mg
1	09GAR-2	serpentine + traces kerolite-pimelite	7.32 Å	$(Mg_{2.06}Ni_{0.77}Fe_{0.14})Si_{2.64}O_{6.69}(OH)_{3.33}\cdot nH_2O$ [6]	0.34	1.13	0.78	0.29	0.37
2	LC100-II	serpentine + minor kerolite-pimelite	7.30 Å + 1.20 Å	$(Mg_{1.57}Ni_{1.37}Fe_{0.06})(Si_{2.84}Al_{0.07})O_{7.27}(OH)_{3.09}\cdot nH_2O$ [7]	0.45	1.03	0.55	0.48	0.87
3	GAR-2	serpentine + kerolite-pimelite	7.40 Å + 10.56 Å	$(Ni_{2.42}Mg_{0.56}Fe_{0.01})Si_{2.71}O_{6.81}(OH)_{3.28}\cdot nH_2O$ [4]	0.36	1.10	0.21	0.89	4.32
4	GAR-6	pimelite	10.14 Å (±7.34 Å)	$(Ni_{1.83}Mg_{1.17})(Si_{3.54}Al_{0.01})O_{8.88}(OH)_{2.45}\cdot nH_2O$ [5]	0.78	0.85	0.33	0.52	1.56
5	LC100-IV	pimelite	9.94 Å (+ 7.39 Å)	$(Ni_{1.90}Mg_{1.10})(Si_{3.52}Al_{0.01})O_{8.83}(OH)_{2.47}\cdot nH_2O$ [4]	0.77	0.85	0.31	0.54	1.73
6	FALC-4	Ni-sepiolite	12.07 Å	$(Mg_{3.51}Ni_{0.26}Fe_{0.06})(Si_{6.05}Al_{0.01})O_{15}(OH)_2\cdot 6H_2O$ [16]		0.63	0.58	0.04	0.07
7	FALC-3	falcondoite	12.15 Å	$(Mg_{2.03}Ni_{1.95}Fe_{0.01})(Si_{5.95}Al_{0.06})O_{15}(OH)_2\cdot 6H_2O$ [4]		0.66	0.34	0.33	0.96

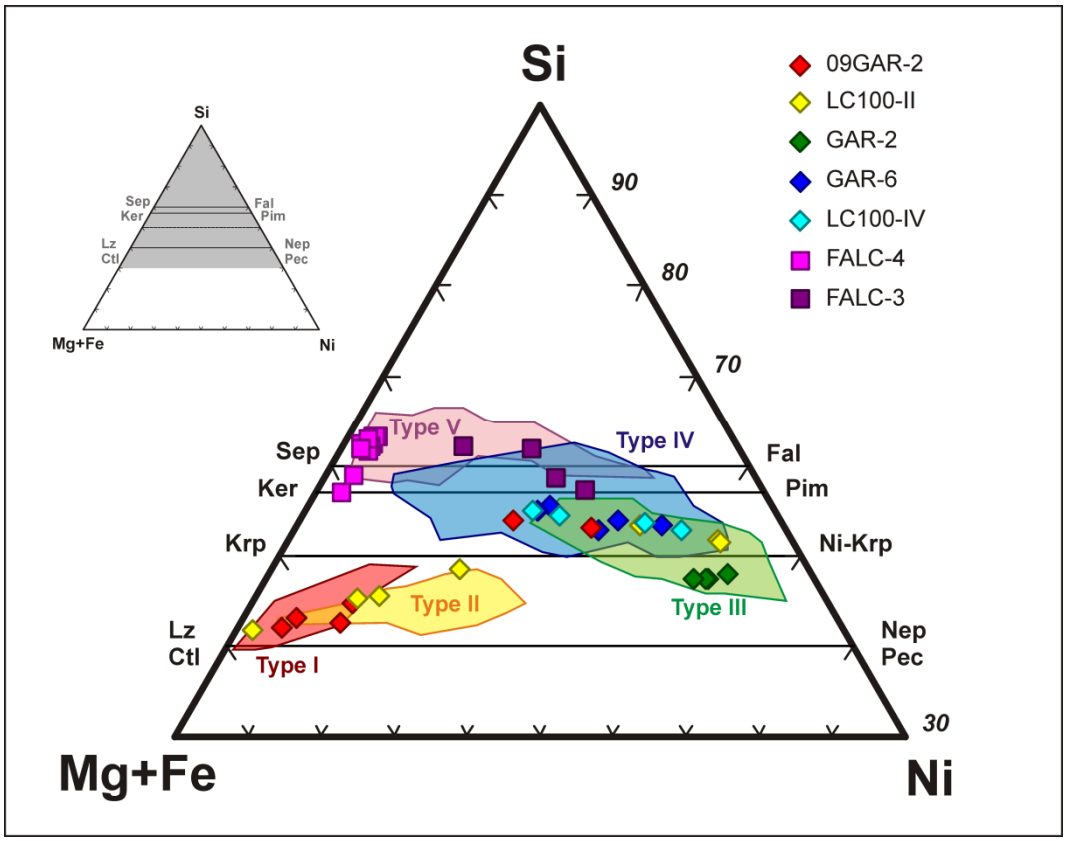

FIGURE 8.1. Triangular plot showing the composition of the six samples selected for the flow-through experiments (black circles), compared to the composition of the five garnierite types identified in **Chapter 4** (coloured fields), obtained by EMP.

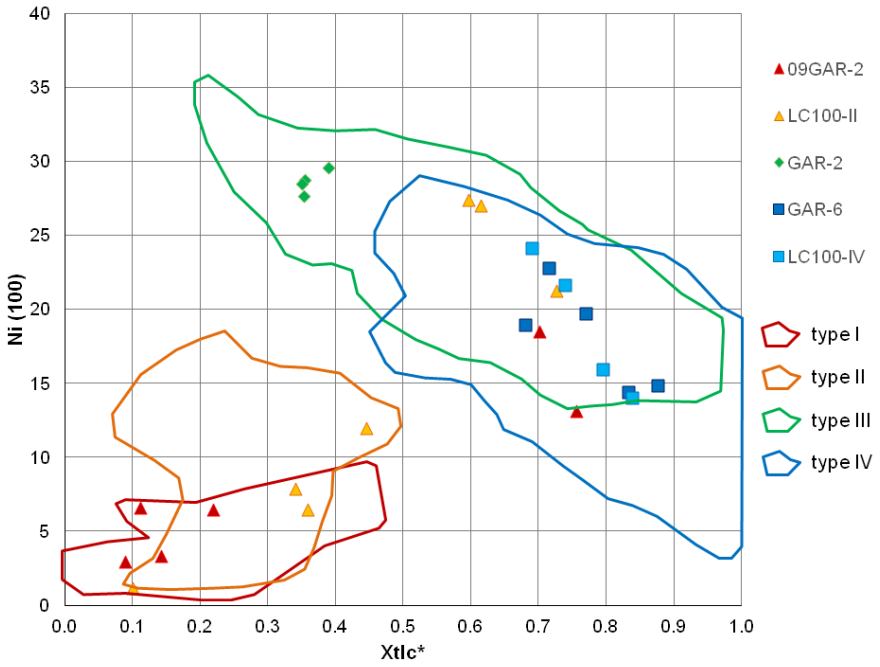

FIGURE 8.2. Binary plot of the talc fraction (Xtlc, see **Section 3.6.2**) versus the Ni content (calculated on the basis of 100 oxygens) of the samples selected for the dissolution experiment. The fields correspond to the Xtlc versus Ni(100) of all the analysed samples by garnierite type (see **Fig. 4.11** in **Chapter 4**).

pH~3 (**Figs. 8.3a1-2, b1-2, c1-2, d1-2, e1-2, f1-2, g1-2; 8.4**). Serpentine-dominated garnierites (09GAR-2 and LC100-II; **Figs. 8. 3a1-2, b1-2**) seem to display faster release of Mg, Ni and Si than kerolite (hydrated talc)-dominated garnierites (GAR-6 and LC100-IV; **Figs. 8.3c1-2, d1-2, e1-2**) and sepiolite-falcondoite (FALC-4 and FALC-3; **Figs. 8.3f1-2, g1-2**). Ni is always the less abundant element in the output solution, except in kerolite-dominated garnierites at pH~3 (**Figs. 8.3c1-2, d1-2**).

The steady-state dissolution rates, calculated according to **Eq. 7** (**Section 3.10.2**) and normalised to the final reactive surface area, are higher at pH~3 ($logR_{Mg\ BET}$ between -12.0 and -12.9 mol m^{-2} s^{-1}) than at pH~5 ($logR_{Mg\ BET}$ between -12.8 and -13.3 mol m^{-2} s^{-1}) (**Table 8.2**).

In serpentine-dominated garnierites, $logR_{Mg\ BET}$ equals -12.0 - -12.4 at pH~3, and -12.9 at pH~5; in kerolite-dominated garnierites, $logR_{Mg\ BET}$ varies from -12.6 to -12.9 at pH~3, and from -12.9 to -13 at pH~5 (**Table 8.2**). At pH~5, the Ni-poor sepiolite (0.25 apfu Ni, FALC-4) shows lower dissolution rate than the Ni-rich sepiolite (1.35 apfu Ni, FALC-3). At pH~3, the release of Ni is larger than that of Mg and Si in the sepiolite with higher Ni content. In both cases, the dissolution rates are lower than in serpentine-dominated and kerolite-dominated garnierites ($logR_{Mg\ BET}$ = -12.4 at pH~3, $logR_{Mg\ BET}$ = -12.8 - -13.1 at pH~5) (**Table 8.2**).

These rates are comparable to those obtained by Soler *et al*. (2008), with $logR_{Mg\ BET}$ ranging from -11.7 to -12 at pH around 3, and from -12.2 to -13 at pH around 5, in a garnierite with Xtlc 0.63 and 0.07 apfu Ni, and also close to those of talc published by Saldi *et al*. (2007), but far from those of chrysotile obtained at pH 7-10 and 25ºC in batch experiments (Bales & Morgan, 1985) (**Fig. 8.4**).

The equation of the dissolution rate for each sample was calculated according to **Eq. 8**:

$$R = k_{H^+} \times a_{H^+}^{n_{H+}} \quad \text{[Eq. 8]}$$

where R is the dissolution rate, k_{H^+} is the constant of the dissolution rate (equals 10 raised to the power of the independent term of the regression lines in **Fig. 8.4**), $a_{H^+}^{n_{H+}}$ indicates the variation of the rate with pH, and n_{H^+} is the slope of the regression lines in **Fig. 8.4** (Lasaga *et al*., 1994).

8.2. STOICHIOMETRY OF THE DISSOLUTION REACTION

The dissolution of the different garnierites from the Falcondo Ni-laterite deposit can be expressed by the reactions listed in **Table 8.3**.

In sample 09GAR-2 (Xtlc 0.34, 0.77 apfu Ni) at pH~5 the octa/tetra and Mg/Si ratios in the solution smoothly decrease with time, and are higher than but close to the ratios in the solid, and get closer to them with time. However, the Ni/Mg and Ni/Si ratios in the solution are below those of the solid. In short, Mg and Si are released at the same rate, and Ni is released at a very low rate (**Fig. 8.3a3**). At pH~3 the tetra/octa and Mg/Si ratios increase rapidly at the beginning of the experiment and get close to the solid ratios with time, whereas the Ni/Mg and Ni/Si ratios decrease at the beginning of the experiment and are kept constant, far away from the solid ratios. That is to say, Mg is released more rapidly than the other elements (**Fig. 8.3a4**).

In LC100-II (Xtlc 0.45, 1.37 apfu Ni), at pH~5 the octa/tetra and Mg/Si ratios increase smoothly. Only the solution octa/tetra ratio approaches the solid ratio, which is close to 1 (**Fig. 8.3b3**). At pH~3 the octa/tetra and Mg/Si ratios behave similarly as at pH5 but with an early increase. The Ni/Si and Ni/Mg ratios slightly increase with time. In this case, the octa/tetra ratio is the only one close to the solid value as well (**Fig. 8.3b4**).

In GAR-2 (Xtlc 0.36, 2.42 apfu Ni), at both pH~5 and pH~3 the octa/tetra ratio is approximately constant, and Mg/Si and Ni/Si ratios have an early increase and immediate decrease with time. These three ratios approach their corresponding solid ratios. In contrast, the Ni/Mg ratio increases slowly and does not get so close to the solid ratio (**Fig. 8.3c3**). However, at pH~3 the Ni/Mg ratio increases and decreases steeply at the beginning of the experiment and approach the solid ratio. The other three are approximately constant and keep near their corresponding solid ratios. This is exclusive of this garnierite type (**Fig. 8.3c4**).

In GAR-6 (Xtlc 0.78, 1.83 apfu Ni), at pH~5 the octa/tetra and Mg/Si solution ratios increase and decrease at the beginning of the experiment and Ni/Si and Ni/Mg ratios increase. Only Ni/Si ratio becomes near the solid ratio with time (**Fig. 8.3d3**). At pH~3 the behaviour of octa/tetra and Mg/Si is the opposite to that of pH~5, and the behaviour of Ni/Si and Ni/Mg is similar to that of octa/tetra and

TABLE 8.2. Experimental conditions and steady-state values used to calculate the dissolution rate constants ($mol \cdot m^{-2} \cdot s^{-1}$).

Label (Fig. 8.1)	Sample	Run time (h)	initial pH	final pH	Output Mg (μM)	Output Ni (μM)	Output Si (μM)	Mg/Si	(Mg+Ni)/Si	Ni/Si	Ni/Mg	Initial mass (g)	Initial BET surface ($m^2 \cdot g^{-1}$)	Final mass (g)	Final BET surface ($m^2 \cdot g^{-1}$)
1	09GAR2-3	3067.8	3.02	3.05	47.01	4	41.77	1.13	1.22	0.1	0.09	0.217	106	0.11	144
	09GAR2-5	3067.5	4.61	6.12	10.24	1.8	10.81	0.95	1.11	0.17	0.18	0.1891	106	0.1681	110
2	LC100II-3	2299.2	2.997	3.03	23.38	3.9	24.74	0.95	1.1	0.16	0.17	0.1576	90	0.0409	117
	LC100II-5	2299	4.66	5.75	14.73	1.77	14.19	1.04	1.16	0.12	0.12	0.1678	90	0.1268	110
3	GAR2-3	1202.5	3.06	3.2	33.39	145.38	118.87	0.28	1.5	1.22	4.35	0.8342	103	0.6949	144
	GAR2-5	1202.3	4.9	5.22	2.35	5.41	6.13	0.38	1.27	0.88	2.3	0.7863	103	0.7332	82
4	GAR6-3	1527.4	3.02	3.05	15.73	15.13	11.35	1.39	2.72	1.33	0.96	0.3447	70	0.3004	126
	GAR6-5	1527.5	4.9	5.43	2.83	3.06	5.18	0.55	1.14	0.59	1.08	0.3473	70	0.3289	126
5	LC100IV-3	1100.1	3.03	3.05	10.09	11.67	19.37	0.52	1.12	0.6	1.16	0.4726	33	0.4483	107
	LC100IV-5	1100	4.84	5.4	8.7	1.44	9.19	0.95	1.1	0.16	0.17	0.4805	33	0.4663	93
6	FALC4-3	998.2	3.04	3.14	40.95	3.28	35.01	1.17	1.26	0.09	0.08	0.1085	135	0.1673	183
	FALC4-5	997.9	4.79	5.34	13.33	1.38	19.15	0.7	0.77	0.07	0.1	0.1122	135	0.1552	194
7	FALC3-3	998.4	3.07	3.18	67.04	16.78	84.99	0.79	0.99	0.2	0.25	0.3681	176	0.2914	181
	FALC3-5	998	4.71	5.44	12.76	1.39	17.55	0.73	0.81	0.08	0.11	0.3409	176	0.3355	164

Label (Fig. 8.1)	Sample	$R_{Mg\text{-}BET}$ ($mol \cdot m^{-2} \cdot s^{-1}$)	$R_{Si\text{-}BET}$ ($mol \cdot m^{-2} \cdot s^{-1}$)	$R_{Ni\text{-}BET}$ ($mol \cdot m^{-2} \cdot s^{-1}$)	$LogR_{Mg\text{-}BET}$ ($mol \cdot m^{-2} \cdot s^{-1}$)	$LogR_{Si\text{-}BET}$ ($mol \cdot m^{-2} \cdot s^{-1}$)	$LogR_{Ni\text{-}BET}$ ($mol \cdot m^{-2} \cdot s^{-1}$)	$R_{Mg\text{-}mass}$ ($mol \cdot g^{-1} \cdot s^{-1}$)	$R_{Si\text{-}mass}$ ($mol \cdot g^{-1} \cdot s^{-1}$)	$R_{Ni\text{-}mass}$ ($mol \cdot g^{-1} \cdot s^{-1}$)	$LogR_{Mg\text{-}mass}$ ($mol \cdot g^{-1} \cdot s^{-1}$)	$LogR_{Si\text{-}mass}$ ($mol \cdot g^{-1} \cdot s^{-1}$)	$LogR_{Ni\text{-}mass}$ ($mol \cdot g^{-1} \cdot s^{-1}$)
1	09GAR2-3	4.13E-13	1.74E-13	1.78E-12	-12.4	-12.8	-11.7	5.93E-11	2.50E-11	7.43E-11	-10.2	-10.6	-10.1
	09GAR2-5	1.40E-13	6.63E-14	3.94E-13	-12.9	-13.2	-12.4	1.54E-11	7.29E-12	1.26E-11	-10.8	-11.1	-10.9
2	LC100II-3	9.25E-13	1.39E-13	6.40E-13	-12	-12.9	-12.2	1.08E-10	1.62E-11	7.46E-11	-10	-10.8	-10.1
	LC100II-5	1.35E-13	2.01E-14	8.61E-14	-12.9	-13.7	-13.1	1.49E-11	2.21E-12	9.45E-12	-10.8	-11.7	-11
2	GAR2-3	3.30E-13	1.46E-12	2.44E-13	-12.5	-11.8	-12.6	5.65E-11	2.63E-10	2.12E-10	-10.2	-9.6	-9.7
	GAR2-5	6.63E-14	1.51E-13	3.55E-14	-13.2	-12.8	-13.4	5.63E-12	1.24E-11	1.41E-11	-11.2	-10.9	-10.9
3	GAR6-3	2.74E-13	1.61E-13	6.41E-14	-12.6	-12.8	-13.2	3.45E-11	2.02E-11	8.06E-12	-10.5	-10.7	-11.1
	GAR6-5	4.59E-14	3.07E-14	2.63E-14	-13.3	-13.5	-13.6	5.76E-12	3.85E-12	3.30E-12	-11.2	-11.4	-11.5
4	LC100IV-3	1.40E-13	1.02E-13	9.10E-14	-12.9	-13	-13	1.49E-11	1.09E-11	9.71E-12	-10.8	-11	-11
	LC100IV-5	1.40E-13	1.31E-14	4.52E-14	-12.9	-13.9	-13.3	1.30E-11	1.21E-12	4.20E-12	-10.9	-11.9	-11.4
5	FALC4-3	4.24E-13	5.70E-13	2.28E-13	-12.4	-12.2	-12.6	7.78E-11	1.05E-10	4.18E-11	-10.1	-10	-10.4
	FALC4-5	1.47E-13	2.04E-13	1.17E-13	-12.8	-12.7	-12.9	2.85E-11	3.95E-11	2.27E-11	-10.5	-10.4	-10.6
6	FALC3-3	3.67E-13	1.56E-13	1.73E-13	-12.4	-12.8	-12.8	6.64E-11	2.83E-11	3.14E-11	-10.2	-10.5	-10.5
	FALC3-5	7.82E-14	1.49E-14	4.14E-14	-13.1	-13.8	-13.4	1.28E-11	2.44E-12	6.78E-12	-10.9	-11.6	-11.2

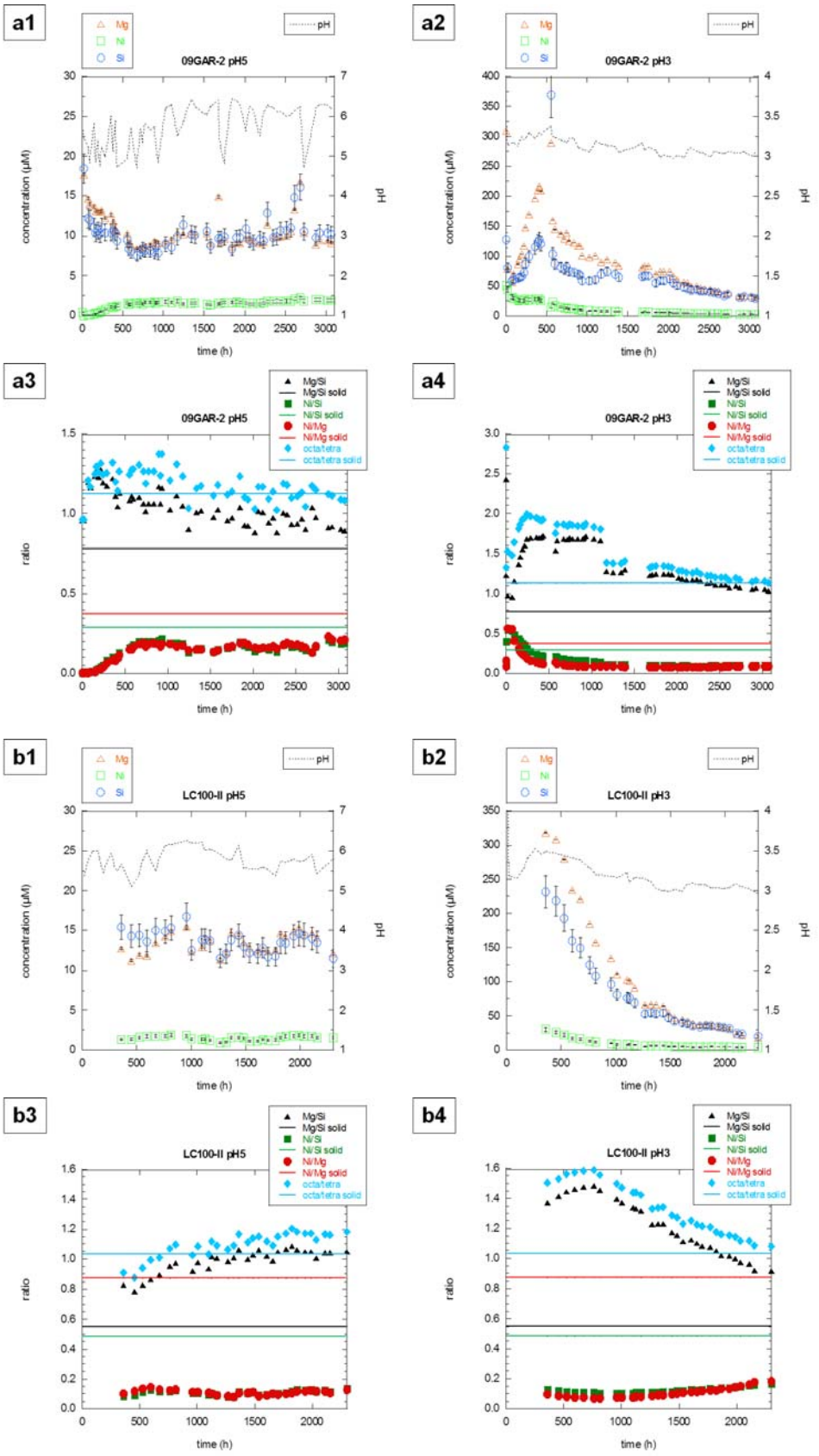

FIGURE 8.3. Variation of the pH and the output concentration of Ni, Mg and Si with time, at pH~5 (**1**) and pH~3 (**2**); and variation of the Mg/Si, Ni/Si, Ni/Mg and octahedral/tetrahedral molar ratios in the solution with time, compared to their corresponding ratios in the solid at pH~5 (**3**) and pH~3 (**4**) of samples **a**) 09GAR-2, and **b**) LC100-II.

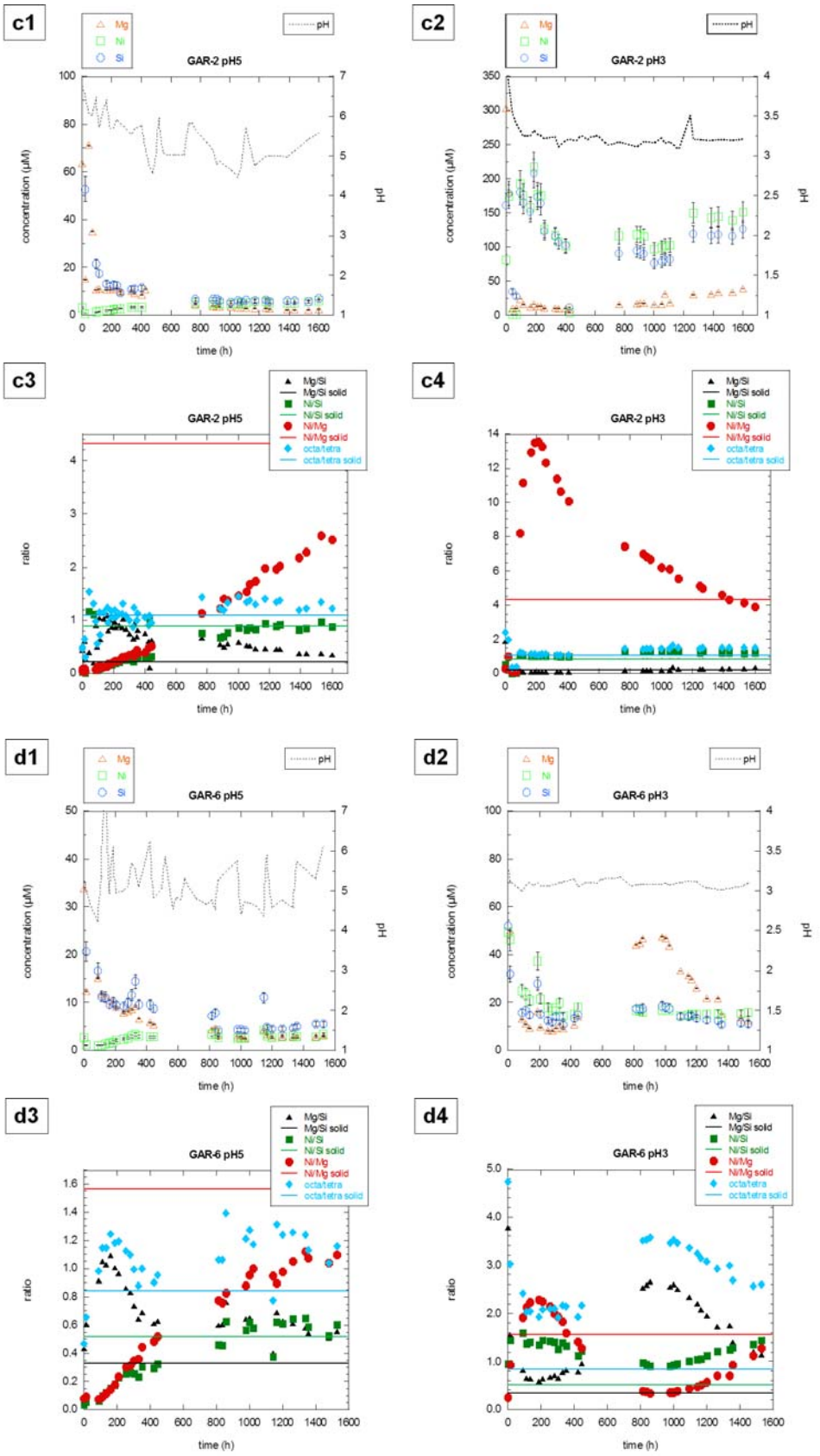

FIGURE 8.3. (CONTINUED). Variation of the pH and the output concentration of Ni, Mg and Si with time, at pH~5 (**1**) and pH~3 (**2**); and variation of the Mg/Si, Ni/Si, Ni/Mg and octahedral/tetrahedral molar ratios in the solution with time, compared to their corresponding ratios in the solid at pH~5 (**3**) and pH~3 (**4**) of samples **c**) GAR-2, and **d**) GAR-6.

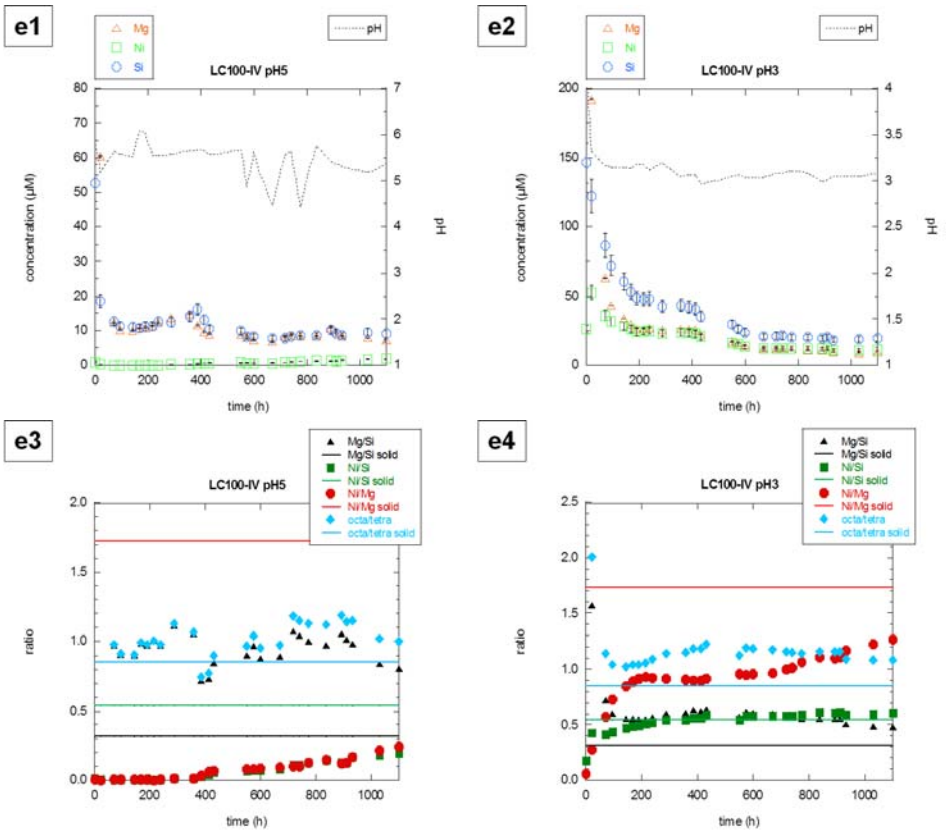

FIGURE 8.3. (CONTINUED). Variation of the pH and the output concentration of Ni, Mg and Si with time, at pH~5 (**1**) and pH~3 (**2**); and variation of the Mg/Si, Ni/Si, Ni/Mg and octahedral/tetrahedral molar ratios in the solution with time, compared to their corresponding ratios in the solid at pH~5 (**3**) and pH~3 (**4**) of sample **e**) LC100-IV.

Mg/Si at pH~5. Solution ratios do not get as close to their corresponding solid ratios with time as at pH~5 (**Fig. 8.3d4**).

In LC100-IV (Xtlc 0.77, 1.90 apfu Ni), at pH~5 the octa/tetra and Mg/Si ratios show an early decrease and stabilise around 1.0, close to the solid ratio of octa/tetra but higher than the solid ratio of Mg/Si, therefore Mg and Si are released at the same rate. However, the Ni/Si and Ni/Mg ratios increase slightly with time but do not reach the solid ratios, in particular the Ni/Mg ratio of the solution is much lower than that of the solid, so Ni is released at a very low rate (**Fig. 8.3e3**). At pH~3 the octa/tetra and Mg/Si ratios behave similarly to those under pH~5, except that they get closer to the solid ratios. Both Ni/Si and Ni/Mg ratios in the solution increase rapidly with time and get much closer to the solid ratios than in pH~5 (**Fig. 8.3e4**).

In FALC-4 (Ni-poor sepiolite), at pH~5 octa/tetra and Mg/Si ratios in the solution increase rapidly at the beginning and become stabilised close to their corresponding ratios in the solid. Ni/Si and Ni/Mg ratios also increase at the beginning and approach rapidly their respective solid ratios. Therefore, Mg is released a bit more rapidly than the other elements (**Fig. 8.3f3**). At pH~3 octa/tetra and Mg/Si ratios in the solution show an early decrease, and later become constant and far from the ratios in the solid. The Ni/Si and Ni/Mg ratios have a similar behaviour but with lower values, but they do approximate the ratios in the solid. Mg and Si are released more rapidly than Ni. The dissolution is more stoichiometric at pH~5 than at pH~3, and more stoichiometric than that of FALC-3 (**Fig. 8.3f4**).

In sample FALC-3 (Ni-rich sepiolite), at both pH~5 and pH~3 the octa/tetra and Mg/Si ratios behave similarly, with an early rapid increase and a later stabilisation, being the ones at pH~5 the closest to the solid ratio. At pH~5 and pH~3 this sample behaves similarly as FALC-4 at pH~5. At pH~3 there is a higher release of Ni (but still lower than Mg and Si). Both dissolution experiments are far from stoichiometry (**Fig. 8.3g3-4**).

In general, the large Mg/Si and octa/tetra ratios indicate that Mg is released faster than Si, which is

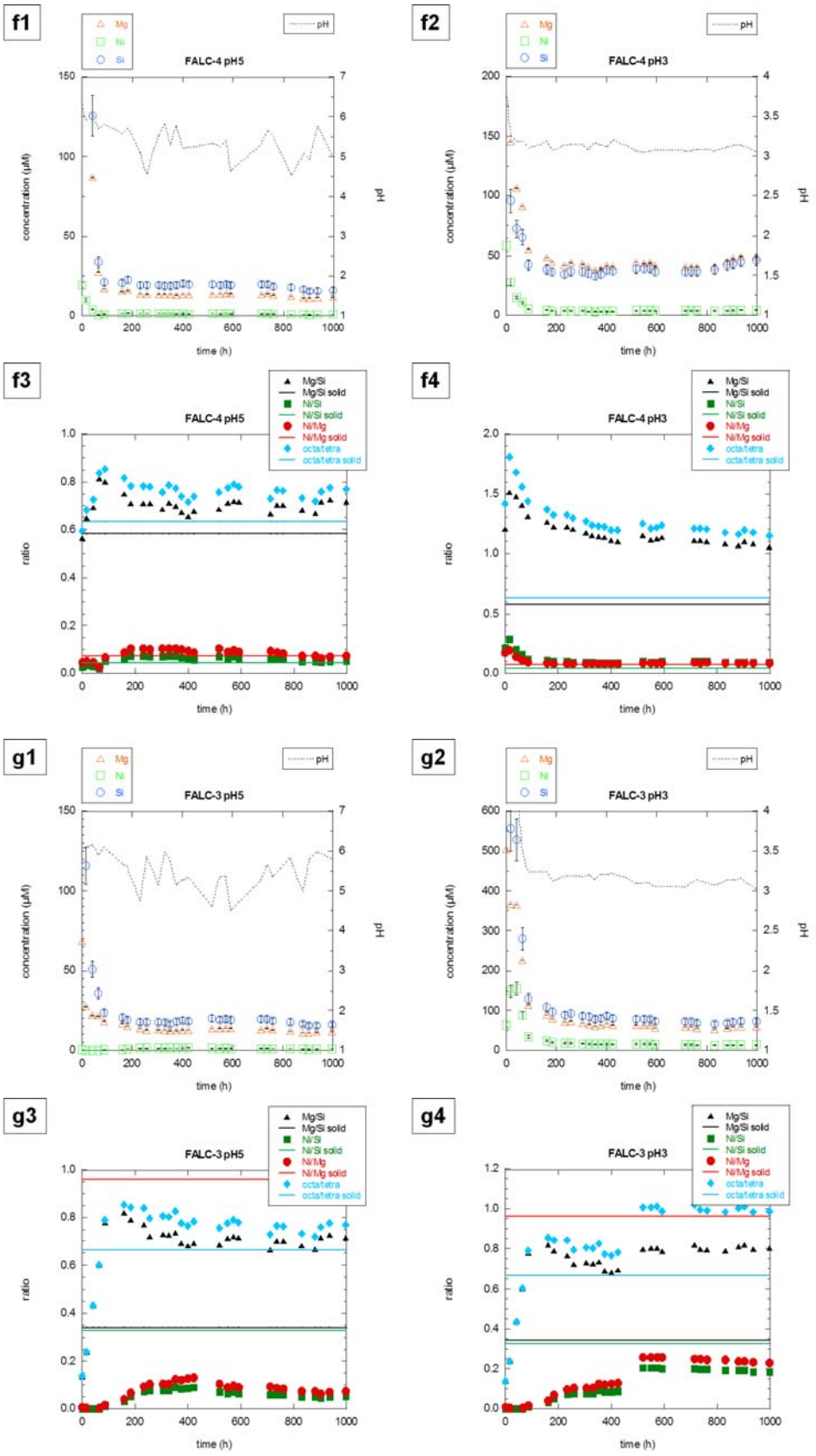

FIGURE 8.3. (CONTINUED). Variation of the pH and the output concentration of Ni, Mg and Si with time, at pH~5 (**1**) and pH~3 (**2**); and variation of the Mg/Si, Ni/Si, Ni/Mg and octahedral/tetrahedral molar ratios in the solution with time, compared to their corresponding ratios in the solid at pH~5 (**3**) and pH~3 (**4**) of samples **f**) FALC-4 and **g**) FALC-3.

TABLE 8.3. Dissolution reactions for the seven garnierites studied.

Sample	Reaction
09GAR-2	$(Mg_{2.06}Ni_{0.77}Fe_{0.14})(Si_{2.64})O_{6.68}(OH)_{3.33}\cdot nH_2O + 6.12H^+ + 0.57H_2O$ $= 2.06Mg^{2+} + 0.77Ni^{2+} + 0.14Fe^{3+} + 2.64H_4SiO_4$
LC100-II	$(Mg_{1.57}Ni_{1.37}Fe_{0.06})(Si_{2.84}Al_{0.07})O_{7.27}(OH)_{3.09}\cdot nH_2O + 6.30H^+ + 0.98H_2O$ $= 1.57Mg^{2+} + 1.37Ni^{2+} + 0.06Fe^{3+} + 0.07Al^{3+} + 2.84H_4SiO_4$
GAR-2	$(Ni_{2.42}Mg_{0.56}\ Fe_{0.01})(Si_{2.71})O_{6.81}(OH)_{3.28}\cdot nH_2O + 6.04H^+ + 0.77H_2O$ $= 2.42Ni^{2+} + 0.56Mg^{2+} + 0.01Fe^{3+} + 2.71H_4SiO_4$
GAR-6	$(Ni_{1.83}Mg_{1.17})(Si_{3.54}\ Al_{0.01})O_{8.88}(OH)_{2.45}\cdot nH_2O + 6.06H^+ + 2.82H_2O$ $= 1.83Ni^{2+} + 1.17Mg^{2+} + 3.54H_4SiO_4$
LC100-IV	$(Ni_{1.90}Mg_{1.10})(Si_{3.52}Al_{0.01})O_{8.83}(OH)_{2.47}\cdot nH_2O + 6.04H^+ + 2.79H_2O$ $= 1.90Ni^{2+} + 1.10Mg^{2+} + 0.01Al^{3+} + 3.52H_4SiO_4$
FALC-4	$(Mg_{3.51}Ni_{0.26}Fe_{0.06})(Si_{6.05}Al_{0.01})O_{15}(OH)_2\cdot 6H_2O + 7.88H^+ + 1.21H_2O$ $= 3.51Mg^{2+} + 0.26Ni^{2+} + 0.06Fe^{3+} + 0.01Al^{3+} + 6.05H_4SiO_4$
FALC-3	$(Mg_{2.03}Ni_{1.95}\ Fe_{0.01})(Si_{5.95}\ Al_{0.06})O_{15}(OH)_2\cdot 6H_2O + 8.18H^+ + 0.82H_2O$ $= 2.03Mg^{2+} + 1.95Ni^{2+} + 0.01Fe^{3+} + 0.06Al^{3+} + 5.95H_4SiO_4$

coherent with Soler *et al*. (2008) and references therein; and the small Ni/Si and Ni/Mg ratios indicate that Ni is the slowest element to be released.

8.3. DISCUSSION

First, garnierite dissolution rates decrease with increasing pH. Jurinski & Rimstidt (2001) observed little to no pH dependence in dissolution rates when dissolving talc at pH between 2 and 8 and 37ºC in mixed-flow reactors. However, the results of this chapter are consistent with Soler *et al*. (2008).

Second, the dissolution rates of serpentine-dominated garnierites are higher than those of kerolite-dominated garnierites and sepiolite-falcondoite. Soler *et al*. (2008) stated that the dissolution is congruent at pH>5 and incongruent at pH<5, and this indicates a different contribution from serpentine and talc to the total dissolution rate, because the serpentine component of the garnierite mixture dissolves faster under more acidic conditions. Furthermore, Stoessell (1988), as suggested by Jones (1986), found: metastability of kerolite relative to sepiolite, when dissolving sepiolite and kerolite from marine sediments at 25ºC and 1 atm during 10 years. They concluded that with increasing pH and aqueous Mg content and decreasing aqueous SiO_2 content, kerolite would precipitate rather than sepiolite).

Third, the rapid release of Mg with respect to Si detected in this study was already observed by Luce *et al*. (1972) when dissolving serpentine at pH between 1.6 and 9, and 25ºC in batch experiments and by Hume & Rimstidt (1992) when dissolving chrysotile at pH between 2 and 6 at 37 ºC. The authors explained that the initial Mg release was due to a stoichiometric exchange of one Mg^{2+} for two H^+ from the aqueous solution. Lin & Clemency (1981) observed that Mg from the octahedral sheets was released more rapidly than Si from the octahedral sheets, when dissolving talc at pH close to 5 and at 25ºC in a closed system reactor. They suggested that talc dissolution rates are controlled by the destruction of the slower tetrahedral Si-O bonds.

In agreement with Luce *et al*. (1972), Lin & Clemency (1981) and Jurinski & Rimstidt (2001), Saldi *et al*. (2007) explained that under acidic pH, Mg is initially preferentially removed from the talc surface but at basic pH it is preferentially retained in agreement with the relative fast equilibration of the Mg for proton exchange reaction. These conclusions were extracted from dissolution

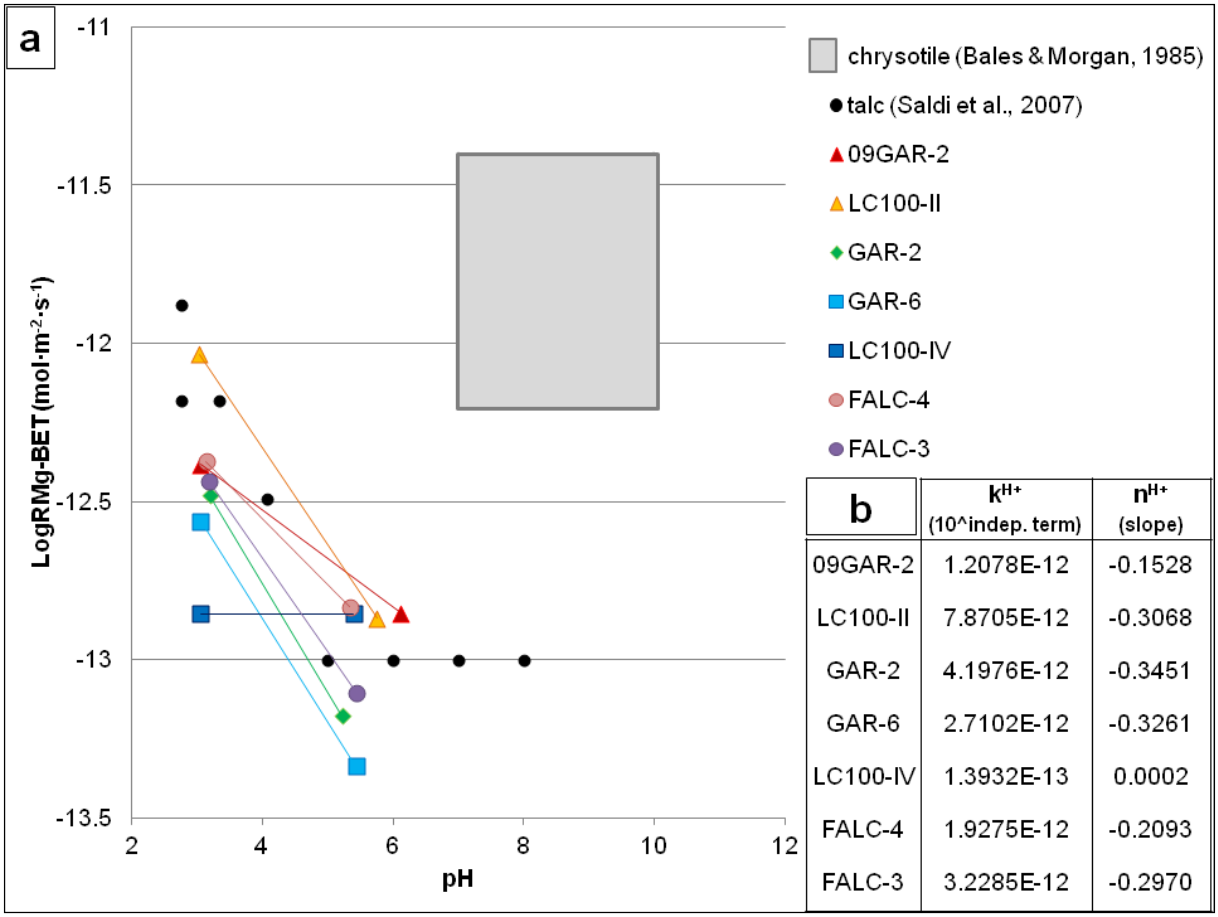

b

	k^{H+} (10^indep. term)	n^{H+} (slope)
09GAR-2	1.2078E-12	-0.1528
LC100-II	7.8705E-12	-0.3068
GAR-2	4.1976E-12	-0.3451
GAR-6	2.7102E-12	-0.3261
LC100-IV	1.3932E-13	0.0002
FALC-4	1.9275E-12	-0.2093
FALC-3	3.2285E-12	-0.2970

FIGURE 8.4. Log dissolution rate for Mg normalised to the final BET specific surface area versus pH, compared to the chrysotile rates from Bales & Morgan (1985) and talc rates from Saldi *et al.* (2007) (**a**). The regression lines enabled the calculation of the dissolution rate equation parameters (see **Eq. 8**), displayed in the table (**b**).

experiments of talc at pH between 1 to 10.6 and temperatures between 25 and 150ºC, and it must be noted that their experiments were supersaturated with respect to one or more secondary phases, and in one case with respect to talc itself.

8.4. FINAL REMARKS

The results show that the dissolution rates of the garnierites from the Falcondo deposit decrease with increasing pH. This is consistent with the results obtained in garnierites from Loma de Hierro, Venezuela (Soler *et al.*, 2008). In addition, the dissolution rates of serpentine-dominated garnierites are faster than those of kerolite-dominated garnierites and sepiolite-falcondoite. In general, the behaviour of the studied garnierites from the Falcondo Ni-laterite is comparable to that of Ni-free serpentine, talc, kerolite and sepiolite from the literature, with a release of Mg faster than that of Si.

In particular, in the mixtures of serpentine and talc, the fact that octa/tetra and Mg/Si molar ratios are in general above the molar solid ratio (may indicate that the phase that is being dissolved is the one with less silica, that is to say, serpentine (instead of talc). Actually, the octa/tetra molar ratios are close to 1.5, which is the molar solid ratio of an ideal serpentine. Therefore, the dissolution is not congruent.

Furthermore, it is widely observed that the system (Ni-Mg-phyllosilicates in contact with an acidic solution) retains Ni and minor Si (Ni and Si are the slowest elements to be incorporated in the solution), which may favour the precipitation of phases rich in Ni and Si in the profile.

However, it must be noted that non-stoichiometry is extensively observed in all samples at both pH~3 and pH~5. Further work is needed, taking into account solid solution models (incongruent dissolution) in the interpretation of the obtained results.

9. CONCLUSIONS

The results of this multiscale study provide new data on the mode of occurrence, mineralogy and mineral chemistry at the micrometre and nanometre scale, the local environment of Ni, speciation of Fe and dissolution rates of Ni-bearing Mg-phyllosilicates from the Falcondo Ni-laterite deposit (Dominican Republic). The results altogether provide further insight on the formation of these Ni-bearing Mg-phyllosilicates in a lateritic environment.

During laterisation, the primary ferromagnesian silicates (mainly serpentine and olivine), containing small amounts of Ni (~0.5 wt.% NiO), are altered to Ni-enriched secondary phases, principally the Ni-bearing serpentines that constitute the bulk saprolite horizon (~3 wt.% NiO). This process involves the transformation of Fe^{2+} and the Ni in homogeneous distribution in the octahedral layer (solid solution) of the primary serpentines to Fe^{3+} and Ni concentrated in discrete domains in the octahedral layer (clustered) of the secondary Ni-bearing serpentines.

The Mg of these primary silicates is solubilised and progressively leached out of the weathering profile, whereas oxidised Fe is residually concentrated as goethite in the limonite horizon. The Ni leached from the silicates is adsorbed in goethite. This Ni may subsequently be released by percolating acidic solutions to deeper levels in the profile. This Ni is first incorporated in the saprolite Ni-bearing serpentines. When the solution is saturated in Ni and Si and with a sudden change in Eh/pH, Ni-Mg-phyllosilicates precipitate in fractures near the low water table (**Fig. 9.1**).

In particular, with regards to the formation of garnierites, the stability of Ni-bearing Mg-phyllosilicates in lateritic environments is determined by the Eh, pH, and chemical composition of permeating groundwater. In an Al-free system, such as in the Falcondo profile, the stability of serpentine- and talc-like garnierites, and sepiolite-falcondoite is controlled by the activity of silica. According to the paragenetic sequence deduced from the textural relationships at the specimen scale, the micrometre scale and the nanometre scale, the first to precipitate are the serpentine-dominant garnierite types (I and II), followed by talc-like (type IV or kerolite-pimelite); and sepiolite-falcondoite tends to form in an amorphous silica matrix. In addition, the chemical analyses indicate that Ni is mostly concentrated in the talc-like fraction. Therefore, the replacement, cementing and coating of serpentine particles by talc-like (kerolite-pimelite) lamellae is an evidence of Si- and Ni-enrichment. This is coherent with the rapid dissolution of the serpentine fraction in the garnierite mixtures and a previous thermodynamic model explaining the precipitation of Ni-bearing Mg-phyllosilicates as a succession of mineral phases progressively enriched in Si (serpentine-talc-sepiolite-sepiolite and quartz) and Ni (from Ni-poor serpentine to Ni-rich talc), because silica activity increases with time and through the profile (**Fig. 9.2**). However, the Ni enrichment is not a linear

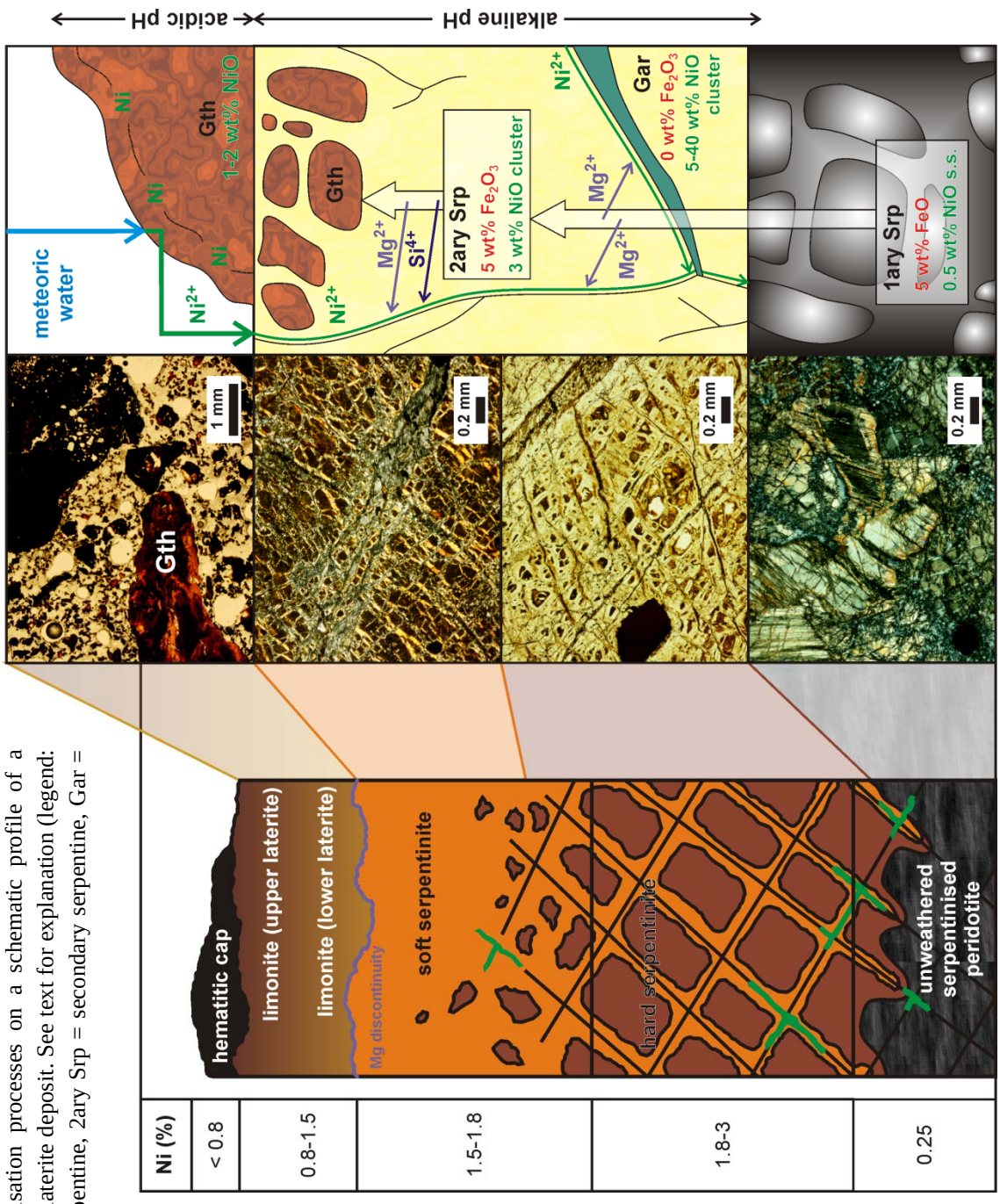

FIGURE 9.1. The laterisation processes on a schematic profile of a hydrous Mg silicate Ni-laterite deposit. See text for explanation (legend: 1ary Srp = primary serpentine, 2ary Srp = secondary serpentine, Gar = garnierite).

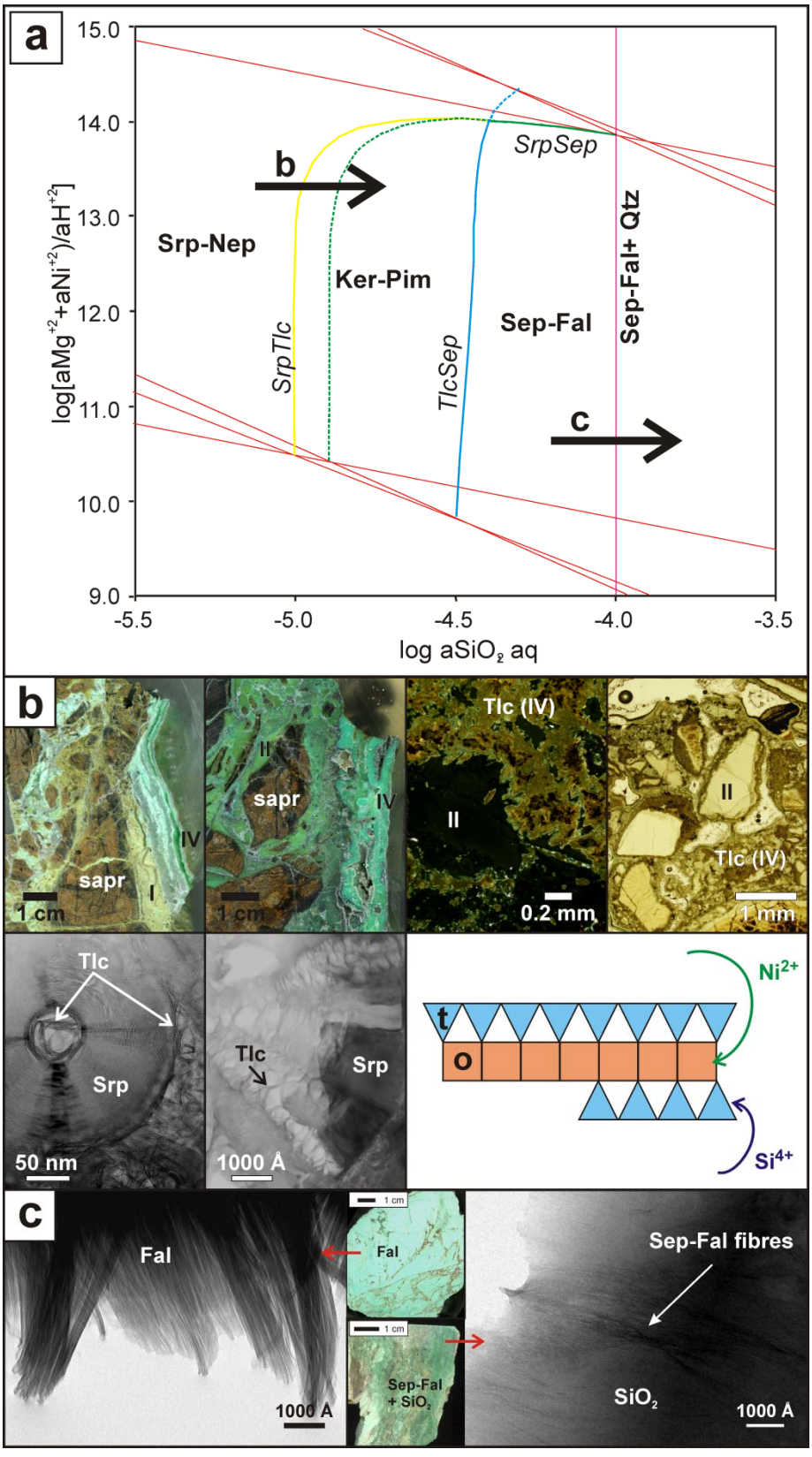

FIGURE 9.2. The textural relationships between different types of garnierites are consistent with the garnierites thermodynamic model (modified from Galí *et al.*, 2012). **a**) fields corresponding to the three solid solutions: serpentine (Srp)-népouite (Nep), kerolite (Ker)-pimelite (Pim), sepiolite (Sep)-falcondoite (Fal); and boundaries: serpentine-talc (SrpTlc), talc-sepiolite (TlcSep) and serpentine-sepiolite (SrpSep), the arrows correspond to the sequences described by the sample photographs, optical micrographs, HRTEM images and the sketch (t = tetrahedral site; o = octahedral site) in **b**) and **c**). See text for explanation.

process, since the highly variable and oscillatory Ni content in talc-like garnierite suggests several stages of growth, possibly caused by recurrent changes in the physical-chemical conditions of the aqueous solution. However, it is worth noting that the existence of kerolite and pimelite as mineral phases with talc affinity but extra water in their structure has been proved by chemical and thermal analyses.

In summary, the results exposed and discussed in this thesis report a detailed characterisation of a group of significant Ni ores with high complexity of up to the nanometre scale, controversial nomenclature and classification, low crystallinity and mainly occurring as mixtures.

REFERENCES

Abad I, Mata MP, Nieto F, Velilla N (2001). The phyllosilicates in diagenetic-metamorphic rocks of the South Portuguese Zone, southwestern Portugal. Canadian Mineralogist, 39: 1571-1589.

Abazi S, Hyseni S, Durmishaj B, Krasniqi R (2012). Perspective laterites of Ni-silicate mineralization in Kosovo. Buletini i Shkencave Gjeologjike (Bulletin of the Geological Sciences), Konference Jubilare "90 vjet Gjeologji Shqiptare" (Jubilee Conference "90 years of Geology in Albania") (Tirana, Albania; October 26-28), 31: 124-128.

Akai J (1988). Incompletely transformed serpentine-type phyllosilicates in the matrix of Antarctic CM chondrites. Geochimica et Cosmochimica Acta, 52: 1593-1599.

Alekseeva EF, Godlevsky MM (1937). Rontgenometrisches Studium der Hydrosilikate des Nickels (X-ray study of the nickel hydrous silicates). Записки Всесоюзного Минералогического Общества (Zapiski Vsyesoyuznogo Mineralogicheskogo Obshchestva - Notes on the Mineralogical Society of the Soviet Union), 66: 51-106 (title in German, article in Russian).

Andréani M, Baronnet A, Boullier A-M, Gratier J-P (2004). A microstructural study of a "crack seal" type serpentine vein using SEM and TEM techniques. European Journal of Mineralogy, 16: 585-595.

Andréani M, Grauby O, Baronnet A, Muñoz M (2008). Occurrence, composition and growth of polyhedral serpentine. European Journal of Mineralogy, 20: 159-171.

Andréani M, Muñoz M, Marcaillou C, Delacour A (2013). μXANES study of iron redox state in serpentine during oceanic serpentinization. Lithos 178: 70-83.

Andreoli MAG, Hart RJ, Ashwal LD, Tredoux M (1997). Nickel-and platinum-group-element-enriched quartz norite in the latest Jurassic Morokweng impact structure, South Africa. Large meteorite impacts and planetary evolution (Suddury, Ontario, Canada; September 1-3), 3.

Anthony JW, Bideaux RA, Bladh KW, Nichols MC (2001) Handbook of Mineralogy. Mineralogical Society of America, Chantilly, VA 20151-1110 (http://www.handbookofmineralogy.org/).

Auzende A-L, Devouard B, Guillot S, Daniel I, Baronnet A, Lardeaux J-M (2002). Serpentinites from Central Cuba: petrology and HRTEM study. European Journal of Mineralogy, 14: 905-914.

Avias J (1968). L'évolution des idées et des connaissances sur la genèse et sur la nature des minerais de nickel, en particulier latéritiques, de leur découverte à nos jours (The evolution of ideas and knowledge on the genesis and nature of nickel ores, in particular lateritic, from their discovery to our days). Bulletin du Bureau de Recherches Géologiques et Minières (BRGM), Section II (Géologie Appliquée), 3: 165-172 (in French).

Bailey SW (1980). Summary of recommendations of AIPEA nomenclature committee on clay minerals. American Mineralogist, 65: 1-7.

Bailey SW, Brindley GW, Johns WD, Martin RT, Ross M (1971). Clay Mineral Society Report of nomenclature committee, 1969-1970. Clays and Clay Minerals, 19: 132-133.

Bales RC, Morgan JJ (1985). Dissolution kinetics of chrysotile at pH 7 to 10. Geochimica et Cosmochimica Acta, 49: 2281-2288.

Bard D, Yarwood J, Tylee B (1997). Asbestos fibre identification by Raman microspectroscopy. Journal of Raman Spectroscopy, 28: 803-809.

Baronnet A, Devouard B (1996). Topology and crystal growth of natural chrysotile and polygonal serpentine. Journal of Crystal Growth, 166: 952-960.

Baronnet A, Devouard B (2001). Microstructural and microchemical aspects of serpentinization. 11th Annual Goldschmidt Conference (Hot Springs, Virginia, USA; May 20-24), #3382.

Baronnet A, Devouard B (2005). Microstructures of common polygonal serpentines from axial HRTEM imaging, electron diffraction, and lattice-simulation data. Canadian Mineralogist, 43: 513-542.

Baronnet A, Andréani M, Grauby O, Devouard B, Nitsche S, Chaudanson D (2007). Onion morphology and microstructure of polyhedral serpentine. American Mineralogist, 92: 687-690.

Barros de Oliveira SM (1990). Estágio atual do conhecimento a cerca do minério laterítico de níquel no Brasil e no mundo (State of the art of the knowledge on nickel lateritic mining in Brazil and worldwide). Revista do Instituto Geológico, 11: 49-57 (in Portuguese).

Barros de Oliveira SM (1995). The role of residual 2:1 phyllosilicates in lateritic metallogenesis: Ni and Cu deposits in Serra dos Carajás, Brazilian Amazonia. Geochimica Brasil, 9: 161-171.

Bence AE, Albee AL (1968). Empirical correction factors for the electron microanalysis of silicates and oxides. Journal of Geology, 76: 382-403.

Berman H (1937). Constitution and classification of the natural silicates. American Mineralogist, 22: 342-408.

Beyschlag FHA, Krusch JP (1913). Die Erzlagerstätten von Frankenstein und Reichenstein in Schlesien (The ore deposits of Frankenstein and Reichenstein in Silesia). Abhandlungen der Königlich preussischen geologischen landesanstalt (Memoirs of the Royal Prussian Geological Survey), neue folge 73 (in German).

Bish DL, Brindley GW (1978). Deweylites, mixtures of poorly crystalline hydrous serpentine and talc-like minerals. Mineralogical Magazine, 42: 75-79.

Blaha JJ, Rosasco GJ (1978). Raman microprobe spectra of individual microcrystals and fibers of talc, tremolite, and related silicate minerals. Analytical Chemistry, 50: 892-896.

Bosio NJ, Hurst VJ, Dmith RL (1975). Nickeliferous nontronite, a 15 Å garnierite at Niquelândia, Goiás, Brazil. Clays and Clay Minerals, 23: 400-403.

Bowin CO (1966). Geology of the central Dominican Republic (a case history of part of an island arc). *In:* Caribbean Geological Studies (Hess H, Ed.). Geological Society of America Memoirs, 98: 11-84.

Brand NW, Butt CRM, Elias M (1998). Nickel laterites: classification and features. Australian Geological Survey Organisation, Journal of Australian Geology & Geophysics, 17: 81-88.

Breithaupt JFA (1823). Vollständige Characteristik des Mineral-Systems (Full characteristics of the mineral systems). Arnoldischen Buchhandlung, Dresden, 46 p.

Breithaupt JFA (1859). Neue Mineralien: 2. Röttisit; 3. Konarit (New Minerals: 2. Röttisite; 3. Connarite) Berg- und hüttenmännische Zeitung (Mining and Ore Processing Newspaper), 18, 1-2 (in German).

Brindley GW (1978). The structure and chemistry of hydrous nickel containing silicate and aluminate minerals. Bulletin du Bureau de Recherches Géologiques et Minières (BRGM), Section II (Géologie Appliquée), 3: 233-245.

Brindley GW (1980). The structure and chemistry of hydrous nickel-containing silicate and nickel-aluminium hydroxy minerals. Bulletin de Minéralogie, 103: 161-169.

Brindley GW, Bish D, Wan HM (1977). The nature of kerolite, its relation to talc and stevensite. Mineralogical Magazine, 41: 443-452.

Brindley GW, Bish DL, Wan HM (1979). Compositions, structures, and properties of nickel-containing minerals in the kerolite-pimelite series. American Mineralogist, 64: 615-625.

Brindley GW, Brown G (1980). Crystal structures of clay minerals and their X-ray identification. Mineralogical Society Monograph 5, London: 495 p.

Brindley GW, Hang PT (1973). The nature of garnierite: I. Structure, chemical compositions and color characteristics. Clays and Clay Minerals, 21: 27-40.

Brindley GW, Maksimović Z (1974). The nature and nomenclature of hydrous nickel-containing silicates. Clay Minerals 10: 271-277.

Brindley GW, Wan HM (1975). Compositions, structures and thermal behaviour of nickel-containing minerals in the lizardite-népouite series. American Mineralogist, 60: 863-871.

Brindley GW, de Souza Jefferson V (1975). Nickel-containing montmorillonites and chlorites from Brazil, with remarks on schuchardtite. Mineralogical Magazine, 40: 141-152.

Brunauer S, Emmet P, Teller E (1938). Adsorption of gases in multimolecular layers. Journal of the American Chemical Society, 60: 309-319.

Brush GJ (1872). (First) Appendix to the Fifth Edition of Dana's Mineralogy. J. Wiley & Sons, New York, 19 p.

Bunjaku A, Kekkonen M, Taskinen P, Holappa L (2011). Thermal behaviour of hydrous nickel-magnesium silicates when heating up to 750 ºC. Mineral Processing and Extractive Metallurgy, 120: 139-146.

Burke EAJ (2006). A mass discreditation of GQN minerals. Canadian Mineralogist, 44: 1557-1560.

Burns RG (1970). Mineralogical Applications of Crystal Field Theory. Cambridge University Press, Cambridge, 551 p.

Butt CRM, Cluzel D (2013). Nickel laterite ore deposits: weathered serpentinites. Elements, 9: 123-128.

Caillère S (1936). Contribution à l'étude des minéraux des serpentines (Contribution to the study of serpentine minerals). Bulletin Société Française de Minéralogie, LIX: 163-326 (in French).

Caillère S (1965). Composition minéralogique des differents types de minerais de nickel de la Nouvelle-Calédonie (Mineralogical composition of the different types of nickel minerals of New Caledonia). Mémoires du Muséum National d'Histoire Naturelle, 12: 105-124 (in French).

Caillère, S. & Hénin, S. (1957a). VI. The mica minerals. *In*: The differential thermal investigation of clays (Cameron Mackenzie R; Ed.). Mineralogical Society (of Great Britain), Clay Minerals group, London, 456 p. (p. 176-187).

Caillère, S. & Hénin, S. (1957b). VIII.II. The serpentine and related minerals. *In*: The differential thermal investigation of clays (Cameron Mackenzie R; Ed.). Mineralogical Society (of Great Britain), Clay Minerals group, London, 456 p. (p. 220-230).

Caillère, S. & Hénin, S. (1957c). IX.I. The sepiolite minerals. *In*: The differential thermal investigation of clays (Cameron Mackenzie R; Ed.). Mineralogical Society (of Great Britain), Clay Minerals group, London, 456 p. (p. 231-239).

Cama J, Acero P (2005). Dissolution of minor sulphides present in a pyritic sludge at pH 3 and 25ºC. Geologica Acta, 3: 15-26.

Cathelineau M, Caumon M-C, Massei F, Harlaux M, Brie D (2014). A Raman spectroscopy study of the Ni-Mg kerolite solid solution: sensitivity of the O-H stretching vibrations to Ni-Mg substitution. 11th GeoRaman Conference (Saint Louis, Missouri, USA; June 15-19), #5030.

Cathelineau M, Caumon M-C, Massei F, Brie D, Harlaux M (2015). Raman spectra of Ni-Mg kerolite: effect of Ni-Mg substitution on O-H stretching vibrations. Journal of Raman Spectroscopy. DOI:10.1002/jrs.4746.

Chisholm JE (1992). The number of sectors in polygonal serpentine. Canadian Mineralogist, 30: 355-365.

Clarke FW (1888). Some nickel ores from Oregon. American Journal of Science, 35(3): 483-488.

Clarke FW (1890). Some nickel ores from Oregon. United States Geological Survey Bulletin, Report of the work done in the Division of Chemistry and Physics mainly during the fiscal year 1887-88, 60: 21-26.

Clarke FW (1920). Nickel and cobalt. United States Geological Survey Bulletin, The Data of Geochemistry, Fourth Edition, 965: 698-702.

Cole TG, Shaw HF (1983). The nature and origin of authigenic smectites in some recent marine sediments. Clay Minerals, 18: 239-252.

Colin F, Noack Y, Trescases J-J, Nahon D (1985). L'alteration lateritique débutante des pyroxenites de Jacuba, Niquelândia, Brésil (The incipient lateritic alteration of pyroxenites in Jacuba, Niquelândia, Brazil). Clay Minerals, 20: 93-113 (in French).

Colin F, Nahon D, Trescases J-J, Melfi AJ (1990). Lateritic weathering of pyroxenites at Niquelândia, Goiás, Brazil: The supergene behavior of nickel. Economic Geology, 85: 1010-1023.

Colthup NB, Daly LH, Wiberley JE (1990). Introduction to Infrared and Raman Spectroscopy. Elsevier Academic Press, New York, 547 p.

Cluzel D, Vigier B (2008). Syntectonic mobility of supergene nickel ores of New Caledonia (Southwest Pacific). Evidence from garnierite veins and faulted regolith. Resource Geology, 58: 161-170.

Cressey BA (1979). Electron microscopy of serpentinite textures. Canadian Mineralogist, 17: 741-756.

Cressey G, Cressey BA, Wicks FJ (1984). The significance of the aluminium content of a lizardite at the nanoscale: the role of clinochlore as an aluminium sink. Mineralogical Magazine, 72: 817-825.

Cressey G, Cressey BA, Wicks FJ (2008). Polyhedral serpentine: a spherical analogue of polygonal serpentine? Mineralogical Magazine, 72: 1229-1242.

Cressey G, Cressey BA, Wicks FJ, Yada K (2010). A disc with fivefold symmetry: the proposed fundamental seed structure for the formation of chrysotile asbestos fibres, polygonal serpentine fibres and polyhedral lizardite spheres. Mineralogical Magazine, 74: 29-37.

Dalvi AD, Gordon Bacon W, Osborne RC (2004). The past and the future of nickel laterites. Prospectors and Developers Association of Canada (PDAC) International Convention, Trade Show & Investors Exchange (Toronto, Canada; March 7-10), 1-27.

Dana ES (1875). Second Appendix to the Fifth Edition of Dana's Mineralogy. J. Wiley & Sons, New York, 64 p.

Dana JD & Brush GJ (1868). System of Mineralogy. Descriptive Mineralogy, comprising the most recent discoveries. J. Wiley & Sons, New York, Fifth Edition, 881 p.

De Waal SA (1970a). Nickel minerals from Barberton, South Africa. II. Nimite, a nickel rich chlorite. American Mineralogist, 55: 18-30.

De Waal SA (1970b). Nickel minerals from Barberton, South Africa. III. Willemseite, a nickel rich talc. American Mineralogist, 55: 31-42.

De Waal SA (1978). The nickel deposit at Bon Accord, Barberton, South Africa - a proposed paleometeorite. *In:* Mineralisation in metamorphic terraines (Verwoerd WJ; Ed.). Geological Society of South Africa Special Publication, Johannesburg, 4: 87-98.

De Waal SA (1979). The metamorphism of the Bon Accord nickel deposit by the Nelspruit granite. Transactions of the Geological Society of South Africa, 82: 335-342.

Decarreau A, Colin F, Herbillon A, Manceau A, Nahon D, Paquet H, Trauth-Badaud D, Trescases JJ (1987). Domain segregation in Ni-Fe-Mg-smectites. Clays and Clay Minerals, 35: 1-10.

Decarreau A, Graby O, Petit S (1992). The actual distribution of octahedral cations in 2:1 clay minerals: results from clay synthesis. Applied Clay Science, 7: 147-167.

Des Cloizeaux M (1878). La nouméite. Bulletin de la Société Française de Minéralogie, 1: 28-29.

Devouard B, Baronnet A, Van Tendeloo G, Amelinckx S (1997). First evidence of synthetic polygonal serpentines. European Journal of Mineralogy, 9: 539-546.

Diller JS, Kay GF (1924). Geologic Atlas of the United States, Riddle Folio Nº 218. United States Geological Survey.

Dódony I (1997). Structure of the 30-sectored polygonal serpentine. A model based on TEM and SAED studies. Physics and Chemistry of Minerals, 24: 39-49.

Dódony I, Pósfai M, Buseck PR (2002). Revised structure models for antigorite: an HRTEM study. American Mineralogist, 87: 1443-1457.

Draper G, Gutiérrez G, Lewis JF (1996). Thrust emplacement of the Hispaniola peridotite belt: Orogenic expression of the mid-Cretaceous Caribbean arc polarity reversal? Geology, 24: 1143-1146.

Dubińska E, Sakharov BA, Kaproń G, Bylina P, Kozubowski JA (2000). Layer silicates from Szklary (Lower Silesia): from ocean floor metamorphism to continental chemical weathering. Geologica Sudetica, 33: 85-105.

Dublet G, Juillot F, Morin G, Fritsch E, Fandeur D, Ona-Nguema G, Brown GE Jr (2012). Ni speciation in a New Caledonian lateritic regolith: a quantitative X-ray absorption spectroscopy investigation. Geochimica et Cosmochimica Acta, 95: 119-133

Ducloux J, Boukili H, Decarreau A, Petit S, Perruchot A, Pradel P (1993). Un gîte hydrothermal de garniérites: l'exemple de Bou Azzer, Maroc. European Journal of Mineralogy 5: 1205-1215.

Elias M, Donaldson MJ, Giorgetta N (1981). Geology, mineralogy, and chemistry of lateritic nickel-cobalt deposits near Kalgoorlie, Western Australia. Economic Geology, 76: 1775–1783.

Elias M (2002). Nickel laterite deposits—Geological overview, resources and exploration. *In:* Giant ore deposits—Characteristics, genesis, and exploration (Cooke D, Pongratz J; Eds.), Australian Research Council Centre of Excellence in Ore Deposits (ARC-CODES), University of Tasmania, Hobart, Special Publication, 4: 205–220.

Emmons, E. (1826): Manual of mineralogy and geology. Websters and Skinners, 230 p.

Escayola M, Garuti G, Zaccarini F, Proenza JA, Bédard JH, Van Staal C (2011). Chromitite and platinum-group-element mineralization at Middle Arm Brook, Advocate Ophiolite complex, Baie Verte Peninsula, Newfoundland, Canada. Canadian Mineralogist, 49: 1523-1547.

Escuder-Viruete J, Pérez-Estaún A, Contrera F, Joubert M, Weis D, Ullrich TD, Spadea P (2006). Plume mantle source heterogeneity through time: insights from the Duarte Complex, Hispaniola, northeastern Caribbean. Journal of Geophysical Research, 112: B04203.

Esson J, Carlos L (1978). The occurrence, mineralogy and chemistry of some garnierites from Brazil. Bulletin du Bureau de Recherches Géologiques et Minières (BRGM), Section II (Géologie Appliquée), 3: 263-274.

Fan R, Gerson AR (2011). Nickel geochemistry of a Philippine laterite examined by bulk and microprobe synchrotron analyses. Geochimica et Cosmochimica Acta, 75: 6400-6415.

Faust GT (1966). The hydrous nickel-magnesium silicates – the garnierite group. American Mineralogist, 51: 33-36.

Faust GT, Fahey JJ (1962). The serpentine group minerals: Studies of the natural phases in the system MgO-SiO_2-H_2O and the systems containing the congeners of magnesium. United States Geological Survey Professional Paper, 384A: 99 p.

Faust GT, Fahey JJ, Mason B, Dwornik EJ (1969). Pecoraite, $Ni_6Si_4O_{10}(OH)_8$, nickel analog of clinochrysotile, formed in the Wolf Creek meteorite. Science, 165: 59-60.

Faust GT, Fahey JJ, Mason B, Dwornik EJ (1973). The disintegration of the Wolf Creek meteorite and the formation of pecoraite, the nickel analog of clinochrysotile. United States Geological Survey Professional Paper, 3480C: 107-135.

Favreau G, Dietrich JE (2006). Die Mineralien von Bou Azzer (The minerals from Bou Azzer). Lapis, 31: 27-68 (in German).

Fleischer M (1957a). New mineral names. Karpinskyite. American Mineralogist, 42: 117-124.

Fleischer M (1957b). New mineral names. Karpinskite. American Mineralogist, 42: 580-586.

Fleischer M (1969). New mineral names. Nimite, willemseite, pecoraite. American Mineralogist, 54: 1937-1942.

Fleischer M (1973). New mineral names. Nimesite. American Mineralogist, 58: 1111-1115.

Fleischer M (1975). Deweylite. *In:* Glossary of Mineral Species. United States Geological Survey, Second Edition, 145 p. (p. 32).

Foshag WF (1930). New mineral names. American Mineralogist, 15: 274-276.

Foster L, Eggleton RA (2002). The Marlborough nickel laterite deposits. *In:* Regolith and landscapes in Eastern Australia (Roach IC; Ed.), Cooperative Research Centre for Landscape Environments and Mineral Exploration (CRC LEME), Bentley, 136 p. (p. 33-36).

Freyssinet Ph, Butt CRM, Morris RC (2005). Ore-forming processes related to lateritic weathering. Economic Geology, 100th Anniversary Volume: 681-722.

Frost RL, Reddy BJ, Dickfos MJ (2008). Raman spectroscopy of the nickel silicate mineral pecoraite – an analogue of chrysotile (asbestos). Journal of Raman Spectroscopy, 39: 909-913.

Fu W, Zhou Y, Chen Y, Hu Y, Chen N, Niu H, Zhang Z, Li X (2010). Geological and geochemical characteristics of laterite nickel deposit and ore genesis - a case study of Kolonodale deposit in Indonesia Sulawesi, Southeast Asia. Earth Science Frontiers, 17: 127-139 (in Chinese, with English abstract).

Fu W, Yang JW, Yang ML, Pang BC, Liu XJ, Niu HJ, Huang XR (2014). Mineralogical and geochemical characteristics of a serpentinite-derived laterite profile from East Sulawesi, Indonesia: Implications for the lateritization process and Ni supergene enrichment in the tropical rainforest. Journal of Asian Earth Sciences, 93: 74-88.

Gaines RV, Skinner HC, Foord EE, Mason B, Rosenzweig A (1997). Dana's New Mineralogy. The System of Mineralogy of James Dwight Dana and Edward Salisbury Dana. Wiley & Sons, New York, 1819 p. (8th edition).

Galí S, Soler JM, Proenza JA, Lewis JF, Cama J, Tauler E (2012). Ni-enrichment and stability of Al-free garnierite solid-solutions: a thermodynamic approach: Clays and Clay Minerals, 60: 121-135.

Gallardo T, Chang A, Tauler E, Proenza JA (2010a). El yacimiento de San Felipe (Camagüey, Cuba): un ejemplo de lateritas niquelíferas tipo arcilla (The San Felipe deposit (Camagüey, Cuba): an example of clay type Ni-laterites). Macla, 13: 87-88 (in Spanish).

Gallardo T, Tauler E, Proenza JA, Lewis JF, Galí S, Labrador M, Longo F, Bloise G (2010b). Geology, mineralogy and geochemistry of the Loma Ortega Ni laterite deposit, Dominican Republic. Macla, 13: 89-90.

Galoisy L, Calas G, Brown G E Jr (1995). Intracrystalline distribution of Ni in San Carlos olivine: An EXAFS study. American Mineralogist, 80: 1089-1092.

García-Casco A (2007). Magmatic paragonite in trondhjemites from the Sierra del Convento mélange, Cuba. American Mineralogist, 92: 1232-1237.

Garnier J (1867). Essai sur la géologie et les ressources minérales de la Nouvelle-Calédonie. *In*: Annales des mines, 6ème série, tome XII. Dunod, Paris, 92 p.

Garnier J (1876). Le minerai de nickel de la Nouvelle-Calédonie ou "garniérite" (The nickel mineral of New Caledonia or "garnierite". Comptes Rendus Hebdomadaires des Séances de l'Académie des Sciences, 82: 1454-1455 (in French)

Garnier J (1878). Note sûr la garniérite (A note on garnierite). Comptes Rendus Hebdomadaires des Séances de l'Académie des Sciences, 86: 684-686 (in French).

Gaudin A, Grauby O, Noack Y, Decarreau A, Petit S (2004a) Accurate crystal chemistry of ferric smectites from the lateritic nickel ore of Murrin Murrin (Western Australia). I. XRD and multi-scale chemical approaches. Clay Minerals, 39: 301-315.

Gaudin A, Petit S, Rose J, Martin F, Decarreau A, Noack Y, Borschneck D (2004b) The accurate crystal chemistry of ferric smectites from the lateritic nickel ore of Murrin Murrin (Western Australia): II. Spectroscopic (IR and EXAFS) approaches. Clay Minerals, 39: 453-467.

Gaudin A, Decarreau A, Noack Y, Grauby O (2005) Clay mineralogy of the nickel laterite ore developed from serpentinised peridotites at Murrin Murrin, Western Australia. Australian Journal of Earth Sciences, 52: 231-241.

Genna A, Maurizot P, Lafoy Y, Augé T (2005). Contrôle karstique de minéralisations nickélifères de Nouvelle-Calédonie. Comptes rendus de l'Académie des Sciences, série IIa (Sciences de la Terre et des planètes), 337: 367-374.

Genth FA (1851). Nickelgymnit von Texas, Lancaster County, Pa (Nickel-gymnite from Texas, Lancaster County, Pennsylvania). Nordamerikanischer Monatsbericht für Natur-und Heilkunde (North American Monthly Report of Nature and Medicine), 3: 487-488 (in German).

Genth FA (1875). Deweylite, Gymnite. Preliminary report on the Mineralogy of Pennsylvania. Second Geological Survey Pennsylvania, 117B-118B.

Genth FA (1891). Deweylite, Kerolite, Genthite. The Minerals of North Carolina. United States Geological Survey, pp. 63 and 88.

Gerard P, Herbillon AJ (1983). Infrared studies of Ni-bearing clay minerals of the kerolite–pimelite series. Clays and Clay Minerals, 31: 143-151.

Glasser E (1907). Note sûr une espèce minérale nouvelle: la népouite, silicate hydraté de nickel et de magnésie. (Note on a new mineral species: népouite, a hydrated silicate of nickel and magnesium). Bulletin de la Société Française de Minéralogie, 30: 17-28 (in French).

Gleeson SA, Butt CR, Elias M (2003). Nickel laterites: a review. SEG Newsletter, 54: 11-18.

Gleeson SA, Herrington RJ, Durango J, Velásquez CA, Koll G (2004). The mineralogy and geochemistry of the Cerro Matoso S.A. Ni laterite deposit, Montelíbano, Colombia. Economic Geology, 99: 1197-1213.

Glocker EF (1845). Über ein neues Nickelsilicat aus Schlesien (On a new nickel silicate from Silesia). Journal für Praktische Chemie, 34: 502-505.

Golightly JP (1979). Geology of Soroako nickeliferous laterite deposits. International Laterite Symposium, 3: 38-55.

Golightly JP (1981). Nickeliferous laterite deposits. Economic Geology, 75th Anniversary volume: 710-735.

Golightly JP (2010). Progress in understanding the evolution of nickel laterites. Economic Geology, Special Publication, 15: 451-485.

Golightly JP, Arancibia ON (1979). The chemical composition and infrared spectrum of nickel- and iron-substituted serpentine from a nickeliferous laterite profile, Soroako, Indonesia. Canadian Mineralogist 17(4): 719-728.

Gritsaenko GS, Bocharova AP, Lyamina AN (1943). On népouite from the Tyulenevskoye deposit, middle Urals. Записки Всесоюзного Минералогического Общества (Zapiski Vsyesoyuznogo Mineralogicheskogo Obshchestva - Notes on the Mineralogical Society of the Soviet Union), 72: 7-28.

Grobéty B (2003). Polytypes and higher-order structures of antigorite: a TEM study. American Mineralogist, 88: 27-36.

Groppo C, Rinaudo C, Cairo S, Gastaldi D, Compagnoni R (2006). Micro-Raman spectroscopy for a quick and reliable identification of serpentine minerals from ultramafics. European Journal of Mineralogy, 18: 319-329.

Gruner JW (1934). The crystal structures of talc and pyrophyllite. Zeitschrift für Kristallographie, 88: 412-419.

Guggenheim S, Adams JM, Bain DC, Bergaya F, Brigatti MF, Drits VA, Formoso MLL, Galán E, Kogure T, Stanjek H (2006). Summary of recommendations of nomenclature committees relevant to clay mineralogy: report of the Association Internationale pour l'Étude des Argiles (AIPEA) nomenclature committee for 2006. Clays and Clay Minerals, 54, 761-772.

Haldemann EG, Buchan R, Blowes JH, Chandler T (1979). Geology of lateritic nickel deposits, Dominican Republic. International Laterite Symposium, 4: 57-84.

Haranczyk C, Prchazka, K (1974). Hydrous magnesium-nickel silicates from Wiry, Lower Silesia. Prace Muzeum Ziemi (Works of the Museum of the Earth), 22: 3-64 (in Polish, with English abstract)

Hermann HR (1867). Über Rewdanskit, ein neues Nickelerz so wie über Darstellung von Nickel aus diesem Minerale (On revdanskite, a new nickel ore and subsequent production of nickel from this mineral). Journal für Praktische Chemie, 102: 405-409 (in German).

Hess D (1980). Letter. Friends of Mineralogy – Pennsylvania Chapter Newsletter, 8(2): 5-6.

Hiemstra SA, de Waal SA (1968a). Nickel minerals from Barberton. II. Nimite, a nickelian chlorite. National Institute for Metallurgy Research Report (Republic of South Africa), 344: 1-10.

Hiemstra SA, de Waal SA (1968b). Nickel minerals from Barberton- III. Willemseite, a nickelian talc. National Institute for Metallurgy Research Report (Republic of South Africa), 352: 1-14.

Hood JW (1883). Nickel ore from Piney Mountain, Douglas Co., Oregon. Mineralogical Magazine, 5(24): 193.

Hotz PE (1964). Nickeliferous laterites in Southwestern Oregon and Northwestern California. Economic Geology, 59: 356-394.

Huggins CW (1961). Electron diffraction study of garnierite. United States Bureau of Mines Report of Investigations, 5837, 10 p.

Hume LA, Rimstidt JD (1992). The biodurability of chrysotile asbestos. American Mineralogist, 77: 1125-1128.

Jones BF (1986). Clay mineral diagenesis in lacustrine sediments. *In:* Studies in diagenesis (Mumpton FA, Ed.). United States Geological Survey Bulletin, 1578: 291-300.

Jurinski JB, Rimstidt JD (2001). Biodurability of talc. American Mineralogist, 86: 392-399.

Kato T (1961). A study on the so-called garnierite from New-Caledonia. Mineralogical Journal, 3: 107-121.

Kato T (2005). New accurate Bence-Albee a-factors for oxides and silicates calculated from the PAP correction procedure. Geostandards and Geoanalytical Research, 29: 83-94 (http://www.nendai.nagoya-u.ac.jp/gsd/a-factor/).

Kato T, Minato H (1960). Deweylite from the Akaishi Mine, Ehime Prefecture. Journal of the Mineralogical Society of Japan, 5: 11 (in Japanese).

Kay GF (1906). Nickel deposits of Nickel Mountain, Oregon. United States Geological Survey Bulletin, 120-128.

Karsten DLG (1800). Mineralogische Tabellen mit Rücksicht auf die neuesten Entdeckungen (Mineralogical tables with regard to the latest discoveries), 28-29 (in German).

Keep FE (1930a). Notes on nickel occurrences in the Great Dyke of Southern Rhodesia. Transactions of the Geological Survey of South Africa, 32: 103-110.

Keep FE (1930b). The geology of the chromite and asbestos deposits of the Umvukwe Range, Lomagundi and Mazoe Districts. Southern Rhodesia Geological Survey Bulletin, 16: 105 p.

Klaproth MH (1788). Chemische Untersuchungen des Schlesischen Chrysoprases (Chemical analyses of the Silesian chrysoprases). Sitzungsberichte der Gesellschaft Naturforschender Freunde (Proceedings of the Society of Natural Research Friends), Berlin, 8: 17-46 (in German).

Kloprogge JT, Frost RL, Rintoul L (1999). Single crystal Raman microscopic study of the asbestos mineral chrysotile. Physics Chemistry, Chemical Physics, 1: 2559-2564.

Koenig GA (1889). Chloantite, niccolite, desaulesite, annabergite, tephrowillemite, fluorite and apatite, from Franklin, New Jersey. Proceedings of the Academy of Natural Sciences of Philadelphia, 184-189.

Kuck PH (2013). Nickel. United States Geological Survey Mineral Commodity Summaries, 108-109.

Kuhnel RA, Roorda HJ, Steensma JJS (1978). Distribution and partitioning of elements in nickeliferous laterites. Bulletin du Bureau de Recherches Géologiques et Minières (BRGM), Section II (Géologie Appliquée), 3: 191-206.

Lacroix A (1942). Les peridotites de la Nouvelle-Calédonie, leurs serpentines et leurs gîtes de nickel et de cobalt: les gabbros qui les accompagnent (The peridotites of New Caledonia, their serpentines and their nickel and cobalt deposits: the associated gabbros). Mémoires de l'Académie de Sciences de Paris, 66: 143 p. (in French).

Lapham DM (1961). New data on deweylite. American Mineralogist, 46: 168-188.

Lasaga AC, Soler JM, Ganor J, Burch TE, Nagy KL (1994). Chemical weathering rate laws and global geochemical cycles. Geochimica et Cosmochimica Acta, 58: 2361-2386.

Leguéré J (1976). Des corrélations entre la tectonique cassante et l'altération supergène des péridotites de Nouvelle Calédonie (Correlations between brittle tectonics and supergene alteration of peridotites of New Caledonia). PhD Thesis. University of Montpellier, France, 95 pp (in French).

Lewis JF, Draper G (1990). Geological and tectonic evolution of the northern Caribbean margin. *In:* Dengo G, Case JE (Eds.). The Geology of North America, Volume H: The Caribbean region. Geological Society of America, Colorado, p. 77-140.

Lewis JF, Draper G, Proenza JA, Espaillat J, Jiménez J (2006). Ophiolite-Related Ultramafic Rocks (Serpentinites) in the Caribbean Region: A Review of their Occurrence, Composition, Origin, Emplacement and Ni-Laterite Soils Formation. Geologica Acta, 4: 237-263.

Lewis JF, Escuder-Viruete J, Hernáiz-Huerta PP, Gutiérrez G, Draper G, Pérez-Estaún A (2002). Geochemical subdivision of the Circum-Caribbean Island Arc, Dominican Cordillera Central: implications for crustal formation, accretion and growth within an intra-oceanic setting. Acta Geologica Hispanica, 37: 81-122.

Lewis JF, Jiménez JG (1991). Duarte Complex in the La Vega-Jarabacoa-Janico Area, Central Hispaniola: Geological and Geochemical Features of the Sea Floor during the Early Stages of Arc Evolution. *In*: Mann P, Draper G, Lewis JF (Eds.). Geologic and tectonic development of the North America-Caribbean plate boundary in Hispaniola. Geological Society of America Special Paper, 262: 115-142.

Lewis IR, Chaffin NC, Gunter ME, Griffiths PR (1996). Vibrational spectroscopic studies of asbestos and comparison of suitability for remote analysis. Spectrochimica Acta Part A, 52: 315-328.

Lin F-C, Clemency CV (1981). The dissolution kinetics of brucite, antigorite, talc, and phlogopite at room temperature and pressure. American Mineralogist, 66: 801-806.

Lithgow EW (1993). Nickel laterites of central Dominican Republic Part I. Mineralogy and ore dressing. *In*: The Paul E. Queneau International Symposium, Extractive Metallurgy of Copper, Nickel and Cobalt, Volume I: Fundamental Aspects. The Minerals, Metals and Materials Society (Reddy RG, Weizenbach RN; Eds.), Portland, p. 403-425.

Liversidge A (1874a): Note on a New Mineral from New Caledonia. Journal of the Chemical Society of London, 27, 613-615.

Liversidge A (1874b): Nickel minerals from New Caledonia. Transactions of the Royal Society of New South Wales, 8, 75-80.

Liversidge A (1888): Nickel. The minerals of New South Wales, Cambridge University Press, 275-281.

Lopez-Rendon JE (1986). Geology, mineralogy and geochemistry of the Cerro Matoso nickeliferous laterite, Cordoba, Colombia. MSc Thesis, Colorado State University, Fort Collins, 378 p.

López Munguira A, Nieto F (2000). Transmission Electron Microscopy study of very low-grade metamorphic rocks in Cambrian sandstones and shales. Ossa-Morena Zone. South-West Spain. Clays and Clay Minerals, 48: 213-223.

Luce RW, Bartlett RW, Parks GA (1972). Dissolution kinetics of magnesium silicates. Geochimica et Cosmochimica Acta, 36: 35-50.

Maksimović Z (1966). β-kerolite-pimelite series from Goles Mountain, Yugoslavia. Proceedings of the International Clay Conference, 1, 97-105.

Maksimović Z (1969). Nickeliferous minerals found in the fossil crust of weathering in Goles (Yugoslavia). Geološki anali Balkanskog poluostrva (Geological Annals of the Balkan Peninsula), 34, 577-596.

Maksimović Z (1972). Nimesite, a new septechlorite from a bauxite deposit near Megara (Greece). Bulletin Science Yugoslavia, 17, 224-226.

Maksimović Z (1973). Изоморфная серия лизардит-непуит (The isomorphous series lizardite-nepouite). Записки Всесоюзного Минералогического Общества (Zapiski Vsyesoyuznogo Mineralogicheskogo Obshchestva - Notes on the Mineralogical Society of the Soviet Union), 102: 143-149 (in Russian).

Maksimović Z, Bish DL (1978). Brindleyite, a nickel-rich aluminous serpentine mineral analogous to berthierine. American Mineralogist, 63: 484-489.

Maksimović Z (1975). The isomorphous series lizardite-népouite. International Geology Review, 17: 1035-1040.

Manceau A, Calas G (1985a). Heterogeneous distribution of nickel in hydrous silicates from New Caledonia ore deposits. American Mineralogist, 70: 549-558.

Manceau A, Calas G (1985b). Heterogeneous distribution of nickel in hydrous silicates from New Caledonia ore deposits. 5th Meeting of the European Clay Groups (Prague, Czech Republic; August 3-September 3, 1983), 547-552.

Manceau A, Calas G (1986). Nickel-bearing clay minerals: II. Intracrystalline distribution of Nickel: An X-ray absorption study. Clay Minerals 21: 341-360.

Manceau A, Calas G, Decarreau A (1985). Nickel-bearing clay minerals: I. Optical spectroscopic study of nickel crystal chemistry. Clay Minerals 20: 367-387.

Manceau A (1990). Distribution of cations among the octahedral of phyllosilicates: insight from EXAFS. Canadian Mineralogist, 28: 321-328.

Mann P, Burke K, Matumoto T (1984). Neotectonics of Hispaniola: plate motion, sedimentation, and seismicity at a restraining bend. Earth and Planetary Science Letters, 70: 311-324.

Mann P, Draper G, 914 Lewis JF (1991). An overview of the geologic and tectonic evolution of Hispaniola. *In:* Mann P, Draper G, Lewis JF (Eds.). Geological and tectonic development of the North American-Caribbean plate boundary in Hispaniola. Geological Society of America Special Paper, 262: 1-28.

Marchesi C, Garrido CJ, Proenza JA, Konc Z, Hidas K, Lewis JF, Lidiak E (2012). Mineral and whole rock compositions of peridotites from Loma Caribe (Dominican Republic): insights into the evolution of the oceanic mantle in the Caribbean region. European Geosciences Union General Assembly (Vienna, Austria; April 22-27), 14: EGU2012-12161.

Marcus MA, MacDowell AA, Celestre R, Manceau A, Miller T, Padmore HA, Sbulett RE (2004). Beamline 10.3.2 at ALS: a hard X-ray microprobe for environmental and materials sciences. Journal of Synchrotron Radiation, 11: 239-247.

Martín de Vidales JL, Pozo M, Alia JM, García-Navarro F, Rull F (1991). Kerolite-stevensite mixed-layers from the Madrid Basin, central Spain. Clay Minerals, 26: 329-342.

McKeown DA, Post JE, Etz ES (2002). Vibrational analysis of palygorskite and sepiolite. Clays and Clay Minerals, 50: 667-680.

Mellini M (1982). The crystal structure of lizardite 1T: hydrogen bonds and polytypism. American Mineralogist, 67: 587-598.

Mellini M (1986). Chrysotile and polygonal serpentine from the Balangero serpentinite. Mineralogical Magazine, 50: 301-305.

Mellini M (2014). Structure and microstructure of serpentine minerals. *In:* Minerals at the Nanoscale (Nieto F, Livi KJT; Eds.), European Mineralogical Union (EMU) Notes in Mineralogy, 14: 153-179.

Mellini M, Viti C (1994). Crystal structure of lizardite 1T from Elba, Italy. American Mineralogist, 79: 1194-1198.

Mellini M, Zanazzi PF (1987). Crystal structures of lizardite-1T and lizardite-2H1 from Coli, Italy. American Mineralogist, 72: 943-948.

Milton C, Dwornik EJ, Finkelman RB (1981). Pecoraite, the nickel analogue of chrysotile, $Ni_3Si_2O_5(OH)_4$ from Missouri. Geological Society of America Abstracts, 13: 310.

Milton C, Dwornik EJ, Finkelman RB (1983). Pecoraite, the nickel analogue of chrysotile, $Ni_3Si_2O_5(OH)_4$ from Missouri. Neues Jahrbuch für Mineralogie - Monatschefte, 11: 513-523.

Mitchell DRG. Dave Mitchell's Digital Micrograph™ Scripting Website (http://www.dmscripting.com/alphabeticscriptlisting.html).

Mitchell RH, Putnis A (1988). Polygonal serpentine in segregation-textured kimberlite. Canadian Mineralogist, 26: 991-997.

Montoya JW, Baur GS (1963). Nickeliferous serpentines, chlorites and related minerals found in two lateritic ores. American Mineralogist, 48: 1227-1238.

Moraes LJ (1935): Niquel no Brasil. Republica dos Estados Unidos do Brasil Boletim, 9: 168 p.

Morandi N, Poppi L (1974). Studio mineralogico della “deweylite” e della “gymnite” di Mezzavalle (Predazzo) (Mineralogical study of the “deweylite” and the “gymnite” of Mezzavalle (Predazzo)). Mineralogica et Petrographica Acta, 20: 49-61 (in Italian).

Mosselmans JFW, Quinn PD, Roqué-Rosell J, Atkinson KD, Dent AJ, Cavill SI, Hodson ME, Kirk CA, Schofield PF (2008). The first environmental science experiments on the new microfocus spectroscopy beamline at diamond. Mineralogical Magazine, 72: 197-200.

Mosselmans JFW, Quinn PD, Dent AJ, Cavill SA, Diaz Moreno S, Peach A, Leicester PJ, Keylock SJ, Gregory SR, Atkinson KD, Roqué-Rosell J (2009). I18 — the microfocus spectroscopy beamline at the Diamond light source. Journal of Synchrotron Radiation, 16: 818-824.

Mudd M (2010). Global trends and environmental issues in nickel mining: sulphides versus laterites. Ore Geology Reviews, 38: 9-26.

Mugnaioli E, Logar M, Mellini M, Viti C (2007). Complexity in 15- and 30-sectors polygonal serpentine: Longitudinal sections, intrasector stacking faults and XRPD satellites. American Mineralogist, 92: 603-616.

Münster ChA (1892). Garnierit (nickelgymnit) von Foldalen, Norwegen. Zeitschrift für Kristallographie, 20: 402.

Naganna C, Phene SG (1968). Study of the nickel silicates associated with the ultrabasic rocks of Nuggihalli schist belt, Mysore state. Proceedings of the Indian Academy of Sciences, B 67(4): 174-179.

Nagy KL (1995). Dissolution and precipitation kinetics of sheet silicates. *In:* Chemical weathering rates of silicate minerals; an overview. Reviews in Mineralogy and Geochemistry (White AF, Brantley SL, Eds.), 31: 173-233.

Nagy KL, Blum AE, Lasaga AC (1991). Dissolution and precipitation kinetics of kaolinite at 80 ºC and pH 3. American Journal of Science, 291: 649-686.

Nahon D, Colin F, Tardy Y (1982a). Formation and distribution of Mg, Fe, Mn-smectites in the first stages of the lateritic weathering of forsterite and tephroite. Clay Minerals, 17: 339-348.

Nahon D, Paquet H, Delvigne J (1982b). Lateritic weathering of ultramafic rocks and the concentration of nickel in the Western Ivory Coast. Economic Geology, 77: 1159-1175.

Nelson CE, Proenza JA, Lewis JF, López-Kramer J (2011). The metallogenic evolution of the Greater Antilles. Geologica Acta, 9: 229-264.

Nickel EH (1973). An occurrence of gaspeite and pecoraite in the Nullagine region of Western Australia. Mineralogical Magazine, 39: 113-115.

Nickel EH, Bridge PG (1975). A garnierite with a high nickel content from Western Australia. Mineralogical Magazine, 40(309): 65-69.

Nickel EH, Davis CES, Bussell M, Bridge PJ, Dunn JG, MacDonald RD (1977). Eardleyite as a product of the supergene alteration of nickel sulfides in Western Australia. American Mineralogist, 62: 449-457.

Nickel EH, Hallberg JA, Halligan R (1979). Unusual nickel mineralization at Nullagine, Western Australia. Journal of the Geological Society of Australia, 26: 61-71.

Nickel EH, Nichols MC (2009). Materials Data (http://www.materialsdata.com).

Ogura Y (1986). Mineralogical studies on the profiles of nickeliferous laterite deposits in the Southwestern Pacific Area. Geological Survey of India Memoirs, 120: 63-74.

Padrón-Navarta JA, López Sánchez-Vizcaíno V, Garrido CJ, Gómez-Pugnaire MT, Jabaloy A, Capitani GC, Mellini M (2008). Highly ordered antigorite from Cerro de Almirez HP-HT serpentinites, SE Spain. Contributions to Mineralogy and Petrology, 156: 679-688.

Palache C (1937). Desaulesite. *In*: The minerals of Franklin and Sterling Hill, Sussex County, New Jersey. United States Geological Survey Professional Paper, 180: 135 p (page 119).

Parkhurst DL, Appelo CAJ (1999). User's guide to PHREEQC (version 2) - A Computer Program for Speciation, batch-reaction, one-dimensional transport, and inverse geochemical calculations. United States Geological Survey Report, 99-4259.

Pecora WT (1944). Nickel-silicate and associated nickel-cobalt-manganese-oxide deposits near São José do Tocantins, Goiaz, Brasil. United States Geological Survey Bulletin, 935-E: 65 p.

Pecora WT, Hobbs SW (1942). Nickel deposit near Riddle Douglas County, Oregon. United States Geological Survey Bulletin, 931-I: 205-225.

Pecora WT, Hobbs SW, Murata KJ (1949). Variations in garnierite from the nickel deposit near Riddle, Oregon. Economic Geology, 44(1): 13-23.

Pelletier B (1983). Localisation du nickel dans les minerais "garniéritiques" de Nouvelle-Calédonie (Location of Ni in "garnieritic" minerals from New Caledonia) (Localisation of nickel in the "garnieritic" minerals of New Caledonia). *In*: International Congress on Alteration Petrology/International Colloquium of the Centre National de Recherche Scientifique (CNRS) "Petrology of weathering and soils" (Paris, France; July 4-7). Sciences Géologiques Mémoires (Nahon D (Ed.), 73: 173-183 (in French).

Pelletier B (1996). Serpentines in nickel silicate ore from New Caledonia. Australasian Institute of Mining and Metallurgy Publication Series - Nickel conference "Mineral to market" (Kalgoorlie, Western Australia; November 27-29), 6/96: 197-205.

Perrier N, Ambrosi JP, Colin F, Gilkes RJ (2006). Biogeochemistry of a regolith: the New Caledonian Koniambo ultramafic massif. Journal of Geochemical Exploration, 88: 54-58.

Petriglieri JR, Bersani D, Salvioli-Mariani E, Mantovani L, Tribaudino M, Lottici PP, Laporte-Magoni C (2014). Polymorphs of serpentine identification by means of Raman spectroscopy. 11th GeoRaman Conference (Saint Louis, Missouri, USA; June 15-19), #5064.

Pouchou JL, Pichoir F (1991). Quantitative Analysis of Homogeneous or Stratified Microvolumes Applying the Model "PAP". *In:* Electron Probe Quantitation (Heinrich KFJ, Newbury DE; Eds.). Springer US, 400 p. (p. 31-75).

Poncelet G, Jacobs P, Delannay F, Genet M, Gerard P, Herbillon A (1979). Étude preliminaire sûr la localisation du nickel dans une garnierite naturelle (Preliminary study on the location of Ni in a natural garnierite). Bulletin de Minéralogie, 102(4): 379-385 (in French).

Post JE, Bish DL, Heaney PJ (2007). Synchrotron powder X-ray diffraction study of the structure and dehydration behavior of sepiolite. American Mineralogist, 92: 91-97.

Pozo M, Casas J (1999). Origin of the kerolite and associated Mg clays in palustrine lacustrine environments, the Esquivias Deposit (Neogene Madrid Basin, Spain). Clay Minerals, 34: 395-418.

Proenza JA, Lewis JF, Galí S, Tauler E, Labrador M, Melgarejo JC, Longo F, Bloise G (2008). Garnierite mineralisation from Falcondo Ni-laterite deposit (Dominican Republic). Macla 9, 197-198.

Proenza JA, Tauler E, Melgarejo JC, Galí S, Labrador M, Marrero N, Perez-Nelo N, Rojas-Puron AL, Blanco-Moreno JA (2007a). Mineralogy of oxide and hydrous silicate Ni-laterite profiles in Moa Bay area, northeast Cuba. 9th SGA Biennial Meeting of the Society for Geology Applied to Mineral Deposits (SGA), Mineral Exploration and Research: Digging Deeper (Dublin, Ireland; August 19-23), 1389-1392.

Proenza JA, Zaccarini F, Lewis J, Longo F, Garuti G (2007b). Chromite composition and platinum-group mineral assemblage of PGE-rich Loma Peguera chromitites, Loma Caribe peridotite, Dominican Republic. Canadian Mineralogist, 45: 211-228.

Ravel B, Newville M (2005). ATHENA, ARTEMIS, HEPHAESTUS: data analysis for X-ray absorption spectroscopy using IFEFFIT. Journal of Synchrotron Radiation, 12: 537-541.

Reddy BJ, Frost RL, Dickfos MJ (2009). Characterisation of Ni silicate-bearing minerals by UV-vis-NIR spectroscopy. Effect of Ni substitution in hydrous Ni-Mg silicates. Spectrochimica Acta, 71A: 1762-1768.

Ressler T, Wong J, Roos J, Smith IL (2000). Quantitative Speciation of Mn-Bearing Particulates Emitted from Autos Burning (Methylcyclopentadienyl) manganese Tricarbonyl-Added Gasolines Using XANES Spectroscopy. Environmental Science & Technology, 34: 950-958.

Rinaudo C, Gastaldi D (2003). Characterization of chrysotile, antigorite and lizardite by FT-Raman spectroscopy. Canadian Mineralogist, 41: 883-890.

Roqué-Rosell J, Mosselmans JFW, Proenza JA, Labrador M, Galí S, Atkinson KD, Quinn PD (2010). Sorption of Ni by "lithiophorite-asbolane" intermediates in Moa Bay lateritic deposits, eastern Cuba. Chemical Geology, 275: 9-18.

Roqué-Rosell J, Villanova-de-Benavent C, Proenza JA, Tauler E, Galí S (2011). Distribution and speciation of Ni in sepiolite-falcondoite- type garnierite by EXAFS. Macla, 15: 183-184.

Roqué-Rosell J, Villanova-de-Benavent C, Proenza JA (*submitted*). The accumulation of Ni in serpentines and garnierites from Falcondo Ni-laterite deposit (Dominican Republic) elucidated by means of μXAS. Geochimica et Cosmochimica Acta.

Rosasco GJ, Blaha JJ (1980). Raman microprobe spectra and vibrational mode assignments of talc. Applied Spectroscopy, 34: 140-144.

Ross CS (1925). The so-called genthite from Webster, North Carolina. American Mineralogist, 10: 444-445.

Ross CS, Shannon EV (1926). Nickeliferous vermiculite and serpentine from Webster, North Carolina. American Mineralogist, 11: 90-93.

Ross CS, Shannon EV, Gonyer FA (1928). The origin of nickel silicates at Webster, North Carolina. Economic Geology, 23: 528-552.

Roy DM, Roy R (1954). An experimental study of the formation and properties of synthetic serpentines and related layer silicate minerals. American Mineralogist, 39: 957-975.

Rukavishnikova IA (1956). О некоторых магнезиально-никелевых водных силикатах Нижне-Тагильского серпентинитового массива (On some magnesium nickel hydrous silicates of the Nizhne-Tagil serpentinite massif). Кора Выветривания (Kora Vyvetrivaniya-The crust of weathering), 2: 12-17 (in Russian).

Saldi GD, Köhler SJ, Marty N, Oelkers EH (2007). Dissolution rates of talc as a function of solution composition, pH and temperature. Geochimica et Cosmochimica Acta, 71: 3446-3457.

Schmidt C (1844). Untersuchung einiger Mineralien, 4. Über eines Pimeliths aus Schlesien (Investigation of some minerals, 4. On the pimelites in Silesia). Annalen der Physik (Poggendorf), 61: 388-38.

Selfridge, G.C. (1936): An X-ray and optical investigation of the serpentine minerals. American Mineralogist 21, 463-503 (in German).

Slansky E (1955). Příspěvek k poznani hydrosilikatu niklu z Kremže v jižnich Čechach (Contribution to the knowledge of nickel hydrosilicates from Krems, in southern Bohemia). Universitas Carolina Pragensis Geologica, 1: 1-28 (in Czech).

Soler JM, Cama J, Galí S, Meléndez W, Ramírez A, Estanga J (2008). Composition and dissolution kinetics of garnierite from the Loma de Hierro Ni-laterite deposit, Venezuela. Chemical Geology, 249: 191-202.

Som SK, Joshi R (2002). Chemical weathering of serpentinite and Ni enrichment in Fe oxide at Sukinda area, Jajpur district, Orissa, India. Economic Geology, 97: 165-172.

Song Y, Moon H-S, Chon H-T (1995). New occurrence and characterization of Ni serpentines in the Kwangcheon area, Korea. Clay Minerals, 30: 211-224.

Spangenberg K (1938). Die wasserhaltigen Nickelsilikate (The hydrous nickel silicate). Zentralblatt für Mineralogie, Geologie und Paläontologie Abteilung A, 360-364 (in German).

Spangenberg K, Müller M (1949). Die lateritische Zersetzung des Peridotites bei der Bildung der Nickelerz Lagerstätte von Frankenstein in Schlesien (The lateritic decomposition of peridotite body in the formation of nickel ore deposit of Frankenstein in Silesia). Heidelberger Beiträge zur Mineralogie und Petrographie (Contributions to Mineralogy and Petrology), 1(5-6): 560-572 (in German).

Speakman K, Majumdar AJ (1971). Synthetic “deweylite”. Mineralogical Magazine, 38: 225-234.

Spencer LJ (1958). Twenty-first list of mineral names. Mineralogical Magazine, 31: 951-977.

Springer G (1974). Compositional and structural variations in garnierites. Canadian Mineralogist, 12: 381-388.

Springer G (1976). Falcondoite, Ni analogue of sepiolite. Canadian Mineralogist, 14: 407-409.

Starkl G (1883): Über Schuchardtit (On schuchardite). Zeitschrift für Kristallographie, 8: 239-240.

Stoch L (1974). Minerały ilaste (Clay Minerals). Wydawnictwo Geologiczne, Warszawa, Poland, 503 p. (in Polish).

Stoessell RK (1988). 25 ºC and 1 atm dissolution experiments of sepiolite and kerolite. Geochimica et Cosmochimica Acta, 52: 365-374.

Strunz H, Nickel EH (2001). Strunz Mineralogical tables. Schweizerbart, Stuttgart, 869 p. (9th edition).

Sudo T, Anzai T (1942). On certain green minerals associated with some Japanese nickel ores. Proceedings of the Imperial Academy, 18: 400-405.

Sutton SR, Bajt S, Delaney J, Schulze D, Tokunaga T (1995). Synchrotron x-ray fluorescence microprobe: Quantification and mapping of mixed valence state samples using micro-XANES. Review of Scientific Instruments, 66: 1464-1467.

Suárez S, Nieto F, Velasco F, Martín FJ (2011). Serpentine and chlorite as effective Ni-Cu sinks during weathering of the Aguablanca sulphide deposit (SW Spain). TEM evidence for metal-retention mechanisms in sheet silicates. European Journal of Mineralogy, 23(2): 179- 196.

Sufriadin AS, Arifudin I, Subagyo P, Imai A, I Wayan W (2011). Study on mineralogy and chemistry of the saprolitic nickel ores from Soroako, Sulawesi, Indonesia: Implication for the lateritic ore processing. Journal of Southeast Asian Applied Geology, 3: 23-33.

Sufriadin AS, Idrus A, Pramumijoyo S, Warmada IW, Nur I, Imai A, Imran AM, Kaharuddin (2012). Thermal and infrared studies of garnierite from the Soroako nickeliferous laterite deposit, Sulawesi, Indonesia. Indonesian Journal of Geology, 7(2), 77-85.

Talovina IV, Lazarenkov GV, Ryzhkova SO, Ugol'kov VL, Vorontsova NI (2008). Garnierite in nickel deposits of the Urals. Lithology and Mineral Resources, 43(6): 588-595.

Talovina IV, Lazarenkov GV, Vorontsova NI, Mezentseva OP (2009). Hydrothermal and supergene mineralization of nickel supergene deposits in ophiolitic massifs in Urals. 3rd International Conference on "Mafic-ultramafic complexes of folded regions and related deposits" (Kahkanar, Sverdlovsk, Russia; August 28), 2: 209-212 (in Russian, English abstract).

Tauler E, Proenza JA, Galí S, Lewis JF, Labrador M, García-Romero E, Suárez M, Longo F, Bloise G (2009). Ni-sepiolite-falcondoite in garnierite mineralization from the Falcondo Ni-laterite deposit, Dominican Republic. Clay Minerals, 44: 435-454.

Thorne R, Roberts S, Herrington R (2012). The Formation and Evolution of the Bitincke Nickel laterite deposit, Albania. Mineralium Deposita, 47: 933-947.

Torres-Roldán RL, García-Casco A, García-Sánchez PA (2000). CSpace: An integrated workplace for the graphical and algebraic analysis of phase assemblages on 32-bit Wintel platforms. Computers & Geosciences, 26: 779-793.

Tredoux M, de Wit M, Hart RJ, Armstrong RA, Lindsay NM, Sellschop JPF (1989). Platinum group elements in a 3.5 Ga nickel-iron occurrence: possible evidence of a deep mantle origin. Journal of Geophysical Research, 94: 795-813.

Trescases J-J (1973). Weathering and geochemical behaviour of the elements of ultramafic rocks in New Caledonia. Bulletin - Bureau Mineral Resources, Geology and Geophysics, Department of Minerals and Energy, 141: 149-161.

Trescases J-J (1975). L'évolution géochimique supergène des roches ultrabasiques en zone tropicale: Formation des gisements nickélifères de Nouvelle-Calédonie (Geochemical supergene evolution of ultrabasic rocks in tropical zone: Formation of the nickeliferous deposits of New Caledonia). Mémoires Office de la Recherche Scientifique et Tecnique Outre-Mer (ORSTOM), Paris, 78, p. 259 (in French).

Trescases J-J (1979). Remplacement progressif des silicates par les hydroxydes de fer et de nickel dans les profils d'altération tropicale des roches ultrabasiques. Accumulation résiduelle et épigènie (Progressive

replacement of silicates by iron and nickel hydroxydes within the tropical alteration profiles of ultrabasic rocks. Residual and epigenetic accumulation). Sciences Géologiques Bulletin, 32: 181-188 (in French).

Troly G, Esterle M, Pelletier B, Reibell W (1979). Nickel deposits in New Caledonia, some factors influencing their formation. International Laterite Symposium, 5: 85-119.

Typke PGW (1876). New nickel mineral from New Caledonia. The Chemical News and Journal of Physical Science, 33: 193-194.

Uyeda N, Hang PT, Brindley GW (1973). The nature of garnierites: II. Electron-optical study. Clays and Clay Minerals, 21: 41-50.

Varela JdD (1984): La estructura de las garnierites (The structure of garnierites). Geología Colombiana, 13, 29-40 (in Spanish).

Viti C (2010). Serpentine minerals discrimination by thermal analysis. American Mineralogist, 95: 631-638.

Viti C, Mellini M (1998). Mesh textures and bastites in the Elba retrograde serpentinites. European Journal of Mineralogy, 10: 1341-1359.

Villanova-de-Benavent C, Aiglsperger T, Jawhari T, Proenza JA, Galí S (2012). Micro-Raman spectroscopy of garnierite minerals: a useful method for phase identification. Macla, 16: 180-181.

Villanova-de-Benavent C, Nieto F, Proenza JA, Galí S (2011a). Talc- and Serpentine-like "Garnierites" from Falcondo Ni-laterite Deposit (Dominican Republic): a HRTEM approach. Macla, 15: 197-198.

Villanova-de-Benavent C, Nieto F, Viti C, Proenza JA, Galí S, Roqué-Rosell J (*in press*). Ni-phyllosilicates (garnierites) from the Falcondo Ni-laterite deposit (Dominican Republic): mineralogy, nanotextures and formation mechanisms by HRTEM and AEM. American Mineralogist.

Villanova-de-Benavent C, Proenza JA, Galí S, Tauler E, Lewis JF, Longo F (2011b). Talc- and serpentine-like "garnierites" in the Falcondo Ni-laterite deposit, Dominican Republic. 11th SGA Biennial Meeting (Antofagasta, Chile; October 26-29): 624-626.

Villanova-de-Benavent C, Proenza JA, Galí S, Tauler E, García-Casco A, Lewis JF, Longo F (2013). "Garnierite" ore and Ni-serpentine mineralizations from the Falcondo Ni-laterite deposit (Dominican Republic): An approach from quantitative XR element imaging. 12th SGA Biennial Meeting (Uppsala, Sweden; August 12-16): 379-382.

Villanova-de-Benavent C, Cama J, Soler JM, Proenza JA, Galí S (2014a). Dissolution kinetics of Ni-phyllosilicates from the Falcondo Deposit, Dominican Republic. Macla, 19: a-z (page numbers not yet available to date).

Villanova-de-Benavent C, Proenza JA, Galí S, García-Casco A, Tauler E, Lewis JF, Longo F (2014b). Garnierites and garnierites: Textures, mineralogy and geochemistry of garnierites in the Falcondo Ni-laterite deposit, Dominican Republic. Ore Geology Reviews, 58: 91–109.

Villanova-de-Benavent C, Proenza JA, Galí S, Nieto F, García-Casco A, Roqué-Rosell J, Tauler E, Lewis JF (2014c). Mineralogy of Ni-phyllosilicates in the Falcondo Ni-laterite deposit (Dominican Republic): A multiscale approach. 21st Meeting of the International Mineralogical Association (Gauteng, South Africa; September 1-5): 298.

Villanova-de-Benavent C, Tredoux M, Aiglsperger T, Proenza JA (2014d). Ni-Mg-phyllosilicates from Bon Accord, Barberton, South Africa: New data on willemseite and nimite. IMA2014 abstracts: 657.

Vitovskaya, I.V., Berkhin, S.I., 1968. К вопросу о природе керолита (On the nature of kerolite). Кора Выветривания (Kora Vyvetrivaniya-The crust of weathering), 10: 134-159 (in Russian).

Vitovskaya, I.V., Berkhin, S.I., 1970. К вопросу о природе гарниерита (On the nature of garnierite). Кора Выветривания (Kora Vyvetrivaniya-The crust of weathering), 11: 26-39 (in Russian).

Walker PH (1888). Analysis of "genthite" from North Carolina. Journal of the American Chemical Society, 10: 44.

Wang Z-G (2010). Geological features of lateritic nickel deposits and mineral exploration methods in the Dinagat Island, Philippines. Geology and Exploration, 46: 361-366 (in Chinese with English abstract).

Wang A, Freeman J, Kuebler KE (2002). Raman spectroscopic characterization of phyllosilicates. 33th Lunar and Planetary Science Conference (Houston, Texas, USA; March 11-15), #1374.

Wells MA, Ramanaidou ER, Verrall M, Tessarolo C (2009). Mineralogy and crystal chemistry of "garnierites" in the Goro lateritic nickel deposit, New Caledonia. European Journal of Mineralogy, 21: 467-483.

White JS Jr, Henderson EP, Mason B (1967). Secondary minerals produced by weathering of the Wolf Creek meteorite. American Mineralogist, 52: 1190-1197.

Whitney DL, Evans BW (2010). Abbreviations for names of rock-forming minerals. American Mineralogist, 95: 185-187.

Whittaker EJW (1953). The structure of chrysotile. Acta Crystallographica, 6: 747-748.

Whittaker EJW (1954). The diffraction of X-rays by a cylindrical lattice. I. Acta Crystallographica, 7: 827-832.

Whittaker EJW (1955a). The diffraction of X-rays by a cylindrical lattice. II Acta Crystallographica, 8: 261-265.

Whittaker EJW (1955b). The diffraction of X-rays by a cylindrical lattice. III Acta Crystallographica, 8: 265-271.

Whittaker EJW (1955c). A classification of cylindrical lattices. Acta Crystallographica, 8: 571-574.

Whittaker EJW (1955d). The diffraction of X-rays by a cylindrical lattice. IV Acta Crystallographica, 8: 726-729.

Wicks FJ, Dunn PJ, Back ME, Ramik RA (in press). Maufite dirscredited: not a mineral species but an important interstratified Ni-bearing lizardite/clinochlore. Canadian Mineralogist.

Wicks FJ, Plant AG (1979). Electron-microprobe and X-ray-microbeam studies of serpentine textures. Canadian Mineralogist, 17: 785-830.

Wicks FJ, Zussman J (1975). Microbeam X-ray diffraction patterns of the serpentine minerals. Canadian Mineralogist, 13: 244-258.

Wicks FJ, Dunn PJ, Back ME, Ramik RA (in press). Maufite discredited: not a mineral species but an important interstratified Ni-bearing lizardite/clinochlore. Canadian Mineralogist.

Wiewióra A (1978). Ni-Containing Mixed-Layer Silicates from Szklary, Lower Silesia, Poland. Bulletin du Bureau de Recherches Géologiques et Minières (BRGM), Section II (Géologie Appliquée), 3: 247-261.

Wiewióra A, Dubińska E, Iwasińska J (1982): Mixed-layering in Ni-containing clay grade minerals from Szklary, Lower Silesia, Poland. International Clay Conference (Developments in Sedimentology): 339-340.

Wierióra A, Szpila K (1975). Nickel containing regularly stratified chlorite-saponite from Szklary, Lower Silesia. Clays and Clay Minerals, 23: 91-96.

Wilkerson AS (1962). The minerals of Franklin and Sterling Hill, New Jersey. New Jersey Geological Survey Bulletin, 65: 80 p.

Yada K (1967). Study of chrysotile asbestos by a high resolution electron microscope. Acta Crystallographica, 23: 704-707.

Yada K (1971). Study of microsctructure of chrysotile asbestos by high resolution electron microscope. Acta Crystallographica, 27: 659-664.

Yada K (1979): Microstructures of chrysotile and antigorite by high-resolution electron microscopy. Canadian Mineralogist (GAC-MAC and GSA Symposium) 17: 679-691.

Yada K (1984). Alternation of clino- and orthochrysotile in a single fiber as revealed by high-resolution electron microscopy. Clays and Clay Minerals, 32: 429-432.

Zega TJ, Garvie LAJ, Dódony I, Friedrich H, Stroud RM, Buseck PR (2006): Polyhedral serpentine grains in CM chondrites. Meteoritics and Planetary Sciences. 41: 681-688.

Zussman J (1955): Recent X-ray structural work on serpentine minerals. Clays and Clay Minerals 4: 80-81.

Zussman J, Brindley GW (1957): Electron diffraction studies of serpentine minerals. American Mineralogist 42: 133-153.

APPENDIX A1.1. List of names used in the literature to refer to Ni-bearing Mg-phyllosilicates, including the origin of the name, possible synonyms, a short definition of the mineral species, its physical properties, chemical formula, type locality, the status by the International Mineralogical Association and all the publications citing the mineral name (extended version of **Table 1.1**). Legend: H = hardness, SG = specific gravity, n = refraction index, Δn = birrefringence, np = minimum refraction index, ng = maximum refraction index, DTA = differential thermal analysis, endo = endothermic peak, exo = exothermic peak, TG = thermogravimetry.

Name	Origin of the name	Synonyms	Definition	Physical properties	Chemical formulae	Type locality	IMA status	References
Garnierite *sensu stricto*	Named after its discoverer, the French civil engineer Jules Garnier. First documented in 1863 in New Caledonia, in a mining report on the geology and mineral resources of the French colony (Garnier, 1867; Pecora, 1949). However, the first detailed description and chemical analysis of garnierite sensu stricto were performed by Archibald Liversidge, who initially named the mineral "noumeïte". Liversidge worked on the samples given by Garnier to the Rev. William Branwhite Clarke, who suggested to Liversidge to keep the term "garnierite" (Liversidge, 1874a). Actually, when Liversidge sent a copy of his paper to Garnier, Garnier replied that the new mineral nouméite being described in the paper sounded very much like a mineral he had described in his 1869 paper. Liversidge decided to designate the new species, a pale green adhesive mineral, in honor to Garnier and described a second, darker green, unctuous mineral found in the same area in New Caledonia as "noumeïte", name formerly given to the first variety (Liversidge, 1974b). Currently it is the generic name for all green nickel silicate ores.	-	Mixture of pimelite and serpentine-group minerals (Faust, 1966), variety of nouméite (Des Cloizeaux, 1878)	Green; shiny and waxy lustre; soft; white when powdered; similar to Chinese jade; found within serpentines; nickel may be the cause of the green colour (Garnier, 1867); Similar to pimelites (Garnier, 1874); Apple green; conchoïdal fracture; amorphous; H 2-2.5; SG 2.27; adheres to tongue, falls to pieces in water (Liversidge, 1874b)	$(Mg,Ni)^{10}Si^{8}$ + 3H [Liversidge, 1874b; Brush, 1872; Dana, 1875]; (Mg,Ni)Si + nH [Garnier, 1878]	New Caledonia (Garnier, 1876)	Not approved	Garnier (1867), Brush (1872), Liversidge (1874a, 1874b), Dana (1875), Typke (1876), Garnier (1876, 1878), Des Cloizeaux (1878), Hood (1883), Pecora *et al.* (1949), Huggins (1961), Kato (1961), Faust (1966), Springer (1974), Wells *et al.* (2009)
noumeïte	Named for the type locality (Nouméa, the capital of New Caledonia).	nouméite (Glasser, 1907), nouméaite (Clarke, 1888)	Mixture of pimelite and serpentine-group minerals (Faust, 1966)	Apple green, dark; somewhat greasy to touch; amorphous, veins and incrustations; H 2.5; SG 2.58; does not adhere to tongue, does not fall to pieces in water (Liversidge, 1874b). Dark apple green; amorphous, unctuous; does not adhere to tongue, does not fall to pieces in water; H 2.5; SG 2.58 (Hood, 1883). In addition to garnierite, it is found to have equal physical properties as genthite (Clarke, 1888).	-	Nouméa, New Caledonia (Liversidge, 1874b, 1880)	Not approved	Liversidge (1874a, 1874b, 1880), Des Cloizeaux (1878), Hood (1883), Faust (1966)
népouite	Named for the type locality (Népoui) [Glasser, 1907] and later described as the Ni equivalent of lizardite [Maksimović, 1973].	antigorite nickelifère (Glasser, 1907; Caillère, 1936), α-kerolite (Rukavishnikova, 1956; Caillère & Hénin, 1957)	Ni equivalent of lizardite (Brindley & Wan (1975)	Pale green to bright green (depending on Ni content); hexagonal flakes of hundreths of mm thick with good cleavage and nacre lustre, forming vermicular aggregates similar to chlorite; negative sign; H 2; SG 2.47-3.24; n>1.62-1.63, Δn=0.036-0.038 under optical microscope; similar chemistry to garnierite/nouméïte but different features: garnierite/nouméïte are amorphous, spherulitic and positive (Glasser, 1907); Medium green; crudely hexagonal vermiculitic crystal up to 3 mm across and up to 7 mm long; green to yellow-green fibrous crystal, colour banded and fractured normal to fibres, n>1.55, Δn=0.020-0.040 under optical microscope; serpentine-lizardite? by XRD (Springer, 1974)	$2SiO^{2}$, 3(Ni,Mg)O, $2H^{2}O$ [Glasser, 1907], $(Ni_{1.59}Mg_{0.67}Fe^{3+}{}_{0.05})_2Si_{2.17}Al_{0.22}O_5(OH)_4$ [Wells *et al.*, 2009]	Népoui, New Caledonia (Glasser, 1907)	Valid (pre-IMA - "grandfathered")	Glasser (1907), Caillère (1936), Gritsaenko *et al.* (1943), Rukavishnikova (1956), Maksimović (1973, 1975), Springer (1974), Brindley & Wan (1975)
pecoraite	First described by John S. White & coauthors in 1967 as "the nickel analog of clino-chrysotile", and studied in detail by George T. Faust and coauthors in 1969, who named it after Dr William Thomas Pecora, director of the United States Geological Survey and student of nickel silicate deposits (Faust, 1969).	Ni-clinochrysotile (Faust *et al.*, 1969)	Ni equivalent of chrysotile (Faust *et al.*, 1969)	0.1-5 mm diameter green grains that fill cracks in the Wolfe Creek meteorite; weakly birrefringent n 1.565-1.603 depending on the amount of adsorbed water; SG 3.08; (Faust, 1969); Bright green; clear vitreous appearance; weakly birrefringent n 1.63; poorly crystalline by XRD (Nickel, 1973)	$Ni_{5.41}Mg_{0.10}Fe^{2+}{}_{0.08}Al_{0.22}Si_{4.05}O_{10}(OH)_8$ [Faust *et al.*, 1969]	Wolfe Creek meteorite crater, Halls Creek Shire, Western Australia, Australia (White et al., 1967; Faust *et al.*, 1969)	Approved (Fleischer, 1969)	White *et al.* (1967), Faust *et al.* (1969), Fleischer (1969), Faust *et al.* (1973), Nickel (1973), Nickel *et al.* (1979), Bailey (1980), Milton *et al.* (1981), Milton *et al.* (1983), Frost *et al.* (2008)
karpinskite	Named after the president of the Russian Academy of Sciences A.P. Karpinsky (Rukavishnikova, 1956). Inadequately described, not to be confused with karpinskyite (Fleischer, 1957a). Fleischer (1957b) reported the mineral and recommended to revisit the nomenclature of the hydrous magnesium and nickel silicates.	-	-	Colorless to light blue to deep greenish-blue veinlets in "kerolitised" serpentinites; dense, cryptocrystalline, dull to weakly greasy luster; H 2.5-3; SG 2.63(deeply colored)-2.53(lighter); well-crystallised plates and monoclinic prisms under the microscope; no pleochroism; biaxial negative; np1.570 ng 1.594 (deeply colored)-np1.553 ng 1.569(lighter); DTA endo 105-150, 550-625, 840-910º (similar to montmorillonite) (Feischer, 1957b)	(Ni,Mg)O $2SiO_2$ H_2O [Rukavishnikova, 1956], $(Mg_{1.30}Ni_{0.70})Si_2O_5(OH)_2$ [Anthony *et al.*, 2001)]	Mednorudyanskoye Cu Deposit, Nizhny Tagil, Sverdlovskaya Oblast', Middle Urals, Urals Region, Russia (Rukavishnikova, 1956)	Questionable/ doubtful (Fleischer, 1957; Nickel & Nichols, 2009)	Rukavishnikova (1956), Fleischer (1957a, 1957b), Spencer (1958), Anthony *et al.* (2001), Nickel & Nichols (2009)
willemseite	Named after professor Johannes Willemse, who was the head of the Department of Geology at the University of Pretoria. He was a well-known authority on layered mafic intrusions and, in particular, of the Bushveld Igneous Complex (De Waal, 1970b).	-	Ni equivalent of talc (Fleischer, 1969)	Light green, colourless or non pleochroic in thin section; H 2; perfect {001} cleavage; SG 3.281-3.348; nα 1.600 nβ 1.652; a 5.316 b 9.149 c 18.994 α90º β 99.96º γ 90º; cell volume 695.74 Å3 (De Waal, 1970b)	H3.67(Ni4.23Mg1.61Fe3+0. 20Fe2+0.04Co0.06Ca0.05)(Si7.89Al0.07)O24 [De Waal, 1970b], (Ni3.4Mg2.2Fe3+0.4)(Si7.8Al0.08)O20(OH)4 [Villanova-de-Benavent *et al.*, 2014d]	Scotia Talc Mine, Barberton Mountain, Transvaal, South Africa (Hiemstra & De Waal, 1968b)	Approved (Fleischer, 1969)	Hiemstra & De Waal (1968b), Fleischer (1969), De Waal (1970b), Bailey (1980), Villanova-de-Benavent *et al.* (2014d)

APPENDIX A1.1. (CONTINUED).

Name	Origin of the name	Synonyms	Definition	Physical properties	Chemical formulae	Type locality	IMA status	References
kerolite	The name was suggested by Breithaupt (1823) as derived from the Greek κηρος (*keros*, wax) λιθος (*lithos*, stone). The name was widely used in the early years but was later discredited because no adequate definition and chemical formula was obtained. Brindley et al. (1977) stated that a characterisation must be done by XRD, and thus studies prior to the use of this technique had to be discarded. In addition, in some studies the name "kerolite" was used to classify some of the Ni-phyllosilicates into two groups: α-kerolite was used for the serpentine-like minerals, whereas β-kerolite referred to the talc-like phases (e.g. Rukavishnikova, 1956; Varela, 1984). Kerolite was described as a phase closely related to talc, but with significant differences (Brindley, 1978).	cerolite (Brindley *et al*., 1977)	Structure with talc affinity but extra water (Brindley, 1978)	Fine grained, admixed with other minerals so that their definition encounters problems; characterised by 10 Å spacings under TEM with minor 7 Å regions (Brindley, 1978).	$R_3Si_4O_{10}(OH)_2.nH_2O$ with R mainly Mg and n about 0.8-I.2 [Brindley *et al*., 1977], $(Mg,Ni)_{3.04}(Al,Fe)_{0.01}(Si_{3.93}Al_{0.02}Fe_{0.02})O_{10}(OH)_2 \cdot 0.89H_2O$ [Brindley *et al*., 1979]	Ząbkowice-Frankenstein, Lower Silesia, Dolnośląskie, Poland (Breithaupt, 1923)	Discredited (Nickel & Nichols, 2009)	Genth (1891), Breithaupt (1923), Maksimović (1966), Stoch (1974), Brindley *et al*. (1977), Brindley *et al*. (1979), Bailey (1980)
pimelite	The first Ni-bearing phyllosilicate reported in nature was pimelite, in a hydrothermal replacement of Ordovician gabbroic and ultrabasic intrusions into the gneisses of the Precambrian Eulen Massif at Kosemütz, Frankenstein (Silesia, Poland). It was initially named grüner chrysopraserde ("green chrysoprase earth"), because it was thought as the cause of the greenish colour in the gemstone chrysoprase (an apple-greeen Ni-bearing variety of quartz), and also because of the earthy appearance of the mineral (Klaproth, 1788). Finally it was given the name "pimelite" for the Ancient Greek word πιμελή (pimelé, "soft fat, lard") in 1800 by Karsten, for the appearance of the mineral (Faust, 1966). Pimelite was determined to be a smectite as early as 1938 [also American Mineralogist 51:279 [1966]. Later erroneously ascribed to nickel-rich talc. Both nickel-bearing talc, intermediate nickeloan nontronite, and nickel dominant smectite occur at the type locality. A re-validation research project has begun. A significant literature exists verifying that pimelite is nickel-dominant smectite, although there are studies which misidentified the starting material as "pimelite" and reached erroneous conclusions. Often thought to be a coloring agent in chrysoprase (Faust, 1966). The mineral labelled as pimelite in 1800 by D.L.G. Karsten was reported as "probably willemseite or kerolite", although pimelite had historical precedence (Burke, 2006).	grüner chrysopraserde (Klaproth, 1788), β-kerolite (Rukavishnikova, 1956)	Ni equivalent of kerolite (Maksimović, 1966)	Apple green, light; greasy to touch; massive, earthy; H 2.5; SG 2.23-2.76; does not adhere to tongue (Klaproth, 1788); Dark apple green; amorphous, unctuous; does not adhere to tongue, does not fall to pieces in water; H 2.5; SG 2.58 (Hood, 1883); Apple green; massive with conchoidal fracture; occurs in seams and lenses in weathered rusty brown ultramafic rock; dark brown almost opaque under the optical microscope; poorly crystalline serpentine and poorly serpentine talc by XRD/olive green, very porous, soft with conchoidal fracture; yellowish brown, translucent, cobble-stone pattern of nearly isotropic grains surrounded by fibrous aggregates of highly birrefringent material under optical microscope; poorly crystalline serpentine by XRD (Springer, 1974)	$(Mg,Ni)_{3.04}(Al,Fe)_{0.01}(Si_{3.93}Al_{0.02}Fe_{0.02})O_{10}(OH)_2 \cdot 0.89H_2O$ [Brindley *et al*., 1979]	Kosemütz, near Frankenstein, Upper Silesia, Poland (Klaproth, 1788)	Discredited 2006 (Burke, 2006)	Klaproth (1788), Karsten (1800), Liversidge (1874b), Hood (1883), Spangenberg (1938), Faust (1966), Manceau & Calas (1985), Decarreau *et al*. (1987), Burke (2006)
falcondoite	Ni-containing sepiolites were already described in Walker (1888) in North Carolina (USA), although Faust (1966) mentioned that some early descriptions must be considered cautiously. Since then, many studies report the occurrence of Ni-sepiolites in New Caledonia with Ni:Mg ratio of 1:4 (Caillère, 1936), Oregon in the USA with 1.46 % Ni (Hotz, 1964) and Serbia wih 6.65 % Ni (Maksimović, 1969). The Ni-dominant end member falcondoite (Ni,Mg)4Si6O15(OH)2•6(H2O) was described, analysed and named by Springer (1976), from samples of the Falcondo deposit, in the Dominican Republic.	-	Ni equivalent of sepiolite (Springer, 1976)	Whitish green; slightly schistose, soft and friable; H 2-3; density 1.9 g/cm^3; clear to translucent tangled fibrous aggregates under the microscope; n 1.55; birrefringent Δn=0.01-0.02; parallel or nearly parallel extinction; a 13,5 b 26.9 c 5.24; unit cell volume 1903 Å^3; DTA endo 180, 360, 540, 840º; TG 25-200º 7.0%, 200-370º 3.1%, 370-600º 2.3%, 600-850º 2.7% (Springer, 1976)	$\{(Ni_{0.58}Mg_{0.42})_8 \cdot (H_2O)_4 \cdot (OH)_4(Si_{12}O_{30})\} \cdot (H_2O)_8$ [Springer, 1976]	Ni-laterite deposit mined by Falconbridge Dominicana C. por A., Dominican Republic (Springer, 1976)	Approved 1976 (Springer, 1976)	Walker (1888), Caillère (1936), Hotz (1964), Faust (1966), Maksimović (1969), Springer (1976), Bailey (1980), Tauler *et al*. (2009)
brindleyite	Firstly named nimesite, possibly the combination of Ni + amesite (Mg-Al-serpentine) (Fleischer, 1973). The IMA-CNMMN did not accept this name due to the similarity between nimesite and nimite (Ni-bearing chlorite) (Maksimović & Bish, 1978). The mineral was later renamed after Dr. George W. Brindley, Emeritus Professor of Mineral Sciences at The Pennsylvania State University (Maksimović & Bish, 1978).	nimesite (Maksimović, 1972)	Ni equivalent of amesite (Mg-Al-serpentine) and berthierine (Fe-Al-serpentine) (Fleischer, 1973)	Green colour; irregular aggregates composed of extremely thin fibres under electron microscope; SG 3.005; n 1.635; endo 608, 700º, exo 140, 327, 465º (Fleischer, 1973)	$(Ni_{2.56}Mg_{0.51}Fe_{0.34}Al_{1.74}Ti_{0.08})_8(Si_{2.54}Al_{1.46}) \cdot (OH)_{9.02}$, $(Ni_{1.81}Mg_{0.54}Fe_{0.27}Al_{2.50}Ti_{0.08})_8(Si_{2.62}Al_{1.38}) \cdot (OH)_{8.0}$ [Maksimović, 1972]	Marmara bauxite deposit, Megara, Western Attikí, Greece (Maksimović, 1972)	Approved 1973 (Fleischer, 1973)	Maksimović (1972), Fleischer (1973), Maksimović & Bish (1978)
nimite	Despite schuchardite already existed to designate nickel-bearing minerals of the chlorite group, the newly discovered Ni-chlorite was named after the National Institute of Metallurgy of South Africa (NIM). Schuchardite was used for Ni-dominant synthetic chlorites, but the name was discarded because Ni<Mg in natural schuchardite (De Waal, 1970a).	-	Ni equivalent of clinochlore (Mg-Fe^{2+}-chlorite), schuchardite (Fleischer, 1969; Bailey et al., 1971)	Yellowish green, faintly pleochroic in thin section; H 3; pronounced {001} cleavage; SG 3.123-3.210; nα 1.637 nβ 1.647; a 5.320 b 9.214 c 14.302 α90º β 97.10º γ 90º; cell volume 695.74 Å3 (De Waal, 1970a)	H15.42(Ni5.23Mg3.33Fe3+0.72Fe2+0.51Co0.07Ca0.09Mn0.01Al1.97)(Si6.02Al1.98)O36 [De Waal, 1970a], (Ni4.5Mg4.0Al2.0Fe2+1.3Fe3+0.1)(Si6.2Al1.8)O20(OH)16 [Villanova-de-Benavent *et al*., 2014d]	Scotia Talc Mine, Barberton Mountain, Transvaal, South Africa (Hiemstra & De Waal, 1968a)	Approved (Fleischer, 1969)	Hiemstra & De Waal (1968a), Fleischer (1969), De Waal (1970a), Bailey (1980), Villanova-de-Benavent *et al*. (2014d)
deweylite	First described in 1826 by Emmons (Faust & Fahey, 1962; Bish & Brindley, 1978). Since then, poorly defined due to its chemical and mineralogical variability and poor structural order. Various and contradictory descriptions: mixture of platy serpentine and talc (Kato & Minato, 1960; Kato, 1961), 10 A reflection stands for sepiolite and 7 A to antigorite (Lapham, 1961), mixture of serpentine and stevensite (Faust & Fahey, 1962; Fleischer, 1975), metastable mixture of poorly crystalline talc and serpentine (Speakman & Majumdar, 1971), immature cryptocrystalline chrysotile (Morandi & Poppi, 1971). Deweylite is a mixture invariable proportions of a disordered form of talc (kerolite) and a disordered form of serpentine. Both components have excess water, probably associated with unbalanced surface bonds (Bailey, 1980). Currently the name is useful only as a field term (Bish & Brindley,1978).	-	Mixture of lizardite and stevensite (Faust & Fahey, 1962), Ni-free garnierite (Garnier, 1878), gymnite (Genth, 1875; Faust, 1966), variety of gymnite (Genth, 1851)	Whitish, yellowish, brownish, reddish; resinous to waxy lustre, brittle, translucent; amorphous, resembling gum arabic, resinous; H 2-3.5; SG 2-2.3; from the alteration of feldspar (Genth, 1875)	4MgO $3SiO_2$ $6H_2O$ [Genth, 1875, Palache, 1937], $(Mg_{4.83}Fe^{2+}_{0.45}Ca_{0.02})Si_{4.60}O_{10}(OH)_8$ [Faust & Fahey, 1962]	-	Not approved	Genth (1875, 1891), Garnier (1878), Kato & Minato (1960), Kato (1961), Lapham (1961), Faust & Fahey (1962), Morandi & Poppi (1974), Speakman & Majumdar (1971), Fleischer (1975), Bish & Brindley (1978), Bailey (1980)
gymnite	-	-	deweylite (Genth, 1875; Faust, 1966)	-	-	-	Not approved	Genth (1875), Faust (1966)

APPENDIX A1.1. (CONTINUED).

Name	Origin of the name	Synonyms	Definition	Physical properties	Chemical formulae	Type locality	IMA status	References
genthite	Ni-bearing gymnite was reported by Genth (1851) in Pennsylvania and was later called genthite by Dana & Brush (1868). This term was later used to designate a nickel-bearing mineral found in the deposits of Riddle, Oregon (Clarke, 1888; Kay, 1906; Diller & Kay, 1924; Pecora & Hobbs, 1942; Pecora *et al*., 1949) and Webster, North Carolina (Ross *et al*., 1928).	-	Mixture of pimelite and Ni-serpentine (Faust, 1966), nickel-gymnite (Genth, 1875)	Apple-green; resinous lustre, opaque to translucent; hemispherical, mammillary or stalactitic incrustations; H 3-4; SG 2.409; graduating into deweylite; falls to pieces in water (Genth, 1874; Liversidge, 1874b); medium and dark green; thin colloform coating on massive chromite; light green colloform crust; n>1.55, Δn=0.008-0.010 under optical microscope; poorly crystalline serpentine by XRD (Springer, 1974)	$2NiO\ 2MgO\ 3SiO_2\ 6H_2O$ [Palache, 1937]	Pennsylvania, USA (Genth, 1875)	Not approved	Genth (1851, 1891), Dana & Brush (1868), Liversidge (1874b), Clarke (1888, 1890), Kay (1906), Diller & Kay (1924), Ross (1925), Ross *et al.* (1928), Palache (1937), Pecora & Hobbs (1942), Pecora *et al.* (1949)
connarite	Glasser (1907) compared népouite from New Caledonia with a sample of connarite from the collection of Des Cloizeaux, described by Breithaupt, and found similar optical properties. Berman (1937) stated that connarite is more hydrous than the other members of the group, but admits that little is known on its composition because very few analyses have been made. However, népouite has higher Ni and lower Si.	comarite (Glasser, 1907), komarite, conarite, konnarite	Mixture (Faust, 1966), member of the schuchardite group (Spangenberg, 1938)	Apple green; massive, soft, very porous fragments with conchoidal fracture enclosed in a darker green, massive garnierite with irregular fracture; few yellowish brown semi-translucent flakes with micaceous cleavage in cryptocrystalline matrix with low birrefringence under optical microscope; poorly crystalline serpentine and poorly crystalline talc with quartz by XRD (Springer, 1974)	$(Ni,Mg)_8(Si_4O_{10})_3(OH)_4 \cdot 6\ H_2O$ [Berman, 1937]	Hans Georg mine, Röttis, Sachsen, Germany (Breithaupt, 1859)	Not approved	Breithaupt (1859), Glasser (1907), Berman (1937)
röttisite	Named for the type locality.	-	pimelite (Faust, 1966)	-	-	Hans Georg mine, Röttis, Sachsen, Germany (Breithaupt, 1859)	Not approved	Breithaupt (1859), Faust (1966)
de saulesite	Named after the Trotter Mine manager, Major A. B. de Sauler by Koenig in 1889.	-	pimelite (Faust, 1966), a variety of genthite except magnesia is lacking (Wilkerson, 1962)	Yellowish green, apple-green, emerald-green; amorphous; as crusts, aggregates and earthy forms; n=1.59; crusts on or as filling in fluorite, also as porous, spongelike aggregates associated with and altering from nickeline and chloantite (Wilkerson, 1962).	$4NiO\ 3SiO_2\ 6H_2O$ [Palache, 1937]	Trotter Mine, Franklin, New Jersey, USA (Koenig, 1889)	Not approved	Koenig (1889), Wilkerson (1962), Faust (1966)
revdanskite	Named for the type locality.	refdanskite, revdinite, revdinskite, rewdanskite, rewdjanskit, rewdinskit	quartz with pimelite (Faust, 1966)	dirty greyish green; amorphous, laminated lumps; falls to powder on pressure; SG 2.27; adheres to tongue (Hermann, 1867); white to pale green and dark brown; schistose, hard, with slickened sides and an irregular fracture; greenish brown, weakly pleochroic fibrous flakes in matrix of granular quartz under optical microscope; poorly crystalline serpentine+antigorite+quartz by XRD (Springer, 1974)	-	Revdinsk, Ural Mountains, Russia (Hermann, 1867)	Not approved	Herman (1867), Liversidge (1874b), Faust (1966)
alipite	Carl Schmidt (1844), a student in the laboratory of Professor Heinrich Rose, analysed a specimen of pimelite. Unfortunately, he dried the specimen on a water bath, thus, removing the interlaver water of the clay mineral and found only 5.23 per cent of water. Therefore he concluded that pimelite was merely a water-bearing talc or *meerschaum.* Professor Glocker (1845) of Breslau University suggested that the name should be changed to alipidite from the Greek word for "not greasy".	alizit, aalizite, alipidite	Chemically similar to willemseite ≠ spec. grav. (Liversidge, 1874b), pimelite (Faust, 1966)	Apple green; not unctuous; amorphous; H 2.5; SG 1.41-1.46; adheres to tongue, not unctuous (Schmidt, 1844; Liversidge, 1874b)	-	Frankenstein, Poland (Schmidt, 1844)	Not approved	Schmidt (1844), Glocker (1846), Liversidge (1874b), Faust (1966)
maufite	Named after Mr. H. B. Mauf, a director at the Southern Rhodesia Geological Survey (Foshag 1930). The nomenclature recommendations to discredit maufite as a mineral name were accepted by the IMA-CNMMN in May 13th, 1993 (Nickel & Grice, 1998).	-	Interstratified clinochlore-lizardite (Burke, 2006); interstratified nickel-bearing lizardite (polytype group A; Bailey, 1969) and clinochlore (polytype 1a; Bailey, 1988a,b), being lizardite the dominant phase (Wicks *et al*., in press)	It occurs as a quarter inch seam of a peculiar bright emerald green rock within a dark red, speckled, serpentine rock adjacent to a small dolerite dyke (Keep 1930b).	$(Mg,Ni,Fe,O)\ 2Al_2O_3\ 3SiO_2\ 4H_2O$ [Keep, 1930]; $MgAl_4Si_3O_{13} \cdot 4H_2O$ [Nickel & Nichols, 2009]; (Mg1.74Al0.88Ni0.13□0.25)Σ=3.00(Si1.60Al0.40)Σ=2.00O5(OH)4 [Wicks *et al*., in press]	Umvukwe, Great Dyke, Zimbabwe (Keep, 1930a, b)	Discredited (Burke, 2006)	Keep (1930a, b), Foshag (1930), Burke (2006), Wicks *et al*. (in press)
schuchardite	-	schuchardtite	nimite (Fleischer, 1969; Bailey *et al*., 1971)	Pale apple green; schistose to massive greasy, slightly porous; cream to light green polycrystalline material intergrown with almost opaque fibrous aggregates under optical microscope; chlorite+talc+quartz by XRD/apple green; massive to colloform showing both slickensides and irregular fracture; vermicular aggregates in fine-grained matrix; n>1.55, Δn=0.010-0.020 under optical microscope; poorly crystalline serpentine and poorly crystalline talc by XRD (Springer, 1974)	$(Mg_{2.39}Ni_{1.62}Al_{0.51}Fe_{0.26})Si_{3.49}Al_{0.51})O_{10}(OH)_8$ (Springer, 1974)	-	Discredited (Guggenheim *et al*., 2006)	Starkl (1883), Spangenberg (1938), Bailey *et al*. (1971), Brindley & de Souza Jefferson (1975)

APPENDIX A1.2. List of Ni-bearing Mg-phyllosilicate occurrences worldwide.

Country	Locality	Ni-phyllosilicates	References
Albania	Bitincke and other 15 occurrences (Vranisht, Mamez, Surdit, Liqeni i Kuq, Xhumage, Bushtrice-a, Bushtrice-b, Skroske, Cur-Pishkash, Prenjas, Debrove, Hudenisht, Guri i Perojeojur, Cervenake, Guri i Kuq)	garnierite[1]	[1]Thorne *et al*. (2012)
Australia	Greenvale Nickel Deposit (Queensland)	népouite[1]	[1]Reddy *et al*. (2009)
	Marlborough Nickel Deposit (Queensland, Rockhampton)	Ni-smectite and chlorite, chrysoprase[1]	[1]Foster & Eggleton (2002)
	Bulong (Western Australia, Kalgoorlie)	Ni-serpentines and Ni-smectites (Ni-nontronite, saponite and montmorillonite)[1]	[1]Elias *et al*. (1981)
	MKD5 nickel deposit (Western Australia, Wiluna Shire, Mount Keith)	népouite[1]	[1]Nickel & Bridge (1975)
	Murrin Murrin (Western Australia)	Fe-Ni-smectites[2,3]	[1]Wells (2003), [2]Gaudin *et al*. (2004a), [3]Gaudin *et al*. (2004b), [4]Gaudin *et al*. (2005)
	Otter Juan Mine, Otter Shoot Nickel Mine (Western Australia, Coolgardie Shire, Kambalda)	népouite[1]	[1]Nickel *et al*. (1977)
	Otway Prospect (Western Australia, Nullagine Region)	pecoraite[1]	Nickel (1973), [1]Reddy *et al*. (2009)
	Rocky's Reward (Western Australia, Agnew)	pimelite[1]	[1]Reddy *et al*. (2009)
	Scotia Nickel Mine (Western Australia, Kalgoorlie-Boulder Shire, Broad Arrow)	népouite[1]	[1]Nickel & Bridge (1975)
	Wolfe Creek meteorite (Western Australia, Nullagine Region)	pecoraite[1-8]	[1]White *et al*. (1967), [2]Faust *et al*. (1969), [3]Faust *et al*. (1973), [4]Nickel *et al*. (1979), [5]Bailey (1980), [6]Milton *et al*. (1981), [7]Milton *et al*. (1983), [8]Frost *et al*. (2008)
Brazil	Morro do Niquel (Minas Gerais, Pratápolis)	7 Å garnierite, 10 Å garnierite[1], népouite[2]	[1]Brindley & Hang (1973), [2]Brindley & Wan (1975), [3]Barros de Oliveira (1990)
	Jacupiranga (São Paulo)		[1]Barros de Oliveira (1990)
	Morro do Corisco (Paraná, São Paulo; labelled "Morro do Cerisco" in the literature)	7 Å garnierite[1], népouite[2]	[1]Brindley & Hang (1973), [2]Brindley & Wan (1975)
	Barro Alto (Goiás)	serpentine garnierite[1], talc garnierite[1]	[1]Esson & Carlos (1978), [2]Barros de Oliveira (1990)
	Liberdade (Paraná, São Paulo)	garnierite[1], chlorite-vermiculite[1], serpentine garnierite[1], talc garnierite[1]	[1]Esson & Carlos (1978), [2]Barros de Oliveira (1990)
	Angiquinho (Goiás, Niquelandia)	garnierite[1]	[1]Colin *et al*. (1990)
	Jacuba (Goiás, Niquelandia)	pimelite and NI-smectite[1]	[1]Colin *et al*. (1990)
	São José do Tocantins (Goiás)		[1]Pecora (1944)
Canada	Middle Arm Brook Prospect (Newfoundland and Labrador, Baie Verte Peninsula, Advocate Ophiolite complex)	népouite[1]	[1]Escayola *et al*. (2011)
Colombia	Cerro Matoso S.A. (Córdoba Department, Municipio de Montelíbano)	chlorite-nimite[1,2,3], pimelite[2], sepiolite[2], Fe-Ni-smectites[2], népouite[3]	[1]López-Rendón (1986), [2]Gleeson *et al*. (2004), [3]Bunjaku *et al*. (2011)
Czech Republic	Kremze/Krems (Bohemia/Böhmen, South Bohemia Region, České Budějovice/Budweis)	[1]pimelite	[1]Brindley *et al*. (1979)
Dominican Republic	Falcondo Mine (La Vega Province, Bonao, Monseñor Nouel)	népouite[1], falcondoite[3,5,6], pimelite[8]	[1]Brindley & Wan (1975), [2]Springer (1976), [3]Lewis *et al*. (2006), [4]Proenza *et al*. (2008), [5]Tauler *et al*. (2009), [6]Galí *et al*. (2012), [7]Marchesi *et al*. (2012), [8]Villanova-de-Benavent *et al*. (2014)
Germany	Callenberg open cuts (Saxony, Glauchau, Callenberg)	pimelite[1]	[1]Springer (1974)
	Hans Georg Mine (Saxony, Vogtland, Plauen, Jocketa-Neuensalz District, Röttis; labelled "Voigtland" in the literature)	connarite[2], röttisite[1]	[1]Breithaupt (1859), [2]Springer (1974)
Greece	Pavlos	népouite[1]	[1]Brindley & Wan (1975)
India	Nuggihalli schist belt (Mysore State)	7 Å garnierite, 10 Å garnierite[1]	[1]Naganna & Phene (1968)
	Sukinda (Jajpur District, Orissa)	népouite, chlorite, kerolite-pimelite, smectite(montmorillonite) and sepiolite[1]	[1]Som & Joshi (2002)
Indonesia	Petea and Soroako/Soroaka/Sorowako Mines (Sulawesi/Celebes Island, Sulawesi Selatan Province/South Sulawesi Province, Soroako)	pimelite[1], mixture of 7 Å garnierite and 10 Å garnierite[4], sepiolite[4], smectite[4]	[1]Brindley *et al*. (1979), [2]Golightly (1979), [3]Sufriadin *et al*. (2011), [4]Sufriadin *et al*. (2012)
	Pomalaa (Sulawesi/Celebes Island, Sulawesi Tenggara Province)	népouite[1], pimelite[2]	[1]Brindley & Wan (1975), [2]Brindley *et al*. (1979)
	Sua-Sua (East Simeulue)	pimelite[1]	[1]Brindley *et al*. (1979)
	Kolonodale Deposit (Sulawesi/Celebes Island, Sulawesi Tengah Province/Central Sulawesi Province, Petasia)	népouite[1], pimelite[1]	[1]Fu *et al*. (2010), [2]Fu *et al*. (2014)
Ivory Coast	Sipilou and Moyango areas (Western Ivory Coast)	Ni-serpentines and Ni-smectites[1]	[1]Nahon *et al*. (1982)
Japan	Miyagawa Mine (Nagano Prefecture, Suwa-gôri, Miyagawamura)	garnierite[1]	[1]Sudo & Anzai (1942)
	Wakayama Mine (Ôita Prefecture, Mie-mati)	garnierite[1]	[1]Sudo & Anzai (1942)
Kosovo	Glavika Laterite Mine (District of Prishtina, Glavika)	garnierite[1]	[1]Abazi et al. (2012)
	Golesh Mountain (District of Prishtina, Kosovo Polje; labeled "Goles, Yugoslavia" in the literature)	pimelite[1,2], garnierite[3]	[1]Brindley & Hang (1973), [2]Brindley *et al*. (1979), [3]Abazi *et al*. (2012)
Madagascar	Valozoro/Valojoro (Fianarantsoa Province, Matsiatra Region, Ambohimahasoa District)	népouite[1]	[1]Brindley & Wan (1975)
	Ambatondrazaka (Toamasina Province, Tamatave, Alaotra-Mangoro Region, Ambatondrazaka District)	pimelite[1]	[1]Brindley et al. (1979)
Morocco	Aït Ahmane (Souss-Massa-Draâ Region, Ouarzazate Province, Tazenakht, Bou Azzer District)	pimelite[1], népouite[1]	[1]Ducloux et al. (1993), [2]Favreau & Dietrich (2006)
New Caledonia	Goro (Southern Province, Yaté Commune)	népouite[1], pimelite[1]	[1]Wells *et al*. (2009)
	Méa Mine (Northern Province, Kouaoua)	népouite[1]	[1]Glasser (1907)
	Nakéty Mine (Southern Province, Canala Commune)	garnierite[1], népouite[2], pimelite[3]	[1]Kato (1961), [2]Brindley & Wan (1975), [3]Brindley *et al*. (1979)
	Népoui (Northern Province, Nouméa Commune)	népouite[1,2,3], kerolite[4]	[1]Glasser 1907, [2]Caillère 1936, [3]Maksimović (1973), [4]Gerard & Herbillon (1983)
	Nouméa	garnierite[1]	[1]Springer (1974)
	Paragraphe Mine (Northern Province, Kua River)	népouite[1]	[1]Glasser (1907)
	Pita	talc+serpentine garnierite[1]	[1]Kato (1961)

APPENDIX A1.2. (CONTINUED).

Country	Locality	Ni-phyllosilicates	References
New Caledonia	Poum	chrysotile+talc+quarz garnierite[1], antigorite garnierite[1]	[1]Kato (1961)
	Poya	7 Å garnierite[1]	[1]Ogura (1986)
	Reis II Mine (Northern Province, Nouméa Commune)	népouite[1]	[1]Glasser (1907)
	Theodie	garnierite (quartz+talc)[1], népouite[2], garnierite[3]	[1]Kato (1961)
	Thio	talc+antigorite garnierite[1]	[1]Kato (1961), [2]Springer (1974), [3]Gerard & Herbillon (1983)
	Union Mine (Northern Province, Canala Commune)	népouite[1]	[1]Glasser (1907)
	Young-Australia Mine (Southern Province, Comboui River)	népouite[1]	[1]Glasser (1907)
	Undefined locality in New Caledonia	nouméite[1,2], deweylite[3] garnierite[2,3,6,8,10], 7 Å garnierite[4], népouite [5,7,9], pimelite[9]	[1]Des Cloizeaux (1878), [2]Liversidge (1874b), [3]Garnier (1878), [4] Brindley & Hang (1973), [5] Maksimović (1973), [6]Springer (1974), [7]Brindley & Wan (1975), [8]Poncelet (1979), [9]Manceau & Calas (1985), [10]Talovina *et al*. (2008)
Norway	Foldalen	nickel-gymnite[1]	[1]Münster (1892)
Philippines	Loreto (Mindanao, Caraga Region, Dinagat Islands Province, Dinagat Island)		[1]Wang (2010)
	Rio Tuba and Pulot	10 Å garnierite and mixture of 7+10 Å garnierite[1]	[1]Ogura (1986)
Poland	Kozmice/Kosemitz/Kosemutz (Silesia)	pimelite[1,3], chrysoprase[1], népouite[2]	[1]Klaproth (1788), [2]Spangenberg & Müller(1949), [3]Faust (1966)
	Sobotka Mountain (Lower Silesia, Dolnośląskie, Gogołów-Jordanów Massif, Wiry)	pimelite[1]	[1]Haranczyk & Prchazka (1974)
	Szklary/Gläsendorf (Lower Silesia, Dolnośląskie, Ząbkowice District, Ząbkowice, Frankenstein)	[1], pimelite[2,3], schuchardite[2]	[1]Spangenberg & Müller(1949), [2]Springer (1974), [3]Brindley *et al*. (1979)
Russia	Buruktal (Urals Region)	-	[1]Talovina *et al*. (2008), [2]Talovina *et al*. (2009)
	Cheremshanskoe Mine (Urals Region, Southern Urals, Chelyabinsk Oblast', Ufaley/Ufalei District)	chrysotile-pecoraite[1], népouite[1], talc[1], clinochlore[1], sepiolite[1], smectite[1]	[1]Talovina *et al*. (2008), [2]Talovina *et al*. (2009)
	Elov Mine (Urals Region, Serov District, Kola Massif)	pecoraite[1], lizardite[1], phlogopite[1]	[1]Talovina *et al*. (2008), [2]Talovina *et al*. (2009)
	Nizhny Tagil (Urals Region, Sverdlovsk Oblast')	α-kerolite[1], β-kerolite[1], deweylite[1], karpinskite[1], Ni-montmorillonite[1]	[1]Rukavishnikova (1956), [2]Talovina *et al*. (2008), [3]Talovina *et al*. (2009)
	Sakhara (Urals Region)	lizardite[1], clinochlore[1], sepiolite[1], smectite[1]	[1]Talovina *et al*. (2008), [2]Talovina *et al*. (2009)
	Sinar (Urals Region)	pecoraite[1], talc[1], clinochlore[1], sepiolite[1]	[1]Talovina *et al*. (2008), [2]Talovina *et al*. (2009)
	Urals Region (unspecified)	garnierite[1], revdanskite[1]	[1]Springer (1974), [2]Talovina *et al*. (2009)
Serbia	Ba	népouite[1], pimelite[2]	[1]Maksimović (1973), [2]Brindley *et al*. (1979)
South Africa	Scotia Talc Mine (Mpumalanga Province, Barberton District, Bon Accord)	nimite[1,3,5], willemseite[2,4], népouite[6]	[1]De Waal & Hiemstra (1968a), [2]De Waal & Hiemstra (1968b), [3]De Waal (1970a), [4]De Waal (1970b), [5]Springer (1974), [6]Tredoux *et al*. (1989)
	Morokweng Impact Structure (North West Province)	willemseite[1]	[1]Andreoli *et al*. (1997)
South Korea	Buksite and Namsite (Gyeonggi-do/Kyonggi-do, Gwancheon city/ Kwancheon)	népouite[1], pimelite[1], pecoraite[1]	[1]Song *et al*. (1995)
Spain	Aguablanca Ni-Cu Deposit (Extremadura)	népouite[1]	[1]Suárez *et al*. (2011)
Taiwan	Kwanson	népouite[1]	[1]Brindley & Wan (1975)
USA	Trotter Mine/Lehigh Mine (New Jersey, Sussex Co., Franklin Mining District, Franklin Mine)	de saulesite[1]	[1]Wilkerson (1962)
	California (unspecified)	Ni-lizardite[1,2]	[1]Montoya & Baur (1963), [2]Maksimović (1973)
	Big Ivy and Ivy River (North Carolina, Buncombe Co.)	genthite[1]	[1]Genth (1891)
	Durham (North Carolina)	10 Å garnierite [1]	[1]Brindley & Hang (1973)
	Webster-Addie ultramafic ring dike (North Carolina, Jackson Co., Webster-Balsam)	genthite[1,2], Ni-vermiculite[3,5], Ni-serpentine[3,6], népouite[4], talc[4]	[1]Genth (1891), [2]Ross (1925), [3]Ross & Shannon (1926), [4]Ross *et al*. (1928), [5]Springer (1974), [6]Brindley & Wan (1975)
	Democrat (North Carolina)	pimelite[1]	[1]Brindley *et al*. (1979)
	Culsagee Mine (North Carolina, Macon Co., Cowee Valley, Ellijay District, Franklin)	genthite[1], kerolite[1]	[1]Genth (1891)
	Corundum Hill (North Carolina, Macon Co., Cowee Valley, Ellijay District, Franklin)	deweylite[1]	[1]Genth (1891)
	Nickel Mountain, Hanna Nickel Mine (Oregon, Douglas Co., Riddle District)	genthite[1]	[1]Kay (1906)
	Riddle Mine (Oregon, Douglas Co., Riddle District, Riddle District)	garnierite[2,4], 7 Å garnierite [3], 10 Å garnierite [3], sepiolite[4], népouite[5]	[1]Clarke (1888, 1890, 1920), [2]Pecora *et al*. (1949), [3]Brindley & Hang (1973), [4]Springer (1974), [5]Brindley & Wan (1975)
	Piney Mountain (Oregon, Douglas Co.)	garnierite[1], nouméite[1]	[1]Hood (1883)
	(Pennsylvania, Chester Co.)	kerolite[1]	[1] Springer (1974)
	(Pennsylvania, Lancaster Co.)	genthite[1,2]	[1] Faust (1966), [2]Springer (1974)
	Wood's Chrome Mine (Pennsylvania, Lancaster Co., State Line Chromite District)	deweylite[1], genthite[1]	[1]Genth (1874)
Venezuela	Loma de Hierro	mixture of 7 Å garnierite and 10 Å garnierite []	[1]Lewis *et al*. (2006), [2]Soler *et al*. (2008)

APPENDIX A2. Sample photographs and XRD patterns of the Ni-free Mg-phyllosilicates analysed by DTA-TG, EMP and Raman spectroscopy (see **Chapters 4** and **6**) to be compared to the Ni-bearing Mg-phyllosilicates from the Falcondo Ni-laterite deposit: a) lizardite from Lizard, Cornwall (sample LIZ-1); b) lizardite from Elba Island (LIZ-2); c) chrysotile from Huelva (CRIS); d) talc from León (TLC); e) sepiolite from Setcases (SEP).

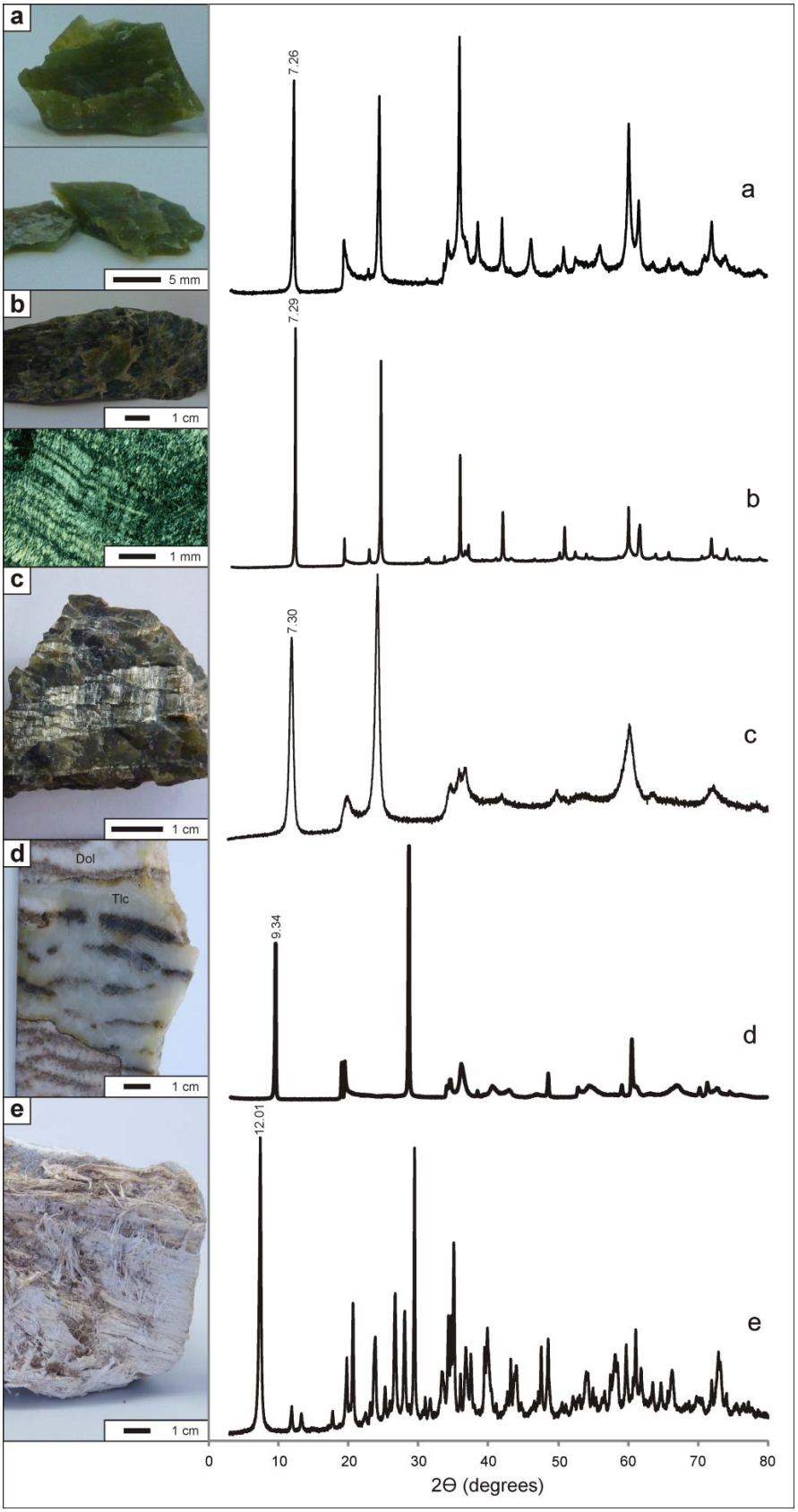

APPENDIX A3

APPENDIX A3. Complete list of the Raman bands detected using the 325, 785, 1064 and 532 nm lasers in the garnierites from the Falcondo Ni-laterite deposit, compared to the Raman bands obtained from the Mg-phyllosilicates from other localities and Mg-Ni-phyllosilicates from the literature. Legend: s = strong, m = medium, w = weak, sh = shoulder, d = doubtful.

325 nm		785 nm				1064 nm					532 nm						532 nm							
Type IV (GAR-4)	**Type V (FALC-4)**	**Type I (LC-101)**	**Type III (GAR-3)**	**Type IV (GAR-6)**	**Type V-Sep (FALC-1)**	**Type I (09GAR-1)**	**Type II (LC-100)**	**Type III (GAR-2)**	**Type IV (GAR-6)**	**Type V (FALC-3)**	**Type I (09GAR-1)**	**Type II (LC-100)**	**Type III (GAR-2)**	**Type IV (LC-100)**	**Type V-Sep (FALC-4)**	**Type V-Fal (FALC-3)**	**Lz (LIZ-1)**	**Lz (LIZ-2)**	**Ctl (CRIS)**	**Tlc (TLC)**	**Sep (SEP)**	Ctl	**Kloprogge *et al.* (1999) 633 nm**
																						-	-
				105**s**																		-	-
																						-	-
																						-	-
											127.6**w**											-	-
										131.7**s**							135.1**w**	135.1**w**	135.1**m**			-	-
																						-	-
			183**s**	188**s**			186.1**s**	183.6**s**	186.7**s**			178.8**w**	182.4**w**	184.3**s**							182**d**		
					195**s**					195.5**s**					195.5**w**	193.4**w**				196.6**s**		199	M-O
			208**m**					209.3**m**														-	-
		230**s**				230.6**s**	230.5**s**				226.1**m**	229.7**w**					234.7**s**	239**m**	235.3**s**			231	M-O
					263**w**							271.3**w**	271.3**w**									-	-
				292**w**	294**w**																	-	-
																						-	-
					332**w**					333.8**w**													
					354**w**	343.0**w**	344.6**sh**												355.9**w**			345	M-O
360**m**			366**m**	361**w**		364.4**sh**	367.7**sh**	368.4**m**	363.9**w**				366.4**w**							363.4**w**			
																						-	-
		384**s**		383**w**	385**m**	385.8**s**	384.2**s**		385.1**w**	384.9**w**	382.5**m**	382.5**m**		382.5**w**			388.3**m**	394.2**s**	389.8**s**			388	M-O
																						-	-
																						-	-
																						-	-
																						-	-
															492.5**w**	481.7**s**						-	-
																						-	-
		531**w**																				-	-
																						-	-
						618.8**w**	620.3**w**												625.2**w**			-	-
		634**w**			634**d**																	629	M-O/Si-O bridging or stretching, also 623 Lewis (1996) and 622 Bard (1997)
							649.7**sh**		639.6**m**	639.5**w**											644.5**d**	-	-
674**s**	673**d**		679**s**	677**m**	671**s**	668.2**sh**	674.3**s**	680.4**s**	675.9**s**	673.4**s**			678.6**s**	671.7**s**	673.6**s**	670.0**s**				679.6**s**	675.2**d**	-	-
		690**s**				686.5**s**	686.5**s**				688.9**m**	687.2**m**					689.8**m**	694.2**m**	694.2**s**			692	Si-O bridging or stretching, also 692 Lewis (1996) and 622 Bard (1997)
					706**d**																	-	-
																						-	-
																						-	-
																						-	-
									822.9**w**													-	-

APPENDIX A3. (CONTINUED).

Ctl	Atg	Lz	**Rinaudo *et al*. (2003) 1064 nm**	Atg	Lz	Ctl 0-1%wt Al_2O_3	Ctl 2-3%wt Al_2O_3	Ctl 4-5%wt Al_2O_3	Ctl 2-3%wt NiO	**Groppo *et al*. (2006) 632.8 nm**	Pec	Pec	Ctl	**Frost *et al*. (2008) 633 nm**	Tlc	**Blaha & Rosasco (1978 514.5 nm**	Tlc	**Rosasco & Blaha (1980) 514.5 nm**
-	-	-	-	-	-	-	-	-	-	-	-	-	-	-	-	-	64	-
-	-	-	-	-	-	-	-	-	-	-	-	-	-	-	109**s**	external lattice mode region	109**s**	parallel "brucite"
-	-	-	-	-	-	-	-	-	-	-	-	-	-	-	113**s**	external lattice mode region	113**s**	parallel "brucite"
-	-	-	-	-	-	-	-	-	-	-	-	-	-	-	119**s**	external lattice mode region	119**s**	-
-	-	-	-	-	-	-	-	-	-	-	-	-	-	-	-	-	-	-
-	-	-	-	-	-	-	-	-	-	-	-	-	-	-	-	-	-	-
-	-	-	-	-	-	-	-	-	-	-	-	151	-	-	-	-	-	-
-	-	-	-	-	-	-	-	-	-	-	-	-	-	-	-	-	-	-
199	-	-	A1g mode of Mg(O,OH)6 (Kloprogge *et al*., 1999)	197-202	195-197	192	191	193	194	Mg(O,OH)6 groups vibrations	-	194	-	-	197**vs**	Metal-O	197**vs**	perpendicular "brucite"
-	-	-	-	-	213-214	212	211	213	213	vibrations of O-H-O groups	-	-	-	-	-	-	-	-
231, 231**s**	230**vs**	233**vs**	vibrations of O-H-O groups (also Kloprogge *et al*., 1999)	230-231	234-236	235	232	233	234	vibrations of O-H-O groups	-	235	-	OSiO bend	232**m**	Metal-O	232**m**	-
-	-	-	-	-	-	-	-	-	-	-	-	-	-	-	-	-	-	-
-	-	-	-	-	-	-	-	-	-	-	-	-	-	-	294**m-s**	Metal-O	294**m**	-
304, 318	-	-	bending of SiO4 (Kloprogge *et al*., 1999)	-	-	-	-	-	-	-	-	-	-	-	-	-	307**vw**	-
-	-	-	-	-	-	-	-	-	-	-	-	-	-	-	335**w**	Metal-O	-	-
345, 345**m**	-	350**m**	bending of SiO4 (also Kloprogge *et al*., 1999)	-	-	348	-	-	-	bending of SiO4	-	-	-	-	-	-	355**w**	-
-	-	-	-	-	-	-	-	-	-	-	-	-	-	-	366**s**	Metal-O	366**s**	-
374	-	-	symmetric Mg-OH vibrations (Kloprogge *et al*., 1999)	-	-	-	-	-	-	-	-	-	-	-	-	-	-	-
388, 389**vs**	375**vs**	388**vs**	symmetric v5(e) SiO4 (also Kloprogge *et al*., 1999)	379	380-388	391	390	394	392	symmetric v5(e) SiO4	-	-	-	-	383**w**	Metal-O	383**w**	-
-	-	-	-	-	-	-	-	-	-	-	-	397	-	NiO	-	-	-	-
432	-	-	antisymmetric Mg-OH translation (Kloprogge *et al*., 1999)	-	-	-	-	-	-	-	447	-	432	(Mg,Ni)-O stretch (Pec1), OSiO bend (Ctl)	435**m-s**	Metal-O	435**m**	E1 parallel silicate
458	-	-	v3(a1) SiO4 (Kloprogge *et al*., 1999)	-	-	-	-	-	-	-	-	451	-	(Mg,Ni)-O stretch	456**m-s**	Metal-O	456**m**	OH-transition
466	-	-	Mg-OH translation + v6(e) SiO4	463	-	-	-	-	-	Mg-OH translations + v6(e) SiO4 vibrations	-	-	466	(Mg,Ni)-O stretch	471**m-s**	-	471**m**	perpendicular "brucite"
-	-	-	-	-	-	-	-	-	-	-	-	-	-	-	-	-	-	-
-	-	510**m** (506,515)	SiO4-AlO4 deformation modes	-	-	-	-	-	-	-	512	-	-	(Mg,Ni)-O stretch	511**w**	-	511**vw**	OH libration
-	520**m**	-	-	-	-	-	-	-	-	-	-	-	-	-	519**w**	-	519**vw**	vs A1
607	-	-	libration of inner Mg-OH (Kloprogge *et al*., 1999)	-	-	-	-	-	-	-	-	616	607	NiO libration	-	-	-	-
622, 620**m**	-	-	antisymmetric OH-Mg-OH translation modes (Kloprogge *et al*., 1999)	-	-	-	-	-	-	-	-	-	-	-	-	-	-	-
629	635**m**	630**m**	antisymmetric OH-Mg-OH translation modes	-	-	-	-	-	-	-	-	-	629	OSiO bridge	-	-	-	-
				640	640	641	640	640	640	antisymmetric OH-Mg-OH translation modes	-	-	-	-	-	-	-	-
-	-	-	-	-	-	-	-	-	-	-	679	-	-	OSiO bridge	679**vs**	Si-Ob-Si symmetric stretching mode	679**vs**	vs E2 Si-O-Si
692, 692**vs**	683**vs**	690**vs**	vs Si-Ob-Si (also Kloprogge *et al*., 1999)	683-684	688-693	694	693	694	695	vs Si-Ob-Si	-	-	692	OSiO bridge	-	-	-	-
705, 709	-	-	Mg-OH outer symmetric translation modes (Kloprogge *et al*., 1999)	-	-	-	-	-	-	-	-	-	709	NiOH deformation	-	-	-	-
-	-	-	-	-	-	-	-	-	-	-	-	761	-	OSiO bridge	-	-	-	-
-	-	-	-	-	-	-	-	-	-	-	-	-	-	-	788**m**	-	789**m**	-
-	-	-	-	-	-	-	-	-	-	-	-	-	-	-	795**m**	-	795**m**	vSiO- (B1)
-	-	-	-	-	-	-	-	-	-	-	-	821	-	NiOH deformation	-	-	-	-

APPENDIX A3. (CONTINUED).

Ker	**Cathelineau *et al*. (2015) 514.5 nm**	Sep	**McKeown *et al*. (2002) 1064 nm**	bands (laser wavelength listed with the reference)	**RRUFF**
-	**-**	-	**-**	-	-
108**w**	**-**	100**w**		105**m**	talc R050050(514)
-	**-**	-		-	-
	-	-		-	-
-	**-**	-		-	-
140**m**	**-**	-		-	-
-	**-**	160**w**		-	-
187**m**	**-**	-		182**s**, 186**s**	talc R080080(514), R050050(532)
-	**-**	200**m**		201**s**, 194**s**, 193**s**, 194**s**, 191**s**	lizardite R060006, talc R040137(514), R050058(514,532), willemseite R061112(532)
-	**-**	-		-	-
240**m**	**-**	-		233**m**,**s**	chrysotile R070088, R070355
-	**-**	260**w**		265	sepiolite R070311(532)
-	**-**	290**w**		294**w**, 292**w**, 293**w**, 292**w**, 291**w**	talc R040137(514), R050050(514,532), R050058(514,532)
-	**-**	-		309	sepiolite R070311(785)
-	**-**	340**w**		-	-
-	**-**	-	silicate sheet and Mg octahedra deformations	345**w**, 352**w**	chrysotile R070088, R070355
-	**-**	-		363**m**, 361**m**, 359**m**, 361**m**, 363**m**	talc R040137(514), R050050(514,532), R050058(514,532)
-	**-**	-		-	-
-	**-**	380**w**		391**s**, 386**s**	chrysotile R070088, R070355
400**s**	**-**	-		-	-
-	**-**	-		440**w**, 435**w**, 444**w**, 432**w**, 435**w**	talc R040137(514), R050050(514,532), R050058(514,532)
-	**-**	-		-	-
-	**-**	-		476**w**, 474**w**, 467**w**	chrysotile R070355, talc R050058(514,532)
-	**-**	-		-	-
-	**-**	-		-	-
-	**-**	-		519**s**	lizardite R060006
-	**-**	-		-	-
-	**-**	-		-	-
-	**-**	-		623**w**, 624**w**	chrysotile R070088, R070355
-	**-**	-	silicate sheet and Mg octahedra deformations	647	sepiolite R070311(532)
-	**-**	675**s**		679**s**, 681**s**, 678**s**, 675**s**, 675**s**, 675**s**	talc R040137(514), R050050(514,532), R050058(514,532), willemseite R061112(532)
-	**-**	-	**-**	693**s**, 689**s**	chrysotile R070088, R070355
700**s**	**-**	-	**-**	-	-
-	**-**	-	**-**	-	-
-	**-**	-	**-**	-	-
-	**-**	-	**-**	-	-
-	**-**	-	**-**	-	-

APPENDIX A3. (CONTINUED).

325 nm		785 nm				1064 nm					532 nm						532 nm						
Type IV (GAR-4)	Type V (FALC-4)	Type I (LC-101)	Type III (GAR-3)	Type IV (GAR-6)	Type V-Sep (FALC-1)	Type I (09GAR-1)	Type II (LC-100)	Type III (GAR-2)	Type IV (GAR-6)	Type V (FALC-3)	Type I (09GAR-1)	Type II (LC-100)	Type III (GAR-2)	Type IV (LC-100)	Type V-Sep (FALC-4)	Type V-Fal (FALC-3)	Lz (LIZ-1)	Lz (LIZ-2)	Ctl (CRIS)	Tlc (TLC)	Sep (SEP)	Ctl	Kloprogge *et al.* (1999) 633 nm
																						-	-
																						-	-
981**m**																						-	-
	993**d**																					-	-
																						-	-
																						-	-
																						-	-
																						-	-
	1098**d**																					1102	antisymmetric stretch Si-O-Si perpendicular, also 1100 Lewis (1996) and 1105 Bard (1997)
																					1114.3**d**	-	-
																						-	-
																						-	-
																					1187.5**d**	-	-
																						-	-
	1384**d**																					-	-
																						-	-
1610**s**	1612**s**																				1610.4**d**	-	-
																						-	-
																						-	-
																						-	-
			2937**d**																			-	-
			3069**d**																		3072.6**d**	-	-
																						-	-
																						-	-
																						-	-
																						-	-
																						-	-
																						-	-
												3629.2**m**										-	-
												3647.1**s**										3643	inner OH stretch
												3667.3**s**		3674.4**w**			3678.5**s**			3678.5**m**		3678	OH stretch, also 3685 Bard (1997)
											3683.9**s**	3686.3**s**				3681.7**w**	3680.3**w**			3685.1**s**		3686, 3696	OH stretch or external OH stretch, also 3700 Bard (1997)
																	3706.1**w**	3696.1**s**				-	-

APPENDIX A3. (CONTINUED).

Ctl	Atg	Lz	**Rinaudo *et al*. (2003) 1064 nm**	Atg	Lz	Ctl 0-1%wt Al_2O_3	Ctl 2-3%wt Al_2O_3	Ctl 4-5%wt Al_2O_3	Ctl 2-3%wt NiO	**Groppo *et al*. (2006) 632.8 nm**	Pec	Pec	Ctl	**Frost *et al*. (2008) 633 nm**	Tlc	**Blaha & Rosasco (1978) 514.5 nm**	Tlc	**Rosasco & Blaha (1980) 514.5 nm**
-	-	-	-	-	-	-	-	-	-	-	-	-	-	-	-	-	-	-
-	-	-	-	-	-	-	-	-	-	-	921	930	-	in-plane SiO stretch (Pec1), -(Pec2)	-	-	-	-
-	-	-	-	-	-	-	-	-	-	-	-	979	-	in-plane SiO stretch	-	-	-	-
-	-	-	-	-	-	-	-	-	-	-	-	-	-	-	-	-	-	-
-	-	-	-	-	-	-	-	-	-	-	-	-	-	-	1018**m**	Si-Onb-Si stretching mode	1018**m**	TO-E1 parallel vas Si-O-Si
-	1044**s**	-	vas Si-Ob-Si	-	-	-	-	-	-	-	-	-	-	-	1049**m**	Si-Onb-Si stretching mode	1049**m**	LO-A1 perpendicular vas Si-O-
-	-	-	-	-	-	-	-	-	-	-	-	1075	-	in-plane SiO stretch	-	-	-	-
-	-	-	-	-	-	-	-	-	-	-	-	-	-	-	-	-	-	-
1105m	-	1096**d**	vas Si-Onb	-	-	-	-	-	-	-	1102	-	1100	antisymmetric SiO stretch	-	-	-	-
-	-	-	-	-	-	-	-	-	-	-	-	-	-	-	-	-	-	-
-	-	-	-	-	-	-	-	-	-	-	-	1128	-	antisymmetric SiO stretch	-	-	-	-
-	-	-	-	1045	-	-	-	-	-	vas Si-Ob-Si	-	-	-	-	-	-	-	-
-	-	-	-	-	-	-	-	-	-	-	-	-	-	-	-	-	-	-
-	-	-	-	-	-	-	-	-	-	-	1219	-	-	-	-	-	-	-
-	-	-	-	-	-	-	-	-	-	-	-	1384	-	-	-	-	-	-
-	-	-	-	-	-	-	-	-	-	-	-	1593	-	water HOH bend	-	-	-	-
-	-	-	-	-	-	-	-	-	-	-	-	-	-	-	-	-	-	-
-	-	-	-	-	-	-	-	-	-	-	1641	-	-	water HOH bend	-	-	-	-
-	-	-	-	-	-	-	-	-	-	-	-	2854	-	organic impurities	-	-	-	-
-	-	-	-	-	-	-	-	-	-	-	-	2896	-	-	-	-	-	-
-	-	-	-	-	-	-	-	-	-	-	-	2934	-	-	-	-	-	-
-	-	-	-	-	-	-	-	-	-	-	-	-	-	-	-	-	-	-
-	-	-	-	-	-	-	-	-	-	-	-	3271	-	water OH stretch	-	-	-	-
-	-	-	-	-	-	-	-	-	-	-	-	3460	-	-	-	-	-	-
-	-	-	-	-	-	-	-	-	-	-	-	3535	-	-	-	-	-	-
-	-	-	-	-	-	-	-	-	-	-	-	3586	-	-	-	-	-	-
-	-	-	-	-	-	-	-	-	-	-	-	3613	-	inner OH stretch	-	-	-	-
-	-	-	-	-	-	-	-	-	-	-	-	-	-	-	-	-	-	-
-	-	-	-	-	-	-	-	-	-	-	3645	3638	3643	inner OH stretch (Pec1, Ctl), inner surface OH stretch (Pec2)	-	-	-	-
-	-	-	-	-	-	-	-	-	-	-	-	-	-	-	3676**s**	-	3675**m**	OH stretch
-	-	-	-	-	-	-	-	-	-	-	-	-	-	-	-	-	-	-
-	-	-	-	-	-	-	-	-	-	-	3695	-	3696	inner surface OH stretch	-	-	-	-

APPENDIX A3. (CONTINUED).

Ker	**Cathelineau *et al*. (2015) 514.5 nm**	Sep	**McKeown *et al*. (2002) 1064 nm**	bands (laser wavelength listed with the reference)	**RRUFF**
840**w**	-	-	-	-	-
-	-	-	-	-	-
-	-	-	-	-	-
-	-	-	-	-	-
-	-	-	-	-	-
-	-	-	-	1052**w**, 1052**w**, 1052**w**	talc R040137(514), R050058(514,532)
-	-	-	-	1076**w**	talc R050050(514)
-	-	1080**w**	Si-Onb	1088**w**	chrysotile R070355
-	-	-	-	1109**w**	chrysotile R070088(514)
-	-	-	-	1115**w**	talc R050050(514)
-	-	-	-	-	-
-	-	-	-	1158**s**	lizardite R060006
-	-	-	-	-	-
-	-	-	-	-	-
-	-	-	-	-	-
-	-	-	-	-	-
-	-	-	-	-	-
-	-	-	-	-	-
-	-	-	-	-	-
-	-	-	-	-	-
-	-	-	-	-	-
-	-	-	-	-	-
-	-	-	-	-	-
-	-	-	-	-	-
-	-	-	-	-	-
-	-	-	-	-	-
-	-	-	-	-	-
-	-	-	-	-	-
-	-	-	-	-	-
-	-	-	-	-	-
-	-	-	-	-	-
3700	OH stretching	-	-	-	-